Understanding aerosol-fog interactions during nocturnal radiation fog

Craig Yaw Appigyei Poku

Submitted in accordance with the requirements for the degree of

Doctor of Philosophy

University of Leeds

School of Earth and Environment

September 2019

The candidate confirms that the work submitted is his own, except where work which has formed part of jointly-authored publications has been included. The contribution of the candidate and the other authors to this work has been explicitly indicated below. The candidate confirms that appropriate credit has been given within the thesis where reference has been made to the work of others.

Chapter's 1 and 4 mostly contains material from the publication:

Poku, C., Ross, A.N., Blyth, A.M., Hill, A.A. and Price, J.D., (2019). How important are aerosol–fog interactions for the successful modelling of nocturnal radiation fog? *Weather.*

Craig Poku was the lead author of the paper. He performed the experiments discussed in the study, as well as conducting the analysis. The co-authors provided advice and suggestions for further analysis, and helped with the grammar and structure of the final manuscript.

Acknowledgements

First, I would like to thank my supervisors Alan Blyth, Andrew Ross and Adrian Hill. Your supervision and guidance have contributed to making me into the scientist I am today, by encouraging big thinking and to pursue all ideas, regardless of how crazy.

Next, I would like to extend my gratitude to the Natural and Environment Research Council, as well as the Met Office for the financial assistance throughout my PhD. The nature of science is that it's never a solo journey and that collaboration is key to a successful outcome. With that in mind, a huge thank you to Chris Deaden, Jeremy Price, Ian Boutle and Richard Rigby for their constant support with the project, both on the science and technical side. In addition, I would like to give a special mention to the Met Office Research Unit in Cardington, who were extremely helpful in setting up my observational cases used within this project. I would also like to thank the Leeds Cloud Physics group, in particular, Daniel Grosvenor, who was excellent in providing insight into my work whenever I was stuck or needed a different perspective.

4 years is a long period to focus on one topic and it's been a struggle at points. However, I couldn't have got through this without the support of my office family. Namely Sam Hardy, Anne Barber, Sam Clarke, Rory Fitzpatrick, Dean Walker, Jenny Wu and Tash Aylett. You've all dealt with my various moods and I'm so grateful for all of you during my doctorate academic journey. I'm also giving a special shout out to Beth Woodhams. Beth, you have been with me from the start and see you submit your PhD the same day as me made the writing and handing in process that little bit more special. Thank you for being a brilliant friend, accepting my crazy conversations and just being amazing in

every way!

I would also like to thank the crazy community that I'm part of, also known as Jiu-Jitsu. You've all heard me use cloud references both on and off the mat and I'm so glad that you helped me get through this PhD journey. Special thanks to Emma Wilson, Matt Chivers, Fuzz Hussain, Ian Bradley, James Probert, Sam Cobden, Callum Young and Juniata Bellham, who were all a massive support unit, even in the toughest of times. After what I call an "interesting" final year of my undergraduate degree, I pretty much said I wasn't cut out for academia. To Paul Cook, I am thankful that you saw my ability as a scientist and kept encouraging me to apply for this PhD project, even though I may have said no the first few times, and To Ed Watkins, who taught me at school always to dream big. I would like to thank the people close to me in my life, who include Charles Olisanekwu, Jameka Neil, Sam Kidman, Anshul Verma and Mairi Arthur, who have helped me stay motivated throughout the PhD even when I wanted to stop.

Finally, I would like to express my gratitude an appreciation to my mum Antoinette and dad Ernest, my aunt, Juliet and my brother, Rhys. You have all stood by me and believed in my journey to becoming a scientist. And to end this, a heartiest thank you to my best friend and partner in crime, Twinkal Sharma. You have been my rock throughout this PhD and from the phone calls to you coming up to help me post-surgery, I don't think I could have gotten through these times without you.

Abstract

Forecasting and modelling fog formation, development, and dissipation is a significant challenge. Fog dynamics involve subtle interactions between small-scale turbulence, radiative transfer and microphysics. Recent studies have highlighted the role of aerosol and related cloud microphysical properties in the evolution of fog. In this thesis, the impact of aerosol on nocturnal radiation fog is investigated. This has been done using the Met Office NERC Cloud (MONC) model, which can perform very high-resolution large eddy simulations. MONC has been coupled with a newly developed multi-moment cloud microphysics scheme (CASIM) designed to model aerosol-cloud interactions.

The initial results demonstrate the sensitivity of the fog structure to the properties of the aerosol population (e.g. number concentration). An increase in aerosol concentration results in the fog layer becoming well-mixed too quickly. This highlights the importance of aerosol during the fog's transitional period and the requirement for an accurate scheme accounting for aerosol activation.

A new aerosol activation scheme was developed to better represent the cooling mechanisms in fog. It was shown that this scheme results in a lower droplet number for a given aerosol population and hence transitions to a well-mixed fog more in line with observations.

The impact of a nucleation scavenging parameterisation in fog was investigated. It was shown that including nucleation scavenging in simulations of fog resulted in it dissipating too rapidly compared to observations. Turning on nucleation scavenging results in aerosol being depleted through sedimentation. These results also showed that accounting for additional sources of aerosol could not fully negate the impact of the nucleation scavenging

parameterisation on fog.

Overall, this thesis has demonstrated the importance of aerosol treatment during fog formation and development and has outlined recommendations to help improve the accuracy of short-term fog forecasting.

Contents

List of Figures

List of Tables

List of acronyms

ARG	Abdul-Razzak and Ghan
CASIM	Cloud AeroSol Interactive Microphysics scheme
CCN	Cloud Condensation Nuclei
CDNC	Cloud Droplet Number Concentration
GCM	General Circulation Model
IOP	Intense Observation Period
LANFEX	The Local and Non-local Fog Experiment
LEM	Large Eddy Model
LES	Large Eddy Simulation
LWC	Liquid Water Content
LWP	Liquid Water Path
MetUM	Met Office Unified Model
MO	Met Office
MONSOON	Met Office and NERC joint supercomputer system
NERC	Natural Environment Research Council
NWP	Numerical Weather Prediction
NWP	Numerical Weather Prediction
RH	Relative Humidity
RL	Residual Layer
PBL	Planetary Boundary Layer
SBL	Stable Boundary Layer

SCM	Single Column Model
SOCRATES	Suite of Community Radiative Transfer codes
TKE	Turbulent Kinetic Energy
UCLALES-SALSA	UCLA Large-Eddy Simulation Code and the Sectional - Aerosol module for Large-Scale Applications
UTC	Coordinated Universal Time

Success is like failure,
It's how you perceive it, it's what
you do with it, not how you
achieve it.

STEPHEN SONDHEIM'S *MERRILY WE ROLL ALONG*

Chapter 1

Motivation

> Don't be afraid it won't be perfect.
> The only thing to be afraid of really is
> that it won't be.
>
> Stephen Sondheim's *Company*

1.1 Radiation fog

Fog can be defined as a cloud at ground level with a surface visibility of less than 1 km (WMO, 1966). It has the ability to cause major disruption to road, aviation and marine transport, with associated economic losses that are comparable to those resulting from winter storms and hurricanes (Gultepe et al., 2007). Fog can have negative impacts on human health and the safety of certain activities. For example, thick fog on 5th September 2013 resulted in the Sheppey crossing crash in southeast England, which involved 130 vehicles and injured 60 people (BBC, 2013). More recently, thick fog across the UK in November 2018 resulted in over 62 flights cancelled and 380 delayed (Sky News, 2018). Understanding the physics behind fog is crucial in improving fog forecasting and mitigating the impact of such fog events.

Whilst there are several different types of fog (Tardif and Rasmussen, 2007), the two types most commonly experienced in the United Kingdom are radiation and advection

fog. Radiation fog is driven through radiative cooling over land (e.g. Figure 1.1), with advection fog forming as warm air passes over a colder surface (e.g. water). What both of these have in common is that they depend on several small-scale physical processes (radiative, turbulent, thermodynamical, microphysical). This will result in an air mass becoming saturated (relative humidity equal to 100%), with the consequent formation of fog. However, all of these processes interact on a subtle scale and are generally subgrid in typical models. This makes fog forecasting challenging, as they are sensitive to the parameterisation of these subgrid processes.

1.2 Aerosol-fog interactions

The Earth's atmosphere consists of small suspended particles called aerosols, which range in size and composition (Pruppacher and Klett, 2010, p.216). Aerosols are important for both clouds and fog, as they act as the substrate on which water condenses and droplets form. The growth rate of these droplets is dependent on the initial aerosol size and solubility. The aerosols are considered to be 'activated' once these droplets reach a certain size, where they can grow more easily within a saturated environment. Aerosols that can act as a substrate for droplets are known as cloud condensation nuclei (CCN). The aerosol population has been shown to impact the cloud's microphysical structure and its life span (e.g. Twomey, 1974; Albrecht, 1989), and have been studied in great depth over the last few decades, both in the context of climate (e.g. Shine and Forster, 1999; Penner et al., 2004) and meteorology (e.g. Yuan et al., 2008). Research into radiation fog spans the last 100 years (e.g. Taylor, 1917; Roach et al., 1976). However, greater recognition of the role of aerosols is more recent, with Bott (1991) showing that aerosols fundamentally control the optical thickness of radiation fog, and additional studies (e.g. Stolaki et al., 2015; Maalick et al., 2016) complementing this work.

Figure 1.2 outlines the role that aerosol–fog interactions plays in determining the formation and resulting evolution of the fog. At night, prior to fog formation, the ground and lower layers of the atmosphere will experience radiative cooling. The rate of cooling

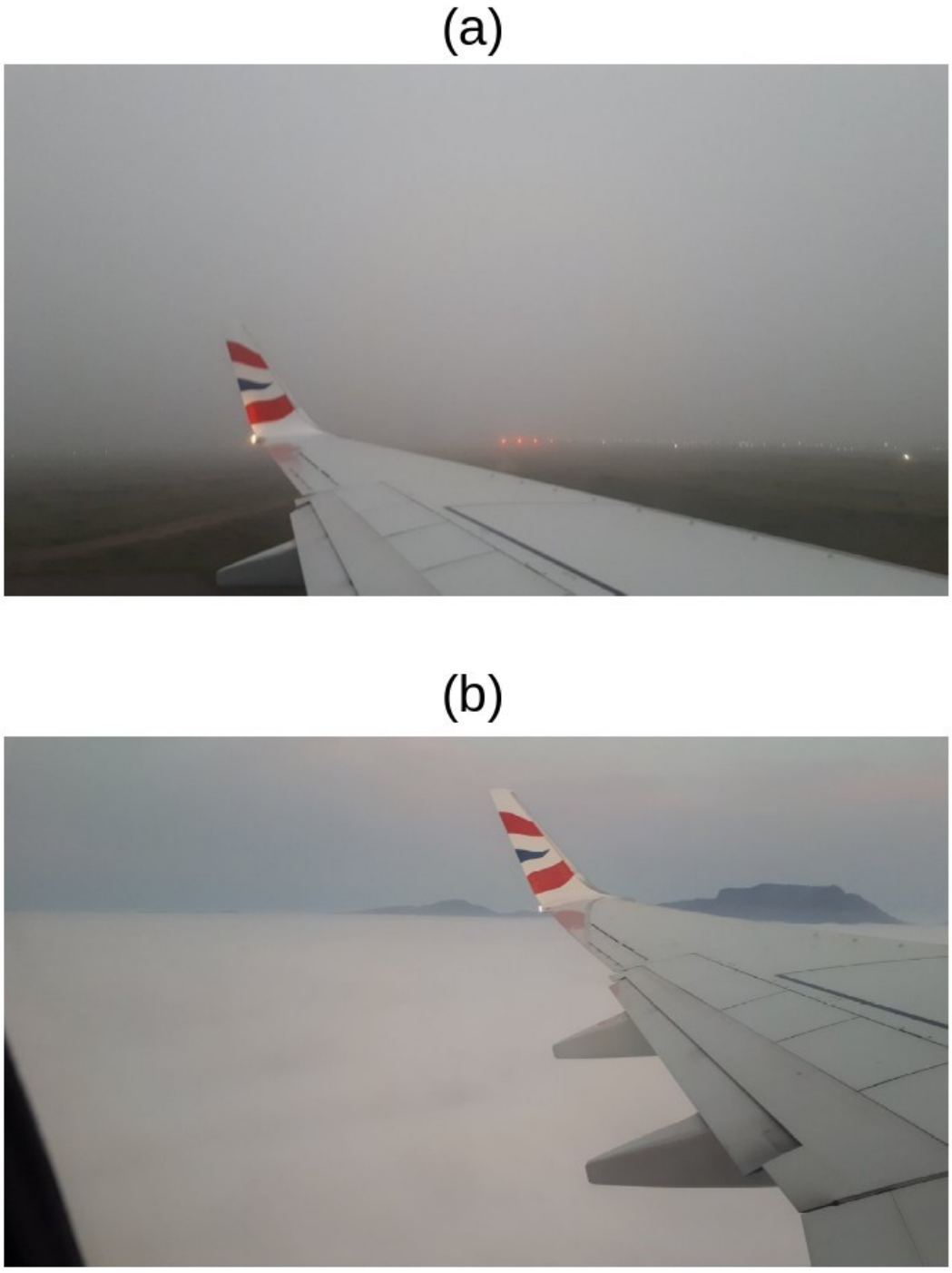

Figure 1.1: An example of a radiation fog event in Cape Town, South Africa, July 2019. (a) - Within the fog at Cape Town International Airport; (b) - Fog top.

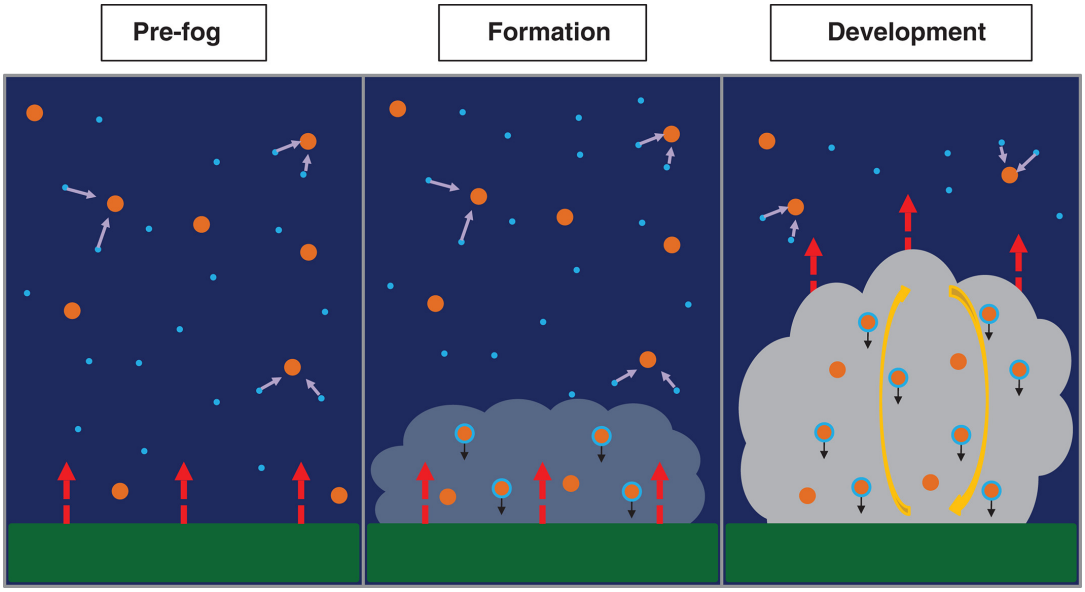

Figure 1.2: Schematic demonstrating the three stages of the evolution of nocturnal radiation fog: pre-fog, fog formation and fog development. Orange dots – CCN; light blue dots – water vapour; red arrows – radiative cooling; yellow arrows – convection; black arrows – sedimentation of droplets by gravity. (Poku et al., 2019)

is influenced by the synoptic conditions: high-pressure systems with low wind speeds and reduced cloud cover can result in a cooling rate sufficient for fog formation (Price, 2011; Haeffelin et al., 2013). As the lower layers of the atmosphere cool, the relative humidity increases and water vapour will condense onto CCN to form fog droplets and a thin fog layer. The number of fog droplets depends on the aerosol size distribution and concentration, as well as the rate of cooling at the surface. The fog layer will absorb and emit longwave radiation, and as the layer thickens, radiative cooling may be strongest at the fog top. The result is that the fog layer becomes well-mixed (with a constant temperature profile within the layer) through convection, increasing its optical thickness. However, the turbulence levels and the humidity profile during fog formation can result in the fog remaining optically thin (Price et al., 2018).

In the UK, around 50% of fog cases will transition into an adiabatic (well-mixed) fog (Price, 2011), and has the ability to persist for days. However, despite aerosols potentially

controlling this transition, most operational models (e.g. Gultepe et al., 2006; van der Velde et al., 2010) do not include an option to vary aerosol or fog droplet number concentration. In addition, the number of studies investigating aerosol-fog interactions in relatively clean environments are limited. Porson et al. (2011) showed that a variable fog droplet number is required to capture the transition to an optically thicker fog. Boutle et al. (2018) discussed the importance of aerosol–fog interactions in Numerical Weather Prediction (NWP) and its impact in cases of fog that may form within a relatively clean environment. A better understanding of the aerosol impacts on fog will lead to a developed knowledge of fog microphysics, resulting in an improved accuracy in short-term fog forecasts.

1.3 Thesis Aims

This thesis aims to develop an understanding of the role and representation of aerosols in the formation and evolution of nocturnal radiation fog. Simulations are undertaken with the Met Office and Natural Environment Research Council Cloud (MONC) model (Brown et al., 2015); a newly developed large eddy simulation model that is a complete rewrite of the Met Office Large Eddy Model (LEM; Gray et al., 2001). MONC is a large eddy scale (LES) model that can resolve turbulent structures at different scales, making it suitable to research atmospheric processes in idealised setups. Studies that have investigated fog using LES include Nakanishi (2000), Porson et al. (2011), Bergot (2013), Maronga and Bosveld (2017), Mazoyer et al. (2017) and Schwenkel and Maronga (2019). For this work, MONC has been coupled with the Cloud AeroSol Interactive Microphysics (CASIM) scheme, which has been developed at the Met Office as a long-term replacement for the Met Office Unified Model (MetUM) microphysics scheme. CASIM has been specifically developed to simulate and investigate aerosol-cloud interactions, and has been used as a tool for research in both the MetUM (e.g. Grosvenor et al., 2017; Miltenberger et al., 2018; Stevens et al., 2018) and MONC (e.g. Dearden et al., 2018; Poku et al., 2019).

The thesis structure is as follows. Chapter 2 describes the current literature discussing aerosol-cloud interactions and nocturnal radiation fog, and will formulate three key re-

search questions to be addressed in this thesis. Next, the model description of MONC and CASIM will be outlined in Chapter 3. The key research questions for this thesis are addressed in Chapter's 4, 5 and 6. Finally, overall conclusions and future work will be discussed in Chapter 7.

Chapter 2

Background

Chapter 1 discussed the motivations behind this research, including the problems related to fog modelling, and why aerosol particles are an important consideration for fog development. Literature within this chapter will be focused around the work in aerosol-cloud interactions, and in particular, the work that has been done to understand the importance of aerosol representation in simulations of fog. Section 2.1 will describe the atmospheric aerosol, as well as droplet formation and growth, Section 2.2 will examine the radiative impact of aerosol-fog interactions, and Section 2.3 will discuss the interactions between fog microphysics and dynamics. A summary will follow, highlighting key research questions to be addressed in the thesis.

2.1 Aerosols in the atmosphere

2.1.1 Atmospheric Aerosol

The Earth's atmosphere consists of multiple components, with one being aerosols. Aerosols are small solid or liquid particles (sometimes both) in a state of gaseous suspension, which do not include water vapour and hydrometers such as cloud droplets and rain (Pruppacher and Klett, 2010, p.216). Aerosols range in both size and composition, and have been detected in a wide range of environments, both throughout the planetary boundary layer (PBL) and above (Pruppacher and Klett, 2010, p.220-223). These environments include

the tropics, the Arctic and both continental and maritime settings. Although aerosols are studied in a number of disciplines, for example, chemistry, they are studied in meteorology to understand processes in the atmosphere such as cloud formation, and their impact on climate variables such as global radiative forcing.

Most aerosols are injected into the atmosphere from either natural (e.g. volcanoes, biological material) or anthropogenic (burning of fossil fuels) sources. They are formed either through gas-to-particle conversion, drop-to-particle conversion or bulk-to-particle conversion (BPC; Pruppacher and Klett, 2010, p.226). The majority of aerosol sourced from the Earth's surface is through BPC, which involves the mechanical and chemical disintegration of the solid and liquid surface. In addition, the aerosol concentrations vary temporally and spatially, and depends strongly on the source and rate of emission, as well as the strength of convective transfer rates. However, it has been shown that 80% of the total aerosol population is contained within the lowest kilometre of the troposphere, the part of the atmosphere that contains the PBL (Pruppacher and Klett, 2010, p.226).

2.1.2 Aerosol mass, concentration and size distribution

In the literature, the aerosol population is split by size categories. These size categories (hereafter known as modes) are defined as: the Aitken mode, where the diameter, d, of an aerosol is < 0.1 μm; the accumulation mode, where $0.1 \leq d \leq 1.0$ μm; and the coarse mode, where $d > 1.0$ μm (Whitby, 1978). The residence time of aerosol particles in the atmosphere strongly depends on their size. Aerosols in the Aitken and coarse modes both have relatively short life spans in comparison to aerosols in the accumulation mode (Pruppacher and Klett, 2010, p.249). Aitken mode aerosols have an increased tendency to coagulate with other particles, whereas coarse mode aerosols have greater fall velocities due to their size, resulting in them sedimenting out of the atmosphere faster. The distribution of these modes can be written in terms of aerosol concentration. If $n(r)dr$ represents the number of aerosols with radii between r and $r + dr$, then the total concentration, $N(r)$, of aerosols with radii greater than r is (Pruppacher and Klett, 2010, p.261):

$$N(r) = \int_r^\infty n(r)dr. \tag{2.1}$$

The literature subdivides aerosol air masses into the categories of urban, rural, remote continental, background, desert and polar (Jaenicke, 1988), and it has become customary to represent $n(r)$ as a lognormal distribution. Figure 2.1 shows distributions of $n(r)$ in a range of environmental conditions, showing that the skewness and properties of the distribution described in Equation (2.1) varies with its environment. Measurements of aerosol within rural environments have verified their composition, in addition to their size and concentration. Wiedensohler et al. (1997) showed that during orographic cloud formation in the UK, accumulation mode aerosols range between 400 to 500 cm^{-3}. In addition, Birmili et al. (1999) showed that there was a reduction in accumulation mode aerosol particles due to cloud droplet formation.

2.1.3 Cloud droplet formation and population growth

A number of mechanisms can cause an environment to become supersaturated with respect to water, such as cooling and mixing. Supersaturation with respect to a plane surface of water, results when the water vapour pressure is greater than the equilibrium value (Pruppacher and Klett, 2010, p.103). In a supersaturated environment, a change of physical state from water vapour to liquid water can occur and is known as nucleation (Pruppacher and Klett, 2010, p.191). Nucleation can be either homogeneous when no aerosols are required to form droplets, or heterogeneous when the phase change is assisted by an aerosol particle. Homogeneous nucleation cannot occur within the PBL, due to a required relative humidity (RH) of several hundred percent (Pruppacher and Klett, 2010, p.287). In this section, only droplet formation through heterogeneous nucleation will be discussed.

Köhler theory

If an environment is saturated, some aerosol can take up water vapour to become liquid droplets with a solute, which will grow in response to the increase in RH. These aerosol are

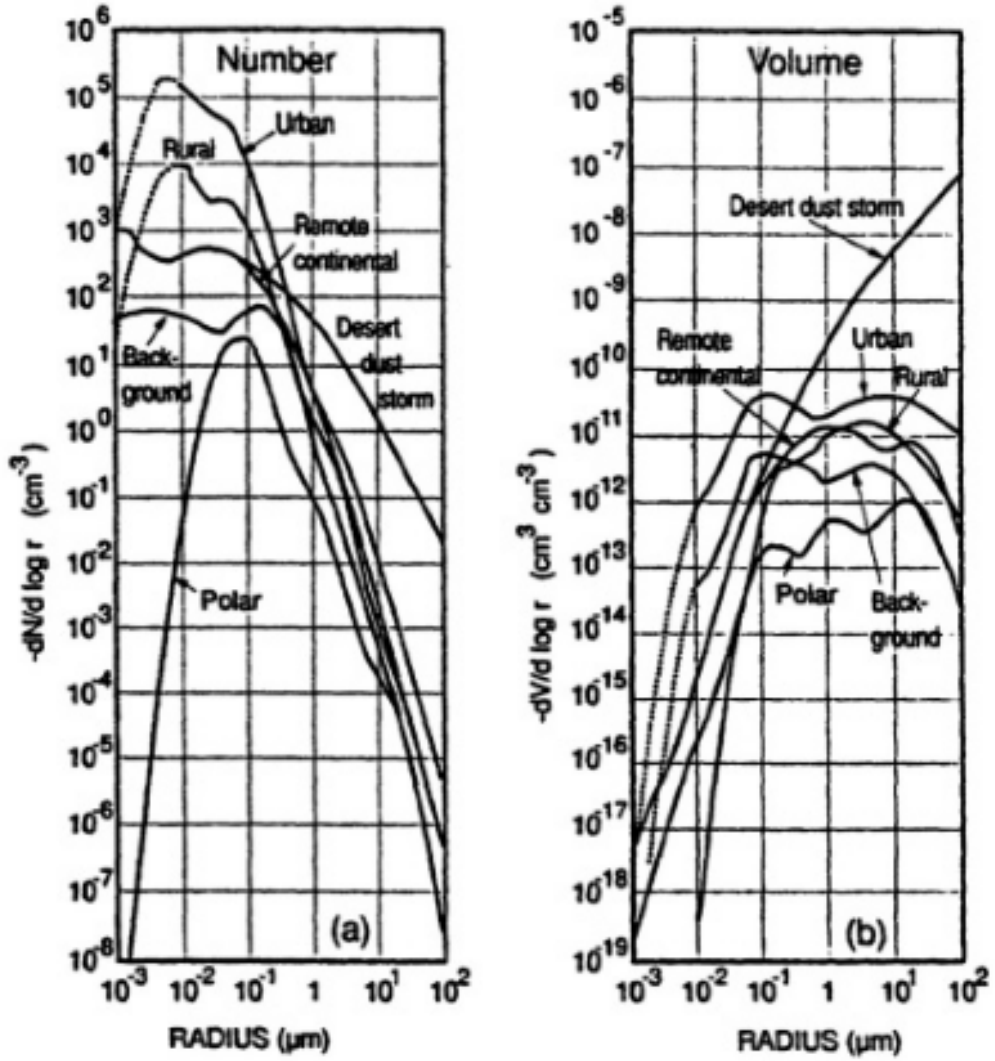

Figure 2.1: The number and volume size distribution of aerosol particles of various types (p.265 Fig 8-20 Pruppacher and Klett, 2010).

known as cloud condensation nuclei (CCN). Typically, CCN particles have a high water solubility, with examples including NaCl (sodium chloride), $NaNO_3$ (sodium nitrate) and $(NH_4)_2SO_4$ (ammonium sulfate). Köhler theory describes the process of water vapour condensing on a CCN, which may result in the formation of a cloud droplet. For a liquid droplet that contains a solute, radius r, the saturation equilibrium ratio, S_{eq}, is defined as (Pruppacher and Klett, 2010, p.173):

$$S_{eq} = \frac{e_s(r)}{e_s(\infty)} = 1 + \underbrace{\frac{A}{r}}_{\text{Kelvin effect}} - \underbrace{\frac{B}{r^3}}_{\text{Solute effect}}, \tag{2.2}$$

where,

$$A = \frac{2\sigma_t}{R_v \rho_L T} \text{ and } B = \frac{3 i m_v M}{4\pi \rho_L m_s}.$$

Terms A and B describe the growth of a liquid droplet's dependency on its curvature and composition respectively. $e_s(r)$ is the saturation vapour pressure near the surface of a droplet, radius r, and $e_s(\infty)$ is the saturation vapour pressure of a plane of pure water. R_v is the water vapour gas constant, and σ_t and ρ_L are the surface tension and density of the liquid droplet at temperature T, respectively. M is the total mass of the solute, m_s is the molecular weight of the solute, m_v is the molecular weight of water vapour, and i is the Van't Hoff factor; the number of ions through disassociation in a molecule for a dilute aqueous solution (McDonald, 1953).

The second term on the right-hand side of Equation (2.2) is the contribution to the growth of a droplet due to its curvature, known as the Kelvin effect. When only considering the Kelvin effect, a smaller droplet would require a larger supersaturation to maintain equilibria with its environment than a larger droplet, as the smaller droplet would have a higher surface energy barrier to overcome nucleation. The third term on the right-hand side of Equation (2.2) is the contribution to the growth of a droplet due to its composition, known as the solute effect. When a solute is dissolved in a solvent (in this example, the solvent being water), the solute takes the place some of the solvent molecules at the surface, reducing the likelihood of the solvent evaporating. The solute effect will have a

greater impact on a smaller liquid droplet for the same mass of solute, due to a higher concentration of solute components.

Figure 2.2 is an example of a Köhler curve of a droplet formed on an ammonium sulphate nucleus, as demonstrated by Equation (2.2), and describes the size of a droplet that is in equilibrium with its environment. The Kelvin and solute effects (Figure 2.2) are competing to change the saturation vapour pressure of a droplet, changing the likelihood for the droplet to eventually become nucleated and grow without any limits. The point where these terms are at equal competition is defined as the critical supersaturation, S^* that occurs at the critical radius, r^* (Figure 2.2). The critical supersaturation is obtained by finding the differential maximum of Equation (2.2):

$$S^* = 1 + \frac{2}{3}\sqrt{\frac{A^3}{3B}}. \tag{2.3}$$

There are two stages a droplet will encounter in Figure 2.2. Prior to the maximum of the solid line curve, an environment containing aerosols approaches saturation and a liquid droplet will begin to form. As the humidity increases, the liquid droplet can grow to remain in equilibrium with its environment. The liquid droplet during this first stage is currently unactivated (where $r < r^*$, the critical radius) and will decrease in size if the environmental humidity decreases. Once the liquid droplet reaches its critical size, r^*, it has the ability to continue growing, as shown by the decrease in the equilibrium curve for $r > r^*$ in Figure 2.2. The droplet during this second stage has now activated into a cloud droplet. The initial aerosol size can change the likelihood of it activating into a cloud droplet. Should the aerosol be bigger in size, the required critical supersaturation needed for activation is relatively low due to the solute effect.

It has been long debated whether aerosol activation physically occurs within fog, and in particular, in cases of fog that are optically thick (e.g. Roach et al., 1976). An early observational study of a thick fog by Gerber (1981) had conducted measurements of RH within its layer, and showed that the RH oscillated between 98 to 100.5%, while maintaining an average RH of less than 100% (Figure 2.3). Despite these subsaturated conditions, it is possible for droplets to continue growing, due to radiative cooling enhancing diffusive

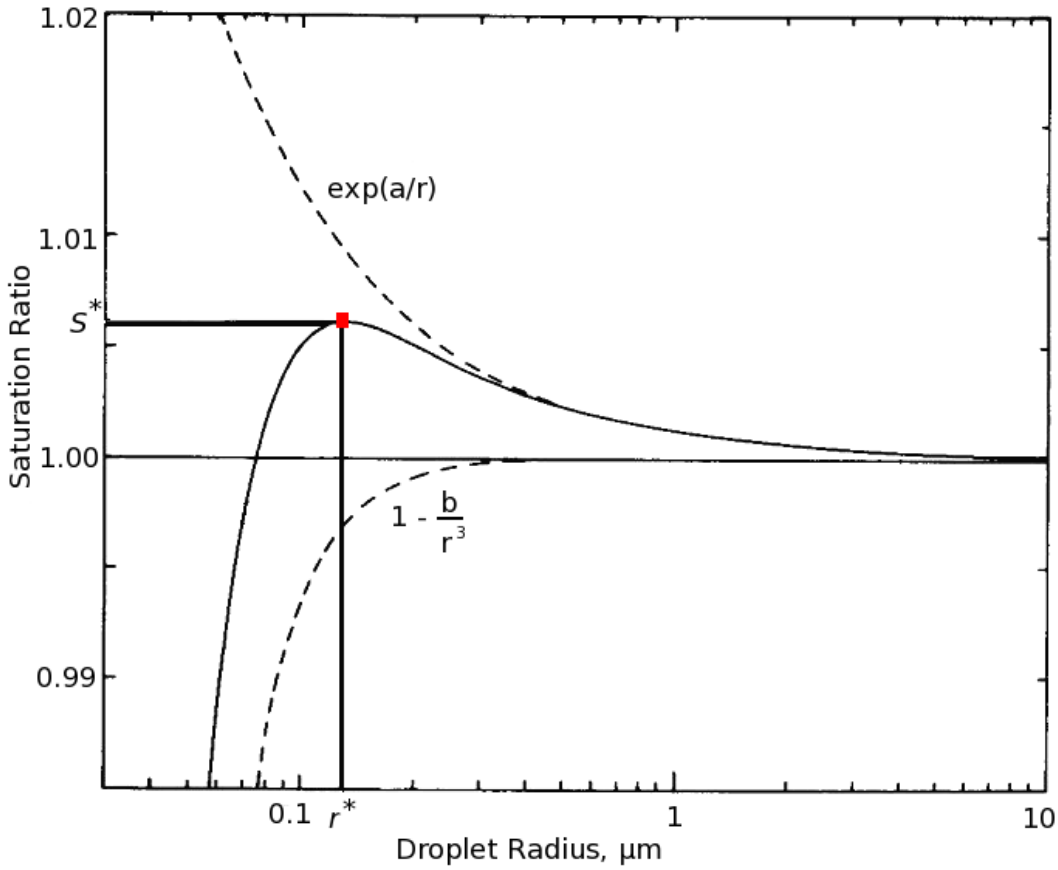

Figure 2.2: An equilibrium saturation ratio curve of a droplet that formed on an ammonium sulphate nucleus. Critical radius and supersaturation denoted as r^* and S^* respectively (red square). Dashed lines represent Kelvin and solute effect respectively (adapted from Rogers and Yau, 1989).

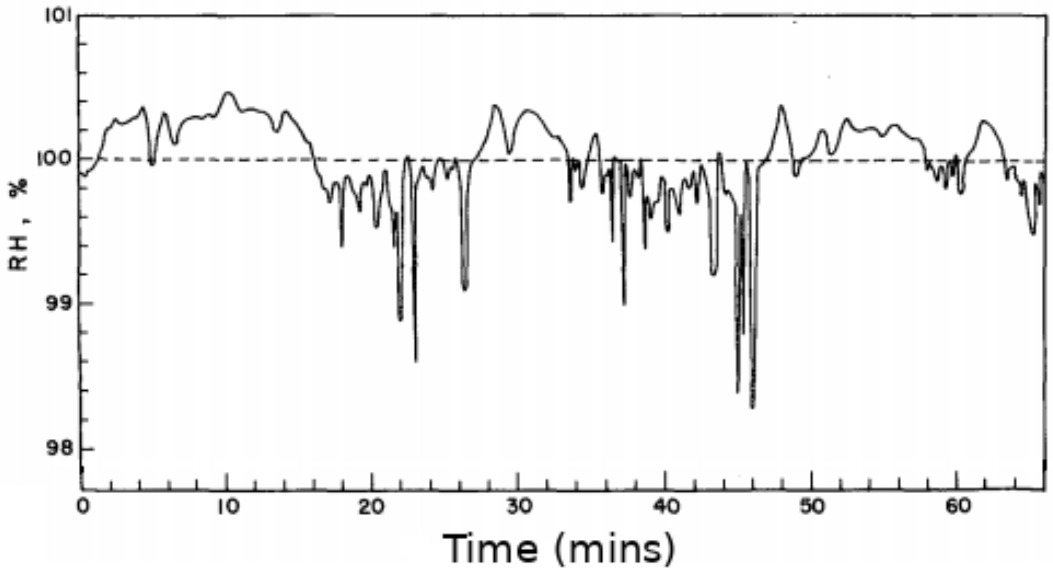

Figure 2.3: Time variation of the relative humidity (%) of an observed radiation fog on the 20th November 1979 in Reston, Virginia (adapted from Gerber, 1981).

growth (Roach, 1976; Bott et al., 1990). Depending on the mass of the aerosol particle, droplets can grow to more than 1 μm in these conditions, and Elias et al. (2015) calculated that they can contribute to 68% of the total light scattered within the fog layer. More recently, Haeffelin et al. (2013) investigated the cloud droplet spectrum from observations of fog from the Paris fog (PARISFOG) campaign. They showed that in some cases of thick fog, the proportion of activated aerosols was only around 10% due to the size they grew to given the environment's aerosol composition.

These studies suggest the assumption of aerosol activation in fog is not appropriate; an assumption used in the majority of models that account for aerosol treatment. It also suggests that methods such as bin microphysics schemes may be a more appropriate option (for example a bin microphysics scheme used in Boutle et al., 2018). However, using a bin microphysics scheme or explicitly modelling droplet growth is not computationally feasible for some models such as general circulation models (GCMs). Therefore, using an aerosol activation scheme is a suitable proxy solution to understand the aerosol indirect effects in fog, while saving on computational expense. The suitability of aerosol activation schemes

in fog will be discussed in more detail in Section 2.2.1 of this chapter.

Droplet population growth: distribution characteristics

Through measurements of RH and cloud droplet spectra within convective clouds, Squires (1952) showed the relation between the number of droplets that form with respect to the aerosol spectra and maximum supersaturation. During initial formation, there is a large concentration of small droplets and progressively fewer big droplets. This results in the shape of the drop-size distribution being positively skewed and a long tail towards droplets of a bigger size (Pruppacher and Klett, 2010, p.26). For a droplet population with a concentration, $n(r)$, and drop size, r, the distribution can be represented by a gamma distribution:

$$n(r) = Ar^{\mu_d}\exp(-Br^{\lambda_d}), \tag{2.4}$$

where A, B, μ_d and λ_d are parameters that relate to the moments of the distribution described in Equation (2.4). During fog formation, the observed cloud-drop size distribution has been observed to follow a gamma distribution and may either evolve into a bi-modal, skewed or platykurtic during its development (Price, 2011). Therefore, the suitability of the parameters chosen for Equation (2.4) should be accounted for when trying to understand the role of microphysics during the fog evolution.

2.2 Radiative impact of aerosol-fog interactions

Categories of fog, and the fog layer's radiative impact were discussed by Price (2011). Radiation fog in the UK can be categorised as either stable or adiabatic (well-mixed). Initially, a formed fog layer can grow in depth and remain stable, whilst growing in optical thickness. The strength of the layer's optical thickness can transform a stable fog into an adiabatic fog, as the radiative cooling rate may become greater at the fog top than at the surface. This could trigger a convective instability and allow for the layer to become well-mixed. As the layer becomes well-mixed, the growth rate in the fog depth increases.

The next section will describe how the cloud droplet number concentration (CDNC) may control the transition to a well-mixed layer, which includes discussion on the treatment of aerosols in fog.

2.2.1 Aerosol indirect effects

Properties of the aerosol distribution, e.g. number concentration, can indirectly control both the optical depth and life span of a cloud. The literature commonly splits the aerosol indirect effects into two. The first indirect effect, also known as the Twomey effect, describes the link between aerosol concentration and the cloud's optical depth. For a given liquid water path, an increase in the aerosol concentration will result in an increase of cloud droplets of a smaller size. As a result, the cloud's effective radius will decrease, leading to an increase in the cloud's optical depth and albedo (Twomey, 1974). In addition, an increase in optical depth will increase the absorptivity of longwave radiation by the cloud (Garrett et al., 2002).

The secondary indirect effects describes how increasing the aerosol concentration impacts the cloud's life span. An increase in concentration and therefore cloud droplets, may decrease the number of droplets large enough to form drizzle through collision-coalescence. As a result, the reduction in drizzle will suppress a sink, increasing the cloud's life span (Albrecht, 1989). However, a change in aerosol concentration may feedback on other processes that could influence the cloud's life span. These processes include sedimentation (Mauritsen et al., 2011), entrainment (Ackerman et al., 2004; Bretherton et al., 2007; Hill et al., 2009) and aerosol scavenging (Miltenberger et al., 2018). For this work, particular attention has be given to sedimentation and scavenging, and how aerosol-fog interactions control both these processes.

Nocturnal radiation fog is directly impacted by a number of these indirect effects. For example, Porson et al. (2011) showed that halving a fixed CDNC used in simulations of fog from 100 to 50 cm^{-3} reduced the downwelling longwave at the surface by a maximum of 12 W m^{-2}, indicative in the fog's decrease in optical thickness. More recently, Maronga and Bosveld (2017) quantified the relationship between the fog's radiative impact and change

in CDNC, and showed that doubling the CDNC from 100 to 200 cm^{-3} led to an increase in the fog top cooling rate by 1.2 K hr^{-1}. These results can provide direct insight as to why aerosol treatment is important for fog. Using a single column model (SCM), Bott (1991) showed that increasing the aerosol concentration results in a deeper fog layer and a delayed dissipation time. This effect was later verified by Stolaki et al. (2015) and Maalick et al. (2016), who both showed a positive relationship between the aerosol concentration and deepening of the fog layer.

The studies described in this section show that the aerosol concentration, and hence CDNC, control the depth of the fog, with its representation potentially being important to capture the transition to a well-mixed fog (Porson et al., 2011). More recently, Boutle et al. (2018) demonstrated that a fixed CDNC used in a numerical weather prediction (NWP) model cannot represent this transitional period. Their work suggested that an aerosol activation scheme could model this transition by allowing for a time-varying CDNC. Although aerosol activation may not occur in fog, a parameterisation can be a computational cheap method to account for its treatment of aerosol. However, Boutle et al. (2018) outlined that most widely used activation schemes may not be suitable to model fog, due to the assumptions made within the parameterisation implementation.

Parameterisation of aerosol activation

Accurate representation of droplet nucleation (i.e. aerosol activation), is essential to represent the indirect effects of aerosols on clouds. However, when investigating aerosol-cloud interactions in models such as GCMs and NWPs, a large number of droplet growth schemes are unsuitable, as the computational power required would dominate the treatment of the rest of the physics in the model (Ghan et al., 1993). Original development of an aerosol activation parameterisation began by Squires (1958), who showed that the number of activated droplets, N, is related to its aerosol spectrum, such that:

$$N(s) = cs^k, \tag{2.5}$$

where s is the environmental supersaturation, and both c and k are activation spec-

trum coefficients. It was shown the number of droplets that activate is dependent on the maximum environmental supersaturation, assuming that these droplets begin growing once $s > 0$. Work by Twomey (1959) expanded on the modelling of aerosol activation, and discussed the link between an aerosol spectrum based on Equation (2.5), supersaturation and CDNC. A parameterisation was formulated based on droplet formation and growth (using Köhler Theory; Section 2.1.3), and assumed that these droplets began to grow once the critical size had been reached.

Twomey (1959) described the change in the supersaturation in an ascending parcel being controlled by two opposing effects: the rise in supersaturation due to a cooling to the parcel and a decrease in supersaturation due to condensation. As a parcel rises, the pressure exerted by the surrounding atmosphere on it decreases, allowing for it to expand. Assuming that the concentration of molecules is constant within the parcel, the number of collisions experienced will decrease, and hence decrease its temperature. As the parcel cools, assuming there is no change in the water vapour mixing ratio, the equilibrium saturation ratio decreases with temperature and hence the RH increases. The increase in RH can result in the parcel being supersaturated, allowing for droplet formation through condensation. However, condensation removes water vapour from the parcel, decreasing its RH. Twomey (1959) accounted for both of these effects and derived the change in supersaturation to be:

$$\frac{ds}{dt} = \alpha - \beta s \int_0^s \nu(\sigma) \left[\int_{\tau(\sigma)}^t s dt \right]^{\frac{1}{2}} d\sigma, \tag{2.6}$$

where α is the source in supersaturation due the cooling of a parcel; β is a constant dependent on the aerosol spectrum and $\nu(\sigma)$ is the number of nuclei in a unit volume with critical supersaturation between σ and $\sigma + \delta\sigma$.

If condensation is assumed to be absent, Equation (2.6) can be solved, such that $s = \alpha t$. However, as condensation results in the decrease in supersaturation, the maximum number of activated aerosols is capped and will occur once the peak supersaturation is reached (i.e. when the condensation term starts to dominate the cooling terms), resulting in no more aerosols activating. At this point, $\frac{ds}{dt} = 0$, and Equation (2.6) becomes:

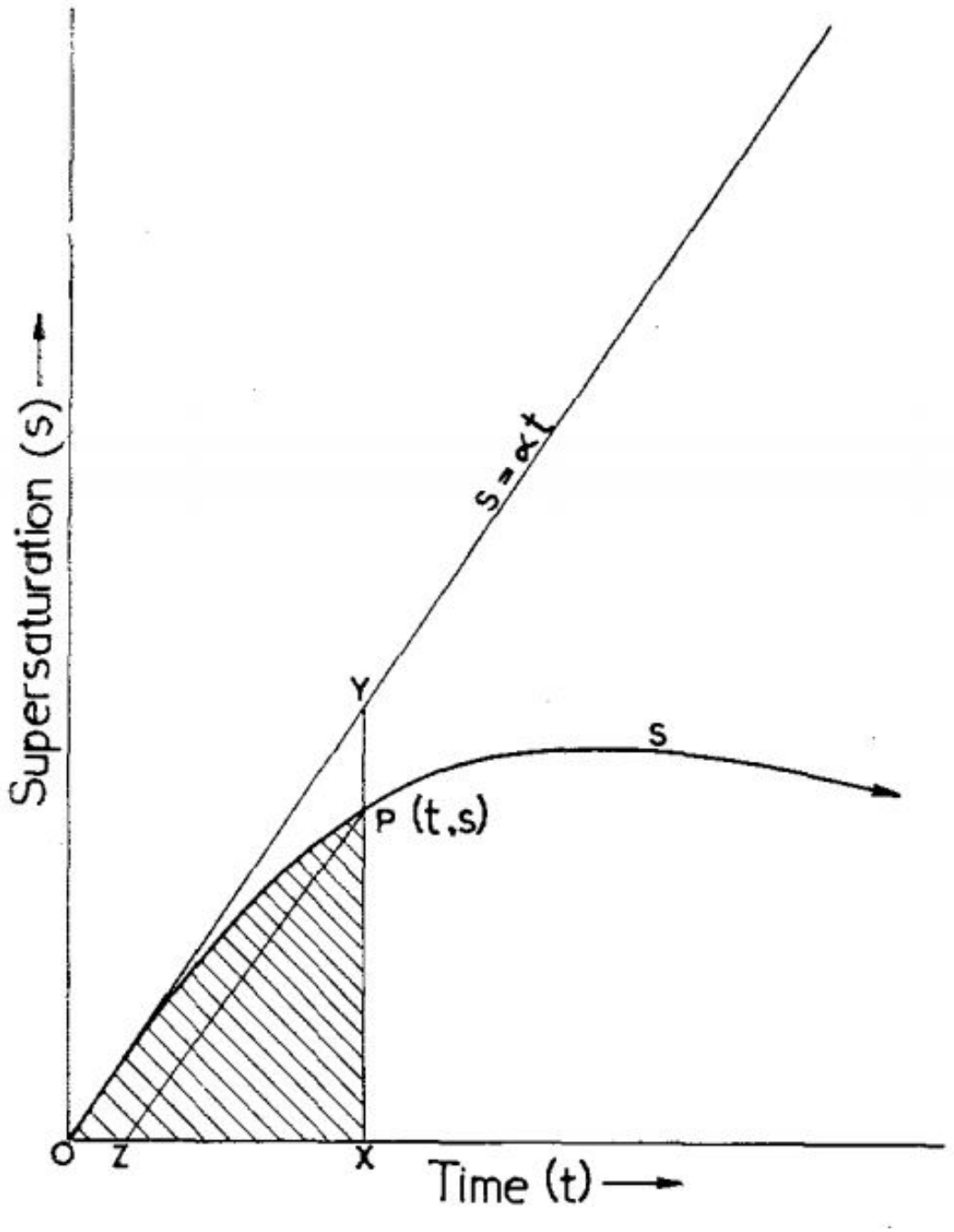

Figure 2.4: Visual representation of the approximation used to account for the inner integral (change in supersaturation between times τ and t) as shown in Equation (2.6) *(term 2 on right hand side) (Twomey, 1959).*

$$\alpha = \beta s \int_0^s \nu(\sigma) \left[\int_{\tau(\sigma)}^t s \; dt \right]^{\frac{1}{2}} d\sigma. \tag{2.7}$$

Calculating the condensation term in Equation (2.7) was computationally expensive in the work by Twomey (1959). Hence an upper and lower bound to calculate $\int_\tau^t s \; dt$ was formulated using a geometric approximation (see Figure 2.4), such that:

$$\frac{1}{2}\alpha \left(t^2 - \tau^2 \right) > \int_{\tau(\sigma)}^t s \; dt > \frac{1}{2\alpha} \left(s_{max}^2 - \sigma^2 \right), \tag{2.8}$$

and Equations (2.5) and (2.8) were used to calculate an approximate number of activated droplets.

Ghan et al. (1993) addressed the limitations of the Twomey scheme in aerosol-cloud simulation models: Twomey (1959) is dependent on an aerosol spectrum rather than a distribution, and so poorly represents activation in high updraft velocity regimes. This is because the scheme cannot account for changes with an evolving aerosol distribution, and the total number of activated droplets not being bounded by the aerosol concentration. Work by Cohard et al. (1998) and Shipway (2015), for example, accounted for these limitations and hence expanded on the original Twomey parameterisation. However, Ghan et al. (1993) developed a scheme that accounted for a more realistic aerosol size distribution, which was naturally bounded by the total aerosol number. For this work, Ghan et al. (1993) amended the cooling term (for example shown in Equation 2.6) to be inclusive of a change in supersaturation due to radiative cooling; different to schemes prior that only assumed adiabatic ascent. Ghan et al. (1993) showed that accounting for a more realistic single mode aerosol-size distribution (lognormal) improved the parameterised number of droplets activated. However, because droplet growth was neglected upon activation in their scheme, the introduction of multi-mode aerosol resulted in big discrepancies between the explicit and parameterised number of activated droplets.

Work by Abdul-Razzak et al. (1998) (and later Abdul-Razzak and Ghan, 2000) combined the benefits of the parameterisations developed by both Twomey (1959) and Ghan et al. (1993). The scheme was not only bounded by the total aerosol number, but in

addition, assumed that growth continued from the point of activation. The result of these assumptions led to the parameterised number of activated aerosols agreeing better with the explicit calculation for activation, even in regimes of high updraft velocities (Abdul-Razzak and Ghan, 2000). More recently, Shipway (2015) showed that Abdul-Razzak and Ghan (2000) may not be a suitable scheme for aerosol activation in relatively clean environments. Their results demonstrated that the rate of condensation is overestimated, due to the competition for water vapour being too high, leading to an underestimation of the maximum supersaturation. Hence for some cases of fog (e.g. Boutle et al., 2018), a more suitable method of aerosol activation may need to be considered.

So far, the schemes discussed in this section (with the exceptions of Ghan et al., 1993, 1995) have been tested to assume that saturation is driven by adiabatic ascent. In addition, a number of the listed schemes impose a fixed minimum updraft velocity threshold, w_{min}, of 0.1 m s^{-1}, corresponding to a cooling rate of 3.51 K hr^{-1} (e.g. Ghan et al., 1997; Abdul-Razzak and Ghan, 2000; Morrison and Gettelman, 2008; West et al., 2014). The reasoning for this threshold is because:

1. These schemes are designed to consider updrafts found in stratocumulus and convective clouds (Abdul-Razzak and Ghan, 2000; Meskhidze et al., 2005);

2. For some models (such as GCMs, NWPs), the subgrid velocity (derived from the subgrid turbulence) is used to calculate the number of droplets. However, the turbulence driven by radiative cooling was poorly resolved above the PBL unless the model's vertical resolution was < 100 m. Therefore, a w_{min} of 0.1 m s^{-1} resulted in the model being computationally feasible to account for aerosol activation (Ghan et al., 1997).

There are some situations in which adiabatic lifting is not the main source of cooling. In radiation fog, a big source of saturation during the initial formation of droplets is through radiative cooling; a non-adiabatic process. Observations have shown that fog forms with a cooling rate between 1 to 4 K hr^{-1} at the surface (cooling rates calculated using data from Price, 2011), and updraft velocities being close to 0 m s^{-1} (Brown and

Roach, 1976; Roach et al., 1976; Price, 2011; Haeffelin et al., 2013). Consequently, the assumptions used in most activation schemes may result in the CDNC calculated in fog being overestimated. Schwenkel and Maronga (2019) showed that the choice in aerosol activation scheme in fog can influence the number of droplets activated, changing both the optical depth and its life span. In addition, Boutle et al. (2018) discussed that the use of a w_{min} in aerosol activation schemes may be the reason for the poor transition times to an optically thicker fog. Therefore, utilising a method of aerosol activation that does not depend on w_{min} and accounts for radiative cooling during fog formation may improve the simulated fog evolution.

Sedimentation of fog droplets

Roach et al. (1976) observed a large fraction of condensed water being detected at the surface, due to fog droplet sedimentation. Combined with a study by Brown and Roach (1976), the role of sedimentation was quantified: simulated liquid water increased by a factor of 5 when accounting for cloud-radiation interactions without sedimentation. Excluding sedimentation (e.g. Zdunkowski and Nielsen, 1969) results in a higher rate of liquid water production due to an increased cooling rate at the fog top. The impact of sedimentation was later verified by Bergot et al. (2007), showing that excluding sedimentation can create large inaccuracies in fog forecasts, as the parameterisation that handles fog microphysics will produce too much liquid water. The simulated thicker fog resulted in errors in the dissipation time, and the exclusion of sedimentation was more problematic for cases of fog that form relatively weak vertical velocities within the fog layer (Bergot et al., 2007). These studies demonstrate the fog's sensitivity to sedimentation, and the importance of its representation during the fog evolution.

The type of parameterisation used represent droplet sedimentation can impact the development of the fog after initial formation. Initially, studies such as Brown and Roach (1976), Corradini and Tonna (1979) and Musson-Genon (1987) parameterised sedimentation as a function of liquid water. However, only accounting for liquid water meant that the sedimentation rate could not evolve with a change in cloud droplet spectrum (Sec-

tion 2.1.3), resulting in the sedimentation rate being too low (Duynkerke and Driedonks, 1988; Duynkerke, 1991). As such, Duynkerke and Driedonks (1988) included a term that allowed for the change in cloud droplet number, and showed an improvement in the fog evolution during the development phase. More recently, Zhang et al. (2014) investigated how changes in the cloud-drop distribution impact sedimentation fluxes. They showed that changing the droplet distribution shape parameters will change the emphasis of certain sized droplets that will fall, impacting the evolution of liquid water in the fog layer. Applying the results of Zhang et al. (2014), Mazoyer et al. (2017) changed the default shape parameter used for the sedimentation in simulations of fog to reflect observations of cloud droplet spectra. These results suggest that the default cloud drop-size distribution shape parameter may need to be adapted based on observations, to ensure the fog evolution is accurately represented.

As well as sedimentation representation, studies that shown the fog evolution's sensitivity to sedimentation in relation to a change in CDNC. Porson et al. (2011) showed a fixed CDNC decrease from 100 to 50 cm^{-3} led to a decrease in the liquid water by 50% and 33% during the formation and development stages of the fog. The effective radius was fixed in their study, therefore demonstrating the sensitivity of the fog layer to just sedimentation. In addition, Maronga and Bosveld (2017) saw a 20% increase (decrease) in the liquid water path (LWP) when doubling (halving) the CDNC using a fixed value in all tests. Changing the fixed CDNC influences the sedimentation rate of liquid water in the fog layer. This will change the fog top radiative cooling rate, which can impact when the fog becomes optically thicker.

The fog's sensitivity to sedimentation is increased when aerosol is accounted for. Rangognio et al. (2009) investigated the sensitivity of the accumulated precipitation of cloud droplets to a change in aerosol. Their work showed that each aerosol loading used influenced in the number of activated droplets changing, thereby impacting surface precipitation rates. More recently, both Stolaki et al. (2015) and Maalick et al. (2016) showed that by doubling the initial CCN concentration, the LWP increased by a maximum of 60% and 30% respectively. These studies show the sensitivity of the fog evolution to sedimentation,

highlighting the importance of droplet representation in fog.

In-cloud aerosol removal - nucleation scavenging

Aerosol can be scavenged in the atmosphere, with cloud formation acting as a major sink (Figure 2.5). The two most common mechanisms of in-cloud scavenging are nucleation and impaction. Nucleation scavenging is the removal of aerosol through droplet condensation (as described in Section 2.1.3), with impaction scavenging being the removal of aerosol through the collision of aerosols with already formed droplets (Pruppacher and Klett, 2010, p.716-720). Although the majority of aerosol particles within the cloud have been scavenged, there are aerosol that remain in the cloud, known as interstitial aerosol (Pruppacher and Klett, 2010, p.716). A consequence of in-cloud scavenging is the change in aerosol distributions, which in turn can impact cloud (fog) development and its life span. Although both scavenging processes occur in-cloud, Flossmann et al. (1985) demonstrated that nucleation scavenging is of greater importance relative to impaction scavenging.

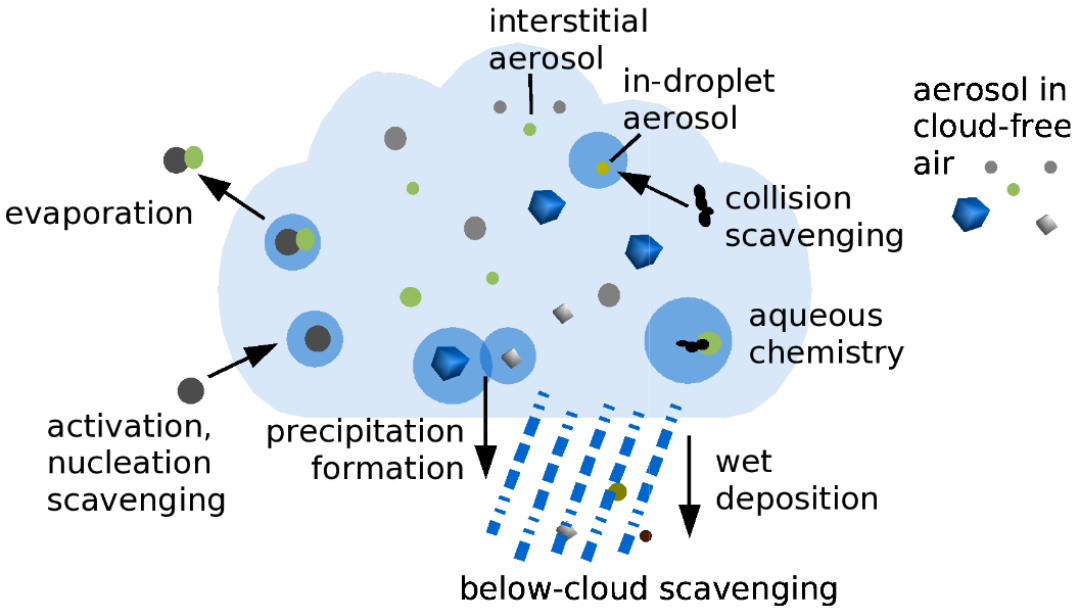

Figure 2.5: Diagram illustrating different mechanisms for aerosol processing, which includes in-cloud aerosol removal (adapted from Hoose et al., 2008).

There have been a number of observational studies investigating aerosol scavenging in fog (hereafter known as fog scavenging). Noone et al. (1992) studied the changes in aerosol measurements during fog events from the Po Valley Fog experiment (Fuzzi, 1992). They showed that 50% of the aerosols scavenged were larger than 0.5 μm (accumulation mode), suggesting nucleation scavenging is of importance to fog development. Collett et al. (2001, 2008) have since investigated the impact of fog scavenging, demonstrating that the majority of these scavenged aerosol contain high water solubilities. More recently, Gilardoni et al. (2014) quantified the impact of fog scavenging, and showed that there is a 60 to 70% processing efficiency of compounds that contain nitrates, ammonium and sulphates. Although these all highlight the importance of aerosol processing in fog, these cases have all been observed in highly polluted aerosol regimes and may not have the same implications on fog development in other environments.

Although bin microphysics schemes can account for aerosol removal in fog (Turton and Brown, 1987; Bott, 1991; Boutle et al., 2018), this method of nucleation scavenging is computationally expensive for models such as NWPs (Lebo and Morrison, 2013). Lebo and Morrison (2013) developed a parameterisation to account for in-cloud aerosol removal for use in a bulk microphysics scheme, providing a potentially computationally inexpensive way to account for aerosol removal. Miltenberger et al. (2018) investigated aerosol processing during the development of mixed-phase clouds using a bulk microphysics scheme. They showed that by including in-cloud aerosol removal, the source of aerosol began depleting through nucleation, resulting in a more open-cell cloud structure and changes in the cloud dynamics.

So far, there are no studies that have investigated aerosol processing in fog using a bulk microphysics scheme. Given that aerosol indirectly impacts the fog evolution, the inclusion of nucleation scavenging may prohibit fog layer development or even initial formation due to aerosol depletion.

2.3 Influence of fog dynamics due to microphysics

2.3.1 Turbulent mixing: fog formation

The role of turbulent mixing at the surface during the fog formation stage has long been debated (Roach et al., 1976; Duynkerke, 1999; Price, 2011). Turbulent mixing can increase moisture fluxes from the surface, therefore enhancing the RH. Authors such as Roach et al. (1976) claimed that any form of turbulent mixing will prohibit fog formation, whereas others such as Duynkerke (1999) argued that turbulence was required to produce saturation, resulting in fog formation. More recently, Price (2011) further clarified the argument for turbulent mixing. They stated that some mixing was required to initially sustain the fog layer, but that too much mixing could result in fog dissipation due to dew deposition.

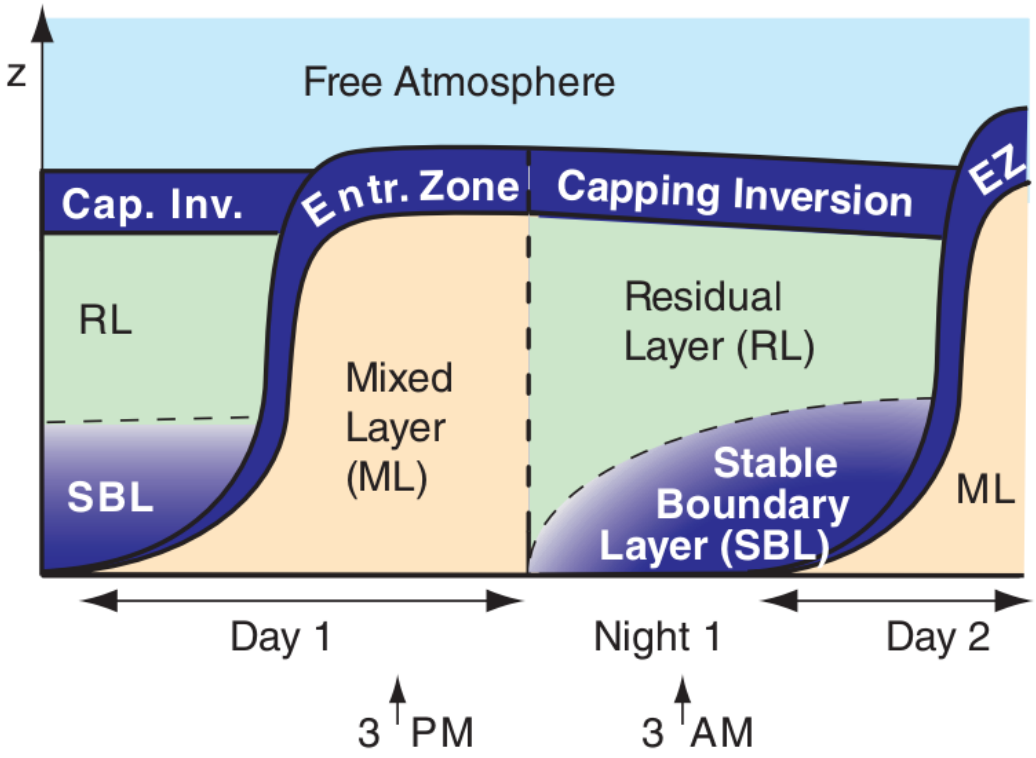

Figure 2.6: A diagram showing the evolution of the PBL throughout a 24 hour period. (Stull, 2017, p.692)

The strength of turbulent eddies in the nocturnal boundary layer depends on both the

dynamical and thermodynamical properties of the prior daytime boundary layer (mixed layer). Both the surface and boundary layer releases heat through infrared radiation, which will strengthen as sunset occurs (radiative cooling). Radiative cooling results the lower levels of the mixed layer becoming statically neutral; forming a stable boundary layer (SBL), with the layer above being known as the residual layer (RL; Figure 2.6). The RL contains moisture and pollutants from the daytime mixed layer, which could impact the structure of the SBL. The RL is statically stable unlike the mixed layer, and hence unstable air masses that generate turbulence begin to cease, resulting in the RL becoming non-turbulent. Although the RL and SBL are non-turbulent, phenomena such as nocturnal jets can generate turbulent eddies through wind shear, due to high-level winds accelerating to supergeostrophic speeds (Stull, 1988, p.15).

Accurately simulating fog formation requires a sufficiently fine resolution to resolve turbulence present, while having a minimal dependency on the turbulent subgrid parameterisation. Porson et al. (2011) conducted sensitivity tests on the subgrid Smagorinsky scheme coefficient and concluded that decreasing this value led to more turbulent energy in the domain being resolved. This resulted in a better agreement with observations of the turbulent structures during the initial stages of fog evolution. Maalick et al. (2016) investigated the impact of turbulence representation in simulations of fog, showing that a 1D model that depends on subgrid turbulence can poorly capture the fog formation. More recently, Maronga and Bosveld (2017) investigated the importance of horizontal grid spacing for simulations of fog, and concluded that by decreasing the grid spacing used in simulations more turbulence was resolved, therefore capturing the changes in heat and moisture fluxes present prior and during fog formation. These studies demonstrate that the subgrid parameterisation may over or underestimate the change in heat and moisture fluxes due to turbulence. As these fluxes impact the environment's RH, resolving these fluxes is important for understanding aerosol-fog interactions during the fog formation and development.

Maronga and Bosveld (2017) assessed the sensitivity of turbulent mixing to the prescribed surface geostrophic wind, showing that it changed both the optical depth and

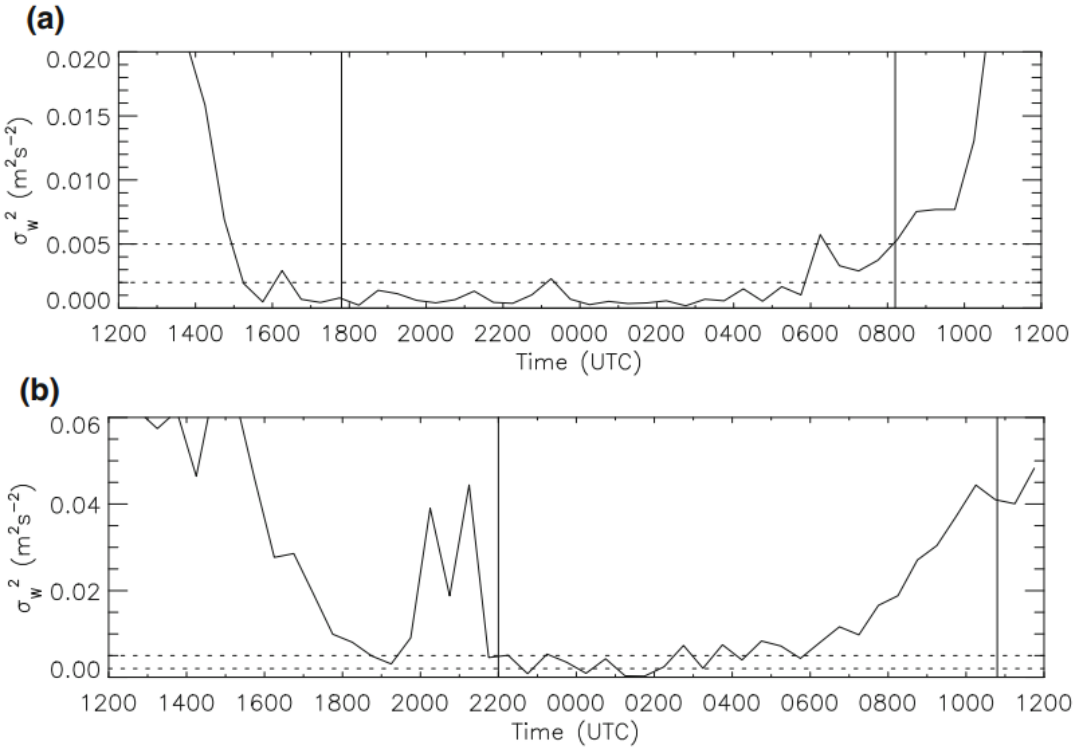

Figure 2.7: (a) Variance to the vertical velocity (σ_w^2) at 2 m during IOP 1. The horizontal lines denote values of σ_w^2 of 0.005 and 0.002 m^2 s^{-2}. Data are averaged over 30 min. The vertical lines denote when fog formed and dissipated (visibility < 1 km). (b) As, (a) but for IOP 18 (Price, 2019).

formation time of the fog. In addition, they discussed how the choice in roughness length could change the level of turbulent mixing present within the grid box domain. Recently, Price (2019) studied a number of radiation fog cases from the 2015 Local and Non-local Fog EXperiment (LANFEX) campaign (Price et al., 2018). Cases that formed coincided with a turbulent threshold (vertical variance) between 0.002 and 0.005 $m^2\ s^{-2}$ (see Figure 2.7). This threshold suggests that a small level of turbulence is required to maintain a humidity suitable for fog formation. However, it also suggested that the number of droplets that form may be influenced. Section 2.2.1 discusses the use of a minimum vertical velocity threshold in many aerosol activation schemes, resulting in assuming an updraft that is unlikely to be present. Boutle et al. (2018) outlined that this can result in a vertical variance to the updraft velocity greater than that found by Price (2019). This illustrates why the minimum threshold is unsuitable for cases of fog, and in addition, how the levels of turbulent mixing may influence aerosol activation through changes in both the roughness length and prescribed geostrophic winds.

2.3.2 Dynamical structures - fog development

Section 2.2 discusses the radiative impact of the fog layer in relation to an enhanced vertical growth. The growth of the fog layer is controlled by the fog's turbulent structures, and was first analysed using large eddy scale (LES) modelling by Nakanishi (2000). Prior to fog formation, a maximum in turbulent kinetic energy (TKE) occurs near the surface, and they concluded that the source of TKE was mostly driven by surface wind shear. The timing for fog development was signalled by another burst of TKE at the fog top, coinciding with the maximum liquid water content (LWC) and cooling rate within the fog layer (Figure 2.8). They concluded that the latter burst of TKE was driven by a convective instability, due to Kelvin–Helmholtz (KH) instabilities forming near the fog top (Nakanishi, 2000). The formation of KH instabilities is the result of turbulent eddies at the top of the layer, causing updrafts and downdrafts to be present within the fog layer which, in turn, enhances vertical growth.

The internal structures show the same burst in TKE during fog development (Bergot,

2013). However, they argued that the transition to a well-mixed fog was poorly timed, as their study could not account for new formed droplets through condensation. Bergot et al. (2015) also showed that the amount of fog liquid water is a stronger influence on the TKE structure (both at the formation and development point), rather than the surface dynamics (heat, moisture). Although Nakanishi (2000) theorised that the TKE structures they formulated are applicable to all types of radiation fog, they did not account for fog types that have a slower transition period to an optically thicker fog. For example, although there was a burst of TKE at the fog top during the development stage, simulations by Porson et al. (2011) did not show a burst of TKE occurring near the surface. However, fog development began too early and it was theorised that this was due to droplet representation. These studies all show that the enhanced vertical growth is linked to the fog's optical thickness, highlighting the importance of fog microphysics and its representation.

The change in transition time and hence the turbulent structures within the fog could be improved by accounting for aerosol-fog interactions and their indirect effects (Section 2.2.1). For example, Mazoyer et al. (2017) investigated the processes used in a more physically representative scheme of aerosol activation and how it impacts the fog dynamical structures. There was a stronger dominance in aerosol activation due to radiative cooling at fog formation; the emphasis changed to droplet formation through an updraft velocity as the fog began to develop. They investigated fog formation within a polluted aerosol regime and hence the changes in dynamical structures due to a choice in aerosol activation scheme may be different formation in a "cleaner" environment (for example, rural locations in the UK). However, their results have highlighted the importance of fog microphysics representation and its interaction with fog turbulence.

2.4 Summary

The focus of this background section has been to explore work understanding aerosol-fog interactions and their role during nocturnal radiation fog. The importance of different aerosol properties in controlling the fog evolution have been highlighted, especially for fog

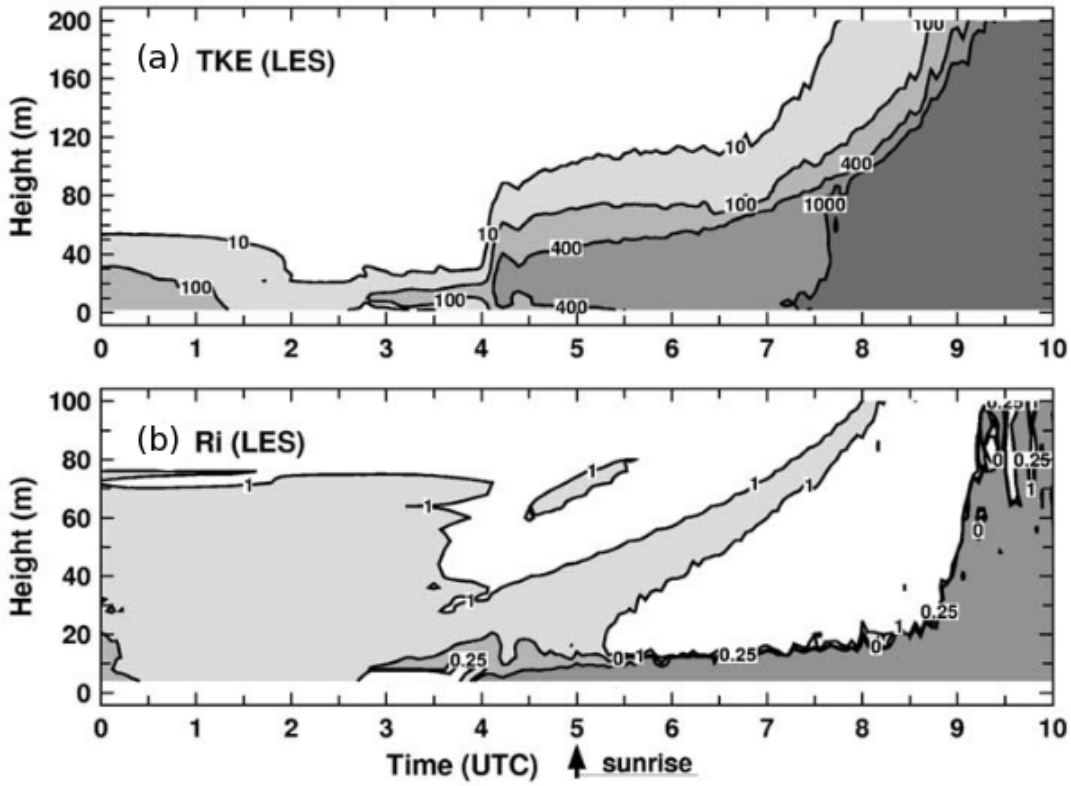

Figure 2.8: Time-height cross sections of (a) the total turbulent kinetic energy (TKE) (10^{-4} m^2 s^{-2}); (b) Richardson number, Ri (Nakanishi and Niino, 2004).

that has a slow transition to an optically thicker fog. Three questions will be addressed in this research; they are discussed in the main results chapters of the thesis, as follows:

- Chapter 4: Is it important to include aerosols to describe the behaviour of a slow transitioning fog, given default modelling assumptions?
- Chapter 5: Can a more realistic aerosol activation scheme be devised that captures the formation of fog observed in a case study of stable fog?
- Chapter 6: Given that fog scavenging has been shown to strongly impact the aerosol-size distribution, how will including nucleation scavenging influence the formation of stable fog?

To answer these questions and subsequent sub-questions, the Met Office NERC Cloud

Model (MONC) alongside the Cloud AeroSol Interactive Microphysics (CASIM) scheme were used to simulate a slow-transitioning fog case from the recent LANFEX field campaign (Price et al., 2018). A thorough description of both MONC and CASIM will be given in Chapter 3, with the LANFEX case that will be the focus of this thesis being described in Chapter 4.

Chapter 3

Met Office NERC Cloud model description

Throughout this study, the main modelling tool used is the Met Office Natural Environment Research Council Cloud (MONC) model; a 3-D LES cloud model (Brown et al., 2015, 2018). The MONC is based on the same equation set as the older Met Office Large Eddy Model (LEM; Gray et al., 2001). It has, however, been totally rewritten to take advantage of modern parallel programming techniques and to ensure it is highly scalable. This allows much larger simulations to be efficiently undertaken. Due to its design, MONC has the ability to turn physical components on and off in order to test different model behaviours; a new feature from the LEM. Unlike the LEM, MONC has been designed to couple with other modules, including the Cloud AeroSol Interactive Microphysics scheme (CASIM; Field et al., 2016) and the Suite of Community Radiative Transfer codes (SOCRATES; Edwards and Slingo, 1996). MONC is widely used in the UK atmospheric science community, which includes users from the Met Office, as well as the University of Leeds, Reading and Manchester. MONC has been used to study atmospheric processes in low level clouds in West Africa (Dearden et al., 2018), fog (Poku et al., 2019) and idealised simulations of convection (Böing et al., 2019).

3.1 Governing equations of resolved fields

MONC has the option to solve incompressible flow using either a Boussinesq or anelastic approximation. A Boussinesq approximation assumes a constant mean reference state with height, whereas anelastic approximation assumes the mean reference state changes as a function of height (Ogura and Phillips, 1962). A Boussinesq approximation is only suitable for particular atmospheric problems e.g. stable boundary layers or shallow convection, as its assumption accounts for small vertical motions. Although the anelastic approximation could be used for shallow convection, it's computationally more expensive (Lilly, 1996).

For this work, MONC will solve the following Boussienesq-type equation set (shown using Einstein summations from Gray et al., 2001):

$$\frac{Du_i}{Dt} = -\frac{\partial}{\partial x_i}\left(\frac{p'}{\rho_s}\right) + \delta_{i3}B' + \frac{1}{\rho_s}\frac{\partial \tau_{ij}}{\partial x_j} - 2\epsilon_{ijk}\Omega_j u_k, \tag{3.1}$$

$$\frac{\partial}{\partial x_i}(\rho_s u_i) = 0, \tag{3.2}$$

$$\frac{D\theta}{Dt} = \frac{1}{\rho_s}\frac{\partial h_i^{\theta}}{\partial x_i} + \left(\frac{\partial \theta}{\partial t}\right)_{mphys} + \left(\frac{\partial \theta}{\partial t}\right)_{rad}, \tag{3.3}$$

$$\frac{Dq_n}{Dt} = \frac{1}{\rho_s}\frac{\partial h_i^{q_n}}{\partial x_i} + \left(\frac{\partial q_n}{\partial t}\right)_{mphys} + \left(\frac{\partial q_n}{\partial t}\right)_{LS}, \tag{3.4}$$

where all variables shown in Equations (3.1) to (3.4) are defined in Table 3.1. For reference, u_i, θ and q_n describe the resolved flow, where the subgrid contribution to the flow is solely from the subgrid parameterisation terms (see Section 3.2). The buoyancy term, B', is defined in the model as:

$$B' = \frac{g\theta_v'}{\theta_s}. \tag{3.5}$$

The terms $\left(\frac{\partial \theta}{\partial t}\right)_{mphys}$, $\left(\frac{\partial \theta}{\partial t}\right)_{rad}$ $\left(\frac{\partial q_n}{\partial t}\right)_{mphys}$ and $\left(\frac{\partial q_n}{\partial t}\right)_{LS}$ are source contributions from microphysics, radiation and large scale forcing, which will all be discussed in Sections 3.5, 3.6 and 3.7 respectively. As convention:

$$\frac{D}{Dt} \equiv \frac{\partial}{\partial t} + u_i \frac{\partial}{\partial x_i}. \tag{3.6}$$

The mean reference state is defined by ρ_s, θ_s and p_s, and deviations from this state are assumed to be small. In MONC, the actual thermodynamical variable is θ'; the perturbation from the reference state of θ. Therefore, Equation (3.3) is rewritten as:

$$\frac{D\theta'}{Dt} + w\frac{d\theta_s}{d_z} = \frac{1}{\rho_s}\frac{\partial h_i^{\theta'}}{\partial x_i} + \frac{1}{\rho_s}\frac{\partial h_3^{\theta_s}}{\partial z} + \left(\frac{\partial \theta}{\partial t}\right)_{mphys} + \left(\frac{\partial \theta}{\partial t}\right)_{rad}, \tag{3.7}$$

where w is the vertical velocity.

3.2 Subgrid motion

The subgrid model is used to parameterise the changes in prognostic fields due to unresolved processes (e.g. diffusion, small scale turbulent mixing). MONC uses a subgrid model based on Brown et al. (1994); an extension on the classic Smagorinsky-Lilly model (Smagorinsky, 1963; Lilly, 1992). The subgrid stress, τ_{ij}, and scalar flux, $h_{n,i}$ are defined as:

$$\tau_{ij} = \rho_s \nu S_{ij} \tag{3.8}$$

and

$$h_{n,i} = -\rho_s \nu_h \frac{\partial q_n}{\partial x_i}, \tag{3.9}$$

where ν is the subgrid eddy-viscosity, ν_h is the corresponding diffusivity for scalars and

$$S_{ij} = \frac{\partial u_i}{\partial x_j} + \frac{\partial u_j}{\partial x_i}; \tag{3.10}$$

the rate of strain tensor. The eddy viscosity and diffusivity can be written as a function of Ri_p; the local Richardson number, such that (Smagorinsky, 1963):

Variable	Explanation
χ_s	denotes a reference state of χ
χ'	denotes a perturbation from the reference state of χ
u_i	is the vector flow velocity
θ	is the potential temperature
q_n	represents all other scalar variables (n denotes the number of scalar variables)
p	is the pressure
ρ	is the density
B'	is the buoyancy
τ	is the subgrid stress
h^θ	is the subgrid scalar flux of θ
h^{q_n}	is the subgrid scalar flux of q_n
δ_{i3}	is the Kroneker delta function
Ω	is the Earth's angular velocity (f-plane approximation)
ϵ_{ijk}	is the alternating pseudo-tensor
$\left(\frac{\partial\theta}{\partial t}\right)_{mphys}$	is the source term of θ due to microphysics
$\left(\frac{\partial\theta}{\partial t}\right)_{rad}$	is the source term of θ due to radiation
$\left(\frac{\partial q_n}{\partial t}\right)_{mphys}$	is the source term of q_n due to microphysics
$\left(\frac{\partial q_n}{\partial t}\right)_{LS}$	is the source term of q_n due to a large-scale forcing
R	Gas constant for dry air
p_0	Constant reference pressure
c_p	Specific heat of dry air at constant pressure
g	Acceleration due to gravity

Table 3.1: MONC's dynamical core variables, adapted from Gray et al. (2001).

$$\nu = \lambda_m^2 S f_m(Ri_p), \tag{3.11}$$

$$\nu_h = \lambda_m^2 S f_h(Ri_p). \tag{3.12}$$

λ_m is the mixing scale length, which filters out motions greater than the grid box size. f_m and f_h are Richardson number dependent functions and $S^2 = S_{ij}S_{ij}$. Ri_p is defined as (Gray et al., 2001):

$$Ri_p = \frac{\partial B}{\partial z} S^{-2}, \tag{3.13}$$

where B is the buoyancy, and is used as a fundamental parameter to describe the stability to turbulence of atmospheric flows. The subgrid scheme utilises a critical Richardson Number, Ri_c, and it is assumed that there are no subgrid contributions to the flow when $Ri_p \geq Ri_c$ (i.e. $f_m(Ri_p) = f_h(Ri_p) = 0$ for $Ri_p \geq Ri_c$).

3.3 Boundary conditions

MONC uses periodic horizontal boundary conditions for all primed prognostic quantities. The top and bottom of the domain are rigid lids, such that at the boundary, $w = 0$. However, other model fields have different top and bottom boundary conditions. The domain bottom should represent the stresses and fluxes associated with flow across the surface, while the top should represent the effects of the remainder of the unmodelled atmosphere (Gray et al., 2001). The rigid lid top boundary may lead to the reflection of gravity waves. To prevent this from occurring, a Newtonian damping layer is implemented in the code, which relaxes all prognostic variables towards their horizontal mean above a given height.

Surface boundary conditions are derived from Monin-Obukhov similarity theory (Monin and Obukhov, 1954), using the Businger-Dyer functions (Businger et al., 1971). This will allow the surface to interact on resolved fields through frictional stresses, as well as sensible and surface heat fluxes. To date, MONC assumes a saturated surface and for the

surface boundary condition calculation, it requires either prescribed surface values input as temperature, or prescribed surface fluxes input as sensible and latent heat (Hill et al., 2018). These conditions can vary with time, and are defined directly in the configuration file.

3.4 Condensation and evaporation

To date, MONC calculates liquid water using a saturation adjustment scheme in the simplecloud component, which is an "all or nothing" approach. Water cannot exist in a sub-saturated grid box and supersaturations are not allowed. Neglecting terms due to diffusion or precipitation, the total change in θ, q_v and q_L can be written as:

$$\frac{D\theta}{Dt} = \frac{L_v}{c_p}\frac{C}{\Pi}, \tag{3.14}$$

$$\frac{Dq_v}{Dt} = -C, \tag{3.15}$$

$$\frac{Dq_L}{Dt} = C, \tag{3.16}$$

where q_v and q_L are the vapour and liquid mixing ratio respectively, C is the rate of change of liquid water due to condensation, L_v is the latent heat of vaporisation and Π is the Exner function, such that:

$$\Pi = \left(\frac{p_s}{p_0}\right)^{\frac{R}{c_p}}. \tag{3.17}$$

p_s is reference state pressure, p_0 is the reference pressure at sea level, R is the gas constant for dry air and c_p is the specific heat of dry air at constant pressure. If q_L^t is q_L on time level, t, C can be defined as (Gray et al., 2001):

$$C = \frac{q_L^{t+1} - q_L^t}{\Delta t}, \tag{3.18}$$

where Δt is the timestep.

3.5 Cloud microphysics - CASIM

The cloud microphysics scheme option MONC can utilise is CASIM. CASIM is a multi-moment bulk microphysics scheme designed to simulate aerosol-cloud interactions and precipitation processes, and has been designed as a long term replacement for the MetUM and LEM microphysics scheme. CASIM has been used to investigate aerosol-cloud interactions, both within the MetUM (e.g. Grosvenor et al., 2017; Miltenberger et al., 2018; Stevens et al., 2018) and MONC (Dearden et al., 2018; Poku et al., 2019).

CASIM represents cloud using five hydrometer types: Liquid cloud; rain; snow; hail and graupel. These can be configured to be specified by one prognostic moment (mass mixing ratio), or by two moments (mass mixing ratio and species number concentration). In addition, rain, snow and graupel can be specified by three prognostic moments (mass mixing ratio, species number concentration and "shape"). CASIM has the ability to represent aerosol activation, ice nucleation processes, and in-cloud aerosol processing through collision-coalescence and removal by cloud sedimentation. Should aerosol processing be selected in CASIM, then once activated, the aerosol is moved to an active in-cloud prognostic, allowing for a change in aerosol fields alongside the cloud's microphysical structure (e.g. a change in aerosol size due to precipitation processes and cloud dynamics).

For this thesis, CASIM has been set to represent a non-precipitating, warm boundary layer cloud (i.e. ice processes and autoconversion to rain are turned off).

In CASIM, the cloud-drop size distribution, $N(D)$, assumes a gamma distribution, which has the form (Shipway and Hill, 2012):

$$N(D) = N_0 D^{\mu_d} e^{-\lambda_d D}, \tag{3.19}$$

where N_0 is the distribution intercept parameter, μ_d is the shape parameter, λ_d is the slope parameter and D is the droplet diameter. The moment of the cloud-drop size distribution, $M(p)$, is described using Equation (3.19):

$$\begin{aligned} M(p) &= \int_0^\infty D^p N(D) dD. \\ &= \frac{N_r}{\lambda_d^p} \frac{\Gamma(1+\mu_d+p)}{\Gamma(1+\mu_d)}. \end{aligned} \tag{3.20}$$

For this work, p is set to 0 and 3; representing the 0th and 3rd moment (i.e. cloud mass and number). The assumption of setting Equation (3.20) to predict two moments, is that the shape parameter is fixed and the slope parameter, λ_d, is a function of cloud mass and number. The slope parameter, λ_d, is defined as:

$$\lambda_d = \left(\frac{\Gamma(1+\mu_d+p_1)}{\Gamma(1+\mu_d+p_2)} \frac{M(p_2)}{M(p_1)} \right)^{\frac{1}{p_2-p_1}}, \tag{3.21}$$

Where p_1 and p_2 are the moments of the distribution used in Equation (3.20), i.e. 0 and 3.

3.5.1 Aerosol activation

In CASIM, the total droplet concentration can be calculated using a parameterisation for aerosol activation. In Chapter's 4 and 6, the scheme used is that of Abdul-Razzak and Ghan (2000). The scheme assumes a lognormal distribution for multi-mode aerosol:

$$\frac{dn}{da} = \sum_{i=1}^{I} \frac{N_i}{\sqrt{2\pi}\sigma_i} \exp\left(-\frac{\ln^2(a/a_m)}{\ln^2\sigma_i} \right), \tag{3.22}$$

where N_i, a_{ci} and σ_i are the total number concentration of aerosol, geometric dry radius and geometric standard deviation of aerosol mode i, respectively. For a given aerosol population, the total number of activated aerosols in each mode is determined by S_{ci} and S_{max}, the critical and environmental supersaturation respectively, where:

$$S_{ci} = \frac{2}{\sqrt{B_i}} \left(\frac{A}{a_{ci}} \right)^{\frac{3}{2}}, \tag{3.23}$$

and

$$S_{max} = \frac{1}{\sum_{i=1}^{I} \frac{1}{S_{ci}} \left[f_i \left(\frac{\eta}{\zeta_i} \right)^{\frac{3}{2}} + g_i \left(\frac{S_{ci}^2}{\zeta_i + 3\eta} \right)^{\frac{3}{4}} \right]}. \tag{3.24}$$

Functions, f_i and g_i, as well as constants A, B_i, η and ζ_i are all defined in both Abdul-Razzak et al. (1998) and Abdul-Razzak and Ghan (2000). Using Equations (3.23) and (3.24), the number of activated aerosols, N_a, is defined as:

$$N_a = \sum_{i=1}^{I} N_i \frac{1}{2} [1 - \text{erf}(u_i)], \tag{3.25}$$

where:

$$u_i = \frac{2\ln(S_{ci}/S_{max})}{3\sqrt{2}\ln\sigma_i}. \tag{3.26}$$

and erf(x) is the error function defined by Abramowitz and Stegun (1965). Finally, MONC converts N_a into a droplet number tendency, such that:

$$\left(\frac{\partial N}{\partial t} \right)_{act} = \frac{N - N_a}{\Delta t}, \tag{3.27}$$

where the number of new activated droplets (N_a) are taken away from already activated droplets (N) from the previous timestep.

CASIM has the option to calculate N_a using the Shipway (2015) activation scheme. The use of the Shipway scheme, as well as the representation of aerosol activation in fog generally will be explored and discussed in Chapter 5 of this thesis.

3.5.2 Sedimentation

CASIM can represent droplet sedimentation, based on the cloud-drop size distribution shown in Equation (3.19). The sedimentation rate, S_d, for a given hydrometer species (in this case, liquid cloud) is defined as:

$$S_d = \hat{v} M(p), \tag{3.28}$$

where $\hat{v}$ is the moment weighted mean terminal velocity, such that:

$$\hat{v} = \frac{\int_0^\infty V(D)D^p N(D)dD}{\int_0^\infty D^p N(D)dD}. \tag{3.29}$$

$V(D)$ is the terminal velocity drop-size distribution (as defined in Shipway and Hill, 2012) and p represents any given moment. Ferrier (1994) defined $V(D)$ as:

$$V(D) = a_r \left(\frac{\rho}{\rho_0}\right)^{g_r} D^{b_r} e^{-f_r D}, \tag{3.30}$$

where a_r, b_r, f_r and g_r are fall constants for cloud droplets, and ρ and ρ_0 is the density of air and the sea surface level density of air respectively (the fall constants are defined in Shipway and Hill, 2012). By inserting Equations (3.19) and (3.30) into Equation (3.29), Equation (3.29) can be rewritten as:

$$\hat{v} = a_r \frac{\Gamma(1+\mu_d+p+b_r)\lambda_d^{1+\mu_d+p}}{\Gamma(1+\mu_d+p)(\lambda_d+f_r)^{1+\mu_d+p+b_r}} \left(\frac{\rho_0}{\rho}\right)^{g_r}. \tag{3.31}$$

Throughout this thesis, sedimentation has been set to deplete liquid water mass (i.e. $p = 3$).

3.5.3 Aerosol processing: In-cloud aerosol removal

CASIM has the option to include aerosol processing, which includes nucleation scavenging; in-cloud mechanical processing (leading to fewer but larger aerosol form through collision-coalescence); precipitation washout of both in-cloud and out of cloud aerosol; and evaporative generation (Miltenberger et al., 2018). There are three levels of processing in CASIM:

- Level 0 - only aerosol activation;
- Level 1 - passive processing: passive processing accounts for nucleation scavenging. Both the aerosol number and mass deplete, and aerosol are transferred to the active in-cloud prognostic;

- Level 2 - mechanical growth of aerosol: leads to a decrease in aerosol number and an increase in aerosol mass, therefore accounting for the change in aerosol size due to either cloud or rain droplets aggregating.

Should evaporation of droplets occur, the recovered aerosol will be replaced back in the unactivated aerosol diagnostic with processing options 1 and 2. Chapters 4 and 5 will have processing set to level 0. In Chapter 6, processing will be set to level 1 and by used to investigate the impact nucleation scavenging has on the fog evolution.

3.6 Radiation

Throughout this thesis, radiation will be calculated using SOCRATES. SOCRATES is a radiative transfer scheme that uses a two-stream equation code in both the short-wave and long-wave regions of the spectrum. The code reads in standard McClatchey profiles, which provides a full atmosphere profile of pressure, temperature, ozone and vapour. These profiles are merged with the MONC domain to ensure that the radiative transfer is performed over a full atmosphere. For this work, the profiles have been set to be representative of a mid-latitude winter environment. The radiative transfer code uses two spectral files, one for the long-wave and and one for the short-wave spectrum. At each level of the atmosphere, the solutions of the two-stream equation require information on the mass extinction coefficients for absorption and scattering, the asymmetry factor and in the short-wave region, the forward-scattering factor. The optical properties of the cloud are considered to be "gray", i.e. the emissivity is assumed to be equal at all bands. The user has the option to represent cooling either via just a clear sky cooling or radiative cooling due to liquid water. Chapters 4 and 5 will assume radiative cooling due to liquid water. In Chapter 6, some tests only apply just a clear sky cooling to understand the impact of nucleation scavenging on fog.

A requirement for the code is to provide information on either a fixed solar variable or a diurnal cycle. Finally, an effective radius needs to be defined, so the code can calculate both the short-wave and long-wave fluxes. The effective radius to date is not coupled

with CASIM, but instead is fixed. The suitability of the chosen effective radius will be discussed throughout the thesis.

3.7 Large-scale forcing

Any atmospheric processes on a larger scale than the typical LES can be accounted for in MONC, by applying a large-scale atmospheric forcing. To date, the large-scale forcing options include a subsidence to the atmosphere, a relaxation to the mean prognostic profile, and a prognostic tendency. In MONC, prognostic tendencies represent local-scale advection, and are defined in the initialisation configuration (either in changes per second or per day). The tendencies are constant with time. Subsidence represents either a large-scale descent, where it can be applied in MONC by defining either a large-scale divergence rate or a subsidence vertical velocity. The subsidence rate will then be converted to a tendency and added to either the global mean profile or local profile. To apply a relaxation to the mean profile, MONC utilises a Newtonian relaxation nudging method for a prognostic variable, X, such that:

$$\left.\frac{\partial X}{\partial t}\right|_{relax} = G(X - X_0), \tag{3.32}$$

where X_0 is the mean profile that X is attempting to relax to, and G is the relaxation timescale and should be carefully considered depending on the application for Equation (3.32).

3.8 Geostrophic winds

MONC accounts for dynamical large-scale forcing in the coriolis component, therefore representing coriolis effects, large-scale pressure gradients, geostrophic wind and thermal wind balances. The geostrophic wind u_g and v_g, is defined as the balance between the pressure gradient and coriolis effect in the u and v wind respectively (Pielke and Cram, 1987):

$$u_g = \frac{\theta}{f}\frac{\partial \pi}{\partial x}\bigg|_{\sigma_g} - \frac{g}{f}\frac{\sigma_g - s_h}{s_h}\frac{\partial z_G}{\partial x};$$
$$v_g = -\frac{\theta}{f}\frac{\partial \pi}{\partial y}\bigg|_{\sigma_g} - \frac{g}{f}\frac{\sigma_g - s_h}{s_h}\frac{\partial z_G}{\partial y}. \tag{3.33}$$

The vertical component of the system for Equation (3.33), σ_g, is defined as:

$$\sigma_g = s_h \frac{z - z_G}{s_h - z_G}; \tag{3.34}$$

where s_h is an arbitrary height in the atmosphere, z_G is the terrain elevation and z is the height about the surface. f is the Coriolis parameter, T is temperature and $\pi = c_p T/\theta$. At the surface, $z = z_G$ and hence $\sigma_g = 0$. Therefore Equation (3.33) reduces to (Pielke and Cram, 1987):

$$u_g = \frac{\theta}{f}\frac{\partial \pi}{\partial x};$$
$$v_g = -\frac{\theta}{f}\frac{\partial \pi}{\partial y}. \tag{3.35}$$

Equation (3.35) displays the surface geostrophic winds for the u and v winds. These are fixed values and are defined by the user. For this work, the surface geostrophic winds are defined as the averaged observed winds in the intialised profile, between 1 and 2 km.

3.9 Summary

This chapter provides an outline of the features of MONC. MONC is the main tool employed for this research, therefore the following results chapters will refer back to subsections of this overview when necessary. Given that MONC and CASIM are both relatively new and are still in development, their default settings will be tested and discussed in Chapter 4 of this thesis.

Chapter 4

How important are aerosol-fog interactions for the successful modelling of nocturnal radiation fog?

4.1 Introduction

Section 2.2.1 of Chapter 2 discussed in detail that the role of aerosols, and in particular, their indirect effects are importance for nocturnal radiation fog. Bott (1991) discussed the importance of aerosol-fog interactions, showing that they fundamentally control the optical thickness of a nocturnal fog. Additional studies have complemented the work by Bott (e.g. Stolaki et al., 2015; Maalick et al., 2016), demonstrating that aerosol will play a crucial part in both the formation and development stages of nocturnal radiation fog. More recently, Boutle et al. (2018) discussed that aerosol-fog interactions may be important for forecasting fog using numerical weather prediction (NWP) models, especially for fog cases that may form within a relatively clean environment.

This chapter aims to understand the role of aerosol-fog interactions on the evolution

of a nocturnal optically thin (stable) fog layer, by performing and comparing various high-resolution numerical simulations that change properties of the aerosol population. Previous studies investigating aerosol-fog interactions simulate fog cases that form in relatively polluted environments (e.g. Paris). However, the fog case analysed in this chapter formed in a "clean" environment, making it ideal to understand aerosol-fog interactions in a different aerosol regime. Simulations are undertaken with MONC coupled with CASIM, and therefore have the capability to simulate and investigate aerosol-cloud interactions. In addition to understanding the role of aerosol in these simulations, the default settings used in both MONC and CASIM will be explored to understand whether they are suitable for tests presented within the thesis. This chapter will address three key objectives:

1. Evaluate how well MONC coupled with CASIM can simulate an optically thin nocturnal fog case;

2. Investigate the impacts of aerosol variables on fog development;

3. Assess whether the default settings for cloud droplet representation in both CASIM and the radiation scheme are suitable for these simulations, and how they could potentially be improved.

Section 4.2 will describe the details of the model, the simulation setup and tests discussed in this chapter. The chapter's objectives will be addressed in Section's 4.3, 4.4, 4.5, 4.6 and 4.7. A summary and conclusions will then follow.

4.2 Model setup

MONC is used to perform a suite of sensitivity tests based on IOP1 (intensive observation period 1) from the recent LANFEX field campaign (Price et al., 2018). IOP1 took place at the UK Met Office research field site at Cardington, Bedfordshire in southeast England (52^{o}06'N, 0^{o}25.5'W) on 24/25th November 2014. The site sits in a wide, shallow valley characterised by a patchwork of mostly arable fields with low hedges. During the night of IOP1, a high-pressure system had developed across most of the UK, resulting in widespread

IOP1	
Horizontal Domain	132 x 132 m^2
Vertical Domain	705 m
Δx, Δy	2 m
Δz	Variable - 1 m first 100 m, stretched up to 6 m afterwards
Simulation duration	12 hours
Timestep	0.1 s
Cloud Microphysics	Cloud AeroSol Interactive Microphysics (CASIM)
Radiative Transfer Scheme	SOCRATES (Edwards and Slingo, 1996)

Table 4.1: The input parameters and model setup for IOP1 in MONC.

fog. At Cardington, fog formed around 1800 UTC and remained stable through the duration of the night. IOP1 was chosen as it was one of the cleanest examples of local fog development, with minimal influence by advection (see Smith et al., 2018, for more details).

The model setup for IOP1 is presented in Table 4.1. MONC was initialised using the observed vertical profiles and surface measurements as shown in Figure 4.1. Surface geostrophic winds were calculated by averaging the wind components between 1 and 2 km, and for IOP1 is $u_g = 1.3$ m s^{-1}, $v_g = 2.1$ m s^{-1}. The grid spacing in MONC was set to 2 x 2 m^2 in the horizontal and 1 m in the vertical up to 100 m. Previous studies have shown the importance of model resolution for simulating the formation period of fog (e.g. Bergot et al., 2007; Maalick et al., 2016; Maronga and Bosveld, 2017); it was therefore critical to run MONC at such a high resolution. As MONC does not have an interactive land surface scheme, temperature and surface water vapour mixing ratio is prescribed at the lower boundaries. Based on observations, surface temperature (shown in Figure 4.1c) and a fixed surface water vapour mixing ratio of 0.004 kg kg^{-1} were both prescribed. While surface-atmosphere interactions and feedbacks can be very important for fog, observed surface fluxes from IOP1 were close to zero or negative (not shown), so feedbacks between

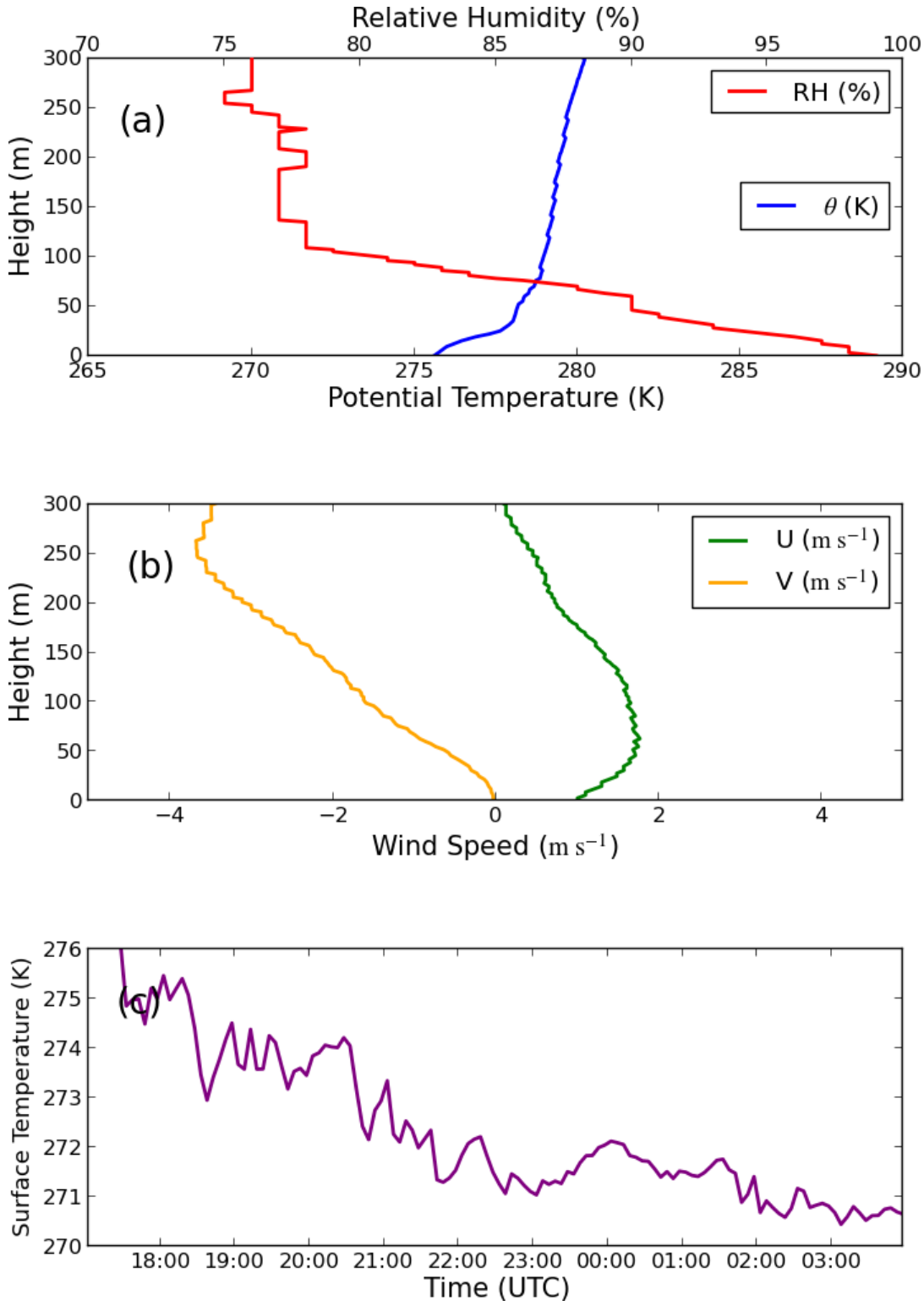

Figure 4.1: Initial conditions at 1700 UTC used to initialise MONC. From sonde data: (a) Potential Temperature (K) and relative humidity (%), (b) wind components. From surface measurements: (c) grass surface temperature.

the surface and atmosphere may not be as important for IOP1 compared with other fog cases (Boutle et al., 2018).

All simulations use CASIM; a multi-moment bulk microphysics scheme designed to simulate and study aerosol-cloud interactions (Field et al., 2016). In this chapter, CASIM uses two moments for cloud droplets. For the cloud-drop size distribution (see Chapter 3 for reference), the default shape parameter is set to $\mu_d = 0$. The default value of μ_d was chosen to represent cloud-size distributions in marine stratocumulus clouds (Pruppacher and Klett, 2010, p.17). The suitability of the default value of μ_d will be discussed further in Section 4.6 of this chapter. For the aerosol population, only larger CCN (the accumulation mode where 0.1 μm $<$ CCN size diameter $<$ 1 μm) are accounted for, and its size distribution is assumed to be lognormal with a standard deviation of 2.0. The aerosol activation scheme used in these simulations is that of Abdul-Razzak and Ghan (2000), which uses an average CCN size that is determined by the total soluble mass, the CCN number concentration and an assumed aerosol size distribution. In-cloud processing of aerosol removal is turned off in these simulations for consistency with previous studies (e.g. Stolaki et al., 2015; Maalick et al., 2016).

Radiation was calculated using the Suite of Community RAdiative Transfer codes (SOCRATES) based on the work by Edwards and Slingo (1996). SOCRATES was called every 5 minutes, allowing for the longwave radiative fluxes at the top of the fog layer to be captured in the model. The longwave radiative fluxes are determined by the cloud's optical depth, τ, (Edwards and Slingo, 1996):

$$\tau = k^{(e)} \Delta m, \tag{4.1}$$

such that Δm is the change in mass for a given spectral band and $k^{(e)}$ is the mass extinction coefficient, which is defined as:

$$k^{(e)} = L \left(a + \frac{b}{r_e} \right). \tag{4.2}$$

L is the mass mixing ratio of liquid water, a and b are constants that vary for a given spectral band and r_e is the cloud droplet's effective radius; the weighted mean droplet

size for a given population (Edwards and Slingo, 1996). Throughout this chapter, MONC coupled with SOCRATES assumes a fixed effective radius, such that $r_e = 10$ μm. The chosen radius is the default value for MONC and is primarily motivated by observations of the effective radius within cumulus clouds (Blyth and Latham, 1991). However, the chosen value of r_e may not be suitable for simulations of fog. This will be discussed further in Section 4.7 of this chapter.

Test	CCN concentration (cm $^{-3}$)	Total soluble mass (ng)	Average CCN radius (μm)	Shape parameter, μ_d	Cloud drop effective radius (μm)
T_control	100	2.7	0.075	0.0	10.0
T_control_800x800	100	2.7	0.075	0.0	10.0
T_double_ccn	200	2.7	0.059	0.0	10.0
T_half_ccn	50	2.7	0.094	0.0	10.0
T_double_mass	100	5.4	0.094	0.0	10.0
T_half_mass	100	1.35	0.059	0.0	10.0
T_mu_1	100	2.7	0.075	1.0	10.0
T_mu_2	100	2.7	0.075	2.0	10.0
T_mu_3	100	2.7	0.075	3.0	10.0
T_er_15.0	100	2.7	0.075	0.0	15.0
T_er_5.0	100	2.7	0.075	0.0	5.0

Table 4.2: A list of tests referred to throughout this study, which includes changes in: properties to the aerosol population; shape parameters; and the effective radius.

Table 4.2 summarises the setup of the simulations presented in this chapter. During IOP1, there were no direct observations of CCN. A value of 100 cm^{-3} in the accumulation mode was set, with a total soluble mass of 2.7 ng throughout the initialised vertical profile, based on typical measurements for a clean rural site similar to Cardington, UK (Boutle et al., 2018). To reduce computational expense, 1D diagnostics are output every 1 minute

and 3D diagnostics are output every 5 minutes (domain averaged profiles).

During preliminary tests (not shown), a simulation was setup to be configured with a multi-mode aerosol distribution (using aerosol data from Boutle et al., 2018). The purpose of this test was to understand whether it was a requirement to run simulations of IOP1 with a full aerosol spectrum, as opposed to just the accumulation mode aerosol used in the control simulation. MONC is a relatively new model and to date, has only been tested with accumulation mode aerosol when coupled with CASIM. Unfortunately, MONC encounters a problem with the checkpoint restart code when ran with a multi-mode distribution, and therefore was only able to produce one hour of simulation output for the multi-mode aerosol run. Consequently, this multi-mode run only captured initial fog formation. However, upon comparing this run to the control simulation, there was no appreciable difference in the initial fog formation between both tests. Chapter 5 will discuss how important it is to include a full aerosol spectrum for simulations of fog.

4.3 Control simulation - T_control

This section will describe the control simulation, T_control, which will be directly compared to observations from IOP1 and will form the basis for further sensitivity experiments. Observations show (Figure 4.2) the visibility at a 2 m altitude (near-surface visibility) dropping below 1000 m at around 1800 UTC, and then decreasing further to 100 m at 2100 UTC. After 2100 UTC the fog remained optically thin, with the near-surface visibility varying between 1000 m and 100 m, implying that the fog was patchy throughout the night.

For all model simulations, the visibility is calculated using the formula of Gultepe et al. (2006), where visibility, Vis, is defined as follows:

$$Vis = \frac{1.002}{(LWC \times CDNC)^{0.6473}}, \tag{4.3}$$

such that LWC is the liquid water content and $CDNC$ is the cloud droplet number concentration. Equation (4.3) was derived based on observations of fog in mainland Europe

and is valid over a range of CDNC from a few per cubic centimetre up to a few hundred per cubic centimetre.

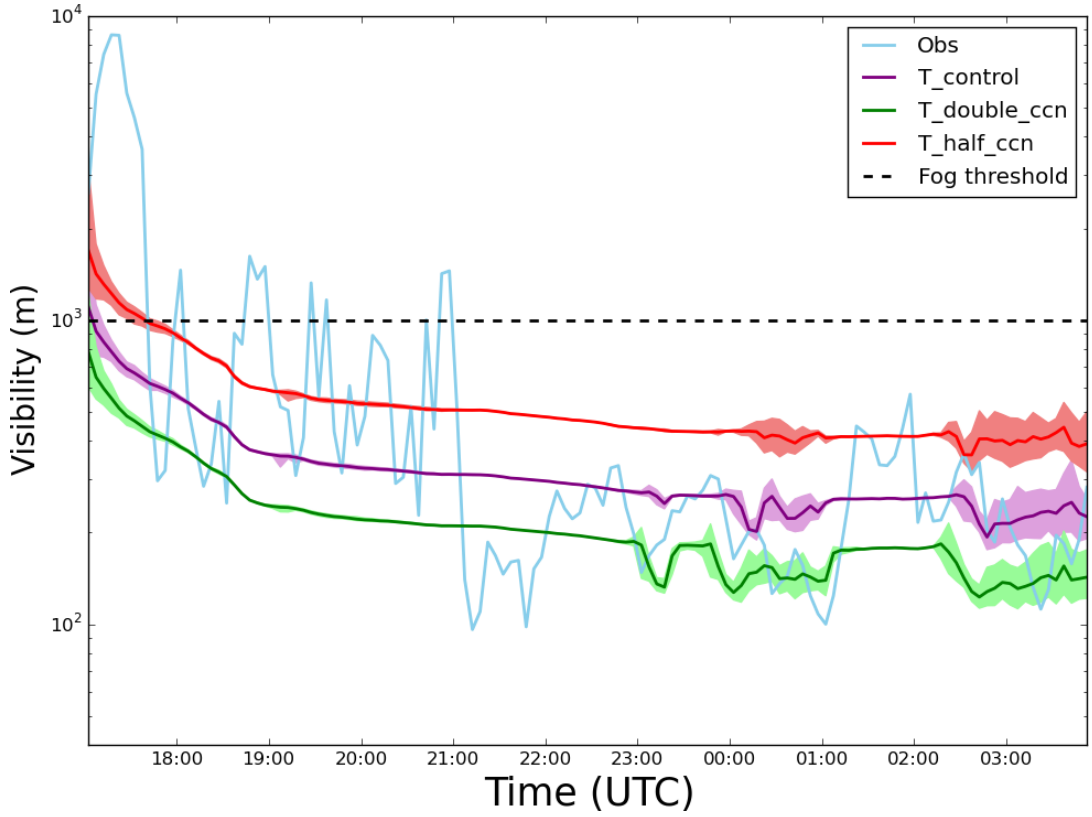

Figure 4.2: Time series of the mean visibility (m) at 2 m altitude. Purple – T_control; green – T_double_ccn; red – T_half_ccn; light blue – observations; dashed black line - fog threshold. Minimum and maximum visibility mark on figure by shaded area.

The simulated near-surface visibility drops under 1 km at 1705 UTC, indicating the formation of fog about an hour before observations, where it continues to decrease and eventually converges to around 230 m. The small near-surface visibility range before 0000 UTC, and between 0100 and 0230 UTC, shows a spatially homogeneous layer of fog, demonstrated by the difference between the minimum and maximum. However, after 0230 UTC the range increases to a maximum of 100 m, showing a more heterogeneous layer, which is indicative of a more turbulent boundary layer. The variability in the simulated near-surface visibility across the domain is similar to the temporal variability in

the observed near-surface visibility for parts of the night, particularly later on. However, the near-surface visibility in T_control within its initial stages is mostly lower than the observations, therefore suggesting that T_control is transitioning to a deeper fog too quickly.

Figure 4.3a shows vertical profiles of potential temperature throughout T_control at 1700, 2230, 0130 and 0330 UTC. T_control at 2230 UTC shows a stable layer at a lapse rate of 0.0754 K m^{-1} till 10 m, and then increases to 0.175 K m^{-1} up to 45 m. Above 45 m, the stability is reduced, suggesting the top of the boundary layer. When compared to observations, the second change in atmospheric stability within T_control is higher than the observed inversion by 30 m. At 0130 UTC, the mixed layer begins growing to a height of 26 m, capped by a stable layer with a lapse rate of 0.147 K m^{-1}. However, the simulation agrees well with observations from a height of 50 m. During T_control, the overall boundary layer at 0130 UTC was colder than the observations by up to 2 K. At 0330 UTC, the mixed layer continues to grow up to a height of 40 m, with a mixed layer still not being present in the observations, and hence the results shown are all consistent with the fog becoming too deep too soon.

Vertical profiles of CDNC were taken throughout the night, as shown in Figure 4.4. At 2230 UTC, the highest concentration of fog droplets is within the first 10 m, at around 100 cm^{-3}. The CDNC gradually decreases with height, and from 20 m it increases again to a maximum of 50 cm^{-3} at a height of 37 m. The CDNC indicates the height of the fog, which at 2230 UTC is 50 m. At 0030 UTC, peak concentration of fog droplets is at the top of the fog: 40 cm^{-3} at a height of 40 m. Although it appears as though the fog layer has decreased in height, a possible explanation for the decrease in the observed CDNC could be an instrumentation limitation. This resulted in only accounting cloud droplets that were of sizes between 2 and 40 μm in diameter, with a 1 μm uncertainty (Price et al., 2018). Therefore, there is a potential that droplets that have begun growing through condensation were not accounted for. Finally, at 0330 UTC, there is a greater variation in CDNC, although it is beginning to homogenise in the middle part of the layer, and it ranges between 20 and 100 cm^{-3}. The peak CDNC is at 40 m, and the fog layer

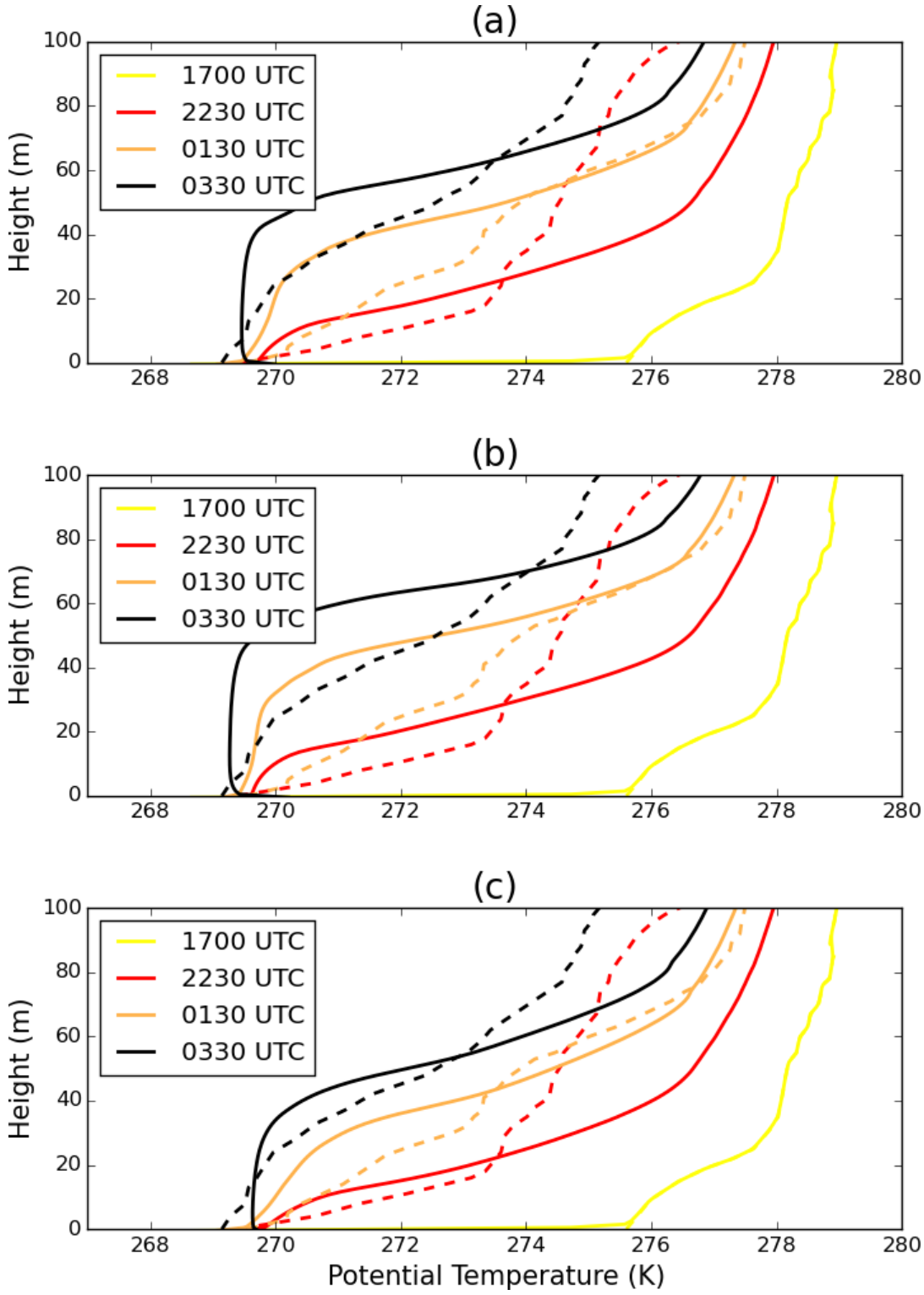

Figure 4.3: Vertical profiles of the potential temperature (K) at 1700 (yellow), 2230 (red), 0130 (orange) and 0330 (black) UTC. The dashed lines represent observations, and solid lines represent simulated values. (a) – T_control; (b) – T_double_ccn; (c) – T_half_ccn.

Test	Time (UTC)		
	2230	0030	0330
T_control	2.1	1.1	2.2
T_double_ccn	3.1	1.8	3.5
T_half_ccn	1.3	0.7	1.3
T_double_mass	2.3	1.2	2.3
T_half_mass	1.9	1.1	2.0

Table 4.3: A table listing the ratio of modelled to observed cloud drop number averaged over the vertical height across tested time frame.

depth is 65 m.

Throughout the night, the activation rate in T_control (the percentage of CCN that activate into fog droplets), is between 60 and 65%. At 2230 UTC, whilst the difference in the fog layer height between T_control and the observations is only 2 m, the proportion of fog droplets averaged over the depth of the fog in T_control is greater than the observations by a factor of 2.1 (Table 4.3). Following on, at 0030 UTC the height of the fog layer in T_control is greater than the observations by 30 m, with T_control forming an average fog droplet density of 1.1 times. Finally, at 0330 UTC the fog layer has a greater height by 20 m in T_control in comparison to observations, with an average of 2.2 times more fog droplets across the fog depth. The number of droplets formed is determined by the aerosol activation parameterisation. The majority of activation schemes (including the scheme in CASIM) were designed for convective cloud formation (Ghan et al., 2011) and so discrepancies within the scheme may be the cause of too many droplets forming within T_control. This will be discussed in more detail in Section 4.5 of this chapter.

Prior to 1930 UTC, there is a noticeable difference in surface deposition rate between T_control and observations, with a maximum difference of 24 g m^{-2} hr^{-1} at 1830 UTC. Observations of surface deposition and liquid water are collected from the site's dewmeters; accounting for both dew deposition and sedimentation (Price and Clark, 2014). The high rate before fog formation suggests the importance of dew deposition, a process cur-

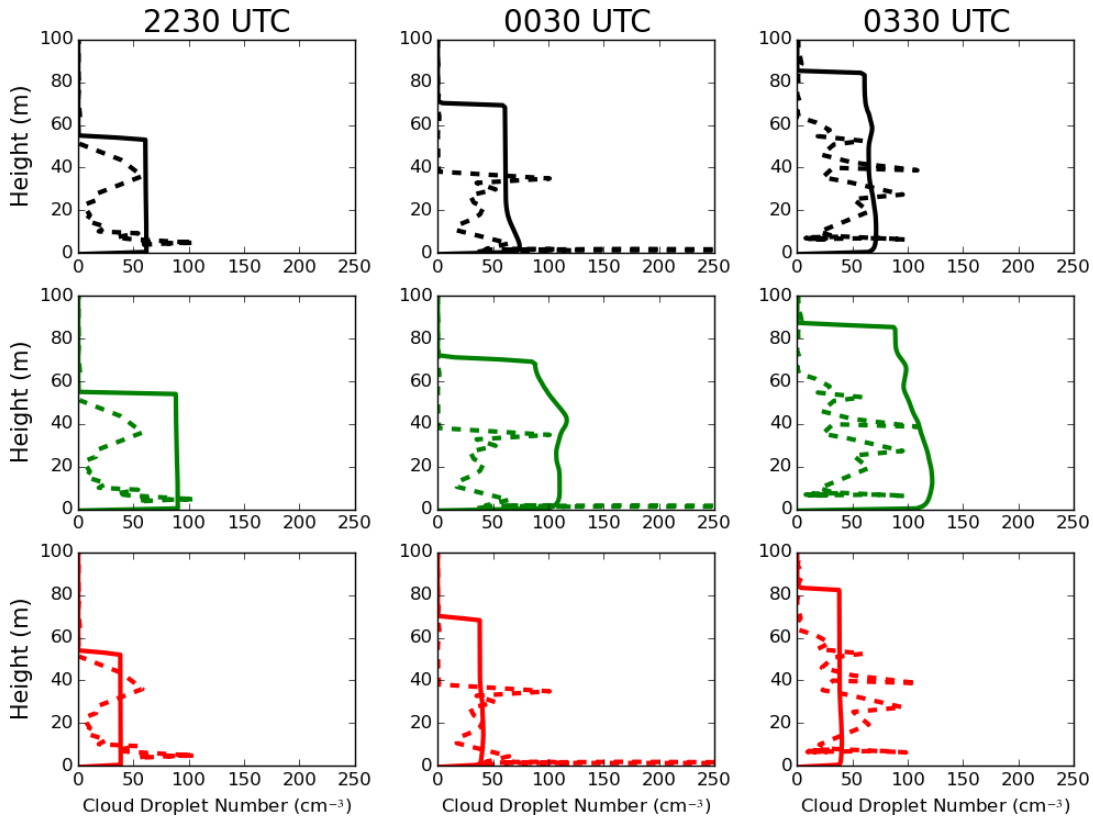

Figure 4.4: Vertical profiles of the cloud droplet number concentration (cm^{-3}) at 2230, 0030 and 0330 UTC. The dashed lines represent observations, and solid lines represent simulated values. Black – T_control; green – T_double_ccn; red – T_half_ccn.

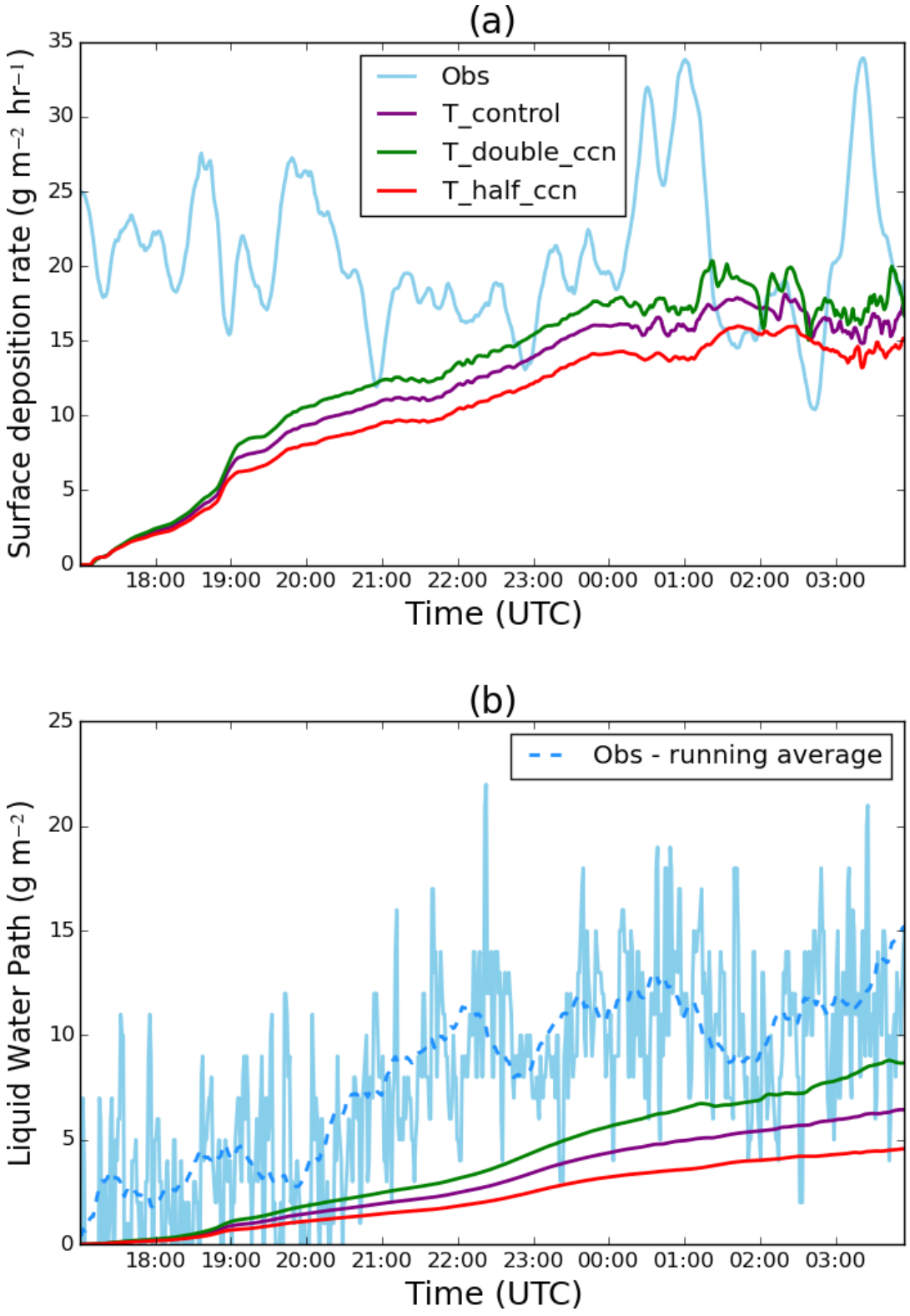

Figure 4.5: (a) - Time series of the surface deposition rate (g m^{-2} hr^{-1}). Purple – T_control; green – T_double_ccn; red – T_half_ccn; light blue – observations. (b) Time series of the liquid water path (g m^{-2}). Purple – T_control; green – T_double_ccn; red – T_half_ccn; light blue – observations; blue dashed – running average over observations (40 points).

rently not included in the model. Another likely explanation for this underestimation is due to MONC currently not accounting for hygroscopic absorption at the surface. As a result, there is an underestimation in the surface saturated specific humidity, and hence impacts latent heat fluxes used in the lower boundary layer parameterisation (as discussed Price and Clark, 2014). After 1830 UTC, the simulated surface deposition rate increases, however, it is mostly at the lower end of the variability in observations by up to 8 g m^{-2} hr^{-1}, signalling that the simulated fog layer in T_control is optically thinner.

Observations show an increase in the liquid water path (LWP, the integrated liquid water across the vertical depth) through the night (Figure 4.5b), with a maximum mean LWP of 15 g m^{-2} (calculated using a 40-point running average) at around 0330 UTC. The maximum mean LWP occurred around the same time that the near-surface visibility dropped below 100 m, as shown in Figure 4.2, suggesting that this was a key stage at which the fog became optically thicker. Throughout the T_control simulation, the modelled mean LWP was lower than what was observed, where for example at 0100 UTC, the modelled mean LWP was 5.4 g m^{-2}; lower than the observations by a factor of 2.1. Work by Stolaki et al. (2015) demonstrated that the LWP is controlled by the sedimentation rate, with Boutle et al. (2018) showing that the LWP is controlled by both the LWC and CDNC. Therefore, the model underestimating the LWP could be linked to the cloud drop-size distribution, which controls the sedimentation representation. This will be discussed in Section 4.6 of this chapter.

In reality, the abundance of small drops forming will result in the radiative impact of the fog layer increasing. As the effective radius is fixed in SOCRATES, the downwelling longwave at 2 m is controlled by the sedimentation of liquid water (Figure 4.6a). Although the modelled and observed downwelling agree well for the first half hour of the tested timeframe, from 1730 UTC onwards they begin to diverge. At 1900 UTC, the difference between the observed and simulated downwelling longwave radiation is 15 W m^{-2}, and whilst the observations suddenly grew from 250 to 260 W m^{-2} at 2100 UTC, the modelled downwelling reached a value of 265 W m^{-2} at 2130 UTC more gradually. Unfortunately, the instrumentation measuring downwelling and upwelling longwave radiation froze from

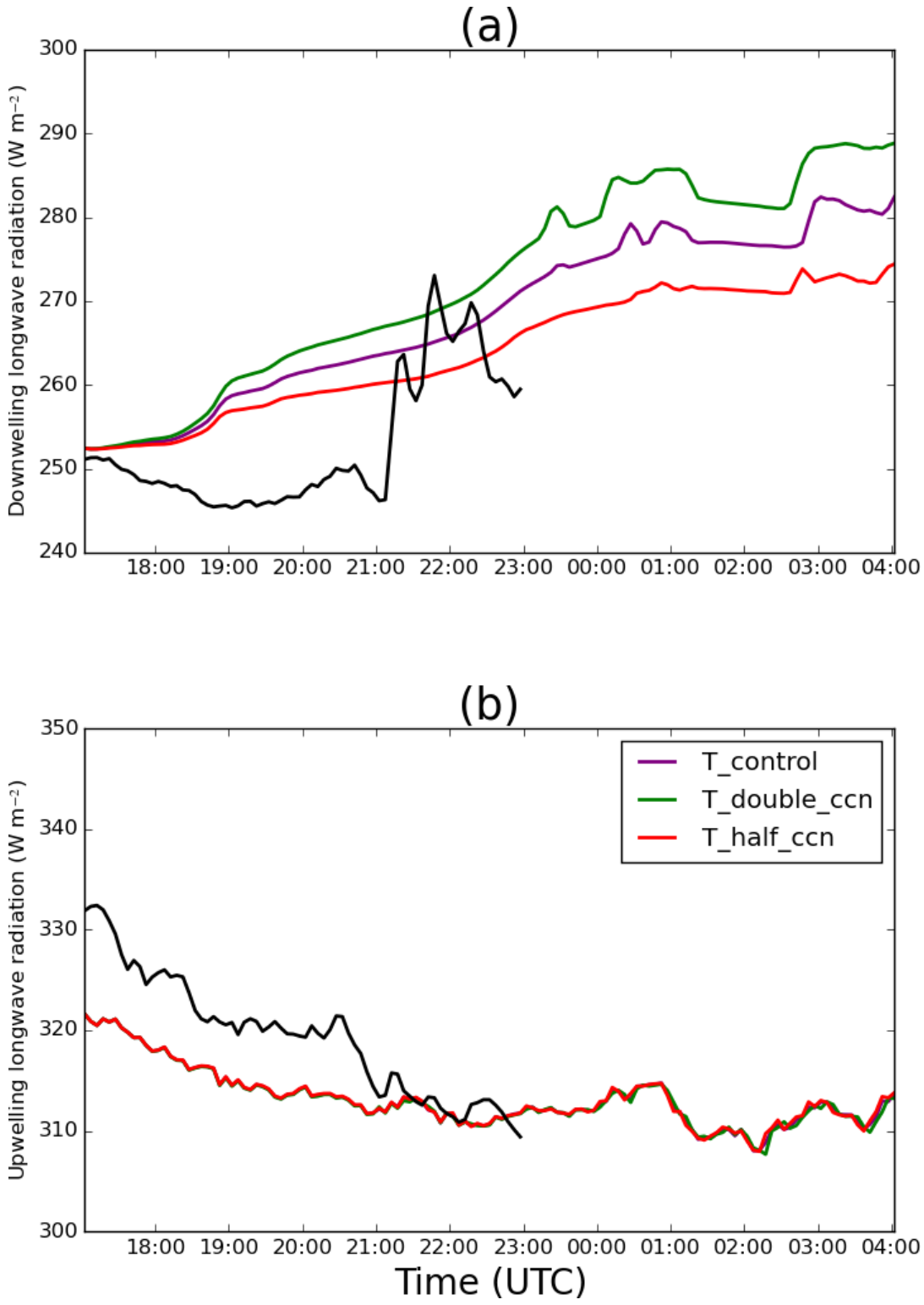

Figure 4.6: Time series of the downwelling (a) and upwelling (b) longwave radiation (W m^{-2}) at a 2 m altitude . Purple – T_control; green – T_double_ccn; red – T_half_ccn; black – observations.

2300 UTC, and thus there is no available data to compare the model to observed flux behaviours. However, despite this, the difference in behaviour provides further evidence that the default settings for aerosol activation are unsuitable to capture the transition to a more optically thick fog in this case, as discussed in Boutle et al. (2018). The modelled upwelling longwave throughout T_control is lower than the observed upwelling longwave, where the difference between the measurements, for example, is 8 W m^{-2} at 2000 UTC. The difference between the simulated and observed upwelling longwave radiation is likely due to the representation of the surface, in which the proportion of longwave radiation being emitted from the surface within MONC could differ from observations.

Figures 4.7a-b directly compares the simulated surface and screen (altitude of 1.2 m) temperature to observations, to firstly check that the model configuration profiles were set up correctly. The simulated surface temperature in T_control shows little to no variation when compared to the observed surface temperature, and the simulated and observed screen temperatures also show good agreement. As MONC was driven by the observed surface temperature, this result implies that the discrepancy in Figure 4.6b is linked to how the upwelling longwave is being calculated in SOCRATES. For a given temperature, T, the emitted radiative energy, $E(T)$ is defined as:

$$E(T) = \epsilon \sigma T^4, \tag{4.4}$$

where ϵ is the emissivity for a given medium and σ is the Stefan-Boltzmann constant, namely $\sigma = 5.67 \times 10^{-8}$ W m^{-2} K^{-4}. The observed upwelling longwave is first compared to the observed emitted radiative energy, $E(T)$, at 1.2 m using Equation (4.4). For this comparison, it was assumed that $\epsilon = 1$ (Figure 4.7c). As there is a good agreement between the two observed measurements, the value for emissivity used in SOCRATES is likely to be $\neq 1$. To understand if this was the case, an estimated emissivity was calculated using the ratio of the observed and simulated upwelling longwave (Figure 4.6b) at 1700 UTC. Applying this correction to the simulated upwelling longwave results in an improved agreement during initial fog formation (Figure 4.7c). However, by 2030 UTC, the two quantities begin to diverge from each other with a maximum difference of 10 W

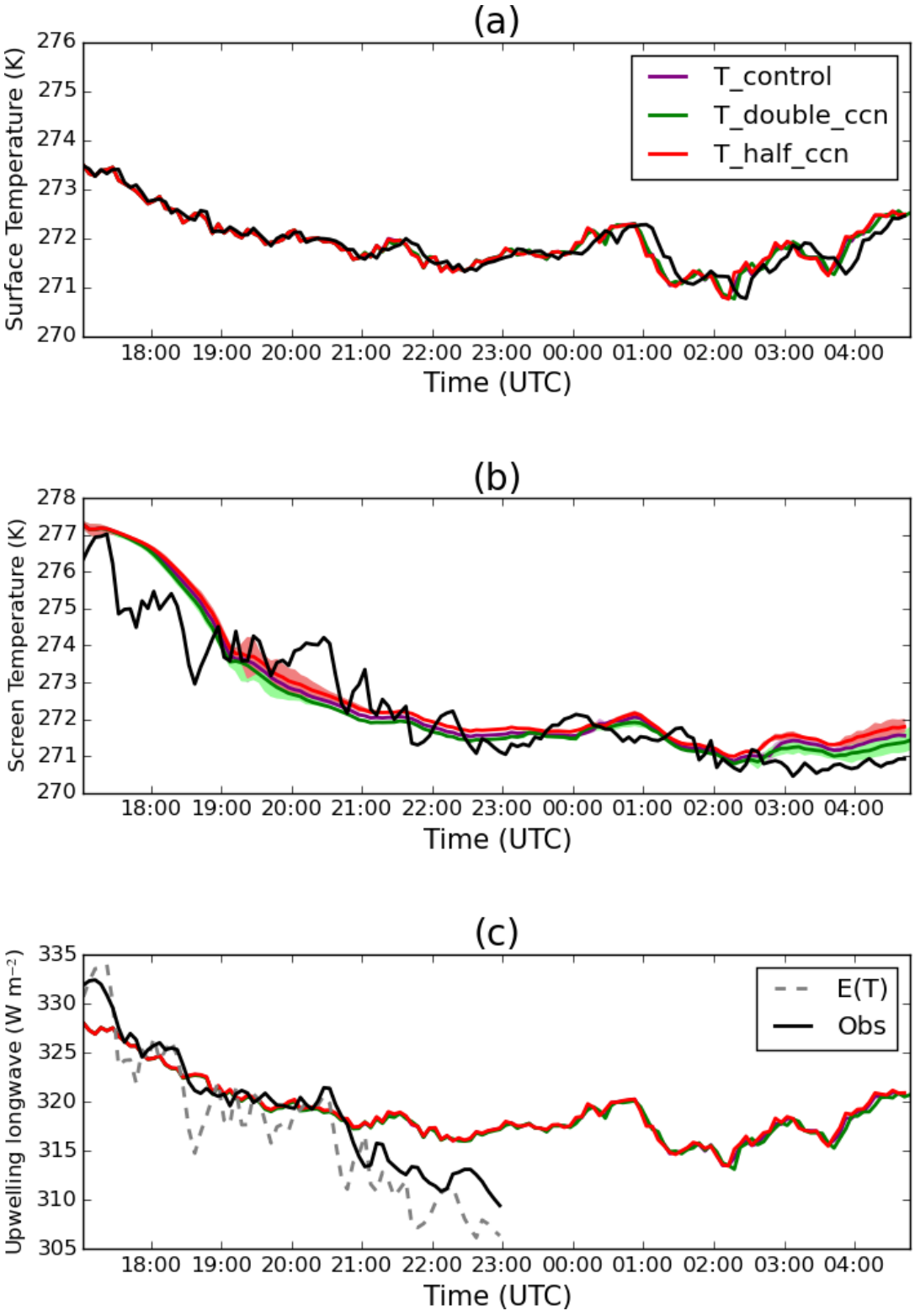

Figure 4.7: Time series of (a) - surface temperature, (b) - temperature at a 2 m altitude and (c) - upwelling longwave radiation (W m^{-2}) at a 2 m altitude with an applied estimated emissivity using the ratio of the observed and simulated upwelling longwave at 1700 UTC, shown in Figure 4.6. Purple – T_control; green – T_double_ccn; red – T_half_ccn; black – observations; grey dashed line - observed emitted energy calculated using Equation (4.4).

m^{-2} at 2300 UTC. By 2100 UTC, the observations show more growth in the fog layer and could suggest that land-atmospheric feedbacks were actually important for IOP1, due to the rate of longwave radiation being emitted and absorbed between the fog layer and the surface.

4.4 Domain size validation

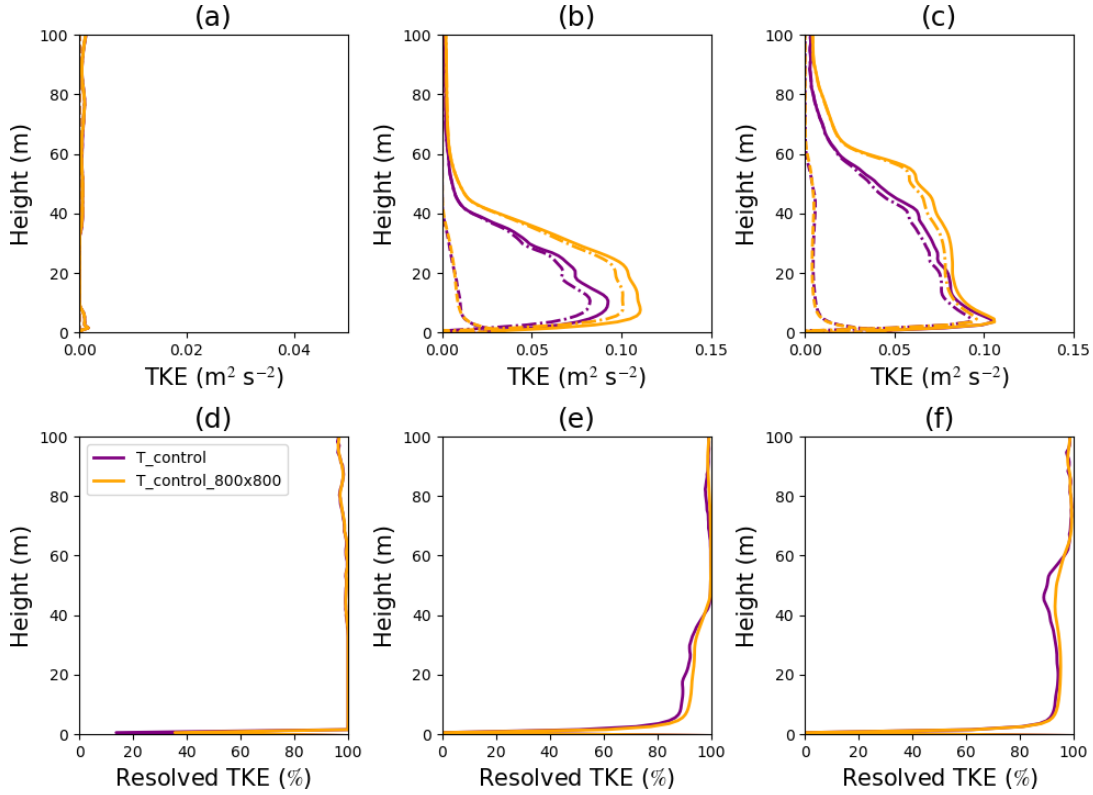

Figure 4.8: Vertical profiles of the TKE and resolved TKE. (a) - (c): total (solid lines), resolved (dashed lines) and subgrid (short dashed lines) turbulent kinetic energy (TKE, m^2 s^{-2}) averaged between 1800 to 1900, 0000 to 0100 and 0300 to 0400 UTC. (d) - (f): resolved scale turbulence contribution to total TKE averaged between 1800-1900, 0000-0100 and 0300-0400 UTC. Purple - T_control; orange - T_control_800x800.

Studies that have previously investigated fog in a LES setup have defined the horizontal domain size to be equivalent to the field size of the observed fog (e.g. Nakanishi,

2000; Porson et al., 2011; Maronga and Bosveld, 2017; Mazoyer et al., 2017). A smaller size domain may potentially not account for the presence of large-scale eddies, therefore impacting the fog's dynamical structures. However, simulations of a smaller domain size can lead to more sensitivity tests being conducted at a reduced computational expense. To understand how important the domain size is to simulate IOP1, a test was set up based on the configuration of T_control (see Tables 5.1 and 5.2), however, the horizontal domain size was set to the same dimensions as the Cardington field site; 800 $\times$ 800 m^2 (referred to as T_control_800x800).

T_control and T_control_800x800 were directly compared by analysing properties of the TKE (Figure 4.8) and LWP (Figure 4.9). Between 1800 and 1900 UTC (Figure 4.8a), the total TKE for T_control has a maximum of 0.0011 m^2 s^{-2} close to the surface, which steadily decreases throughout the boundary layer depth. Given the location of the maximum, the source of TKE is likely to be wind shear at the surface, which supports previous theories in studies such as Bergot (2013). Furthermore, the majority of the TKE in T_control is being resolved during this time frame (Figure 4.8d), therefore suggesting that both the vertical and horizontal resolution and domain size is suitable to capture the dynamical structures present within IOP1. The TKE structure in T_control begins developing between 0000 and 0100 UTC (Figure 4.8b), with a maximum resolved TKE of 0.07 m^2 s^{-2} occurring at a height of 11 m. Given the change in the TKE maximum, the sources of turbulence are most likely to be a combination of both dynamical and thermodynamical sources (Bergot, 2013). The amount of resolved TKE is above 80 % up until a height of 23 m (Figure 4.8e), where it is close to 100 % through the rest of the boundary layer depth. Finally, the structure of TKE begins to homogenise between 0300 and 0400 UTC (Figure 4.8c), with a peak TKE of 0.024 m^2 s^{-2} occurring at a height of 45 m, therefore suggesting that the source of TKE is through convective instabilities (Nakanishi, 2000). The majority of the TKE is being resolved throughout the boundary layer. Although the total resolved TKE can be increased by allowing for a finer grid box size, the computational expense may limit the number of sensitivity tests that can be conducted (as discussed in Maronga and Bosveld, 2017).

During all tested time frames, the LWP is not appreciably different between T_control _800x800 and T_control, with minimal changes in the TKE structure. In addition, when comparing computational costs, T_control took around 4 hours to run using 330 processors on the Met Office and NERC joint supercomputer system (MONSOON), whereas T_control_800x800 completed its simulation in around 6.5 days on the same number of processors. Given the results of these tests and the computational expense, it can be concluded that the domain size will have minimal impact on the simulation results for the same resolution. Therefore, going forward, the domain size of 132 x 132 m^2 in the horizontal will be used for all experiments.

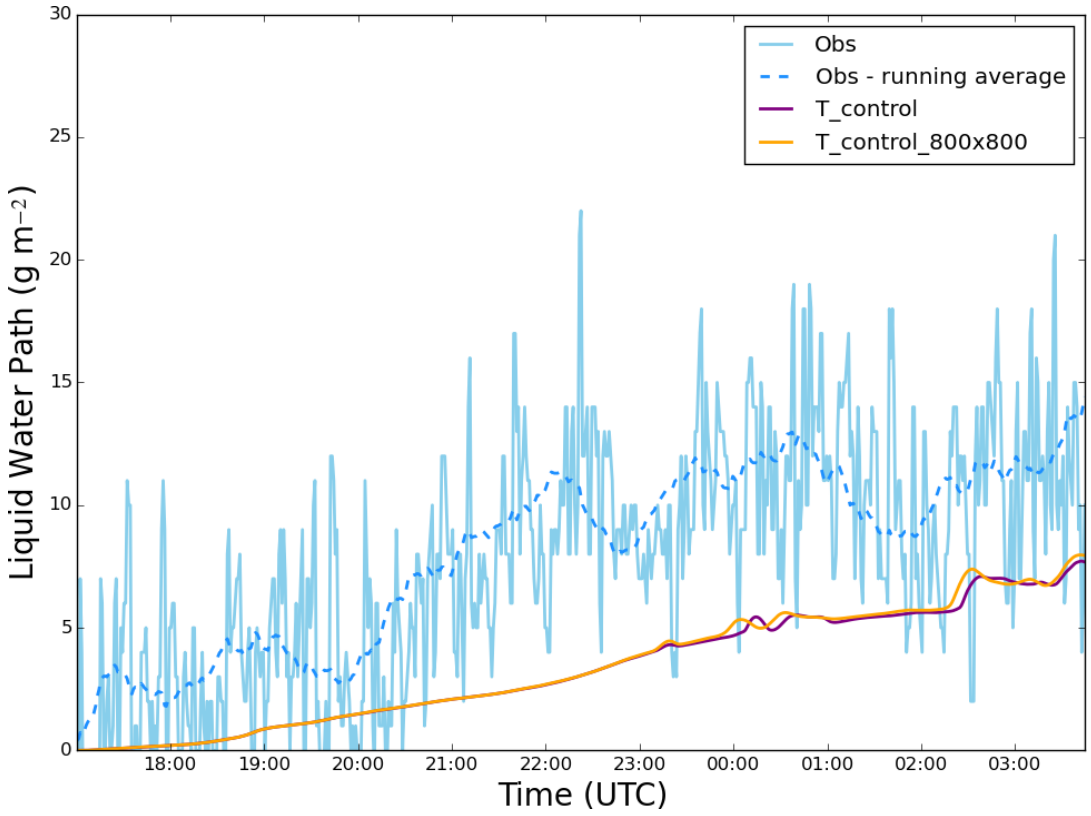

Figure 4.9: Time series of the liquid water path (g m^{-2}). Purple - T_control; orange - T_control_800x-800; light blue – observations; blue dashed – running average over observations (40 points).

4.5 CCN sensitivity tests

Previous studies (e.g. Bott, 1991; Stolaki et al., 2015; Maalick et al., 2016) show that features of the fog evolution, in particular, the fog optical depth, are influenced by properties of the CCN population. This section investigates how the CCN number concentration and size could influence the transition to a optically thick fog. To address this, two sets of experiments were conducted. The first set involved fixing the total soluble mass used in T_control, whilst doubling and halving the CCN concentration to 200 and 50 cm^{-3} respectively (referred to as tests T_double_ccn and T_half_ccn). The second set involved

fixing the CCN number concentration used in T_control, whilst doubling and halving the total soluble mass to 5.4 and 1.35 ng respectively (referred to as tests Test_double_mass and Test_half_mass).

4.5.1 CCN number concentration

As shown in Figure 4.2, the mean near-surface visibility for T_double_ccn is lower than T_control throughout the simulation by up to a factor of 0.61, with fog formation occurring at around 1700 UTC (the beginning of the simulation) and T_double_ccn eventually converging to a visibility of around 142 m. As with T_control, the spatial variation between the minimum and maximum visibility is not appreciably different prior to 2300 UTC for T_double_ccn. However, after this point, the range increases to a maximum of 65 m. A decrease in near-surface visibility with an increase in CCN number concentration is to be expected (Equation 4.3), as increasing the CCN number results in a higher number of smaller fog droplets being formed for a given LWP. This will slow down the sedimentation rate of liquid water (as the effective radius is fixed), causing the fog's optical depth to increase. A consequence of the increase in optical depth is an enhanced rate of radiative cooling above the fog layer, resulting in the fog layer becoming well mixed too quickly. For this example, the cooling rate increased from 1.3 K hr^{-1} to 2.1 K hr^{-1} at the top of the fog layer between T_control and T_double_ccn. This is seen in Figure 4.3b, where an adiabatic mixed layer began to form almost 6 hours prior to observations. At 2230 UTC, the mixed layer grows to a height of 5 m and continues to grow to a height of 38 m at 0330 UTC, leading to a stronger disagreement in comparison to T_control. The increase in liquid water production is shown in the surface deposition rate (Figure 4.5a). In reality, an increase in droplet concentration results in more liquid water in the fog, causing high levels of deposition at the surface as the fog deepens. In the model, the rate of liquid water depletion decreases due to a lower sedimentation rate. This will result in greater levels of liquid water in the layer, allowing for the surface deposition rate to increase.

The simulated mean near-surface visibility in T_half_ccn shows the best agreement with the observed near-surface visibility in the early stages of fog development (Figure

4.2). Fog began to form 15 minutes prior and this is most likely due to the decrease in CDNC throughout the night, as seen in Figure 4.4. The mean near-surface visibility within the simulation eventually converges to around 388 m and is greater than T_control by a factor of 1.6. Of all three simulations, T_half_ccn appears to have the most spatial variation, with most of it occurring from 0200 UTC onwards. In addition, Figure 4.5 shows a decrease in the surface deposition rate and LWP, as the CCN number decreases (as previously shown in Stolaki et al., 2015). This result is again physically expected, as decreasing the CCN concentration results in an increase in the average drop size and hence an enhanced sedimentation rate. This will lead to a reduced radiative cooling rate at the fog top, and therefore decrease the production rate of liquid water. The development of the boundary layer is in better agreement between T_half_ccn and the observations (Figure 4.3). Although it still became well mixed in the lower levels at 0330 UTC, the transitional period within the simulation occurs at a slower rate in comparison to previous CCN number tests.

The modelled downwelling longwave gradually increases, as in T_control, for a change in CCN concentration (Figure 4.6a). For example, at 2130 UTC, the downwelling longwave reaches 257 and 267 W m^{-2} for T_half_ccn and T_double_ccn respectively. In addition, the upwelling longwave does not vary with a change in CCN concentration (Figure 4.6b). As the effective radius is fixed in these tests, the change in downwelling radiation is in relation to the sedimentation rate. By increasing the CCN concentration, the sedimentation rate decreases due to the droplet size decrease, resulting in less liquid water being removed from the fog layer. As less liquid water is removed, the longwave fluxes at the top of the cloud will increase. In addition, the upwelling longwave not varying for a change in CCN concentration increases the likelihood that the difference in the simulated and observed upwelling longwave radiation is due to the representation of the surface.

4.5.2 CCN soluble mass

Increasing the total soluble mass will result in larger CCN, increasing the likelihood that they will activate into cloud droplets according to Köhler theory. The following tests aim

to understand how sensitive the fog layer evolution is to a given CCN size. Across all time frames (Table 4.3), the proportion of activated droplets increase for T_double_mass when compared to T_control, therefore accounting for the decrease in near-surface visibility and increase in LWP, as shown in Figure 4.10. By contrast, the proportion of activated droplets decreases for T_half_mass, therefore accounting for the increase in near-surface visibility and decrease in LWP. However, the relative change in near-surface visibility and LWP for each respective soluble mass test is smaller in comparison to the tests with the equivalent proportion change in CCN number. So, although in this case the change in CCN size, and consequently the change in aerosol-size distribution, influences the evolution of the fog layer, these results suggest that the CCN number is a more important variable to consider when investigating the impact on the fog evolution due to aerosol.

4.6 Sedimentation representation - shape parameter

Section 4.5.1 suggested that the number of activated droplets calculated by T_control is too high to capture the observed behaviours of the initial fog development. However, the biggest discrepancy between the simulated and observed behaviours is shown in Figure 4.5b, where at times the difference in LWP between observations and T_control is up to a factor of 5. These tests all assumed a fixed r_e, implying that the change in LWP is due to the sedimentation rate. As the sedimentation rate is controlled by the cloud drop-size distribution, this may suggest that the sedimentation rate is too high due to the chosen default parameters, that includes the shape parameter, μ_d. A study by Mazoyer et al. (2017) changed the default shape parameter from $\mu_d = 0$ to $\mu_d = 7$ based on the observed cloud drop-size distribution as described in Mazoyer et al. (2016). This transformed the modelled distribution from logarithmic to gamma, and changed the emphasis for given droplet sizes. The following section will discuss whether an increased μ_d will result in an improved simulated LWP, and hence an improved LWC in MONC.

Whilst ideally a chosen μ_d would be determined from the initial cloud droplet spectra data (as done in Mazoyer et al., 2017, for example), the instrumentation only began to

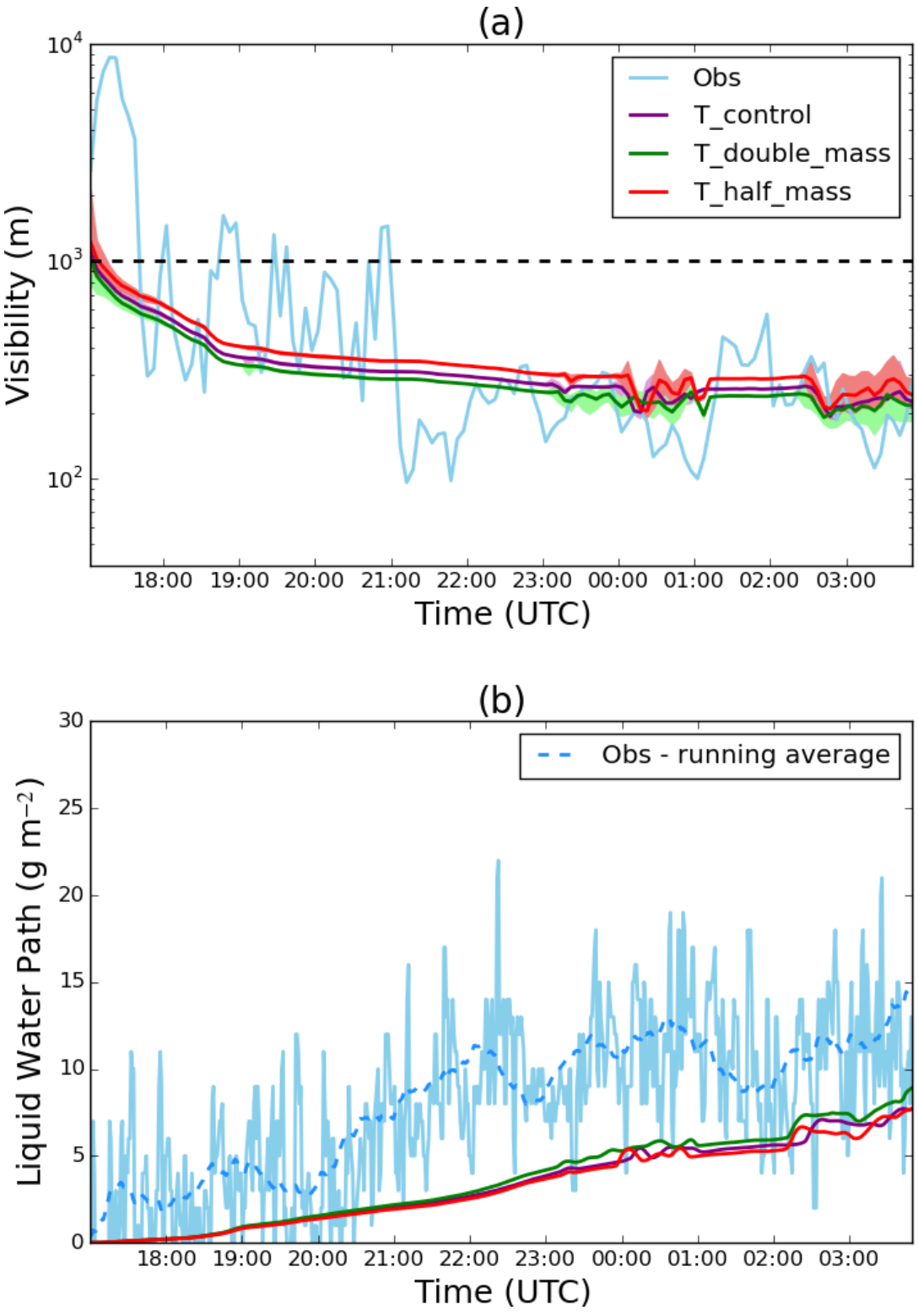

Figure 4.10: (a) - Time series of the mean visibility (m) at 2 m height. Purple – T_control; green – T_double_mass; red – T_half_mass; light blue – observations; dashed black line - fog threshold. Minimum and maximum visibility mark on figure by shaded area. (b) Time series of the liquid water path (g m^{-2}). Purple – T_control; green – T_double_mass; red – T_half_mass; light blue – observations; blue dashed – running average over observations (40 points).

record spectra during IOP1 4 hours into the observed fog case, and by this time, the layer had already begun to grow in optical thickness. To account for this, it was chosen to use the observed LWP to decide a suitable μ_d, given the results displayed in Figure 4.5. In addition, the test shape parameters will be compared to the available IOP1 cloud spectra data, to validate the choice of μ_d. For these sets of tests, the shape parameter was changed to $\mu_d = 1$, 2 and 3, denoted as T_mu_1, T_mu_2 and T_mu_3 respectively. Although simulations were conducted to increase the shape parameter up to a value of $\mu_d = 7$, the LWP for tests where $\mu_d > 4$ were higher than the observed mean LWP and hence these results will not be shown.

Figures 4.11a-b both show an increase in the surface deposition rate and LWP with respect to μ_d. For example, T_mu_3 has a higher LWP than T_control by a factor between 2.6 and 3.3, and a higher surface deposition rate by a factor between 1.1 and 1.9. Changing the shape parameter, such that $\mu_d = 3$, has a stronger impact on the LWP as opposed to the surface deposition rate. It appears to best match the observed averaged LWP, especially around 2000 UTC and between 2300 and 0100 UTC, therefore demonstrating a lower sedimentation rate with an increase in μ_d.

As shown in Figure 4.12, increasing the shape parameter results in the mean weighted velocity of droplets decreasing. For example, increasing the shape parameter to 3 results in the terminal velocity decreasing by 0.022 m s^{-1} at 0100 UTC. The change in terminal velocity is influenced by the cloud drop-size distribution, which is shown in Figure 4.13. Prior to 2200 UTC, all shape parameter tests began with an abundance of small droplets, signalling the formation of fog, and the density of small droplets being greatest in T_control (not shown). As the fog layer evolves, all tests begin moving towards the right in terms of skewness with the exception fog T_control (due to T_control being logarithmic). For the tests where $\mu_d > 0$, increasing the shape parameter results in the peak of the distribution decreasing and moving to the right, for all tested time frames. For example, increasing the shape parameter to $\mu_d = 3$ results in a peak droplet diameter of 11 μm. These results suggest a limitation in the default choice in $\mu_d = 0$ and hence the assumption of a logarithmic distribution for fog development during IOP1. By increasing the shape

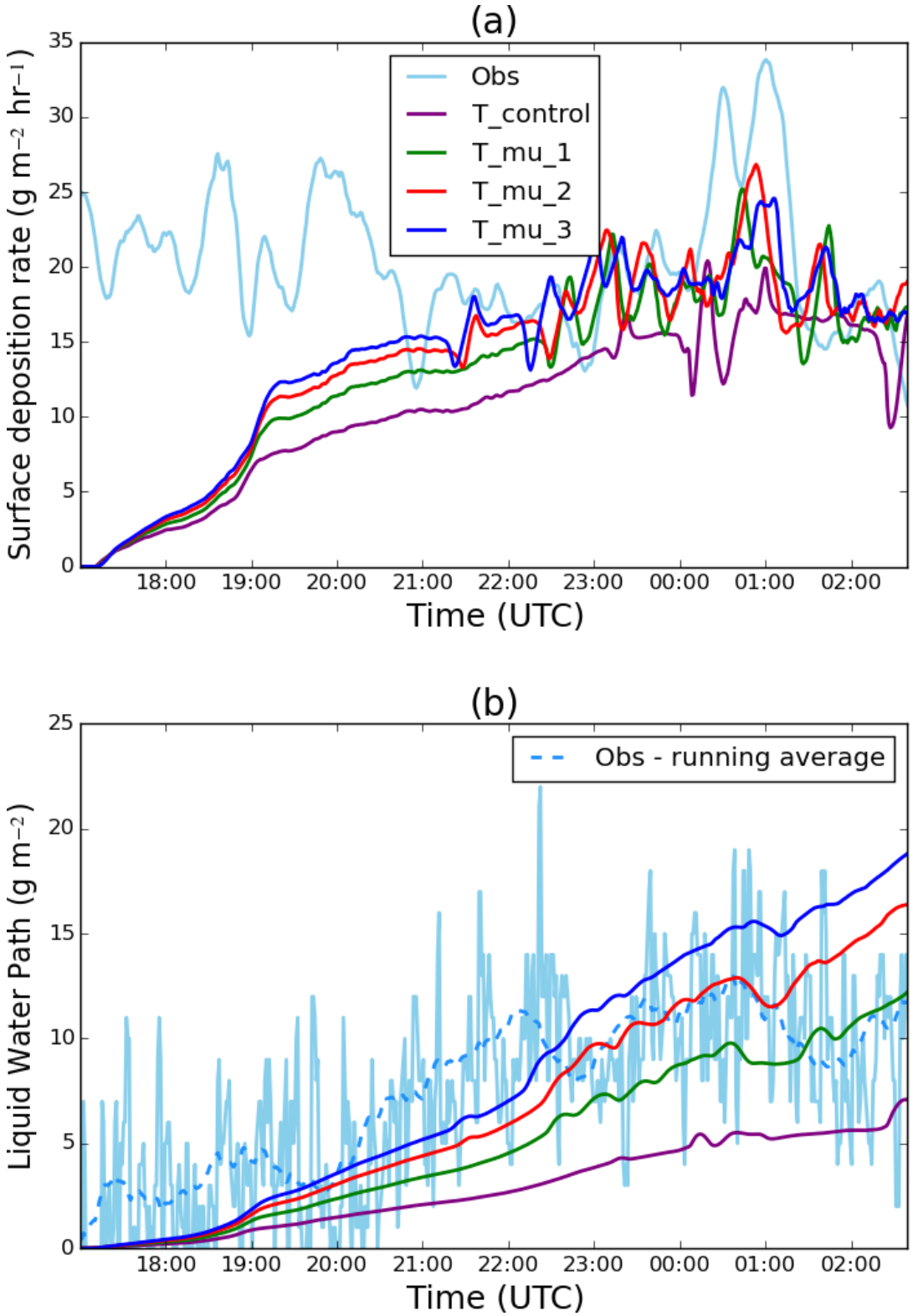

Figure 4.11: (a) - Time series of the surface deposition rate (g m^{-2} hr^{-1}). Purple – T_control; green – T_mu_1; red – T_mu_2; dark blue – T_mu_3; light blue – observations. (b) Time series of the liquid water path (g m^{-2}). Purple – T_control; green – T_mu_1; red – T_mu_2; dark blue – T_mu_3; light blue – observations; blue dashed – running average over observations (40 points).

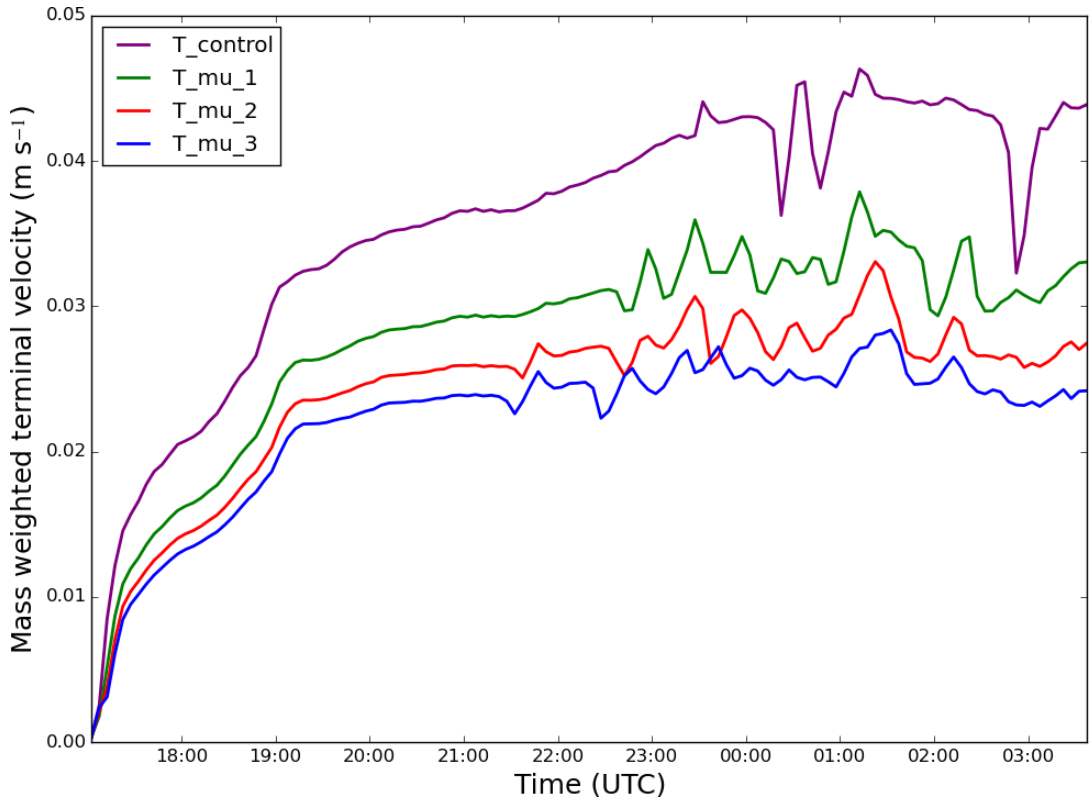

Figure 4.12: Time series of the mass mean weighted velocity. Purple – T_control; green – T_mu_1; red – T_mu_2; dark blue – T_mu_3.

parameter during the fog evolution, fewer large droplets will sediment out of the fog layer, therefore explaining the presence of bigger droplets still within the system in these tests (for example, tests T_mu_1 - 3).

At 2200 UTC, the observed cloud droplet spectrum mostly follows a logarithmic distribution, however, later in the night it evolves more into a bi-modal distribution (as seen in Price, 2011). For example, at 0000 UTC, the peaks occur at 8 and 22 μm. Of the shape parameter tests, the observations are in best agreement with T_mu_3 for droplet size diameters between 22 to 27 μm at 0000 UTC, however, this fit does not take into account the peak shown within the smaller droplets. In an ideal situation, a modelled cloud drop-size distribution would take into account the bi-modal nature shown within the distribution. In reality, it is likely that these smaller droplets have not activated, but instead are a source of hydrated aerosol which can contribute up to 68% of the total light scattered, and hence result in the reduction in visibility within the fog (Hammer et al., 2014). However, although these smaller droplets may potentially change the microphysical structure of the fog, the introduction of a bi-modal distribution (or a varying shape parameter) within CASIM may increase model computational expense, with no appreciable changes in the fog evolution.

Going forward, it is recommended to use a shape parameter of $\mu_d = 3$ and this will be utilised in future simulations shown in Chapters 5 and 6.

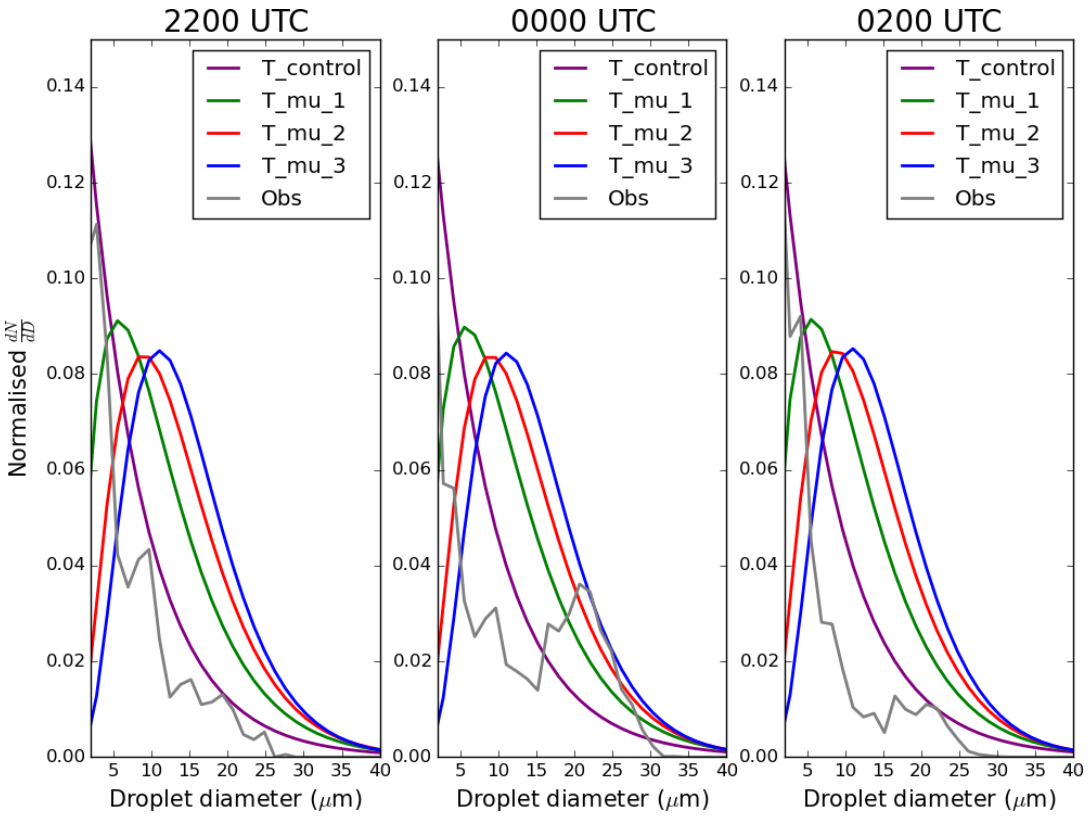

Figure 4.13: Cloud drop-size distributions for shape parameter simulations at 1710, 1800 and 2200 UTC at 2 m. Purple – T_control; green – T_mu_1; red – T_mu_2; dark blue – T_mu_3; grey - observations.

4.7 Fixed effective radius

The final section of this chapter investigates how the fog evolution is influenced by the change in the fixed effective diameter, and hence the effective radius. Previous work (e.g. Stolaki et al., 2015; Boutle et al., 2018) has demonstrated that the CDNC changes the radiative impact of the fog layer. An increase in CCN concentration decreases the average drop size for a given LWP, thus decreasing the effective radius. Consequently, a decrease in the effective radius will increase the cloud's optical depth, resulting in a higher absorptivity of longwave radiation in the fog; a direct consequence of the Twomey (1977) effect.

Whilst the effective radius can be fixed, Slingo (1989) defined the effective radius, r_e, as the ratio of the 3rd to 2nd moment of the cloud drop-size distribution, $n(r)$, such that:

$$r_e = \frac{\int_0^\infty r^3 n(r) dr}{\int_0^\infty r^2 n(r) dr}. \tag{4.5}$$

Similarly, the effective diameter, d_e, can be defined by the cloud drop size distribution, $N(D)$, as defined in Chapter 3, such that:

$$d_e = \frac{\int_0^\infty D^3 N(D) dD}{\int_0^\infty D^2 N(D) dD}. \tag{4.6}$$

Assuming that the $N(D)$ a gamma distribution, Equation (4.6) simplifies to:

$$d_e = \frac{\mu_d + 3}{\lambda_d}, \tag{4.7}$$

where λ_d is the CDNC distribution slope parameter. For this work, the effective radius will be used hereafter, where:

$$r_e = \frac{d_e}{2} = \frac{\mu_d + 3}{2\lambda_d}, \tag{4.8}$$

Assuming that μ_d is fixed and λ_d varies with the fog evolution, Equation (4.8) implies that either an increase in the CDNC or a decrease in the LWC will result in a decrease in r_e; increasing the cloud's optical depth (Equation 4.1). As discussed in Section 4.2,

MONC does not currently have the change in CDNC coupled to the effective radius, and utilises a fixed r_e as a compromise. However, based on Equation (4.8), the assumed value for r_e may not be suitable for simulations of IOP1. To understand the impact the chosen r_e may have on the fog evolution, two tests were set up where r_e changed to 15 and 5 μm, and will be referred to T_er_15.0 and T_er_5.0 respectively.

Throughout the night, a decrease in r_e to 5 μm results is a decrease in near-surface visibility and increase in LWP, when T_er_5.0 is compared to T_control, as shown in Figure 4.14. By contrast, increasing r_e to 15 μm accounts for the increase in near-surface visibility and decrease in LWP. A decrease in r_e replicates the effect that an increase in the CDNC, where an increased droplet popultion will increase the surface area of the emitted longwave radiation. An increase in the surface area will, in turn, increase the rate of cooling at the fog top, therefore increasing the rate of liquid water production. Likewise, increasing the r_e replicates a decrease in CDNC concentration, which may be of importance for low regimes of cloud droplet numbers. Going forward, if the representation of aerosol activation results in a decrease in CDNC, increasing the r_e to 15 μm may better account for changes in the fog's microstructure.

4.8 Discussion and conclusions

The focus of this chapter investigated the importance of aerosol-fog interactions within a nocturnal radiation fog case - LANFEX IOP1. This was split into three objectives. The first was to evaluate how well MONC captures the main physical features within IOP1, and identify any potential discrepancies. The conclusion is that although MONC captures the main physical features within IOP1: the fog transitions too fast in comparison to observations, due to the high proportion of modelled to observed fog droplets. This is despite the default shape parameter sedimenting too many droplets out of the system, and slight discrepancies in the surface dynamics. In addition, it was shown that a smaller domain size is sufficient enough to conduct simulations of IOP1 using MONC with CASIM. The second objective was to investigate how sensitive the fog evolution is to different

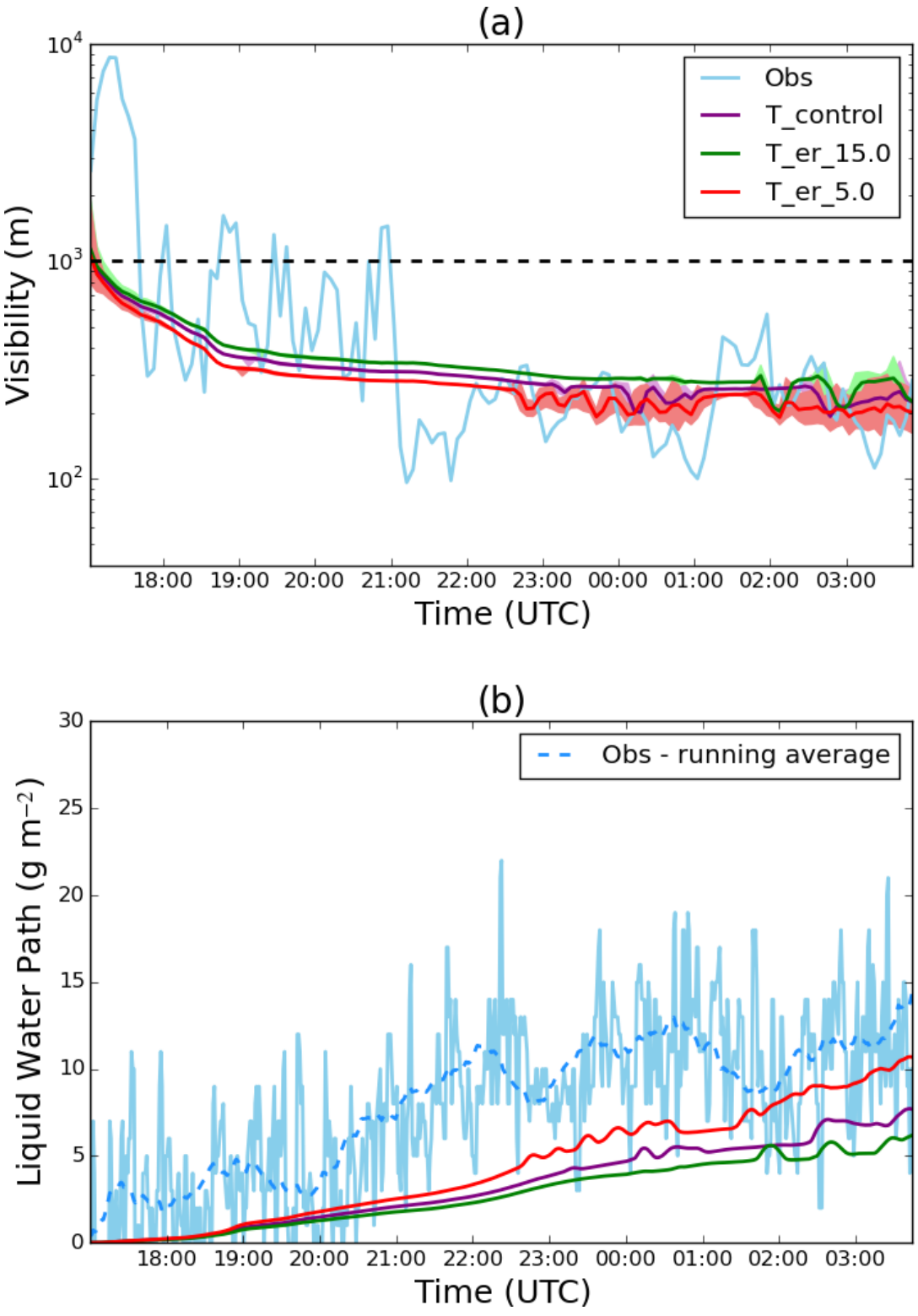

Figure 4.14: Time series of the liquid water path (g m^{-2}). Purple – T_control; green – T_er_15.0; red – T_er_5.0; light blue – observations; blue dashed – running average over observations (40 points).

aerosol properties. By decreasing the CCN number from 100 to 50 cm^{-3}, the simulated rate of transition to optically thick fog is reduced and more in line with observations from IOP1. Furthermore, the evolution of the fog is sensitive to the change in soluble mass for a given CCN concentration. Both of these results highlight the importance of accurate aerosol initial conditions for simulations of fog.

The final objective assessed the default droplet representation used within both CASIM and SOCRATES was suitable for simulating IOP1 within MONC. The LWP simulated in T_control being lower than the observed mean LWP by up to a factor of 5 suggested that the sedimentation rate of cloud droplets was too high. By changing the shape parameter, μ_d, used in the cloud drop-size distribution from 0.0 to 3.0, the sedimentation rate decreased, resulting in the simulated mean LWP agreeing better with the observations. An increase in the shape parameter resulted in the distribution transforming from logarithmic to gamma, moving the skewness of the distribution to the right and therefore changing the emphasis of the peak drop size distribution to bigger droplets. The choice of $\mu_d = 3$ was then verified using the observed cloud droplet spectra. Regarding the effective radius, r_e, although a change in r_e resulted in changes in the fog's near-surface visibility and LWP, further work should be carried out to understand the importance of the choice of a fixed r_e, and whether the use of a coupled effective radius to the CDNC is required for simulations of fog. However, the fixed r_e should be adapted to account for a smaller CDNC calculated by the aerosol activation scheme.

These results have shown that increasing CCN results in optically thicker fog; however, it seems that the model is consistently overpredicting aerosol activation and hence CDNC. Such an overprediction may be the result of the underlying design of the aerosol activation scheme. Traditionally, aerosol activation parameterisations are designed using a system that solves a time variation in supersaturation, combined with Köhler theory (e.g. Twomey, 1959; Abdul-Razzak and Ghan, 2000; Ming et al., 2007; Curry and Khvorostyanov, 2012). Köhler theory states that should the maximum supersaturation within the environment be greater than the critical supersaturation for a given aerosol, the aerosol will become activated (Köhler, 1936). The majority of these schemes assume that the change in super-

saturation is driven by adiabatic lifting, which links directly to an updraft velocity found in convective clouds. Furthermore, as discussed in Boutle et al. (2018), a minimum updraft velocity of 0.1 m s^{-1} is imposed, equivalent to a cooling rate of 3.51 K hr^{-1}, assuming the dry adiabatic lapse rate. The threshold was imposed as these schemes were designed to be implemented into general circulation models (GCMs) to account for cloud top turbulence being poorly resolved for resolutions coarser than 100 m (Ghan et al., 1997). Both of these assumptions are unsuitable to represent aerosol activation in radiation fog since updraft velocities at the formation stage are close to 0 m s^{-1} and the change in saturation is driven by radiative cooling from the ground (Price, 2011). Consequently, this may result in the maximum environmental supersaturation being too high, causing too many aerosols to activate and the fog layer to become optically thick too quickly. These results will motivate future work (Chapter 5) that will investigate the assumptions associated with aerosol activation parameterisations used within CASIM and their validity for simulations of nocturnal radiation fog.

This chapter demonstrated the complexity of aerosol-fog interactions, fog microphysics, and their importance in understanding nocturnal radiation fog. In particular, this chapter has highlighted that the droplet number is important for fog evolution, and why errors in aerosol activation representation may be important. Although previous studies have investigated aerosol-fog interactions, the majority of them simulate case in highly polluted areas (for example the ParisFog field study by Haeffelin et al., 2010). The main characteristic of the LANFEX dataset, and in particular IOP1, is that is it a “clean” case with low aerosol concentrations, representing a different regime. The use of CASIM within MONC has highlighted the importance of including aerosol processes in fog modelling, with the results showing that accounting for different CDNC regimes is needed to represent the transition to optically thick fog. Research is ongoing to develop CASIM, in particular, the aerosol activation scheme, and such developments should provide improved capabilities for operational fog forecasting.

Chapter 5

Can a more accurate representation of aerosol activation improve simulations of fog?

5.1 Introduction

Chapter 4 demonstrated that the CDNC is an important variable that controls the fog's evolution, and its overestimation results in the fog transitioning to a well-mixed layer too quickly. A reason for the overestimation in CDNC may be that the aerosol activation scheme is not accurately representing aerosol activation in fog. The default scheme in MONC (along with most common activation schemes) assumes:

1. A cooling driven by adiabatic ascent, which is to consider updrafts found in convective clouds (Abdul-Razzak and Ghan, 2000; Meskhidze et al., 2005);

2. an applied minimum updraft threshold of 0.1 m s^{-1} to account for poorly resolved turbulence above the planetary boundary layer (Ghan et al., 1997).

In radiation fog, the main mechanism for the initial formation of droplets is radiative cooling; a non-adiabatic process, with measured cooling rates of 1 - 4 K hr^{-1} at the surface and updraft velocities close to 0 m s^{-1}. Consequently, both of these assumptions, especially the use of a minimum threshold (as discussed in Boutle et al., 2018) do not accurately account for aerosol activation in fog. This chapter will focus on addressing both of these assumptions, both in the Shipway scheme (Shipway, 2015) and a new extended Shipway_v2 activation scheme. The Shipway_v2 scheme has the same code infrastructure as Shipway, however, it assumes that supersaturation is driven by both adiabatic and non-adiabatic sources. It was chosen to use Shipway over Abdul-Razzak and Ghan (2000) (hereafter referred to as ARG), as it has been shown that ARG overestimates condensation in low aerosol regimes, making it activate too few droplets (Shipway, 2015). The work presented in this chapter has been split into two sections: firstly comparing Shipway and Shipway_v2 using an offline box model; and secondly comparing LES simulations of IOP1 using MONC coupled with CASIM for both schemes. The chapter will address the following research questions:

1. In what ways can the standard method of cooling used in Shipway be adapted to be suitable for the modelling of fog?

2. What are the potential differences in both maximum supersaturation and number of activated aerosols, when comparing the default setup of the Shipway to the Shipway_v2 scheme?

3. How well does the Shipway scheme in MONC simulate IOP1, and does the reduction in the minimum vertical velocity threshold impact the fog evolution?

4. How well does the Shipway_v2 scheme simulate IOP1, and how is the scheme sensitive to changes in dynamical and radiative parameters?

Section's 5.2 and 5.3 will present a derivation of the Shipway_v2 scheme and how it has been implemented into an offline box model. The research questions for this chapter will be addressed in Section's 5.4, 5.5 and 5.6. A discussion and conclusion will then follow.

5.2 Shipway_v2 - extension of the Shipway activation scheme

5.2.1 Derivation of change in supersaturation - incorporating a non-adiabatic cooling source

Pruppacher and Klett (2010, p.107) defined supersaturation in terms of the water vapour mixing ratio, q_v, as:

$$q_v = (1+s)\left(\frac{\epsilon e_s}{p}\right), \tag{5.1}$$

where p is the pressure of dry air, s is the environment's supersaturation, e_s is the saturation vapour pressure and $\epsilon = \dfrac{R_a}{R_v} = 0.622$; the ratio of the gas constant of dry air to water vapour. Differentiating Equation (5.1) with respect to time gives:

$$\frac{dq_v}{dt} = \frac{ds}{dt}\left(\frac{\epsilon e_s}{p}\right) + \frac{\epsilon(1+s)}{p}\left[\frac{de_s}{dt} - \frac{e_s}{p}\frac{dp}{dt}\right]. \tag{5.2}$$

Rearranging Equation (5.2) gives:

$$\frac{ds}{dt} = \left(\frac{p}{\epsilon e_s}\right)\frac{dq_v}{dt} - (1+s)\left[\frac{1}{e_s}\frac{de_s}{dt} - \frac{1}{p}\frac{dp}{dt}\right]. \tag{5.3}$$

The Clausius-Clapeyron equation is defined in Pruppacher and Klett (2010, p.117) as:

$$\frac{de_s}{dT} = \frac{Le_s}{R_v T^2}. \tag{5.4}$$

Therefore:

$$\frac{de_s}{dt} = \frac{Le_s}{R_v T^2}\left.\frac{dT}{dt}\right|_{tot}. \tag{5.5}$$

The total change in temperature with respect to time $\left.\dfrac{dT}{dt}\right|_{tot}$ is defined as:

$$\left.\frac{dT}{dt}\right|_{tot} = \left.\frac{dT}{dt}\right|_{ad} + \left.\frac{dT}{dt}\right|_{non\_ad} + \left.\frac{dT}{dt}\right|_{lat} \tag{5.6}$$

where:

- $\left.\dfrac{dT}{dt}\right|_{ad}$ is the change in temperature due to adiabatic processes;

- $\left.\frac{dT}{dt}\right|_{non\_ad}$ is the change in temperature due to non-adiabatic processes (e.g. radiative cooling, turbulent mixing), that excludes latent heat release;
- $\left.\frac{dT}{dt}\right|_{lat}$ is the change in temperature due to latent heat release i.e. condensation/evaporation.

Equation (5.6) includes a change in pressure with respect to time. For adiabatic processes, the change in temperature is due to an air parcel's buoyancy, implying $\frac{dp}{dt} \neq 0$. However, for non-adiabatic processes, the change in temperature occurs isobarically and hence $\frac{dp}{dt} = 0$. Therefore, for $\left.\frac{dT}{dt}\right|_{ad}$, by:

1. assuming hydrostatic equilibrium;
2. using the equation for the ideal gas law, where $p = \rho RT$;
3. and noting that $\left.\frac{dT}{dt}\right|_{ad} \equiv -\Gamma \frac{dz}{dt}$, where $-\Gamma = -\frac{g}{c_p}$, the dry adiabatic lapse rate;

the change in pressure with respect to time, $\frac{dp}{dt}$, is written as:

$$\begin{aligned} \frac{dp}{dt} &= \frac{dp}{dz}\frac{dz}{dt} \\ &= \frac{pc_p}{R_aT}\left.\frac{dT}{dt}\right|_{ad}. \end{aligned} \tag{5.7}$$

Pruppacher and Klett (2010, p.493) showed that the change in temperature due to latent heat release is proportional to the change in vapour mixing ratio, such that:

$$\left.\frac{dT}{dt}\right|_{lat} = -\frac{L}{c_p}\frac{dq_v}{dt}. \tag{5.8}$$

In clouds, latent heat release can be influenced by entrainment; a process where turbulent flow captures non-turbulent flow (Pruppacher and Klett, 2010, p.492). Entrainment may impact droplet formation, as entraining a subsaturated parcel into the cloud could change its relative humidity, therefore directly influencing the cloud droplet spectrum (Barahona and Nenes, 2007). Should the fog become well-mixed, entrainment can occur due to the turbulent eddies potentially forming at the fog top (Mazoyer et al., 2017). However, the motivation of this work is focused on fog formation where the turbulent flow

would be minimal. Therefore, latent heat release due to entrainment can be ignored, and Equation (5.8) can be written in terms of condensed water, such that:

$$\frac{dq_v}{dt} = -\frac{dq_l}{dt}. \tag{5.9}$$

Inserting Equation's (5.6), (5.7), (5.8) and (5.9) can be combined into Equation (5.3), giving:

$$\frac{ds}{dt} = (1+s)\left[\left(\frac{c_p}{R_a T} - \frac{L}{R_v T^2}\right)\left.\frac{dT}{dt}\right|_{ad} + \left(-\frac{L}{R_v T^2}\right)\left.\frac{dT}{dt}\right|_{non\_ad}\right] - \left(\frac{p}{\epsilon e_s} + \frac{(1+s)L^2}{R_v c_p T^2}\right)\frac{dq_l}{dt}. \tag{5.10}$$

Only warm microphysical processes are assumed for the change in supersaturation, implying that $1 + s \approx 1$ (see Warner, 1968), and hence simplifies Equation (5.10) to:

$$\frac{ds}{dt} = \alpha_1 \left.\frac{dT}{dt}\right|_{ad} + \alpha_2 \left.\frac{dT}{dt}\right|_{non\_ad} - \gamma\frac{dq_l}{dt}, \tag{5.11}$$

where:

$$\begin{aligned} \alpha_1 &= \frac{c_p}{R_a T} - \frac{L}{R_v T^2}, \\ \alpha_2 &= -\frac{L}{R_v T^2} \\ \gamma &= \frac{p}{\epsilon e_s} + \frac{L^2}{R_v c_p T^2}. \end{aligned} \tag{5.12}$$

As a change in supersaturation due to non-adiabatic cooling results in the dropping of the pressure term displayed in Equation (5.6), this implies that modelling aerosol activation in a non-convective cloud using an adiabatic framework may be an unsuitable option for this work. To verify this impact for fog, the ratio of α_1 to α_2 from Equation (5.12) was tested over a potential temperature range of $268 - 278$ K to reflect observations of radiation fog formation (e.g. Roach et al., 1976; Price, 2011; Haeffelin et al., 2013). Over the tested range, $\frac{\alpha_2}{\alpha_1} \approx 1.2$. As this ratio $\neq 1$, this suggests the unsuitability of using an adiabatic assumption to model saturation in a non-adiabatic environment.

5.2.2 Shipway activation scheme

The Shipway (2015) aerosol activation scheme is designed as an improvement to the original lower bound approximation by Twomey (1959), and utilises a lookup table method that solves the maximum supersaturation at a reduced computational expense. It is modelled on the change in supersaturation combined with Köhler theory, such that:

$$\frac{ds}{dt} = \psi - \gamma s \int_0^s \phi(\sigma) \left[\int_{\tau(\sigma)}^t s dt \right]^{\frac{1}{2}} d\sigma, \tag{5.13}$$

where:

- ψ is a cooling term resulting in the initial rise in supersaturation;
- $\phi(\sigma)$ is the differential activity spectrum, that expresses number of nuclei in a unit volume with critical supersaturation between σ and $\sigma + \delta\sigma$;
- γ is a thermodynamical constant associated with the change in supersaturation due to latent heat release.

Shipway (2015) assumes the differential activity spectrum, $\phi(s)$, to be lognormal and therefore it can be expressed as:

$$\phi(s) = \sum_{i=1}^{I} \frac{N_i}{\sqrt{2\pi}\ln(\sigma_{s,i})s} \exp\left(-\frac{\ln^2(s/s_{0,i})}{\ln^2\sigma_{s,i}} \right), \tag{5.14}$$

where N_i is the number concentration of dry aerosol, $\sigma_{s,i}$ is the dispersion of the distribution of $\phi(s)$ and $s_{0,i}$ is the mean geometric supersaturation for each given aerosol mode. As discussed in Chapter 2, the total number of activated aerosols are determined by the differential maximum of Equation (5.13) (i.e, $\frac{ds}{dt} = 0$):

$$\psi = \gamma s \int_0^s \phi(\sigma) \left[\int_{\tau(\sigma)}^t s \; dt \right]^{\frac{1}{2}} d\sigma. \tag{5.15}$$

Twomey (1959) outlined the computational expense when solving the right hand side of Equation (5.15). To overcome this, they formulated geometric approximation (Figure 5.1), which consisted of a lower bound to the change in supersaturation, such that:

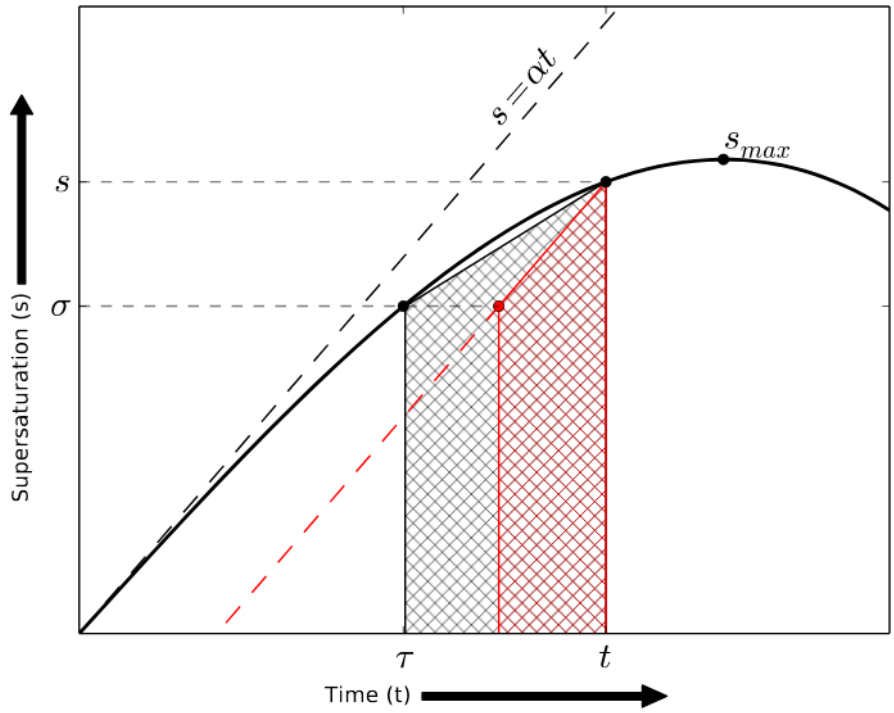

Figure 5.1: A lower bound approximation to integral under the supersaturation curve displayed in Equation (5.15)*. Red hatched region represents lower bound approximation of Twomey, black hatched region represents lower bound approximation of the Shipway scheme (Shipway, 2015).*

$$\frac{1}{2\alpha}\left(s_{max}^2 - \sigma^2\right) < \int_{\tau(\sigma)}^{t} s\ dt. \tag{5.16}$$

Shipway (2015) improved the approximation displayed in Equation (5.16), by firstly investigating the behaviour of Equation (5.13) and then solving it numerically, utilising a range of aerosol loadings and updraft velocities (Figure 5.2). Using a single curve fitting approach, they showed $\frac{ds}{dt}$ could be written in the form:

$$\frac{ds}{dt} = \psi\left(1 - \left(\frac{s}{s_{max}}\right)^{\mu}\right)^{\lambda}, \tag{5.17}$$

where μ and λ are shape parameters for Equation (5.17), defined by Shipway (2015) as $\mu = 3$ and $\lambda = 0.6$. Next, Shipway (2015) adapted the geometric formulation by Twomey

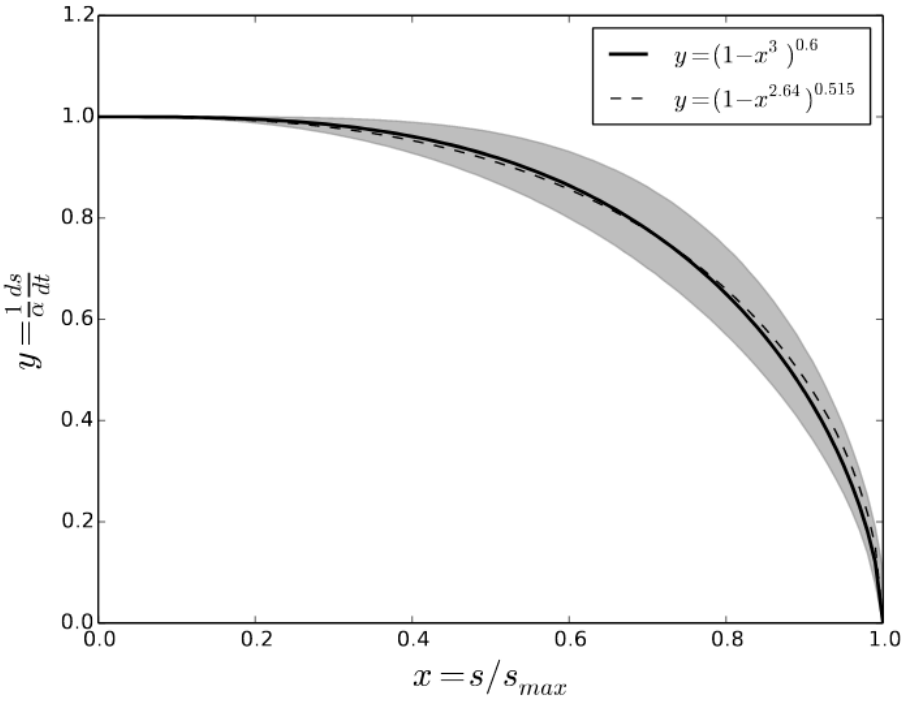

Figure 5.2: A scaled $\frac{ds}{dt}$ *as a function of* $\frac{s}{s_{max}}$ *evaluated from numerical solution of Equation* (5.13) *using a range of updraft velocities and various aerosol loadings (Table 5.1). The solid line represents the parameterisation (Equation* (5.17)*), with* $\mu = 3$ *and* $\lambda = 0.6$ *(Shipway, 2015).*

(1959), by directly using Equation (5.17) to solve the trapezoid area that approximates the change in supersaturation (Figure 5.1). For $s = s_{max}$ and $s(\tau) = \sigma$:

$$\int_{\tau(\sigma)}^{t} s\ dt \approx \frac{1}{2}\left[\psi\left(1-\left(\frac{\sigma}{s_{max}}\right)^{\mu}\right)^{\lambda}\right]^{-1}\left(s_{max}^2-\sigma^2\right), \tag{5.18}$$

and hence a new expression for the maximum supersaturation using Equation's (5.15) and (5.18) was formulated, such that:

$$\frac{\sqrt{2}\psi^{\frac{3}{2}}}{\gamma} = s_{max}\int_0^{s_{max}}\phi(\sigma)\ \left[\frac{1}{2}\left(1-\left(\frac{\sigma}{s_{max}}\right)^{\mu}\right)^{\lambda}\right]^{-1}\left(s_{max}^2-\sigma^2\right)^{\frac{1}{2}}d\sigma. \tag{5.19}$$

Shipway (2015) formulated a precalculated lookup table to solve the right-hand side of Equation (5.19), that gains s_{max} using an inverse lookup procedure. Finally, Shipway

(2015) uses s_{max} as the upper bound to calculate the total number of activated aerosols, N_a:

$$N_a = \int_0^{s_{max}} \phi(\sigma)\ d\sigma. \tag{5.20}$$

As $\phi(\sigma)$ is assumed to be lognormal, Equation (5.20) can be expressed as (Shipway and Abel, 2010):

$$N_a = \frac{N_i}{2}\left[1 + \mathrm{erf}\left(\frac{s_{max}/s_{0,i}}{\sqrt{2}\ln\sigma_{s,i}}\right)\right], \tag{5.21}$$

with $\mathrm{erf}(x)$ being the error function (Abramowitz and Stegun, 1965). To date, the Shipway activation scheme assumes that ψ is driven by an updraft velocity, i.e.

$$\psi = \alpha(T,p)\frac{dz}{dt}, \tag{5.22}$$

where $\alpha(T,p)$ is the thermodynamical constant associated with a change in supersaturation due to adiabatic ascent. For the Shipway_v2 scheme, the term, ψ, in Equation (5.19) has been modified to account for non-adiabatic cooling (based on the derivation from Section 5.2.1), such that:

$$\frac{\sqrt{2}\left(\alpha_1 \left.\frac{dT}{dt}\right|_{ad} + \alpha_2 \left.\frac{dT}{dt}\right|_{non\_ad}\right)^{\frac{3}{2}}}{\gamma} = s_{max}\int_0^{s_{max}} \phi(\sigma)\ \left[\frac{1}{2}\left(1 - \left(\frac{\sigma}{s_{max}}\right)^{\mu}\right)^{\lambda}\right]^{-1}\left(s_{max}^2 - \sigma^2\right)^{\frac{1}{2}} d\sigma. \tag{5.23}$$

The Shipway_v2 scheme differs to Shipway when calculating N_a, in that it uses Equation (5.23) to solve s_{max}.

5.3 The Shipway box model - offline setup

To understand how the removal of the pressure term in Equation (5.11) may impact the change in supersaturation and hence the number of activated aerosols, both the Shipway

Environmental setting	Distribution parameters	Aitken mode	Accumulation mode	Coarse mode
Marine	N (cm $^{-3}$)	340	60	3.1
	σ	1.6	2.0	2.7
	r (μm)	0.005	0.035	0.31
Clean continental	N (cm $^{-3}$)	1000	800	0.72
	σ	1.6	2.1	2.2
	r (μm)	0.008	0.034	0.46
Urban	N (cm $^{-3}$)	10600	32000	5.4
	σ	1.8	2.16	2.21
	r (μm)	0.007	0.027	0.43

Table 5.1: A table displaying the aerosol properties (Whitby, 1978), to test the Shipway and Shipway_v2 scheme used within the offline box model.

and extended Shipway_v2 activation schemes will be directly compared using the Shipway box model. The Shipway box model is designed as a non-interactive offline suite to calculate the number of activated aerosols in a range of different environmental settings. As the model is non-interactive, it permits analysis of parameter space, in the absence of atmospheric feedbacks. Inputs of the model are potential temperature, vertical velocity and aerosol populations properties (number concentration, size, mode and distribution size parameters). The Shipway box model has been used to test the Shipway (2015) and Twomey (1959) activation schemes in different aerosol regimes, in addition to schemes developed by Abdul-Razzak and Ghan (2000) and Nenes and Seinfeld (2003).

For this work, the Shipway box model was changed to account for a temperature change due to both adiabatic and non-adiabatic processes, using Equation (5.23). Aerosol loadings from Whitby (1978) were used to test both activation schemes. These properties considered different environments, ranging from clean to polluted (Table 5.1). The temperature was set as a fixed value of 274 K, based on surface temperatures observed during fog formation (Price, 2011; Haeffelin et al., 2013). All tests were driven by cooling rates found in fog formation (calculated using data from Price, 2011; Haeffelin et al., 2013), in addition to a temperature change due to a nocturnal clear sky cooling (Kiehl and Trenberth, 1997).

Table 5.2 displays the setup of four cases used in the offline box model, which includes the list of tests conducted within each case. Case C_adiabatic was a direct comparison between the Shipway and Shipway_v2 scheme, based on Equation's (5.19) and (5.23), with the non-adiabatic term in Shipway_v2, set to zero. This case has two objectives. The first objective was to check that for the same cooling rate, both schemes calculated the same maximum supersaturation and hence the number of activated aerosols. The second objective investigated what mode was most important for aerosol activation, therefore determining if any modes could be neglected in simulations of fog. Cases C_accumulation, C_coarse and C_Aitken investigated how the removal of the pressure term with a non-adiabatic cooling source (see Equation 5.12), would impact the number of activated aerosols. Within these cases, all tests that ran with the Shipway_v2 scheme had the adiabatic term in Equation (5.23) set to zero, to understand the maximum impact a non-adiabatic framework would have on aerosol activation for a given aerosol mode and environment.

Work by Boutle et al. (2018) discussed that another source for the overestimation of aerosol activation in fog (typically in NWPs) was the use of a minimum threshold, w_{min}, where typically $w_{min} = 0.1$ m s^{-1}. As the Shipway scheme assumes that cooling is driven just by an adiabatic ascent, an additional set of tests applying w_{min} to the Shipway scheme were conducted, and compared to the Shipway_v2 scheme within cases C_accumulation, C_coarse and C_Aitken. The objective of these tests was to understand how the use of $w_{min} = 0.1$ m s^{-1} impacted the number of activated aerosols for a given cooling rate, and these results would motivate how the use of w_{min} should be considered for simulations of fog in MONC.

Case	Tests within case	Scheme		w_{min} applied	Aerosol mode	Environment
		Shipway	Shipway_v2			
C_adiabatic	T_ship_ad	x			Aitken, Accumulation, Coarse	Marine, Clean continental, urban
	T_ship_v2_ad		x			
C_Aitken	T_ship_mar_ait	x			Aitken	Marine
	T_ship_mar_ait_wmin	x		x		
	T_ship_v2_mar_ait		x			
	T_ship_con_ait	x				Clean continental
	T_ship_con_ait_wmin	x		x		
	T_ship_v2_con_ait		x			
	T_ship_urb_ait	x				Urban
	T_ship_urb_ait_wmin	x		x		
	T_ship_v2_urb_ait		x			
C_accumulation	T_ship_mar_acc	x			Accumulation	Marine
	T_ship_mar_acc_wmin	x		x		
	T_ship_v2_mar_acc		x			
	T_ship_con_acc	x				Clean continental
	T_ship_con_acc_wmin	x		x		
	T_ship_v2_con_acc		x			
	T_ship_urb_acc	x				Urban
	T_ship_urb_acc_wmin	x		x		
	T_ship_v2_urb_acc		x			
C_coarse	T_ship_mar_coa	x			Coarse	Marine
	T_ship_mar_coa_wmin	x		x		
	T_ship_v2_mar_coa		x			
	T_ship_con_coa	x				Clean continental
	T_ship_con_coa_wmin	x		x		
	T_ship_v2_con_coa		x			
	T_ship_urb_coa	x				Urban
	T_ship_urb_coa_wmin	x		x		
	T_ship_v2_urb_ait		x			

Table 5.2: A table listing all the tests conducted within the offline box model.

5.4 Aerosol activation within the offline box model - Shipway and Shipway_v2

5.4.1 C_adiabatic - adiabatic direct comparison

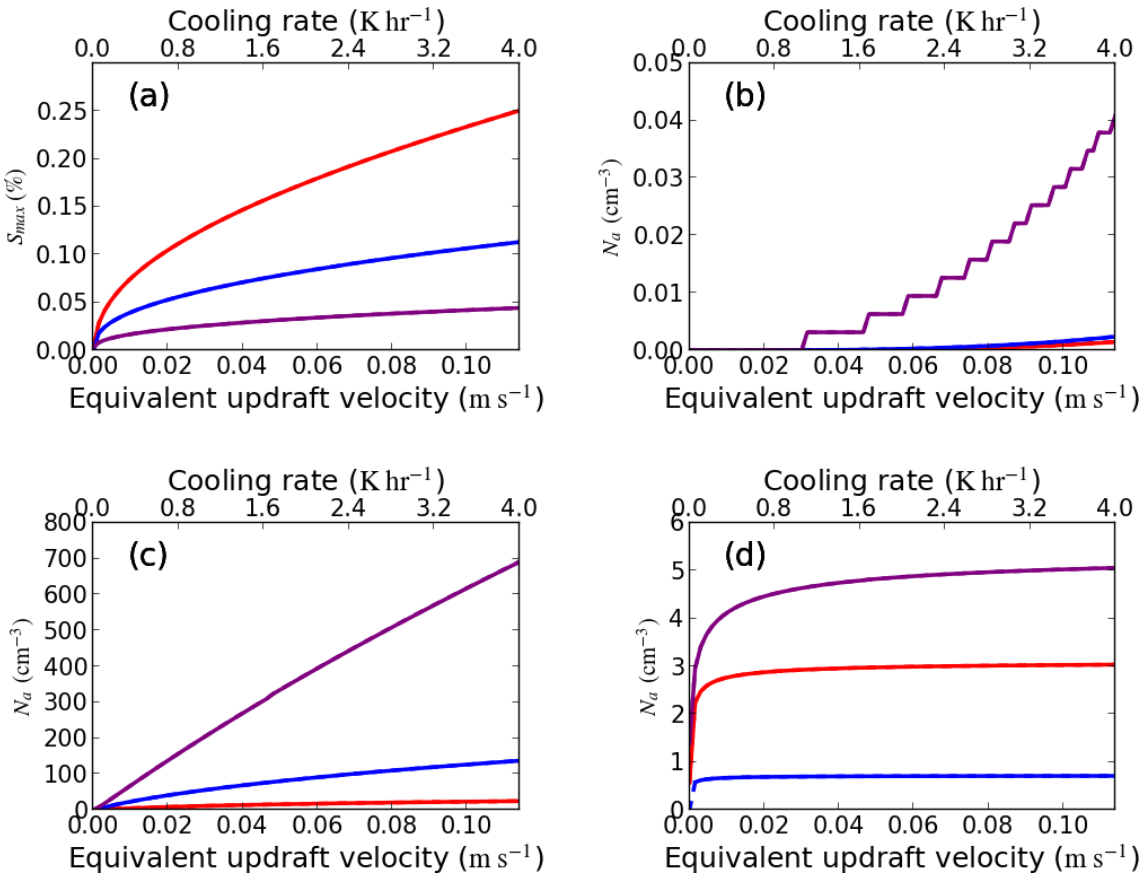

Figure 5.3: Analysis of the maximum supersaturation and number of activated aerosols over different aerosol modes and environmental settings. (a) A plot of the maximum supersaturation, s_{max} (%), against the total cooling rate. (b) - (d) A plot of activated aerosol concentration, N_a (cm^{-3}) against the total cooling rate for Aitken, accumulation and coarse mode aerosols respectively. Red - marine; Blue - clean continental; Purple - urban. Dashed line - T_ship_ad; solid line - T_ship_v2_ad.

To date, many current parameterisations for aerosol activation assume adiabatic ascent found in a convective cloud (e.g. cumulus, stratocumulus), whilst imposing a minimum updraft velocity threshold of typically 0.1 m s^{-1} (Ghan et al., 2011). Figure 5.3a shows a

monotonic increase in the maximum supersaturation, s_{max}, across all environments with respect to updraft velocity. For a fair comparison, an equivalent cooling rate was calculated for the Shipway_v2 scheme using the adiabatic lapse rate assumption (see Equation 5.7). The s_{max} is 0.26% for the marine environment; corresponding to a cooling rate of 4 K hr^{-1}, and decreases as the aerosol concentration increases (0.11 and 0.04% for the clean continental and urban environment respectively). Increasing the aerosol concentration can result in the formation of new droplets, leading to an increased condensation rate. As a result, the maximum supersaturation will decrease, given Equation (5.10), and consequently, reduces the likelihood of newly activated droplets.

Figures 5.3b-d show a monotonical increase in activated aerosols in relation to updraft velocity. An updraft will cause a parcel of air to rise and cool due to the pressure exerted on it by its external environment decreasing. This allows the parcel to expand, and the parcel may reach supersaturation. However, s_{max} will increase with updraft velocity (Equation 5.13), therefore increasing the likelihood of more aerosols being activated. Of the three modes, the proportion of activated aerosols is greatest in the accumulation mode in all tested environments. This is despite that in some environments (e.g. marine), the proportion of aerosol in the Aitken mode is greater than the accumulation mode (see Table 5.1). Aitken mode aerosols have relatively small critical radii compared to aerosols in both the accumulation and coarse modes. This makes the required maximum supersaturation for activation significantly higher, which is shown in tests displayed in Figure 5.3b. Conversely, a similar argument can be applied to coarse mode aerosol, as shown in Figure 5.3d. In reality, supersaturation levels in fog have been shown to only reach several tenths of 1% (Gerber, 1991), and hence would not be great enough to activate Aitken mode aerosol. Given this result, the choice in the activation scheme will be focused predominately on aerosol in the accumulation and coarse mode.

Across the tests in C_adiabatic, a direct comparison in the differences in numerical calculations agree relatively well. There is a maximum absolute difference of 2×10^{-3} % for s_{max} and 0.83 cm^{-3} in the number of activated aerosols, resulting in T_ship_v2_ad overlapping T_ship_ad across all modes (Figure's 5.3a-d). The difference relates to how

the Shipway_v2 scheme is written in terms of $\left.\frac{dT}{dt}\right|_{tot}$, rather than an updraft velocity, suggesting the numerical difference is due to the use of a lapse rate assumption (Equation 5.7). However, despite this difference, these results show that the adiabatic pathway used within the Shipway_v2 scheme has not been impacted upon implementation in the offline box model.

5.4.2 Associated percentage difference for methods of aerosol activation

C_accumulation - accumulation mode aerosol experimentation

Figures 5.4a-c show an increase in N_a with respect to the prescribed cooling rate for aerosols in the accumulation mode (and all subsequent modes); an expected result based on Figure 5.3a. Within C_accumulation, T_ship_v2_mar_acc produces a higher N_a than T_ship_mar_acc for all cooling rates (Figure 5.4a - marine). For example, N_a increases from 22 to 26 cm^{-3} for a cooling rate of 3.51 K hr^{-1}, and the same result is applicable to tests within the clean continental and urban environments (described in Table 5.2). The increase in N_a displayed in tests using the Shipway_v2 scheme (see Equation 5.23) relates to the ratio of the cooling coefficients shown in Equation (5.12), therefore demonstrating the dependency on the total number of activated aerosols with its physical environment. To understand how using a w_{min} threshold of 0.1 m s^{-1} would change the total number of activated aerosols, all tests using the Shipway activation scheme were re-run, with the w_{min} threshold applied (Tests T_ship_mar_acc_wmin, T_ship_con_acc_wmin and T_ship_urb_acc_wmin). Applying this threshold resulted in a fixed N_a for a cooling rate below 3.51 K hr^{-1}, which equivalent to 23, 121 and 595 cm^{-3} in the three tested environments respectively. Consequently, should there be a cooling rate lower than this threshold, N_a will be overestimated and may impact features of the fog evolution i.e. the fog's optical depth.

Each test in the marine environment results in a different N_a. Therefore percentage differences between test's T_ship_mar_acc and T_ship_v2_mar_acc, and T_ship_v2_mar_acc and T_ship_mar_acc_wmin, were calculated, as shown in Figure 5.4d. The same percentage

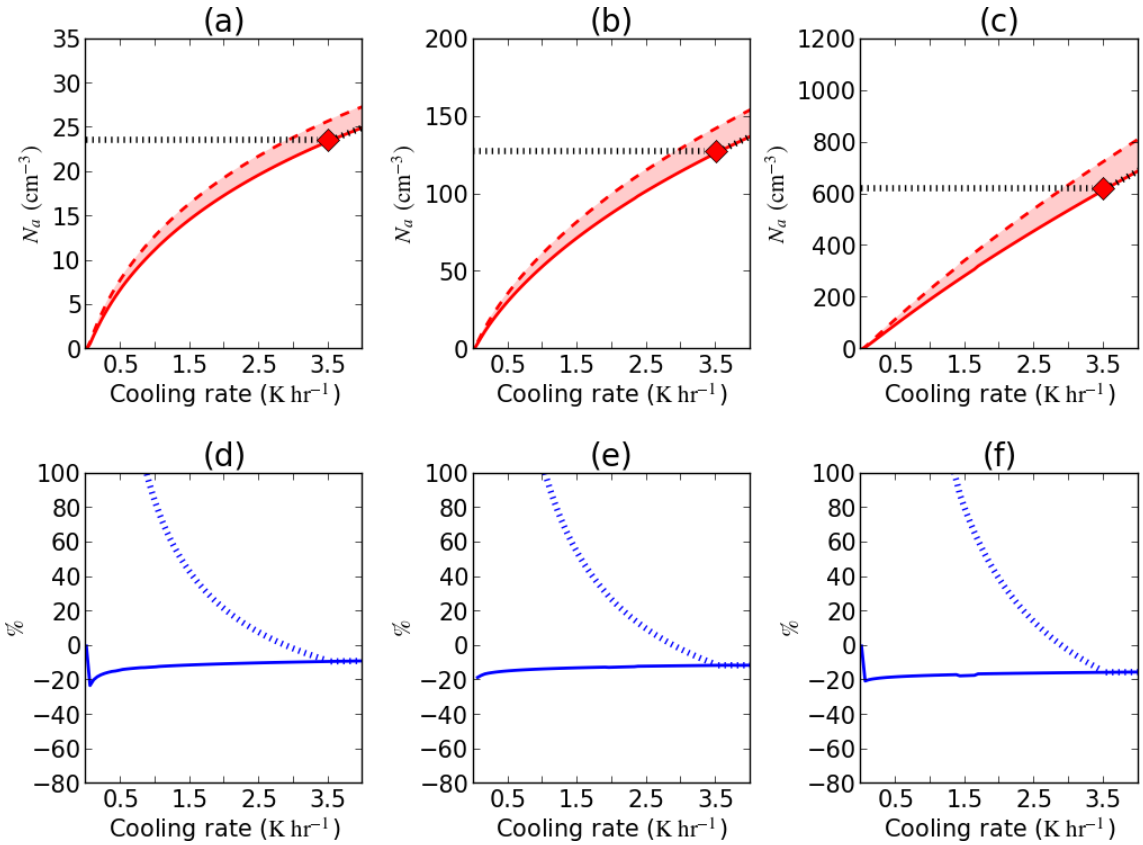

Figure 5.4: Analysis of aerosols in the accumulation mode. (a) A plot of activated aerosols, N_a against the total cooling rate for the marine environment. Solid line - T_ship_mar_acc; dashed line - T_ship_v2_mar_acc; black dashed line - T_ship_mar_acc_wmin. (b) Percentage differences between: dashed line - T_ship_mar_acc against T_ship_mar_acc_wmin; solid line - T_ship_mar_acc against T_ship_v2_mar_acc. (c) - (d): clean continental; (e) - (f): urban.

differences were calculated for a clean continental and urban environment, as shown in Figures 5.4e-f. The percentage difference between the Shipway_v2 and Shipway (with an applied w_{min}) increases as the prescribed cooling rate decreases. When comparing the three environments, the rate of increase in the percentage difference grows, as the tested environment becomes more polluted. For example, a cooling rate of 1.5 K hr^{-1} results in a percentage difference of 40, 50 and 70% for the three environments respectively. Given the associated percentage difference, this indicates aerosol activation in fog simulations is overestimating N_a by an appreciable amount. In reality, for a given liquid water path,

increasing the aerosol concentration will result in a larger concentration of smaller droplets, resulting in an increase in the cloud's optical depth (the first indirect effect as described by Twomey, 1977). Therefore, in the context of aerosol activation in fog, the overestimation of N_a due to the use of w_{min} will overestimate the fog's optical depth, causing the fog to become well-mixed too quickly.

A method to reduce this percentage difference is to reduce the minimum threshold, such that it is equivalent to a cooling rate found in observed cases of fog. Between the Shipway_v2 and Shipway schemes for aerosols in the accumulation mode, the associated percentage change ranges between -10 and -20% for all three environments, and the rate of change in the percentage difference is not appreciably different for any given environment (Figures 5.4d-f). This implies that even if the minimum threshold of w_{min} were to be reduced such that it is representative for updraft velocities found in radiation fog, just using the Shipway scheme could potentially underpredict aerosol activation by 10 to 20%. This is a point of discussion to be investigated in Section 5.5 of this chapter.

C_coarse and C_Aitken - coarse and Aitken mode aerosol experimentation

Regarding coarse mode aerosol, all three environments show a small difference between the Shipway_v2 and Shipway schemes, with the percentage difference being close to 0 (Figure 5.5). Given the size of these aerosol and the total concentration, the environmental supersaturation required for activation is a lot smaller than accumulation mode aerosol, implying that the mechanism of cooling that increases supersaturation is of less importance. When accounting that there is more coarse mode aerosol in the marine environment than the clean continental environment, the rate of increase in the percentage difference grows, as the tested environment becomes more polluted. However, the rate is relatively smaller in comparison to the accumulation mode. For example, a cooling rate of 1.5 K hr^{-1} results in a percentage difference of 3, 5 and 7% for the marine, urban and clean continental environments respectively. Given the rate of change in the percentage difference, the impact of w_{min} is not as great for coarse mode aerosol in comparison to accumulation mode aerosol.

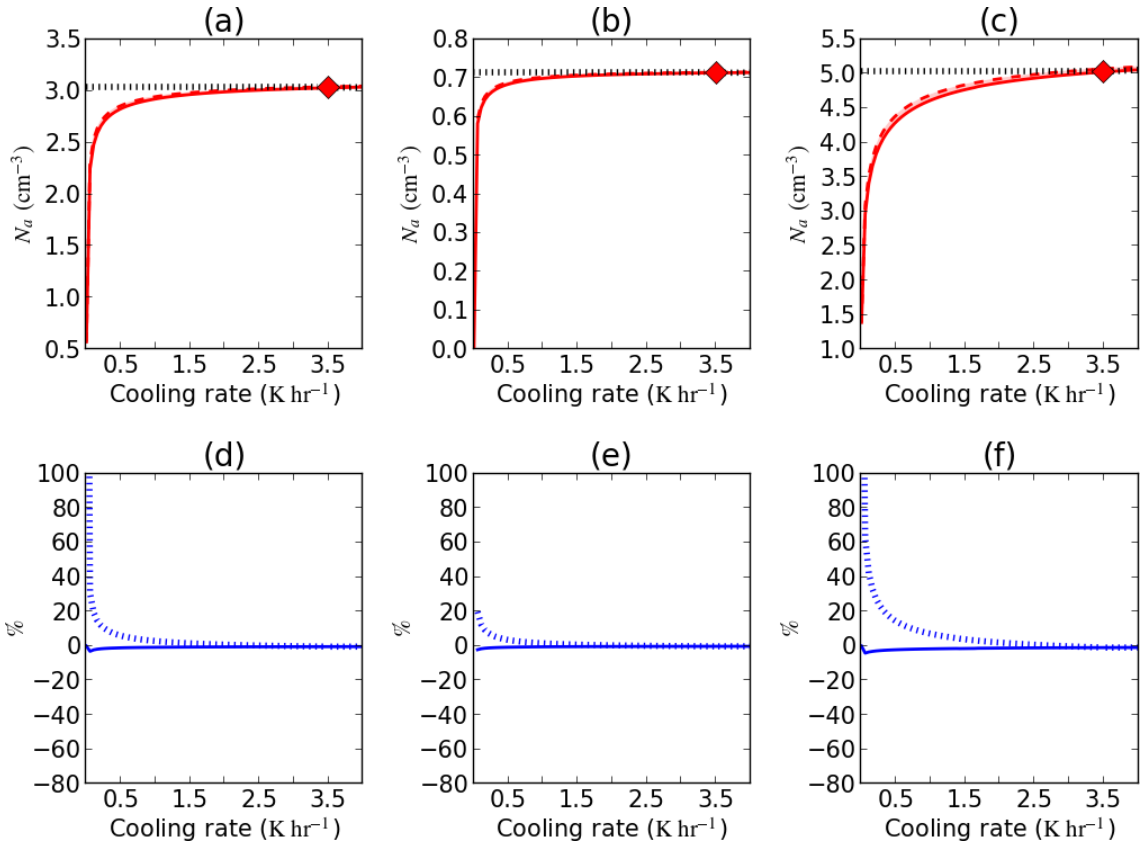

Figure 5.5: Same as Figure 5.4, but for coarse mode aerosol.

Although there is an increase in N_a to the prescribed cooling rate for aerosols in the Aitken mode, the proportion of aerosols that activate in Aitken mode in comparison to the other modes is appreciably smaller, by up to a factor of 1000 in some cases (Figures 5.6a-c). Consequently, there are large fluctuations in the percentage difference -20 to -60% and decreases rapidly to -∞ due to close to zero particles activating for the given cooling range (Figures 5.6d-f). To conclude, Aitken mode aerosol can be disregarded when understanding aerosol activation representation in fog.

5.5 Aerosol activation in MONC - suitability of w_{min}

The results in Section 5.4 of this chapter have demonstrated that the use of a w_{min} threshold may result in overpredicting droplet formation by up to 70%, for typical cooling rates

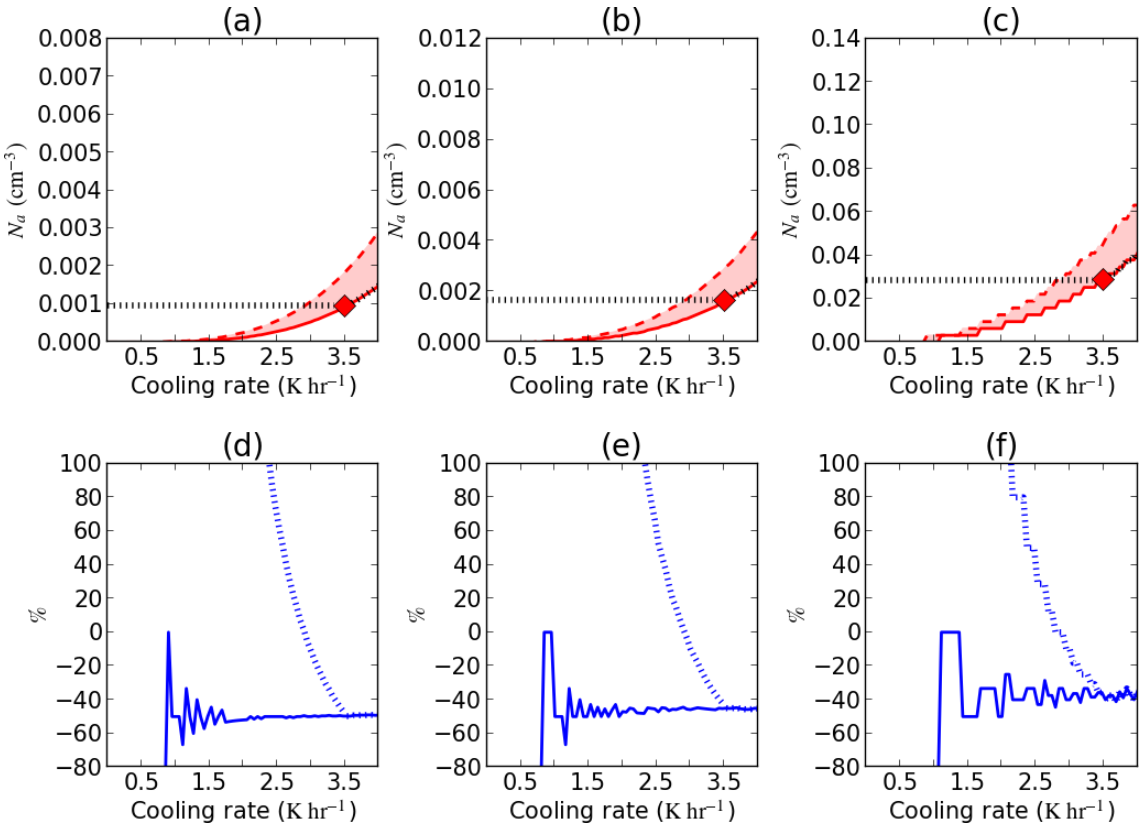

Figure 5.6: Same as Figure 5.4, but for Aitken mode aerosol.

found in fog formation. This section will investigate the suitability of w_{min} in simulations of fog using MONC. The model setup is the same as the control simulation described in Chapter 4. The exceptions to this setup are that Shipway and Shipway_v2 will be used instead of Abdul-Razzak and Ghan (2000), and the shape parameter has been changed to $\mu_d = 3$, based on the results discussed in Chapter 4.

Table 5.3 displays the tests discussed in this section. These tests all run with the Shipway activation scheme, but have adjusted w_{min} thresholds (the equivalent cooling rate shown in Table 5.3 associated with each respective threshold was calculated with the adiabatic lapse rate assumption). A w_{min} of 0.1 m s^{-1} was chosen as the default value based on the threshold being imposed to account for poorly resolved cloud top turbulence in GCMs (Ghan et al., 1997). Next, a threshold of $w_{min} = 0.05$ m s^{-1} was chosen to represent an equivalent surface cooling rate that has been observed in radiation

Test no.	Test name	Imposed w_{min} (m s^{-1})	Cooling rate equivalent (K hr^{-1})
T1	T_shipway_wmin	0.1	3.51
T2	T_shipway_eqv	0.05	1.61
T3	T_shipway_0.01	0.01	0.351

Table 5.3: A table listing all simulations using the Shipway activation scheme. w_{min} has been lowered based on the results from Section 5.4 of this chapter. Cooling rate equivalent calculated using the dry adiabatic lapse rate assumption.

fog (Price, 2011). Finally, a w_{min} of 0.01 m s^{-1} was set to understand what would happen should simulations of fog be run with a relatively low updraft threshold.

5.5.1 Minimum threshold sensitivity results

Fog forms in all three tests displayed in Table 5.3 at 1700 UTC, and all decrease to a mean near-surface visibility of 120 m by the end of the night (Figure 5.7a). For all model simulations, visibility is calculated using the formula of Gultepe et al. (2006), where visibility, Vis, is defined as follows:

$$Vis = \frac{1.002}{(LWC \times CDNC)^{0.6473}}. \tag{5.24}$$

Despite the differences in near-surface visibility, all three tests have the strongest rate of decrease between 1700 and 1845 UTC. During this time, the mean near-surface visibility in T_shipway_wmin, T_shipway_eqv and T_shipway_0.01 decrease to 208, 181 and 151 m respectively. However, T_shipway_0.01 has a noticeably higher near-surface visibility before 1830 UTC and best agrees with observations, before decreasing in visibility at the same rate as T_shipway_wmin and T_shipway_eqv. Upon inspection, T_shipway_0.01 experiences the most spatial variation between the minimum and maximum visibility during initial fog formation, which is indicative of a turbulent boundary layer. However, in this example, it is more likely that the source of spatial variation is due to the model's spin-up period, as opposed to turbulence driven by either wind shear or convective motion. For context, sunset on the 24th November 2014 was 1600 UTC and observations show a

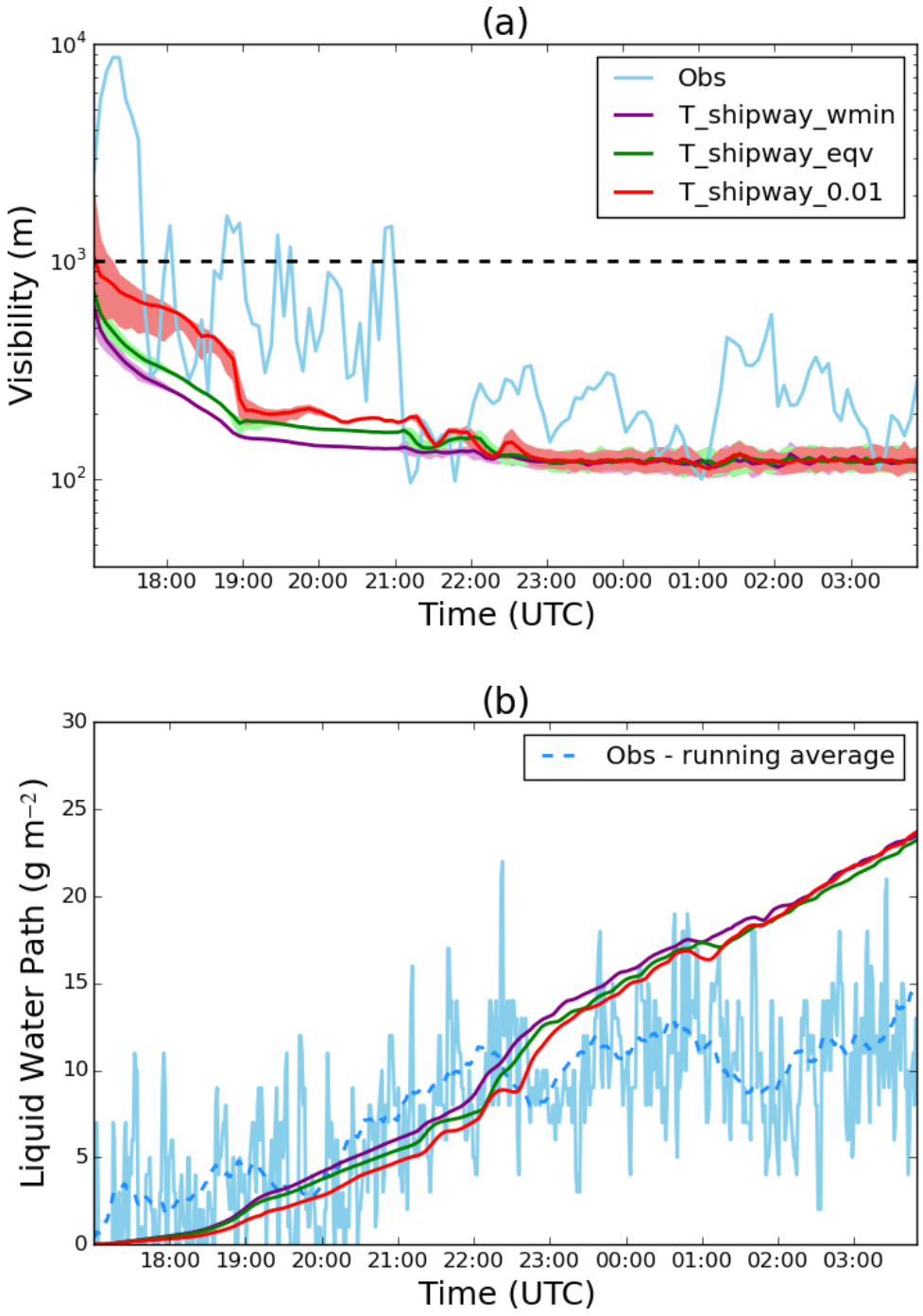

Figure 5.7: (a) - Time series of the mean visibility (m) at a 2 m altitude. Purple – T_shipway_wmin; green – T_shipway_eqv; red – T_shipway_0.01; light blue – observations. Minimum and maximum visibility are marked on the figure by the shaded area. (b) - Time series of the liquid water path (g m^{-2}). Purple – T_shipway_wmin; green – T_shipway_eqv; red – T_shipway_0.01; light blue – observations; blue dashed - running average over observations (40 points).

SBL beginning to form around the time of model initialisation. The model was initialised at 1700 UTC, as this was the time of the first radiosonde for IOP1. When modelling with LES, the initial flow field may be non-turbulent, and hence a spin-up time is required for the model to approach nearly steady values (Mirocha et al., 2018). Consequently, this may result in unusual model behaviours during initial fog formation. Section 5.6.3 will verify whether the model spin-up period is the cause of these behaviours through tests using Shipway_v2. Nonetheless, the lower threshold used in T_shipway_0.01 allows for the simulation to undergo a slower transition in near-surface visibility, indicating that the number of activated droplets calculated may be too high due to the scheme's default assumptions.

Throughout the night, T_shipway_wmin has a higher LWP than both T_shipway_eqv and T_shipway_0.01 (Figure 5.7b). Chapter 4 showed that the CDNC strongly influences the LWP, where a higher LWP resulted in a stronger downwelling longwave flux, signalling the presence of a deeper fog. T_shipway_wmin has the steepest decrease in the visibility during fog formation, suggesting that it has the highest initial CDNC, therefore having the slowest sedimentation rate of all three tests as a result. More liquid water in the fog would lead to a stronger cooling at the fog top, thereby increasing liquid water production. This result provides further evidence that aerosol activation in the fog may not be accurately represented with the use of a w_{min} of 0.1 m s^{-1}, especially during the initial formation stage.

To understand how reducing w_{min} changes the fog structure, contour slices of CDNC, LWC and vertical motion were taken at 1900, 2100, 2300 and 0100 UTC for both T_shipway_wmin and T_shipway_0.01 (Figures 5.8 and 5.9). At 1900 UTC, T_shipway_wmin's fog depth grows to 23 m, with a fixed CDNC of 78 cm^{-3} throughout the layer (Figure 5.8). The LWC is strongest towards the surface and is relatively uniform in structure (Figure 5.8b). However, despite the fixed w_{min} of 0.1 m s^{-1}, the model domain experiences negligible updraft speeds (Figure 5.8c), therefore indicating that too much droplet formation is likely to be occurring. The fog is 41 m in height at 2100 UTC, with a relatively similar structure in LWC to that at 1900 UTC. However, at 2300 UTC, new droplets of around

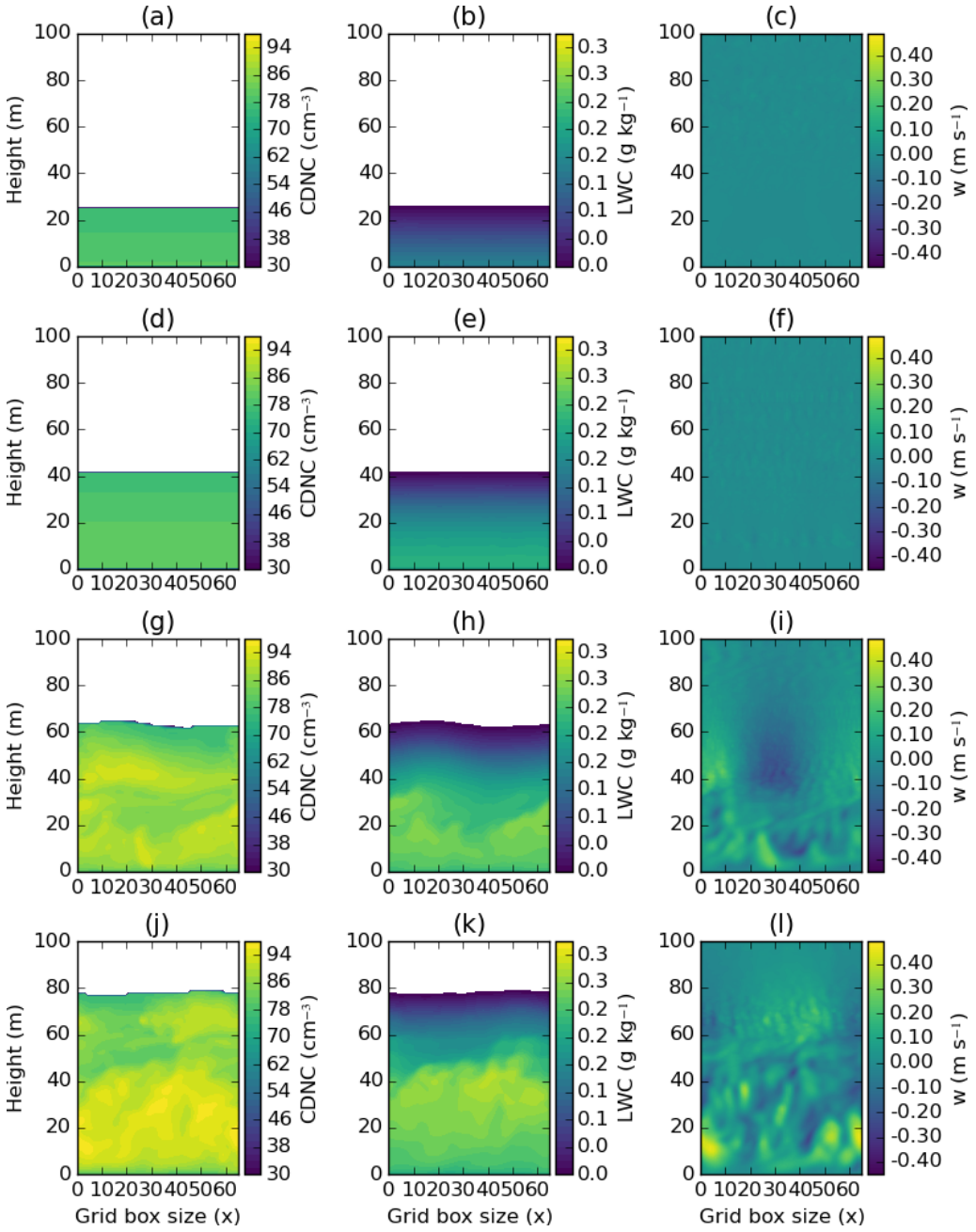

Figure 5.8: Contour slices at y = 66 m of (a) - CDNC (cm^{-3}), (b) - LWC ($g\ kg^{-1}$) and (c) - Vertical motion ($m\ s^{-1}$) at 1900 UTC during T_shipway_wmin. Sub-figures (d)-(f): 2300 UTC, (g)-(i): 0100 UTC.

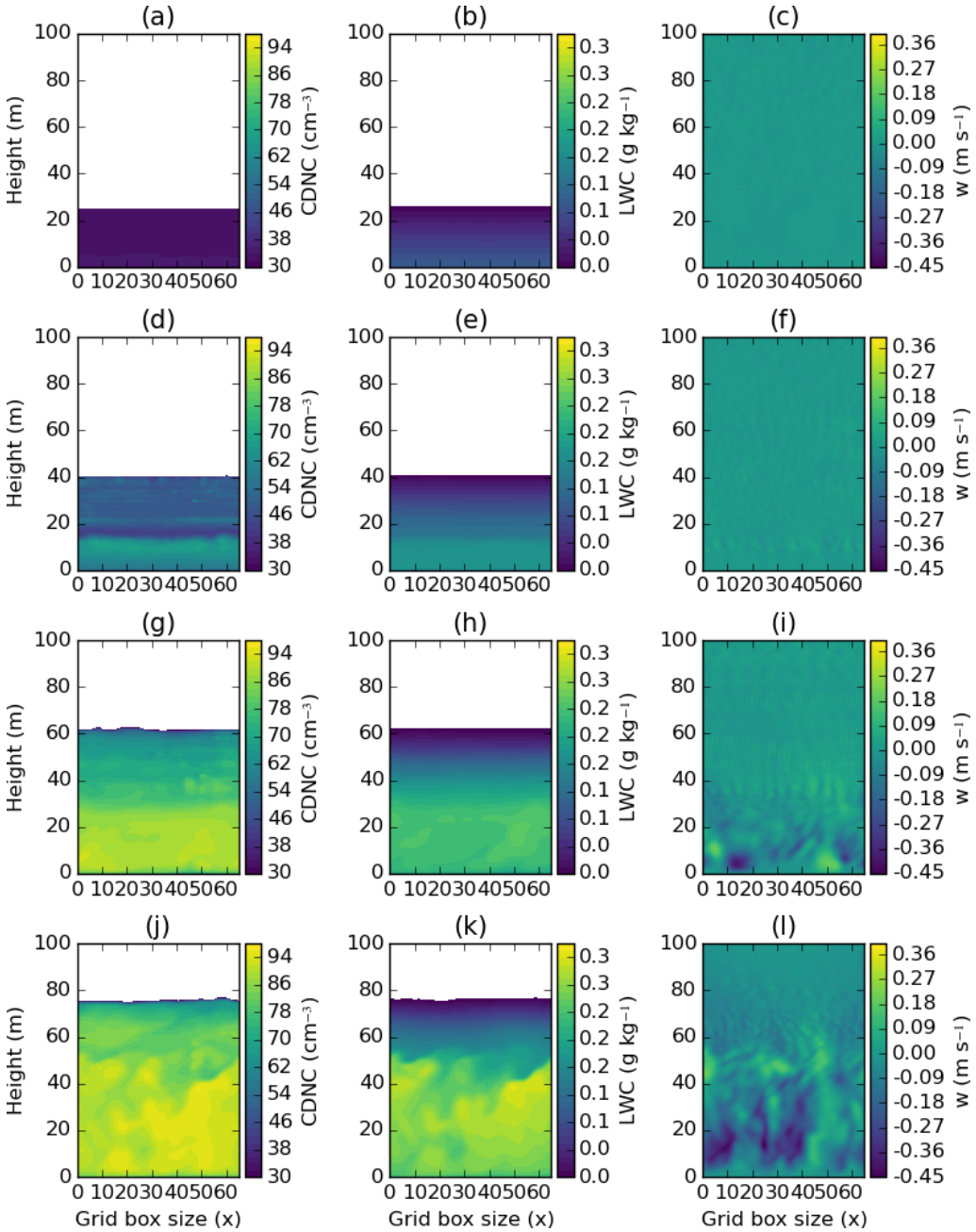

Figure 5.9: Same as Figure 5.8, but instead for T_shipway_0.01.

90 cm^{-3} begin forming throughout the fog depth, and the fog top is less smooth (Figure 5.8h). Although the LWC is still strongest towards the surface, there are some irregular structures in the bottom 20 m of the fog depth (Figure 5.8i), which coincide with an increase in vertical motions, ranging between -0.16 to 0.2 m s^{-1}. These structures become more apparent at 0100 UTC, signalling that turbulence has formed within the fog depth (Figure 5.8k and l).

T_shipway_0.01 has a relatively smooth LWC structure up until 2300 UTC in comparison to T_shipway_wmin, despite the magnitude of vertical motions not being appreciably different between both tests (Figures 5.9a-i). This suggests that the developed turbulence at 2300 UTC onwards in the fog is likely induced by Kelvin-Helmholtz (KH) instabilities, which is driven by shear in the fog layer (Bergot, 2013). To verify these instabilities, vertical profiles of the Richardson number, Ri, were taken at 2300 and 0100 UTC (Figure 5.10). Ri expresses the ratio of turbulence driven by the buoyancy to wind shear, such that:

$$Ri = \frac{g}{T_v} \frac{\partial \theta_v / \partial z}{(\partial \mathbf{u} / \partial z)^2}, \tag{5.25}$$

where g is gravity, T_v is the virtual temperature, θ_v is the virtual potential temperature and $\mathbf{u} = u(x, y)$; a representation of airflow speed. The critical Richardson number is typically 0.25, with unstable flow for $Ri < 0.25$. This suggests the fog layer is unstable below 35 m at 2300 UTC and 60 m at 0100 UTC, with a stable layer above; a near neutral stability aloft.

All three tests at 2300 UTC have a $Ri < 1$ (Figure 5.10a), implying that $(\partial \mathbf{u}/\partial z)^2 > \partial \theta_v / \partial z$ given Equation (5.25), and hence confirming the source of turbulence being driven through wind shear. However, there is a decrease in the peak of Ri as the w_{min} threshold is reduced. For example, the peak of Ri decreases from 0.82 to 0.70 between T_shipway_wmin and T_shipway _0.01. Given that these tests have the same r_e, this would confirm that the strength of the induced KH instabilities is controlled by the fog's sedimentation rate, as w_{min} leads to a lower CDNC. By 0100 UTC, all three tests undergo similar levels of turbulence caused by wind shear. By this stage, the fog begins to homogenise; a strong

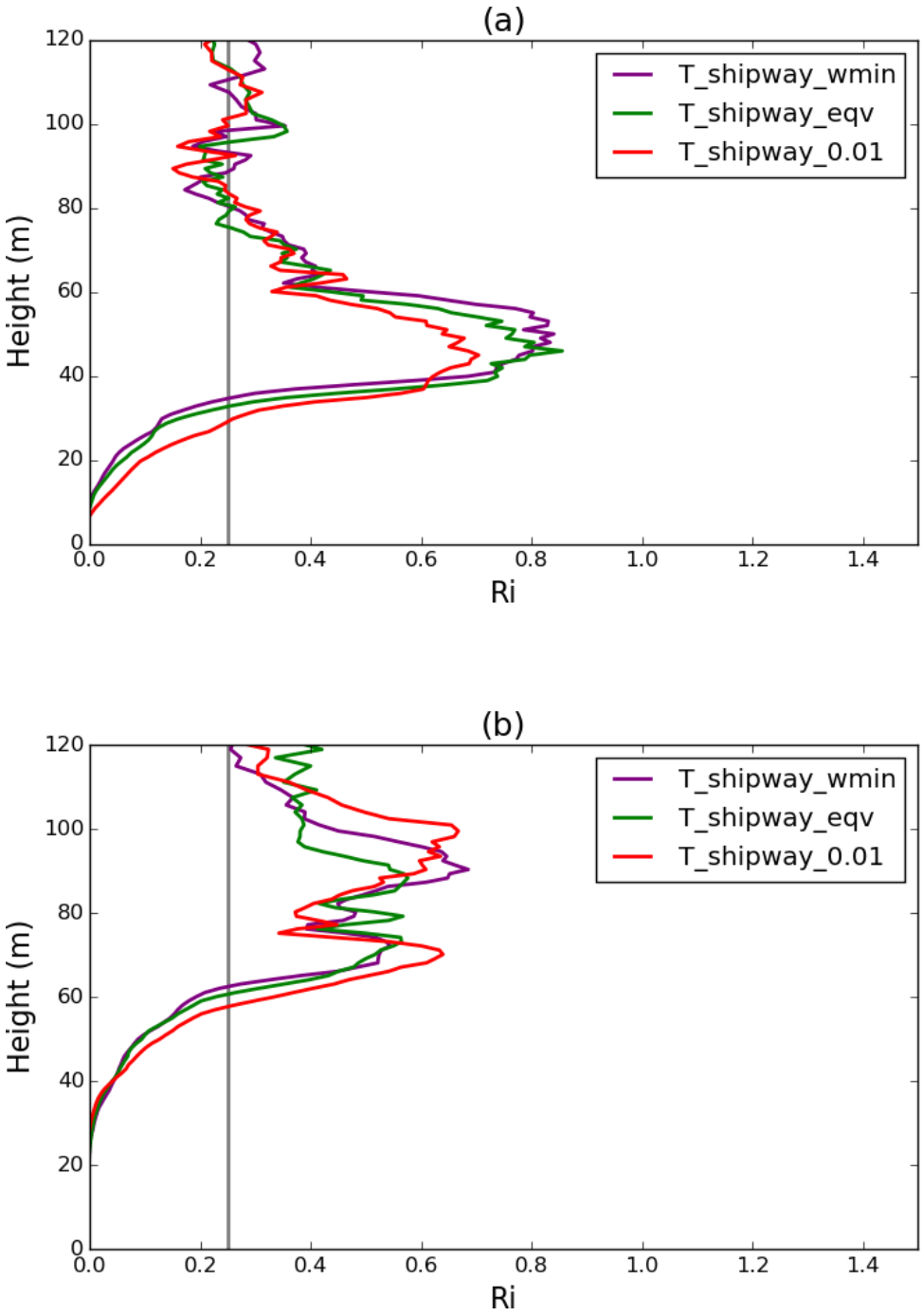

Figure 5.10: Vertical profiles of the Richardson number at (a) - 2300 and (b) - 0100 UTC. Purple – T_shipway_wmin; green – T_shipway_eqv; red - T_shipway_0.01.

indication that the fog is in the development stage (Nakanishi, 2000).

5.5.2 Fog's sensitivity to subgrid mixing

The results so far have demonstrated that the total CDNC is sensitive to the resolved updraft velocity's strength. The strength of the resolved updraft velocity is determined by the model's mixing scale length, λ_m, such that:

$$\lambda_m = c_s \times \max(\Delta \mathrm{x}, \Delta \mathrm{y}), \tag{5.26}$$

where c_s is the Smagorinsky constant and $\max(\Delta \mathrm{x}, \Delta \mathrm{y})$ is the maximum grid box size in the horizontal. Any motions smaller than λ_m is calculated by the subgrid parameterisation, which can account for motions such as diffusion and small scale turbulent mixing.

Porson et al. (2011) discussed the importance of c_s on the fog layer's development. They showed that reducing c_s and hence λ_m resulted in an increase level of TKE that was resolved, leading to the modelled boundary layer to deepen. The work in this chapter uses an aerosol activation scheme as opposed to a fixed droplet number used in the study by Porson et al. (2011), leading to the suggestion that the calculated CDNC is also sensitive to the levels of resolved TKE. Consequently, the initial fog formation may be more sensitive to the level of subgrid mixing, in addition to the change in sedimentation rate, as w_{min} is reduced.

To understand the impact of subgrid mixing on the formation and development of IOP1, two sets of tests were conducted. These tests were set to address two questions:

1. How sensitive is the fog's evolution to the resolved updraft velocity when sedimentation is turned off?

2. How sensitive is the fog's evolution to the choice in mixing length?

For these tests, the default Smagorinsky constant is set to $c_s = 0.23$. Question 1 was addressed by reducing w_{min} from 0.1 m s^{-1} to 0.05 and 0.01 m s^{-1} respectively, however, sedimentation in CASIM was set to false. The objective of this question was to understand

how the level of subgrid mixing may directly impact the fog's development, should the fog's droplet distribution not be accounted for. Secondly, question 2 involved changing the default c_s used in test T_shipway_0.01, by doubled and halved it to 0.46 and 0.115 respectively. The objective of this question aimed to understand the impact the resolved TKE had on the developing fog structure, therefore indicating whether the level of subgrid mixing is an important parameter to consider in the lowering of w_{min}.

Between 1815 and 0100 UTC, there is not an appreciable difference in the mean near-surface visibility as w_{min} is lowered from 0.1 to 0.01 m s^{-1} (Figure 5.11a). There is some variation in the mean near-surface visibility between the time frames of 1700 and 1815 UTC, and from 0100 UTC onwards. Given that the LWP is not appreciably different in all three tests lowering *wmin* (Figure 5.11b), this indicates the the source of variation in visibility is due to the CDNC. To understand how much of an impact the CDNC is having during the time frames where variation occurs in the near-surface visibility, times series of CDNC and maximum updraft velocity were taken throughout the night (Figures 5.11c and d). The periods where the near surface visibility increases with a decrease in w_{min} coincide with the maximum updraft velocity being less than 0.1 m s^{-1}. This result suggests that the fog's evolution may be sensitive to the amount of subgrid mixing in the domain.

Given that the importance of any subgrid mixing is sensitive to the choice in w_{min}, c_s was doubled and halved in tests' T_shipway_wmin_0.01_double_mixing and T_shipway _wmin_0.01_half_mixing respectively, where T_shipway_0.01 was used as a control. Until 1900 UTC, there is no appreciable change in the near-surface visibility or LWP (Figure Figure 5.12a). From 1900 UTC, increasing (decreasing) c_s results in an increase (decrease) in near-surface visibility. As the LWP is not appreciably different in these sensitivity tests (Figure 5.12b), the change in near-surface visibility is due to the amount of TKE being resolved, therefore directly impacting the maximum updraft velocity and hence CDNC (Figure 5.12d and c respectively). However, although the fog's evolution shows a slight sensitivity to subgrid mixing, its development appears to be mostly driven by a change in sedimentation rate due to a decrease in w_{min}.

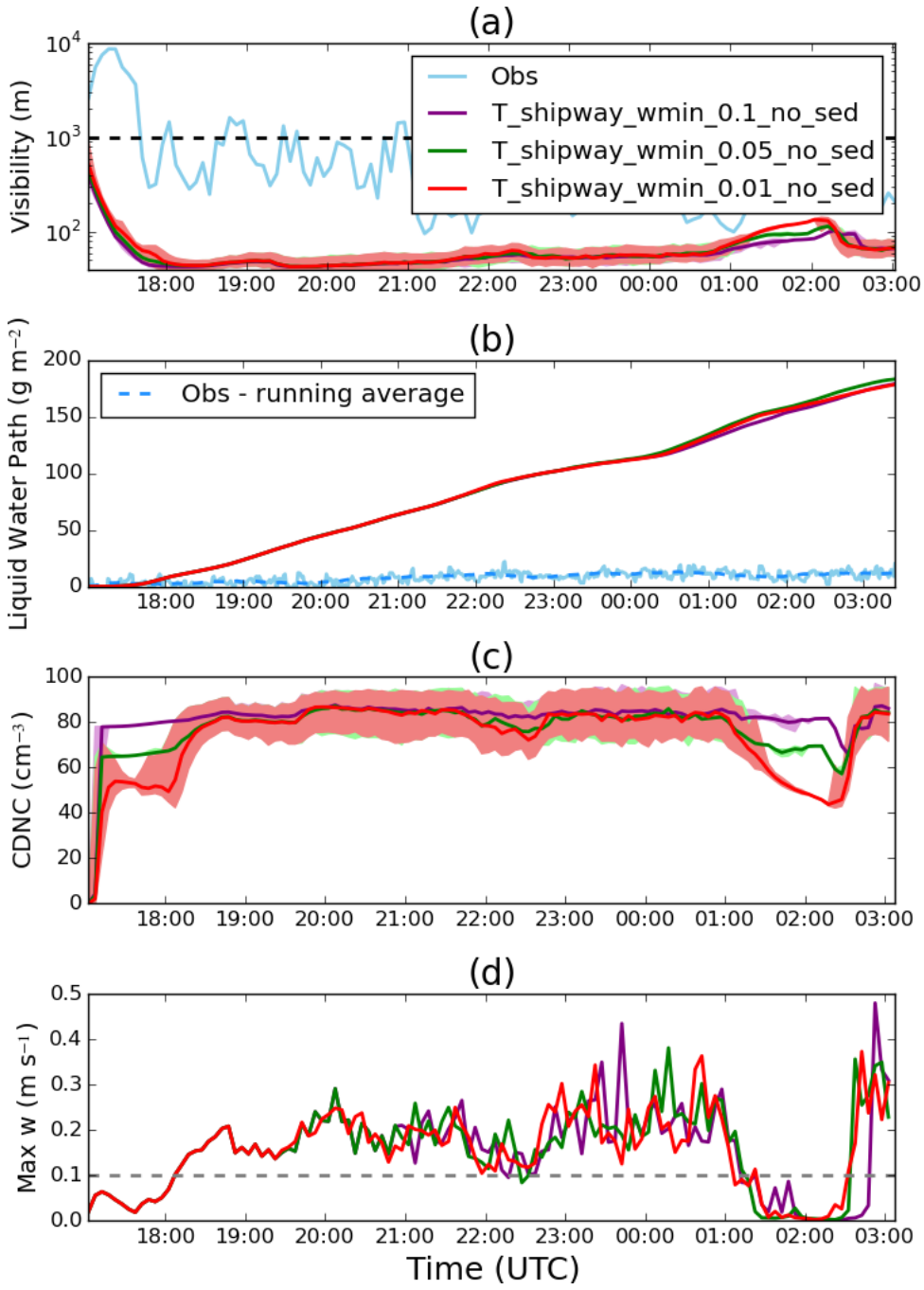

Figure 5.11: Time series of: (a) - mean visibility (m) at a 2 m altitude; (b) - the liquid water path (g m^{-2}); (c) - the mean CDNC (cm^{-3}) at a 2 m altitude; (d) - the maximum updraft velocity (m s^{-1}) at a 2 m altitude. Purple – T_shipway_wmin_0.1_no_sed; green – T_shipway_wmin_0.05_no_sed; red – T_shipway_wmin_0.01_no_sed; light blue – observations of (a) near-surface visibility and (b) liquid water path respectively; black dashed line - fog threshold of 1 km ; grey dashed line - w_{min} threshold of 0.1 m s^{-1}.

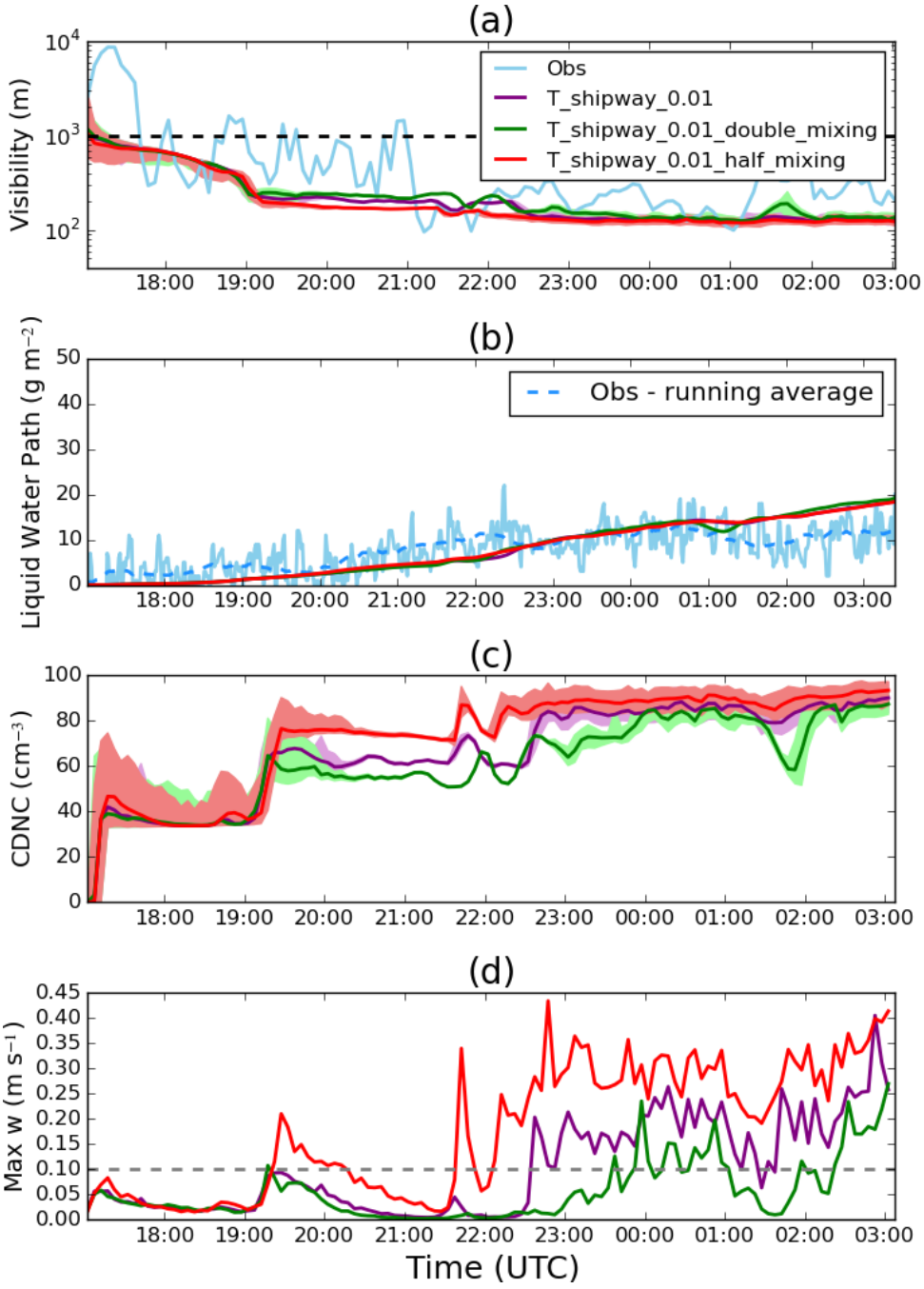

Figure 5.12: Same as Figure 5.11, however: purple – T_shipway_0.01; green – T_shipway_wmin_0.01_double_mixing; red – T_shipway_wmin_0.01_half_mixing.

These results show that by using an unrealistically large value of w_{min}, aerosol activation is overestimated, resulting in a reduced sedimentation rate. Consequently, the fog's liquid water becomes too high and increases the radiative cooling due to liquid water, changing the potential temperature profile. The change in the profile will make the flow unstable, inducing KH instabilities and causing the fog to transition to a well-mixed layer too soon. To conclude, this section demonstrates the fog's sensitivity to aerosol-fog interactions, whereby the assumption of a minimum updraft velocity found in a convective cloud is not suitable for modelling radiation fog.

5.6 Shipway_v2 - Shipway scheme inclusive of non-adiabatic sources

This section will discuss the use of the full Shipway_v2 scheme, with both adiabatic and non-adiabatic sources of cooling being applied. The objective of this section is to understand how the Shipway_v2 scheme for aerosol activation impacts on the fog evolution and where potential differences in the parameterisation currently lie. Shipway_v2 was implemented into MONC based on Equation (5.23). The adiabatic contribution from this equation was derived from the resolved updraft velocity in MONC. The non-adiabatic contribution to date only consists of the longwave heating tendency that is derived using SOCRATES (similar to the scheme used by Vie et al., 2016). Although it has been acknowledged that there are other non-adiabatic contributions to changes in supersaturation such as turbulent mixing, further model development would be required to account for these changes. However, given that radiative cooling is the biggest source of saturation during fog formation (Roach et al., 1976), the results presented in this section should provide useful insight into the representation of aerosol activation during a stable fog case.

Table 5.4 displays all tests that will evaluate Shipway against Shipway_v2. The first part of this section compares tests T1 and T3 from Table 5.3, against T4. The outcome of this comparison will result in a clear understanding of how different cooling contributions influence the CDNC evolution in IOP1. Chapter 4 showed that the fog evolution is sensitive

Test no.	**Test name**	z_0 **(m)**	u_g **(m s^{-1})**	v_g **(m s^{-1})**	r_e **(μm)**
T4	T_shipway_v2	0.05	1.3	2.1	10
T5	T_er_15	0.05	1.3	2.1	15
T6	T_er_20	0.05	1.3	2.1	20
T7	T_0.5_geostro	0.05	0.65	1.05	10
T8	T_2.0_geostro	0.05	2.6	4.2	10
T9	T_0.5_roughness	0.025	1.3	2.1	10
T10	T_2.0_roughness	0.1	1.3	2.1	10

Table 5.4: A List of tests referred to in Section 5.6, which includes changes to the: dynamical; and radiative parameters in MONC.

to the fixed effective radius. As the non-adiabatic contribution in the Shipway_v2 scheme is directly influenced by r_e, two tests were setup testing its sensitivity, which would motivate future work that involves coupling the effective radius to CASIM.

Section 5.5 discussed that the model spin-up period could explain the behaviours during fog formation shown in T_shipway_0.01. However, Maronga and Bosveld (2017) showed that the fog's turbulent structures are sensitive to the geostrophic wind and potentially the choice in roughness length. Therefore, to confirm what are the most important impacts on the fog formation in this case, test's T7 to T10 has been setup up to understand how a change in dynamical parameters may impact simulations that use the Shipway_v2 scheme.

5.6.1 Comparing simulations using the Shipway and Shipway_v2 scheme

The change in LWP and mean near-surface visibility is not appreciably different between T_shipway_wmin and T_shipway_v2 (Figure 5.13). T_shipway_0.01 has the highest near-surface visibility between 1700 and 2300 UTC by up to 340 m, in addition to the lowest LWP by up to 4 g m^{-2}. A reason for the changes in visibility and LWP displayed in T_shipway_v2 suggests that the CDNC in T_shipway_v2 is not appreciably different to that of T_shipway_wmin. To verify this, averaged time-height slices of CDNC and LWC

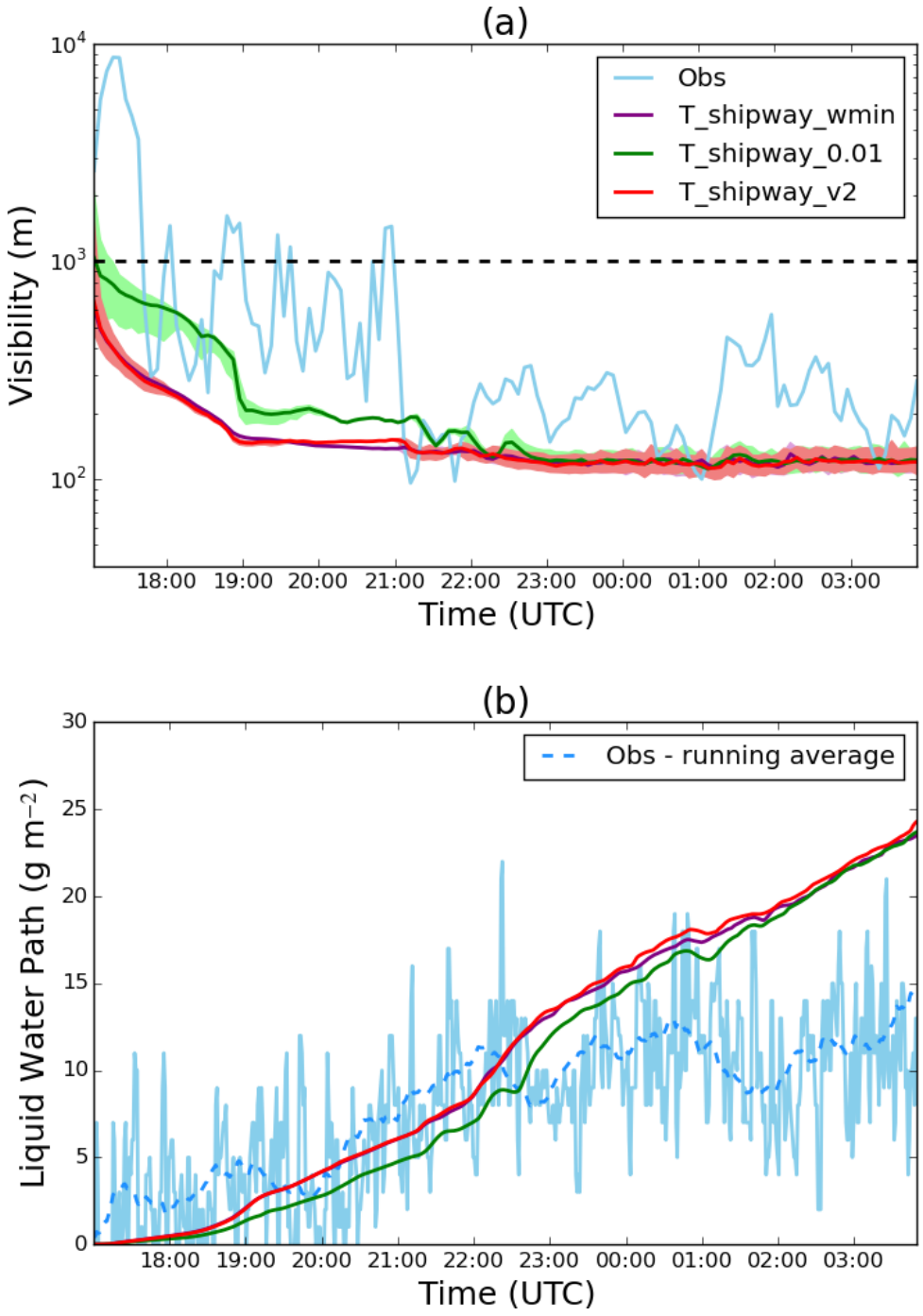

Figure 5.13: (a) - Time series of the mean visibility (m) at a 2 m altitude. Purple – T_shipway_wmin; green – T_shipway_0.01; red – T_shipway_v2; light blue – observations. Minimum and maximum visibility are marked on the figure by the shaded area. (b) - Time series of the liquid water path (g m^{-2}). Purple – T_shipway_wmin; green – T_shipway_0.01; red – T_shipway_v2; light blue – observations; blue dashed - running average over observations (40 points).

were taken for all three tests, showing relatively small changes in the fog layer's CDNC between T_shipway_wmin and T_shipway_v2 (Figure 5.14a and e). As T_shipway_v2 does not use a w_{min}, this result may be due to the combined cooling rate in T_shipway_v2 being equivalent to the cooling rate associated with w_{min} used in T_shipway_wmin. To understand whether this is the case, a horizontal slice at $z = 2$ m of CDNC and the contributions to the relative cooling rates were taken at different times, as shown in Figure 5.15.

At 1730 UTC the CDNC is about 83 cm^{-3}, with 85% the total cooling contribution being due to longwave heating (Figure 5.15m). However, further in the night, the cooling contribution to longwave tendencies increases to around 90% within the fog layer, due to a decrease in the adiabatic cooling tendency to about 0.5 K hr^{-1}. At this time, rolls are visible in the CDNC, but are most noticeable in the cooling contributions (Figures 5.15f, j and n), highlighting the presence of KH instabilities during the early stages of the fog. Finally, as the fog continues developing, the cooling contribution due to longwave heating decreases to around 15%, with a cooling due to vertical motion increasing. This result would occur as the fog begins to grow in optical depth, signalling a well-mixed fog and new droplets beginning to form through convection (Mazoyer et al., 2017).

Based on the current assumptions, this section demonstrates that both dynamical parameters, in addition to the choice in r_e, will impact the fog evolution using the Shipway_v2 scheme. This will now motivate sensitivity tests based on these assumptions to understand what parameters are most crucial, should this scheme be used in future work.

5.6.2 Sensitivity of Shipway_v2 to the effective radius

When increasing r_e from 10 to 20 μm, the near-surface visibility increases by up to 40%, and decreases the LWP by up to 42% (Figure 5.16). However, whilst increasing r_e results in the LWP agreeing better with observations, neither test captures the changes in near-surface visibility during initial fog formation. These simulations do not include a heterogeneous terrain, which has been shown to enhance the fog's spatial variability (Bergot et al., 2015). However, the decrease in liquid water indicates that the fog's development

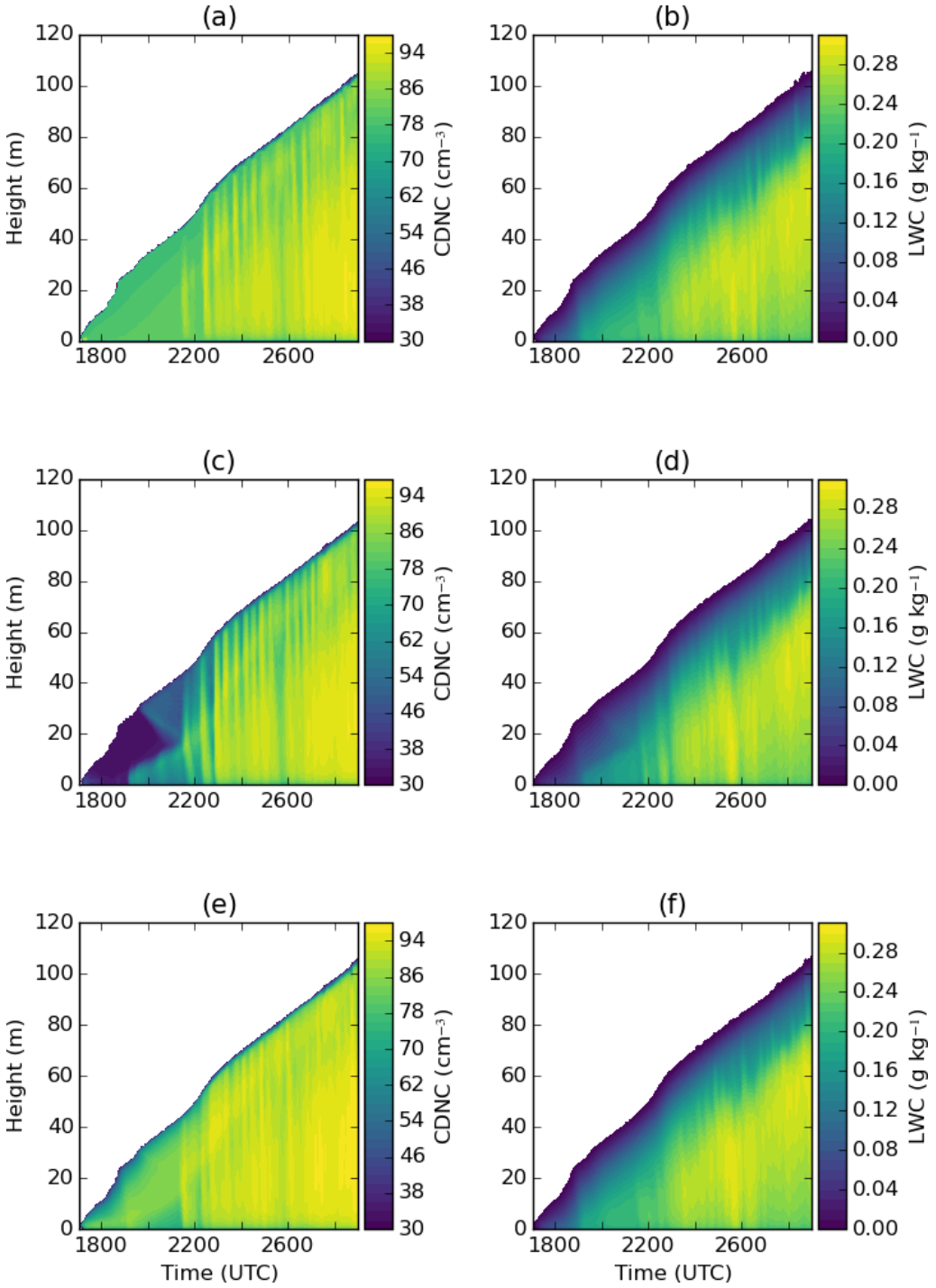

Figure 5.14: Time-height plots: of (a), (c), (e) - mean LWC (g kg^{-1}) and (b), (d), (f) - mean CDNC (cm^{-3}). (a) - (b): T_shipway_wmin; (c) - (d): T_shipway_0.01; (e) - (f): T_shipway_v2.

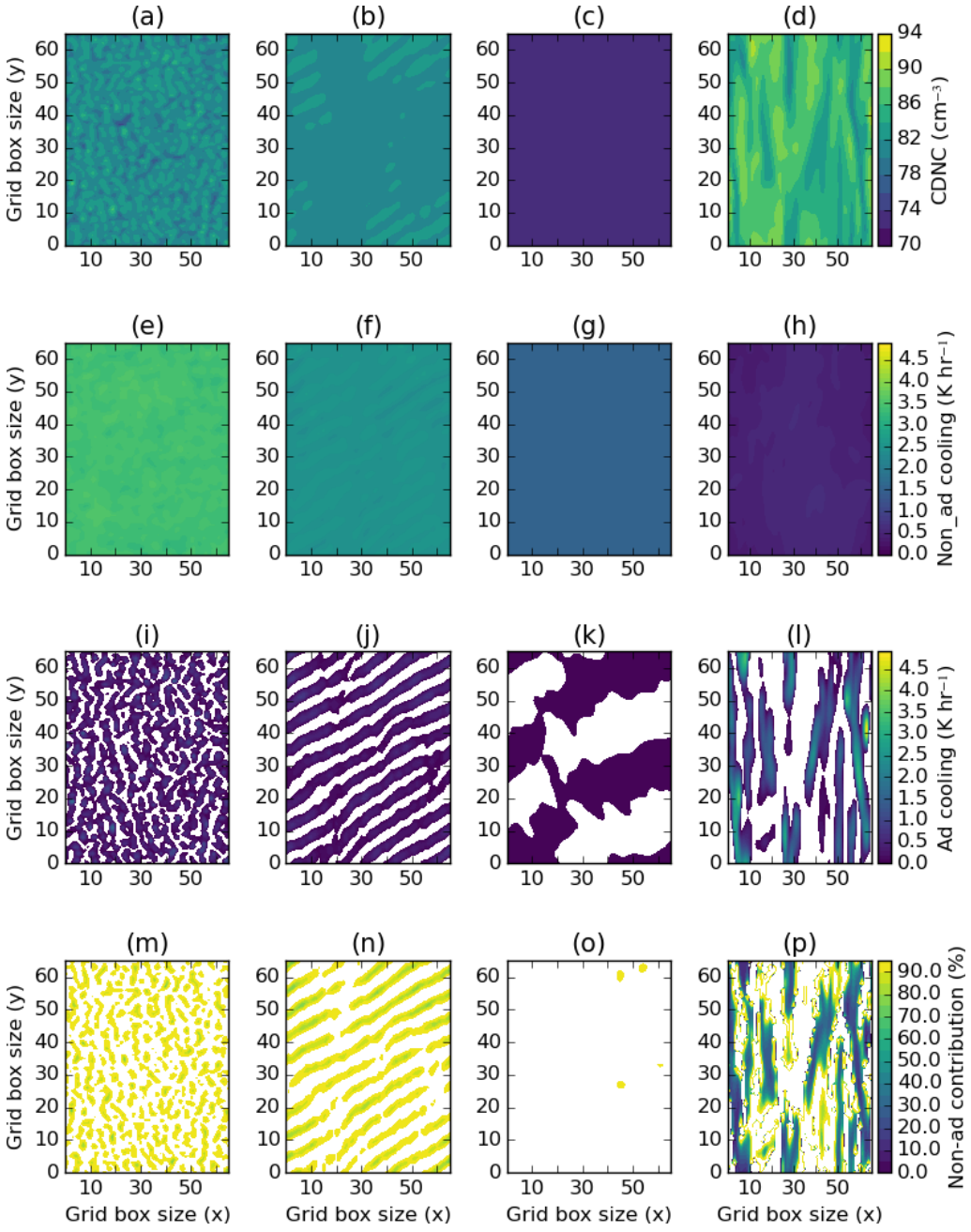

Figure 5.15: Contour slices at z = 2 m of CDNC (cm^{-3}) in T_shipway_v2 at (a) - 1730, (b) - 1900, (c) - 2100 and (d) - 0100 UTC. (e) - (h): non-adiabatic cooling ($K\ hr^{-1}$); (i) - (l): adiabatic cooling ($K\ hr^{-1}$); (m) - (p): Non-adiabatic cooling contribution (%).

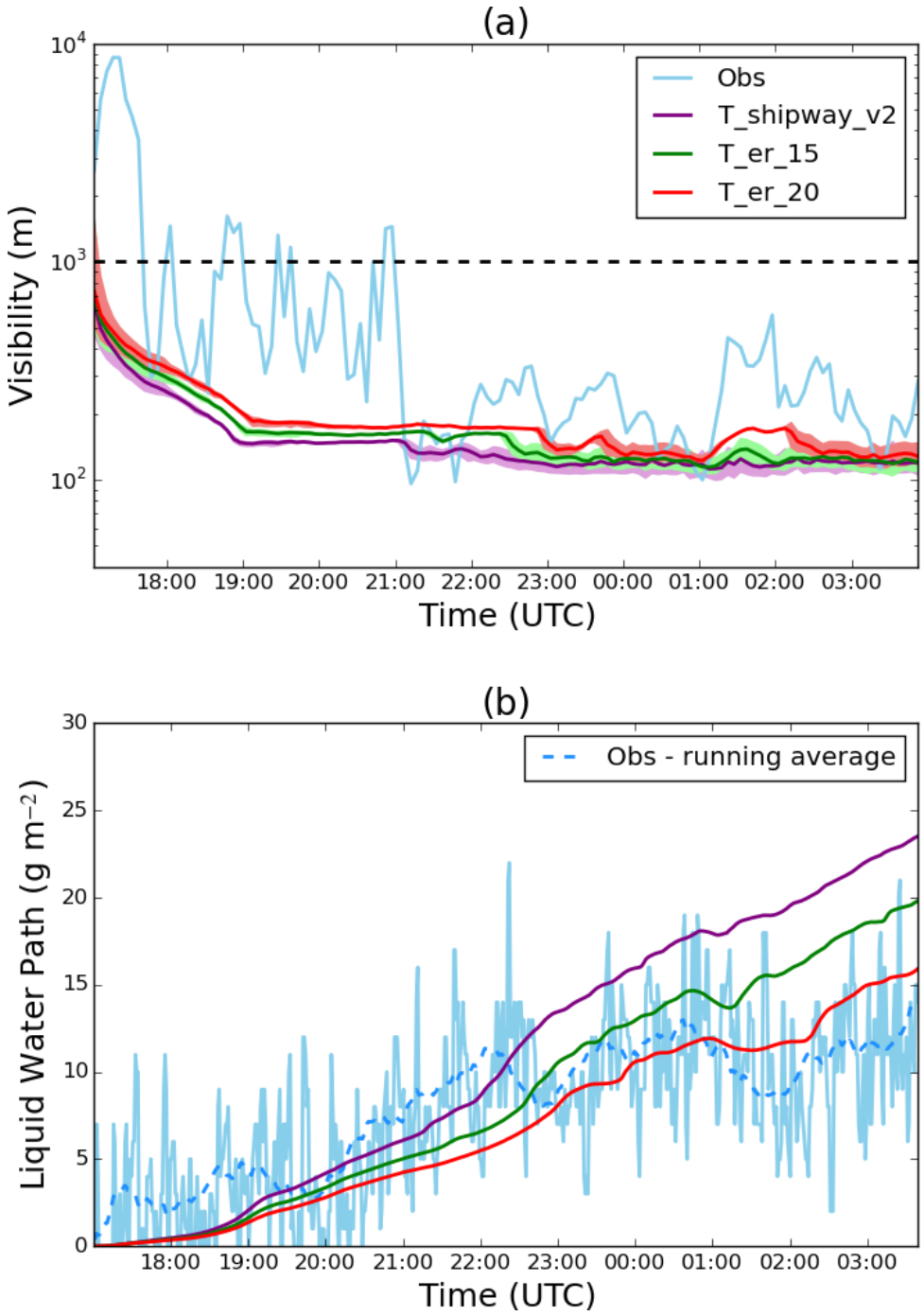

Figure 5.16: (a) - Time series of the mean visibility (m) at a 2 m altitude. Purple – T_shipway_v2; green – T_er_15; red – T_er_20; light blue – observations. The minimum and maximum visibility are marked on the figure by the shaded area. (b) - Time series of the liquid water path (g m^{-2}). Purple – T_shipway_v2; green – T_er_15; red – T_er_20; light blue – observations; blue dashed - running average over observations (40 points).

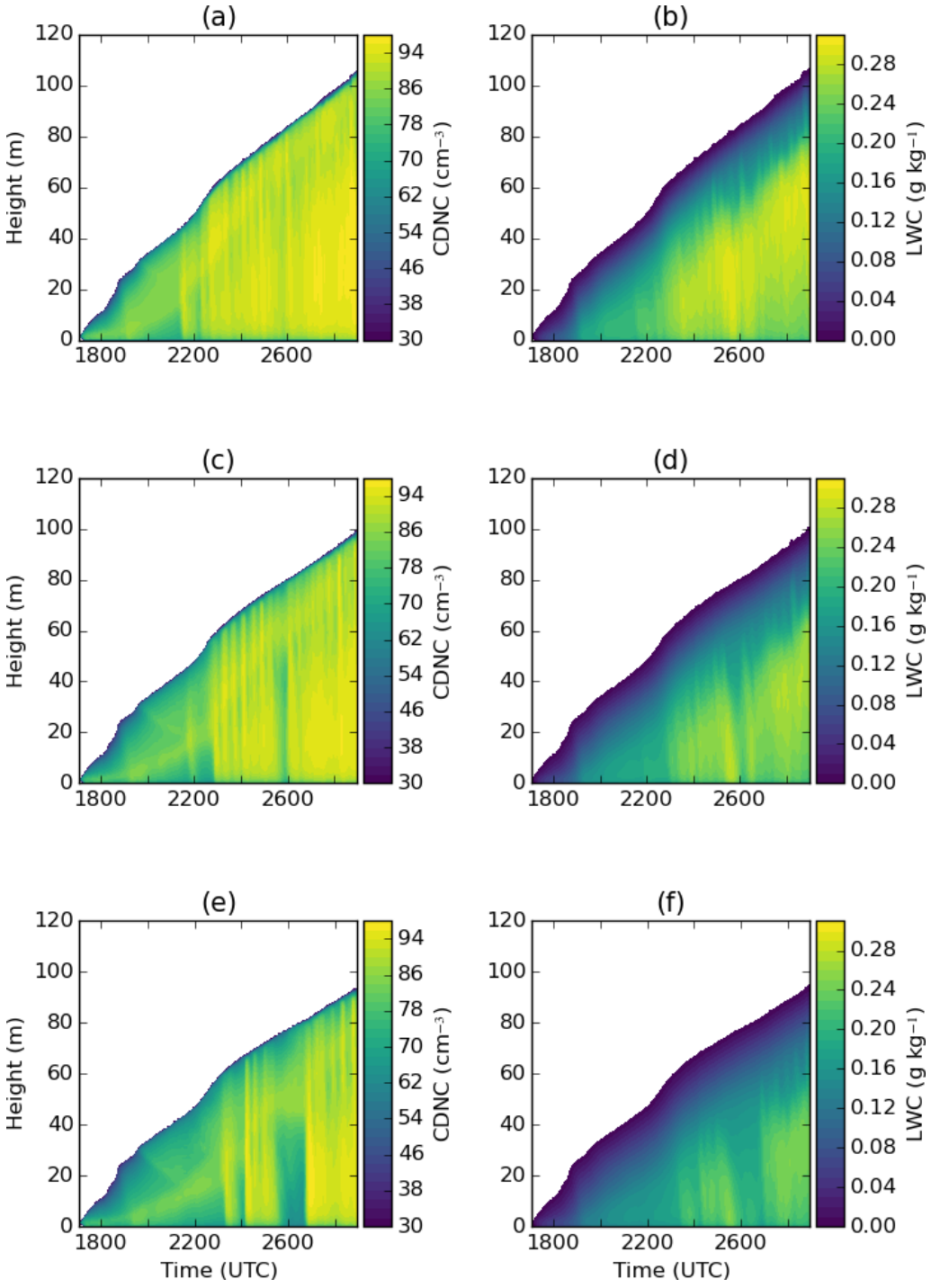

Figure 5.17: Time-height plots of (a), (c), (e) - mean LWC (g kg^{-1}) and (b), (d), (f) - mean CDNC (cm^{-3}). (a) - (b): T_shipway_v2; (c) - (d): T_er_15; (e) - (f):T_er_20.

in optical thickness has slowed down with an increase in r_e. This demonstrates the advantages of utilising the Shipway_v2 scheme when simulating a stable case of nocturnal fog.

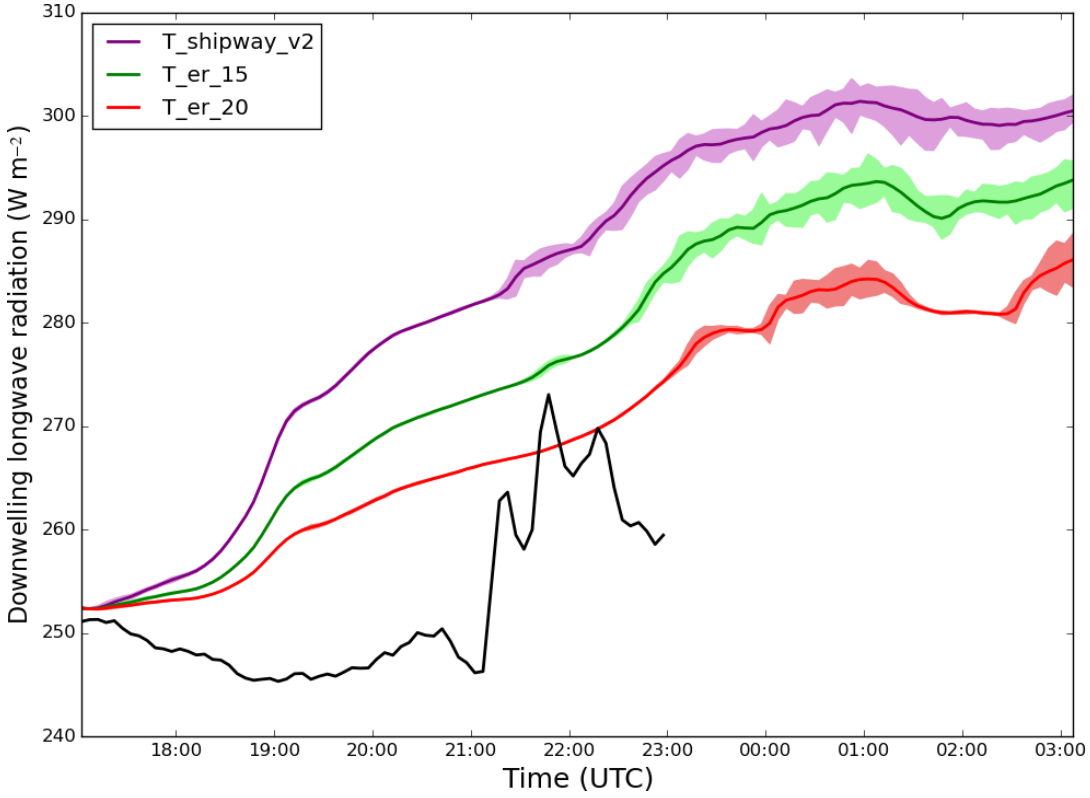

Figure 5.18: Time series of the downwelling longwave radiation (W m^{-2}) at a 2 m altitude. Purple – T_shipway_v2; green – T_er_15; red – T_er_20; black – observations. The minimum and maximum downwelling longwave radiation are marked on the figure by the shaded area.

Figure 5.17 shows time-height slices of CDNC and LWC for T_shipway_v2, T_er_15 and T_er_20. Before 2145 UTC, the CDNC in T_shipway_v2 is strongest towards the top at around 80 cm^{-3}. After this time, it increases throughout the fog layer to a range between 86 and 94 cm^{-3} (Figure 5.17a). Coinciding with this is an increase in LWC from 0.2 to 0.24 g kg^{-1}, suggesting the time at which the fog began to develop and grow in optical thickness. However, an increase in r_e results in the fog layer growing in optical thickness being delayed to 2300 and 0030 UTC for T_er_15 and T_er_20 respectively. The

CDNC on average decreases for both T_er_15 and T_er_20 across the whole fog layer, with a noticeable rise at around 2300 UTC for T_er_15. Although this pattern is the same for T_er_20, there are periods where there are visible decreases in CDNC, e.g. between 0130 and 0230 UTC (Figures 5.17c and e respectively). These gaps could be due to the choice in dynamical parameters, which will be explored in Section 5.6.3.

A combination of both the CDNC and LWC decreasing results in a slower transition in the fog layer, and is shown in the downwelling longwave at 2 m (Figure 5.18). The downwelling longwave decreases by a maximum of 20 W m^{-2} between T_shipway_v2 and T_er_20, with T_er_20 undergoing the slowest rate of increase. There are differences between the observed and simulated downwelling in all three simulations, however, before 2200 UTC, T_er_20 decreases this difference to a maximum of 10 W m^{-2}.

As discussed in Chapter 4, SOCRATES calculates the longwave radiative fluxes by the cloud's optical depth, τ, (Edwards and Slingo, 1996):

$$\tau = k^{(e)} \Delta m, \tag{5.27}$$

such that Δm is the change in mass for a given spectral band and $k^{(e)}$ is the mass extinction coefficient, which is defined as:

$$k^{(e)} = L \left(a + \frac{b}{r_e} \right). \tag{5.28}$$

For Shipway_v2 scheme, both the CDNC and LWC is sensitive to r_e, given Equation's (5.27) and (5.28). This leads to a more physical representation of aerosol activation that should be considered when simulating cases of fog. These results demonstrate the importance of an accurate effective radius and will motivate future work to couple r_e to CASIM, given its impact on the fog evolution.

5.6.3 Sensitivity of Shipway_v2 to dynamical parameters

Section 5.5.1 discussed that initial fog formation potentially coinciding with the model's spin-up time may explain the behaviours in spatial visibility shown in T_Shipway_0.01.

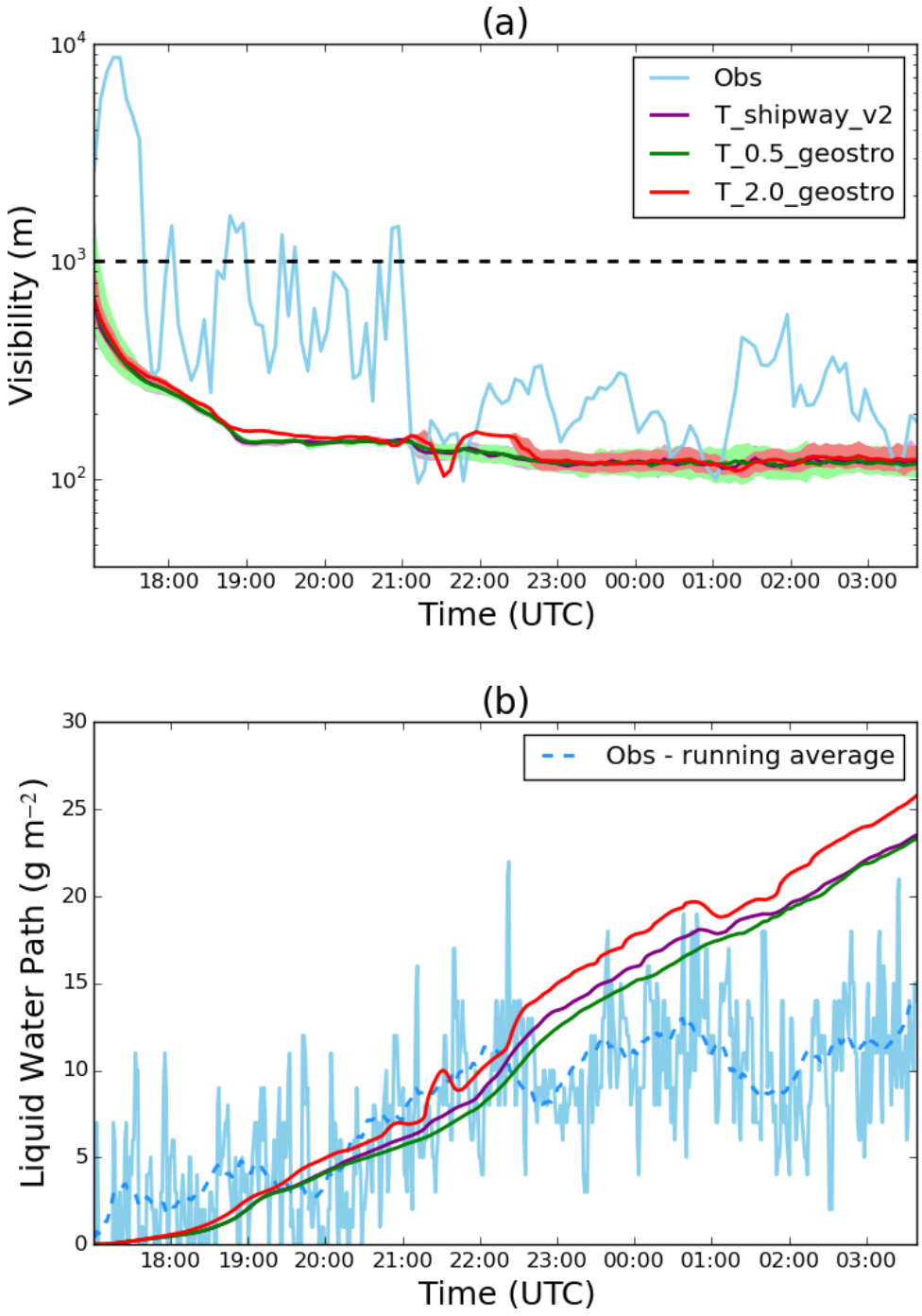

Figure 5.19: (a) - Time series of the mean visibility (m) at a 2 m altitude. Purple – T_shipway_v2; green – T_0.5_geostro; red – T_2.0_geostro; light blue – observations. Minimum and maximum visibility are marked on the figure by the shaded area. (b) - Time series of the liquid water path (g m^{-2}). Purple – T_shipway_v2; green – T_0.5_geostro; red – T_2.0_geostro; light blue – observations; blue dashed - running average over observations (40 points).

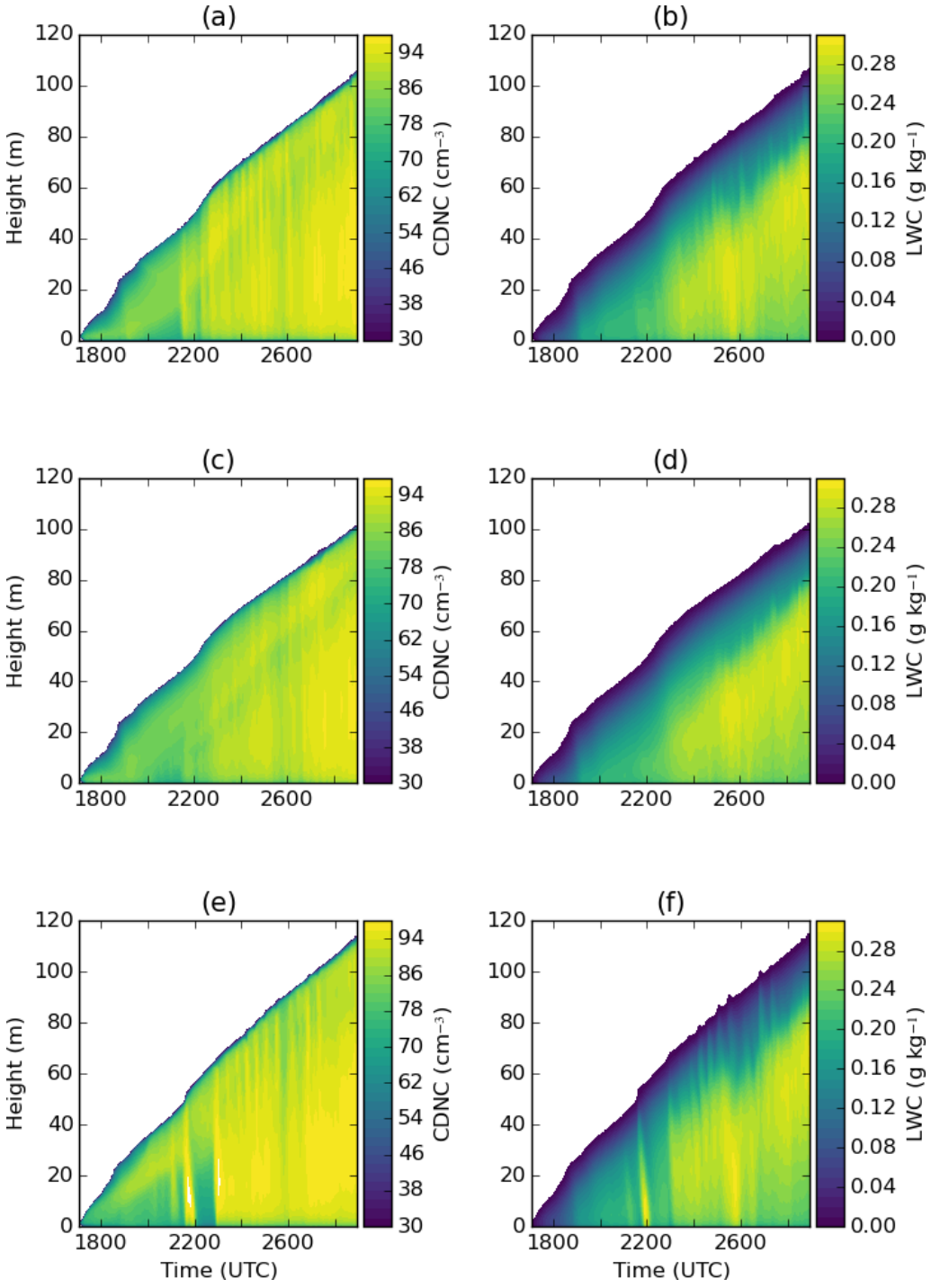

Figure 5.20: Time-height plots of (a), (c), (e) - mean LWC (g kg^{-1}) and (b), (d), (f) - mean CDNC (cm^{-3}). (a) - (b): T_shipway_v2; (c) - (d): T_0.5_geostro; (e) - (f):T_2.0_geostro.

Simulations testing the fog's sensitivity to r_e displayed sudden bursts in both the CDNC and LWC, and this may be controlled by the fog layer's turbulent mixing. Maronga and Bosveld (2017) showed that the choice in surface geostrophic winds controlled the fog's turbulent structures, and they discussed how the roughness length may control initial turbulent mixing experienced in the fog. Therefore, this section will address two objectives. The first will be to confirm whether the model's spin-up time influences fog formation of IOP1, and the second is to understand the impact that the choice of dynamical parameters has on the fog evolution using Shipway_v2.

Surface geostrophic winds

Until 1845 UTC, there is no appreciable difference in the mean near-surface visibility between T_shipway_v2, T_2.0_geostro and T_0.5_geostro (Figure 5.19a). From 1900 UTC onwards, the near-surface visibility remains the same for T_0.5_geostro and T_shipway_v2, however, T_2.0_geostro has higher near-surface visibility, most noticeable between 2100 and 2300 UTC. Coinciding with the increase of T_2.0_geostro's near-surface visibility is a sharp increase in the LWP by 4 g m^{-2} (Figure 5.19b). This result suggests that the increase in geostrophic winds results in the fog layer deepening, with a drying effect on the surface layer (see Figure 5.20). T_0.5_geostro shows the most spatial variation of the three tests before 1900 UTC; coinciding with a slight decrease in LWP before 1900 UTC and a decrease in the fog's TKE (not shown). Based on previous studies, it was predicted that a decrease in geostrophic winds would result in a decrease in spatial variation, especially during the formation stages. However, this result shows that the increase in spatial variation is not due to the change in the geostrophic wind, but instead is driven by the model's spin up period occurring during fog formation. This will be confirmed in tests that change the roughness length.

The timing of the increase in near-surface visibility during T_2.0_geostro occurs as the fog begins to become well-mixed (Figure 5.21e). Vertical motions begin growing within the fog layer, however, despite this increased motion throughout the night, there is a decrease in the fog's Ri in comparison to T_shipway_v2 (Figures 5.23a and b). Conversely,

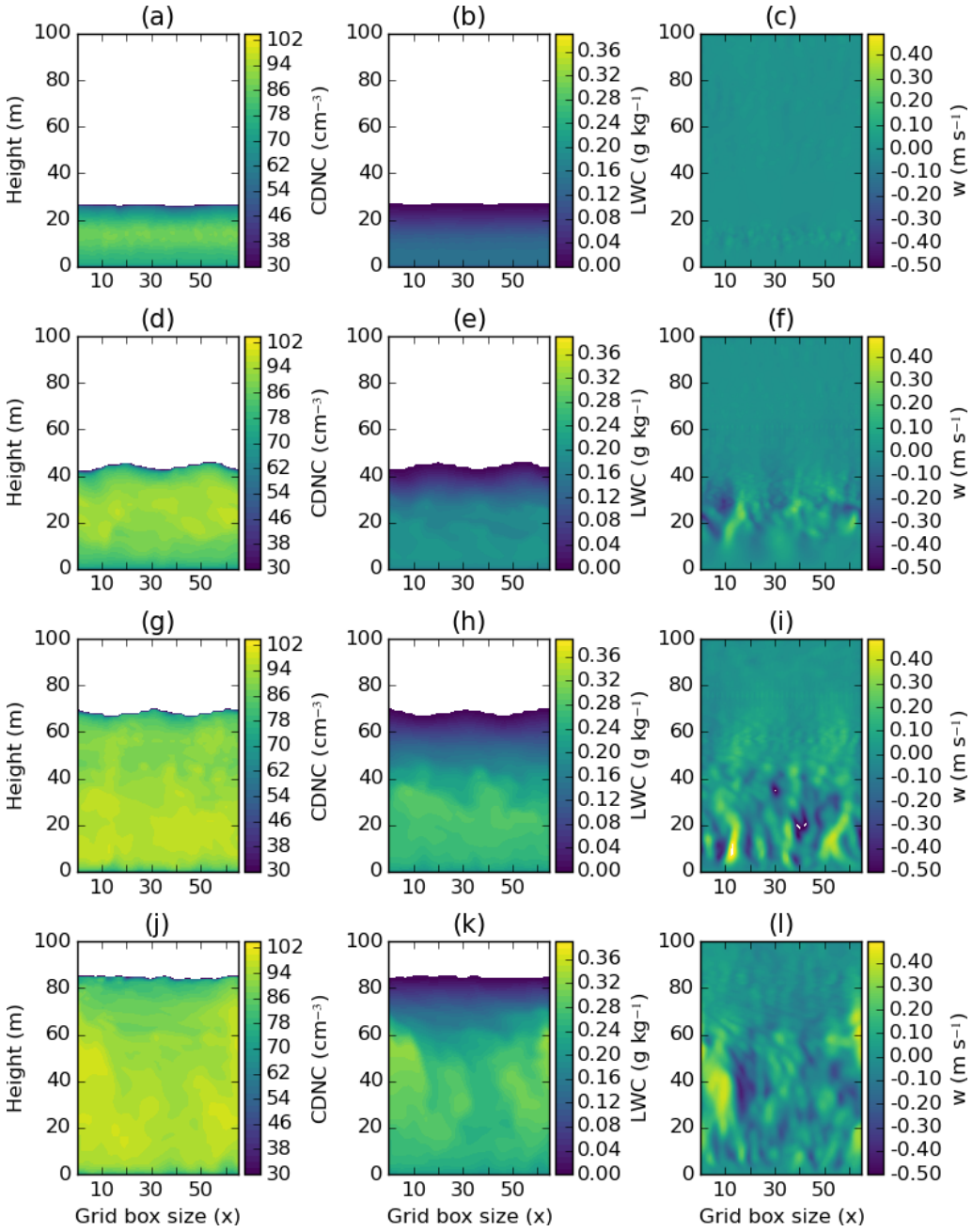

Figure 5.21: Contour slices at y = 66 m of (a) - CDNC (cm^{-3}), (b) - LWC ($g\ kg^{-1}$) and (c) - Vertical motion ($m\ s^{-1}$) at 1900 UTC during T_2.0_geostro. Sub-figures (d)-(f): 2100 UTC; (g)-(i): 2300 UTC; (g)-(i): 0100 UTC.

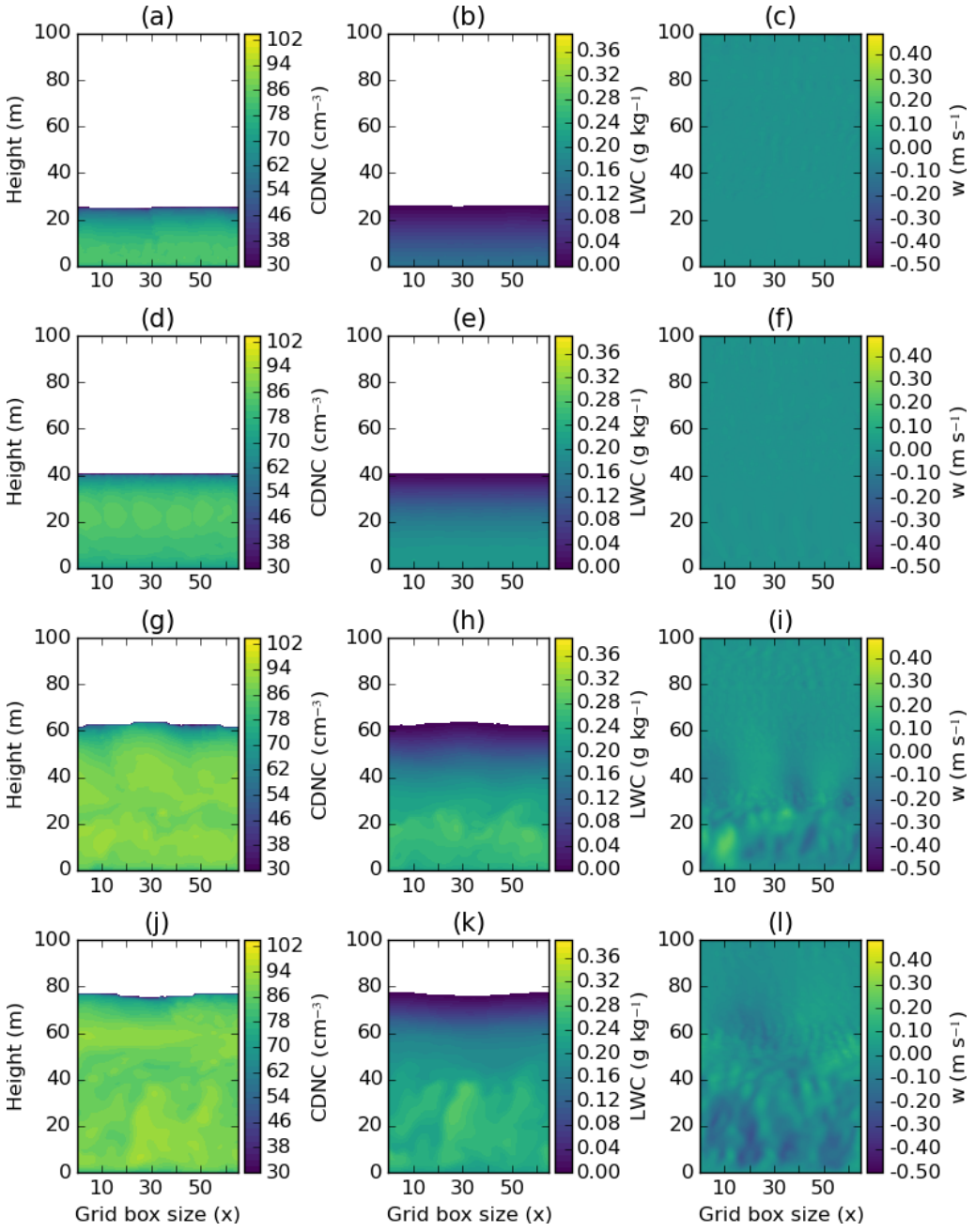

Figure 5.22: Same as Figure 5.21 but for T_0.5_geostro.

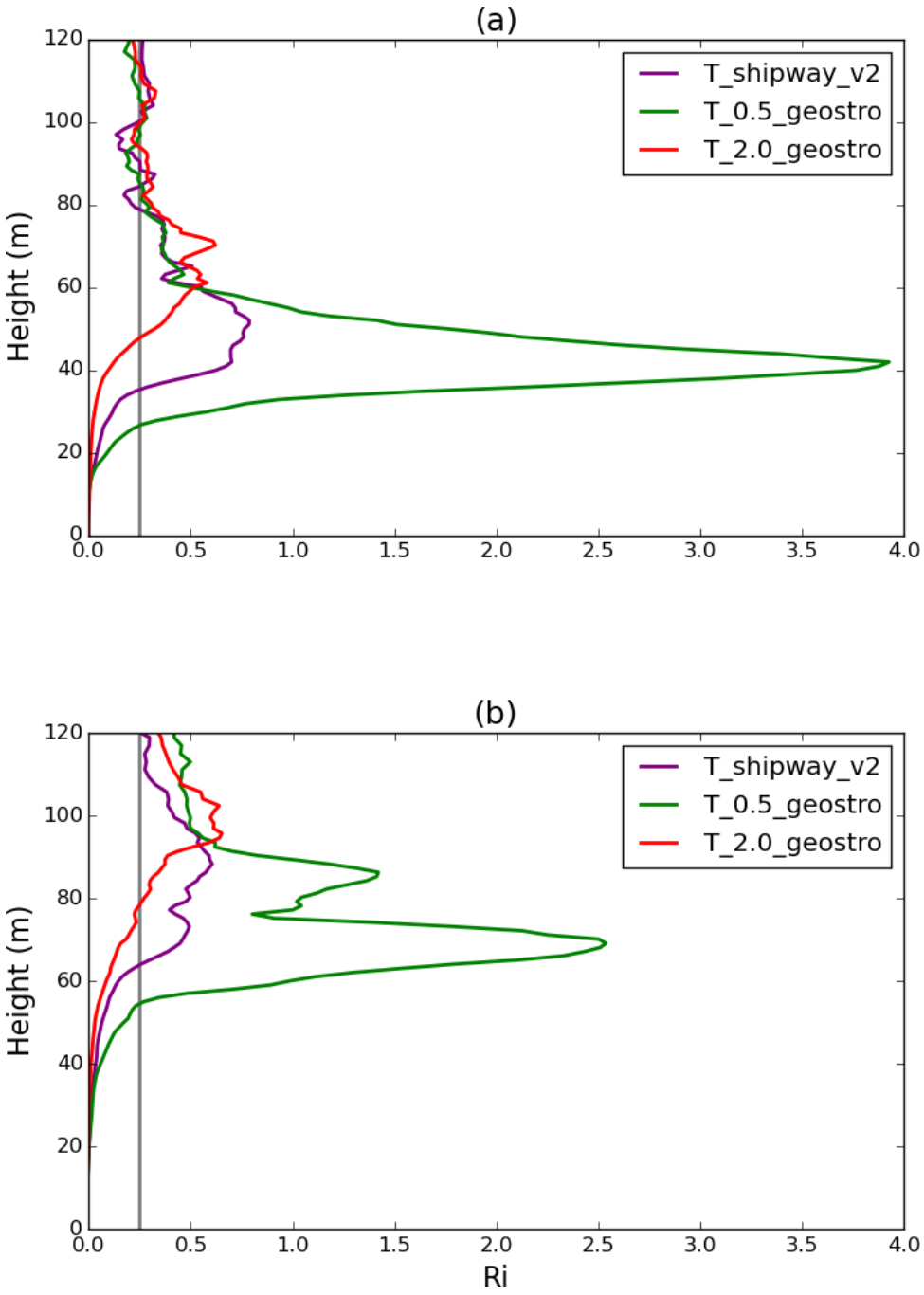

Figure 5.23: Vertical profiles of the Richardson number at (a) - 2300 and (b) - 0100 UTC. Purple – T_shipway_v2; green – T_0.5_geostro; red - T_2.0_geostro.

decreasing the geostrophic winds in T_0.5_geostro results in a $Ri > 1$, demonstrating that convection is the dominant turbulent process. However, both the timing of the fog becoming well-mixed is delayed, in addition to the strength in vertical motions decreasing during T_0.5_geostro (Figure 5.22). Therefore, this confirms that the change in geostrophic winds will impact the levels of wind shear experienced in the fog layer, with the decrease in shear resulting in the fog becoming less turbulent.

Roughness length for momentum

The roughness length, z_0 has been shown to impact the fog evolution, where its increase can result in TKE rising by up to a factor of 6 near the surface (Bergot et al., 2015). However, upon changing z_0, there was no impact to the fog's evolution (Figure 5.24). A reason for this is because the terrain where IOP1 formed is relatively flat, and experienced low winds. Given this result, it seems likely that the fog formation is being influenced by the model's spin-up period.

5.7 Discussion

The key findings presented in this chapter will now be discussed. The objective of this work investigated how the representation of aerosol activation influenced simulations of nocturnal radiation fog. There was a strong focus in critiquing the assumptions used in several aerosol activation schemes used in fog, which are usually designed for clouds that are driven by adiabatic ascent. This work utilised the Shipway (2015) activation scheme, as it was shown to better calculate the change in supersaturation, i.e. CCN < 100 cm^{-3}. For this work, four research questions were addressed.

1. In what ways can the standard method of cooling be used in Shipway, be replaced to be suitable for the modelling of fog?

For this work, a new derivation was presented to be used in the Shipway_v2 scheme, that accounts for a non-adiabatic cooling source. As this source is assumed to be isobaric,

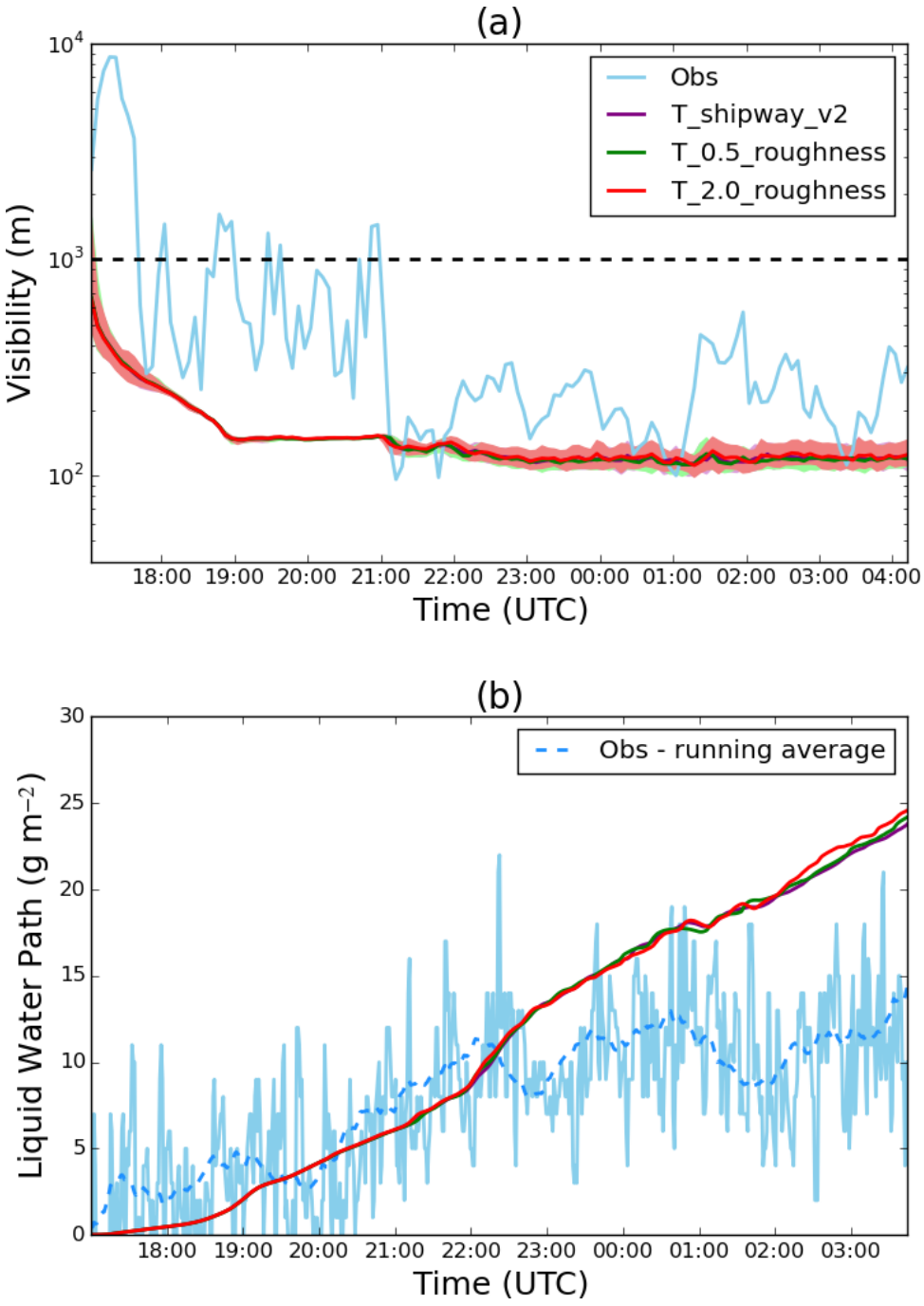

Figure 5.24: (a) - Time series of the mean visibility (m) at a 2 m altitude. Purple – T_shipway_v2; green – T_0.5_roughness; red – T_2.0_roughness; light blue – observations. Minimum and maximum visibility are marked on the figure by the shaded area. (b) - Time series of the liquid water path (g m^{-2}). Purple – T_shipway_v2; green – T_0.5_roughness; red – T_2.0_roughness; light blue – observations; blue dashed - running average over observations (40 points).

the change in pressure is equal to zero and resulted in a new term being required for the change in supersaturation. However, the removal of this pressure term meant that using an aerosol activation scheme that assumes just adiabatic ascent may underestimate N_a by 20% in an environment driven by non-adiabatic cooling processes (i.e. fog formation). The Shipway_v2 scheme was compared to Shipway using an adiabatic setup in an offline box model and there were no differences between the change in supersaturation and N_a, demonstrating that the adiabatic pathway was set up correctly. However, this test also highlighted that Aitken mode aerosol can be ignored when modelling activation in fog, as the required environmental supersaturation for impact is substantially higher than supersaturation's seen in reality.

2. What are the potential differences when comparing the default setup of the Shipway to the Shipway_v2 scheme?

The assumptions used in the Shipway (2015) scheme to date, i.e. the use of just an updraft velocity and a w_{min}, were tested against the Shipway_v2 scheme in an offline box model. For accumulation mode aerosol, there were noticeable percentage differences between the actual cooling rate and the use of a w_{min} to equal 0.1 m s^{-1} by up to 70%, as the environment becomes more polluted. In addition, representing non-adiabatic cooling using just an adiabatic framework could result in an underestimation in N_a by up to 20%. Consequently, both of these results show that the aerosol indirect effects may not be properly accounted for in simulations of fog when using a traditional aerosol activation scheme. For coarse mode aerosol, although there were some slight percentage differences with the use of a w_{min}, these were a lot smaller in comparison to the accumulation mode.

3. How well does the Shipway Scheme in MONC simulate IOP1, and does the reduction in the minimum vertical velocity threshold impact the fog evolution?

The Shipway (2015) activation scheme was used to test the impact w_{min} could have on simulating fog. It was shown that a reduction in w_{min} lowered the initial CDNC during formation, resulting in the fog undergoing a slower transition to a well-mixed layer. Al-

though initially it was assumed that the decrease in turbulence in the layer was due to a decrease in convection, it was shown that the decrease in fog turbulence was a reduction in the strength of induced KH instabilities. Reducing w_{min} to 0.01 m s^{-1} displayed some unusual model behaviours during fog formation, and it was confirmed that this was likely caused by the model's spin-up period, rather than a choice in dynamical parameters. However, the only way to confirm this is to initialise the model earlier, which is not possible with the given radiosonde data from IOP1.

4. How well does the Shipway_v2 scheme simulate IOP1, and how is the scheme sensitive to changes in dynamical and radiative parameters?

The fourth objective discussed the implementation of the Shipway_v2 scheme in MONC and how it could be a suitable alternative to represent aerosol activation in fog. Upon initial analysis, there was not an improved performance using the Shipway_v2 scheme against the Shipway scheme with an applied w_{min} of 0.1 m s^{-1}. However, it was shown that the cause of this result was due to r_e not reflecting the change in CDNC. When r_e was increased from 10 to 20 μm, the result was a slower transition to a well-mixed layer, which was more in line with observations of IOP1. When investigating how the choice in dynamical parameters may impact the performance of Shipway_v2 scheme, increasing the geostrophic winds corresponded in an increase in wind shear, causing the fog layer to become well-mixed quicker. However, changing the roughness length for momentum made no impact on the modelled fog evolution. The suggestion as to why this was the case was that the observed winds were relatively low for IOP1, meaning that shear at the surface was minimal and hence a change in roughness length leads to minimal impact.

5.8 Conclusion

The work in this chapter has shown the unsuitably of using an aerosol activation scheme designed for cloud formation through convection. This complements previous studies such as Schwenkel and Maronga (2019), who have shown how the choice in aerosol activation

scheme impacts the fog evolution through a change in the CDNC. However, by designing a scheme that is also dependent on a non-adiabatic cooling source, the results in this chapter have demonstrated the importance of aerosol activation representation when trying to accurately capture the fog's transition period to a well-mixed layer. Previous studies (e.g. Mazoyer et al., 2017) have investigated the fog evolution while accounting for a radiative cooling tendency in the change in supersaturation. However, this is the first study that has investigated the change in cooling due to non-adiabatic processes in a clean aerosol regime, making it beneficial in aiding the understanding the impact of aerosol-fog interactions during nocturnal radiation fog. Work to develop the Shipway_v2 scheme is still ongoing and will include accounting for additional non-adiabatic processes such as turbulent mixing. By completing this future work, it could be easier to incorporate the Shipway_v2 scheme into a model such as an NWP. This is because the non-adiabatic process would be a change in temperature within the grid box, rather than requiring an explicit additional term. The effective radius was shown to be sensitive in Shipway_v2 especially when considering the decrease in CDNC. Therefore, future work to couple r_e to CASIM will be conducted, and this coupling will be tested using the new scheme. Furthermore, although not investigated within this work, another source of error with regards to aerosol activation is measurement data of aerosol concentrations. It is very difficult to simultaneously constrain the collection of aerosol measurements alongside cloud droplet measurements. Given the sensitivity on the minimum threshold with regards to aerosol concentration, this is another area of further work.

As a wider implication, aerosol-cloud interactions are a big source of uncertainty when modelling atmospheric processes, both within forecasting (NWP) and climate (GCM) models and the choice of aerosol activation can influence how big this uncertainty is. Typically, the resolution of NWP and GCM model simulations is relatively coarse to LES, meaning that any present updraft velocities are usually subgrid and hence cannot be resolved. To represent aerosol activation on a subgrid level, the vertical velocity is either in the form a characteristic vertical velocity (e.g. Ghan et al., 1997) or a PDF function based on the vertical velocity (e.g. West et al., 2014). More recently, authors such as Malavelle

et al. (2014) discussed methods to account for subgrid velocities used in aerosol activation in convection-permitting models. These methods utilise a w_{min}, however, this should be lowered systematically for future work regarding aerosol activation in fog based on this work. Although gaining measurements of vertical velocity PDFs could be difficult in fog, the results presented in this chapter could provide a useful framework to estimate what the variation in vertical velocities in fog could be, therefore providing a good estimation of the types of distributions that best match these velocities. Finally, to have a full cooling term applied in an NWP, it is important to know how these vertical velocities correlate with the changes in non-adiabatic cooling.

The method being presented in this work is computationally efficient and provided an additional level of flexibility consider different cooling sources, should an updraft not be available. Given this flexibility, this will allow the Shipway_v2 scheme to undergo further testing in both high resolution and NWP models. Whilst this has been tested in only the Shipway and Shipway_v2 activation schemes, the framework for a change in supersaturation is generic enough for it to be applied to other activation schemes too.

Chapter 6

Aerosol removal in radiation fog: does it matter?

6.1 Introduction

Section 2.2.1 of Chapter 2 outlined that nucleation scavenging is an important process in fog. As nucleation scavenging depletes the source of aerosol from the fog's environment, it can potentially change the impact on fog development (Fuzzi, 1992). Nucleation scavenging has been shown to influence the cloud's life span in different aerosol regimes and may apply to fog. For example, Mauritsen et al. (2011) concluded that in CCN-repressed regimes in the Arctic, cloud's may be unable to develop, as droplets that do form sediment out too quickly and cannot grow in optical depth. Therefore, considering nucleation scavenging when modelling aerosol-cloud interactions (for this case fog) is crucial in understanding the extent that the fog evolution is sensitive to properties of the aerosol population.

There have been studies that model nucleation scavenging in fog. For example, Bott et al. (1990) utilised a droplet growth equation method to calculate CDNC, while Boutle et al. (2018) had a prognostic variable for supersaturation coupled with a bin microphysics scheme to calculate CDNC. Both of these schemes assume that both the aerosol and cloud

drop size distributions evolve, whereby aerosol that grew past a certain size through condensation would be considered a cloud droplet. However, although both of these methods consider the physics of nucleation scavenging in fog, they are computationally expensive, especially for inclusion in operational NWP models. More recently, work has begun to include a suitable parameterisation of nucleation scavenging in bulk microphysics schemes (e.g. Lebo and Morrison, 2013), with development still ongoing. Although there have been studies using a parameterisation of nucleation scavenging in cloud development, (e.g. Miltenberger et al., 2018), to date, there are no studies that have investigated the use of a nucleation scavenging parameterisation in fog using a bulk microphysics scheme.

This chapter aims to understand the role of nucleation scavenging in simulations of fog, and how to best adapt the parameters that influence fog microphysics should scavenging be turned on. Impaction scavenging; the collision of aerosol particles with fog droplets, will not be considered in this chapter. Although impaction scavenging can occur in fog, it has been shown to have little effect as a source of aerosol depletion during a fog episode (Gilardoni et al., 2014). Therefore, turning it off will enable scavenging effects to be examined at a reduced computational expense. This work will utilise CASIM, which can represent in-cloud aerosol removal and has been used previously to study scavenging in clouds (e.g. Miltenberger et al., 2018). As nucleation scavenging will result in the reduction of aerosol that can activate into droplets, there is a possibility that there may not be enough aerosol available to let the fog develop in optical thickness. Therefore, this chapter will present a method to add an additional aerosol source in these simulations, to prevent complete depletion. Three research questions will be addressed:

1. How does nucleation scavenging influence the fog evolution in MONC, when combined with processes such as sedimentation and cloud-radiation interactions?

2. How do properties that control fog microphysics such as CCN concentration influence the effects of nucleation scavenging on the fog evolution?

3. Does the inclusion of an aerosol source through advection improve the model's fog evolution when compared to observations of IOP1?

Test	Sedimentation	Cloud interaction	Processing
T_control	x	x	x
T_off			
T_sedimentation	x		
T_cloud		x	
T_processing			x
T_cloud_processing		x	x
T_sedimentation_processing	x		x

Table 6.1: A list of tests referred to understanding the impact of nucleation scavenging in simulations of fog. Processing - nucleation scavenging; Cloud - cloud top flux; sedimentation - droplet sedimentation.

Section 6.2 will described the model setup, and each research question will be addressed in Section's 6.3, 6.4 and 6.5. A discussion and conclusion will follow.

6.2 Model setup

MONC coupled with CASIM is used to perform a suite of sensitivity tests based on IOP1, using the same base configuration described in Chapter 4. The aerosol activation scheme used in these simulations is that of Abdul-Razzak and Ghan (2000), which uses an average CCN size that is determined by the total soluble mass, the CCN number concentration and an assumed aerosol size distribution. CASIM has the option to include in-cloud aerosol removal, a feature that has been used to investigate aerosol perturbations during the development of mixed-phased clouds (Miltenberger et al., 2018). In this chapter, only in-cloud aerosol removal through nucleation scavenging is considered when aerosol processing is turned on.

Results from Chapters 4 and 5 have shown sedimentation and the cloud top flux influencing fog formation and development. As this is the first study investigating the impact of using a parameterisation of nucleation scavenging on fog, a range of tests have

been setup that turns nucleation scavenging on and off in conjunction with a cloud top flux and sedimentation (Table 6.1). For reference, tests that turn off the cloud top flux (cloud-radiation interactions) are only considering a clear sky cooling. The outcome of these results will motivate further sensitivity tests conducted in this chapter. A value of 100 cm^{-3} in the accumulation mode was set for these tests, with a total soluble mass of 2.7 ng throughout the initialised vertical profile and a standard deviation of $\sigma = 2.0$, based on environmental conditions found at Cardington (Boutle et al., 2018).

6.3 Nucleation scavenging in MONC

6.3.1 Nucleation scavenging without sedimentation and cloud-radiation interactions

The near-surface visibility at 2 m indicates fog formation at 1700 UTC in T_off, with the near-surface visibility decreasing to around 100 m at 0300 UTC (Figure 6.1a). For all model simulations, the near-surface visibility is calculated using the formula of Gultepe et al. (2006), where near-surface visibility, Vis, is defined as follows:

$$Vis = \frac{1.002}{(LWC \times CDNC)^{0.6473}}. \tag{6.1}$$

There is minimal variation between the minimum and maximum near-surface visibility throughout the night, suggesting the presence of a non-turbulent boundary layer and a spatially homogeneous fog. In comparison, fog forms at 1715 UTC in T_processing, and the near-surface visibility decreases to 186 m at about 0300 UTC. However, whilst there is an increase in near-surface visibility during T_processing, the mean LWP shows no difference between T_off and T_processing (Figure 6.1b). As the fixed effective radius is the same in both tests, without sedimentation, the liquid water will not change. The mean LWP in both tests T_off and T_processing monotonically increases throughout the night and reaches a maximum of 30 g m^{-2}. Between 1700 and 2200 UTC, the simulated and observed mean LWP agree well, but after this time, the simulated LWP is higher than observations by up to 18 g m^{-2}.

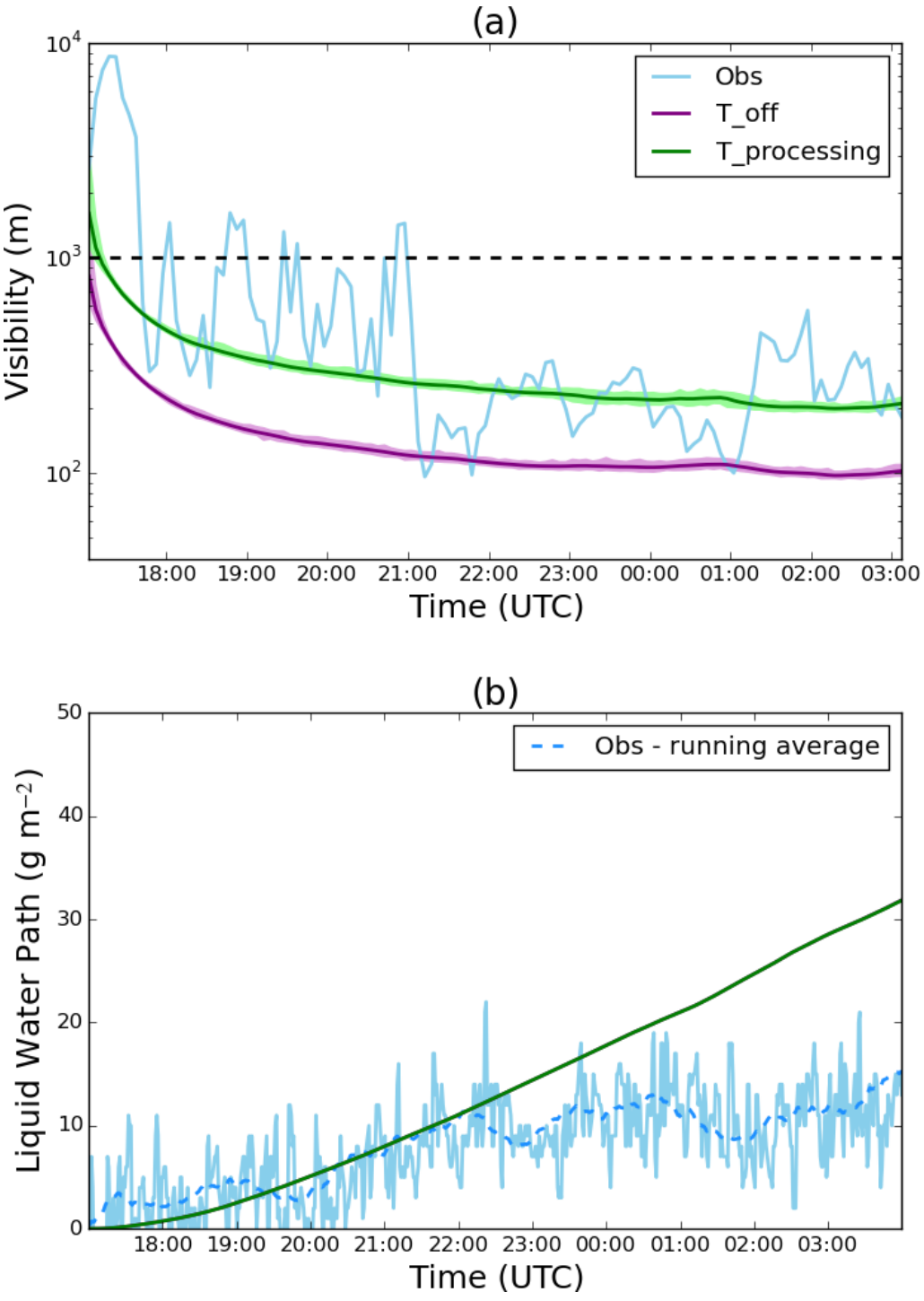

Figure 6.1: (a) - Time series of the mean visibility (m) at a 2 m altitude. Purple - T_off; green - T_processing; light blue - observations. Minimum and maximum visibility are marked on the figure by the shaded area. (b) - Time series of the liquid water path (g m^{-2}). Purple - T_off; green - T_processing; light blue - observations; blue dashed - running average over observations (40 points).

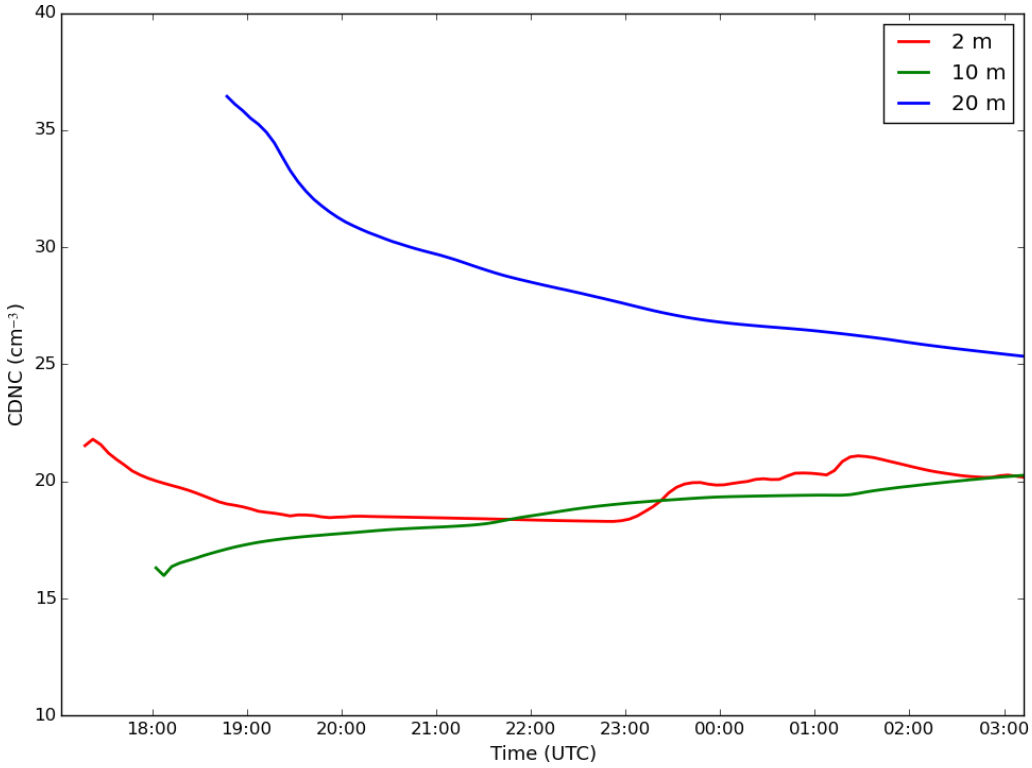

Figure 6.2: Time series of the cloud droplet number concentration (CDNC; cm^{-3}) at altitudes of 2, 10 and 20 m for test T_processing. Red - 2 m; green - 10 m; blue - 20 m.

Since the LWP between T_off and T_processing shows no difference, the increase in near-surface visibility during T_processing is due to a decrease in CDNC, given Equation (6.1) (Figure 6.1b). Throughout the night, the CDNC in T_off has a fixed value of 61 cm^{-3} (not shown). Since cloud-radiation interactions are turned off, the rate of cooling is strongest at the surface and not the fog top. Consequently, a convective instability will not occur and allow for updrafts strong enough to create new droplets (as discussed in Mazoyer et al., 2017). The CDNC is bounded between 16 to 22 cm^{-3} in T_processing at heights 2 and 10 m throughout the simulation, and at 20 m, the CDNC initially begins at 37 cm^{-3}; gradually decreasing to 25 cm^{-3} at 0300 UTC (Figure 6.2). Therefore, these initial tests show that nucleation scavenging results in a decrease in CDNC, due to both aerosol number and mass being depleted as droplets form using CASIM (not shown) and hence less aerosol is available to form new droplets.

6.3.2 Nucleation scavenging coupled with cloud-radiation interactions only

Accounting for just cloud-radiation interactions (T_cloud) results is the deepening of the fog layer, and an increase in LWP (Figures 6.3a and b). Between T_off and T_cloud, the mean 2 m visibility decreases by a maximum of 300 m, and the LWP increases by a maximum factor of 19. The increase in near-surface visibility and LWP in T_cloud is due to the cooling at the fog top being stronger than at the surface as it grows in optical depth. This results in a stronger rate of liquid water production and hence the growth in the fog layer. The cooler air at the top of the fog triggers a convective instability, causing liquid water to sink into the fog layer, and rising the near-surface visibility.

Accounting for nucleation scavenging (T_cloud_processing) leads to a thinner fog layer in comparison to that produced in T_cloud, with an increase in the mean near-surface visibility by a maximum of 230 m (Figure 6.3a). From 1800 UTC, there is an increase in the spatial variation in near-surface visibility in both T_cloud and T_cloud_processing, which is indicative of a more turbulent boundary layer, signalling a more inhomogeneous (well-mixed) fog. There is a small difference in LWP between T_cloud and T_cloud_processing,

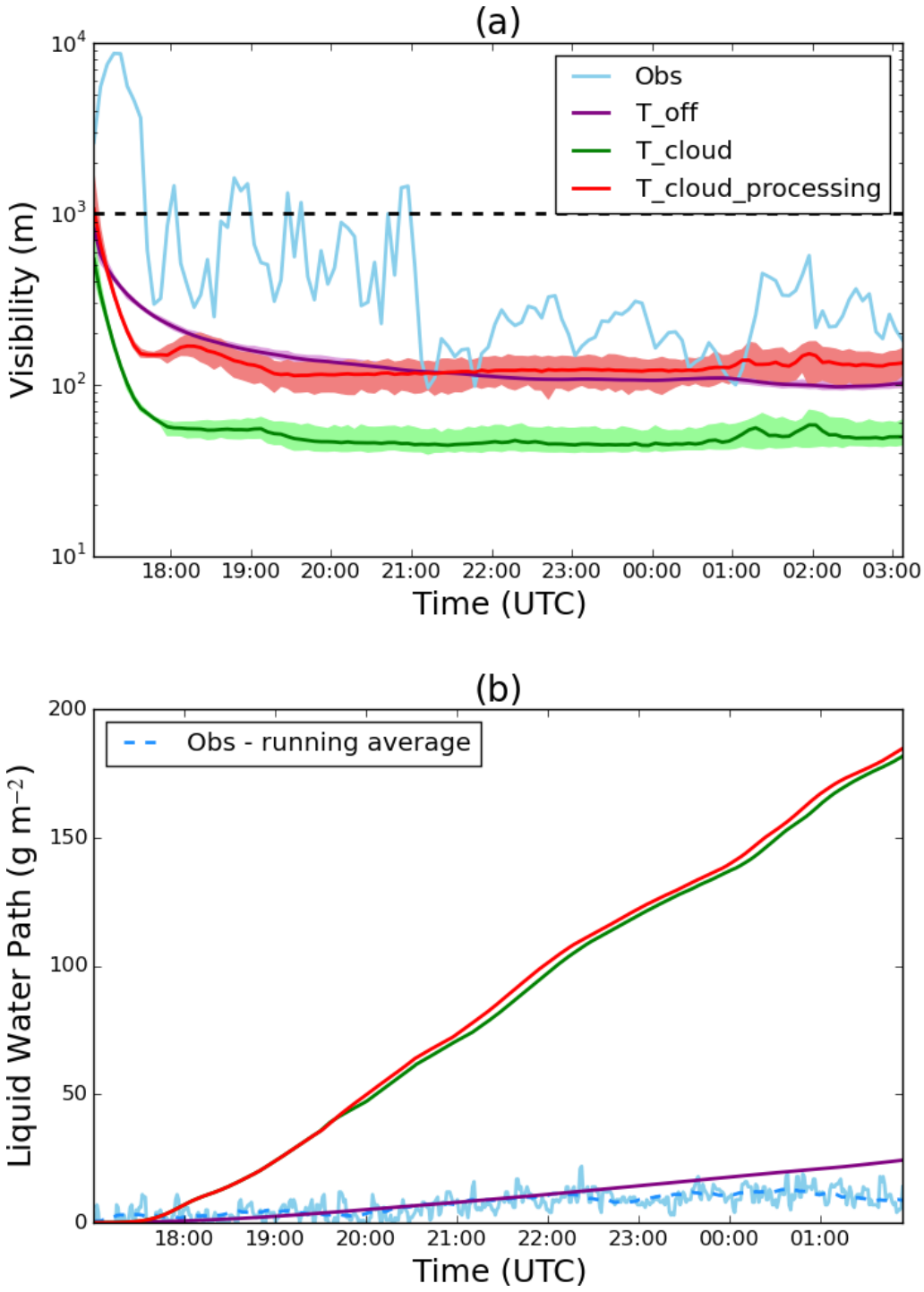

Figure 6.3: (a) - Time series of the mean visibility (m) at a 2 m altitude. Purple – T_off; green – T_cloud; red – T_cloud_processing; light blue - observations. Minimum and maximum visibility are marked on the figure by the shaded area. (b) - Time series of the liquid water path (g m^{-2}). Purple – T_off; green – T_cloud; red – T_cloud_processing; light blue - observations; blue dashed - running average over observations (40 points).

with a maximum percentage difference of 5.1% at 0030 UTC (Figure 6.3b). Given that both tests were setup with the same fixed r_e and ran over the same number of processors, a suggestion for this result is due to the differences in turbulent structures, which therefore may impact the liquid water evolution. To understand whether this may be the reason, contour slices of LWC, CDNC and vertical motion were taken throughout the night for T_cloud and T_cloud_processing (Figures 6.4 and 6.5).

At 1900 UTC, the fog layer in T_cloud grows to a height of 27 m, with the LWC being strongest towards the fog top (1.4 g kg^{-1}; Figure 6.4b). This signals that the cooling rate is greater at the fog top than at the surface, and this cool air will experience negative buoyancy, triggering convection in the fog layer and hence vertical air motions. For this example, T_cloud has updrafts and downdrafts between -0.1 and 0.2 m s^{-1} (Figure 6.4a), with updrafts strong enough to form new droplets in the fog layer (Figure 6.4c). At 2100 UTC, the fog layer grows to a height of 50 m, with some waves at the fog top, a signal of eddies beginning to form (Figure 6.4e). The fog begins transitioning to a well-mixed layer, indicated by the vertical motions increase in strength, ranging between -0.3 and 0.3 m s^{-1} (Figure 6.4f). Finally, at 2100 UTC, the fog layer is a height of 82 m and the LWC being greatest at the top with a value of 1.7 g kg^{-1} (Figure 6.4h). The rate of growth in the fog depth between 1900 and 2300 UTC continually increases, due to the increase in vertical motion strength, which range between -0.6 and 0.7 m s^{-1} (Figure 6.4i). The increased vertical motion lets the fog become well-mixed, as seen in the homogenised CDNC (range between 81 to 83 cm^{-3}; Figure 6.4i) and LWC.

Although the fog evolution is similar for T_cloud_processing, there are some subtle differences between the vertical motion structures between T_cloud and T_cloud_processing. For example, T_cloud_processing shows stronger updrafts than T_cloud throughout the vertical domain at 2100 UTC (Figure's 6.4f and 6.5f); the time after the LWP in T_cloud and T_cloud_processing began to diverge in Figure 6.3b. The CDNC is relatively smaller in T_cloud_processing in comparison to T_cloud (Figure's 6.4d and 6.5d), however, it does not alter the radiative impact of the fog layer, due to sedimentation being turned off. For context, the strength of updrafts experienced in both tests is similar to what is observed in

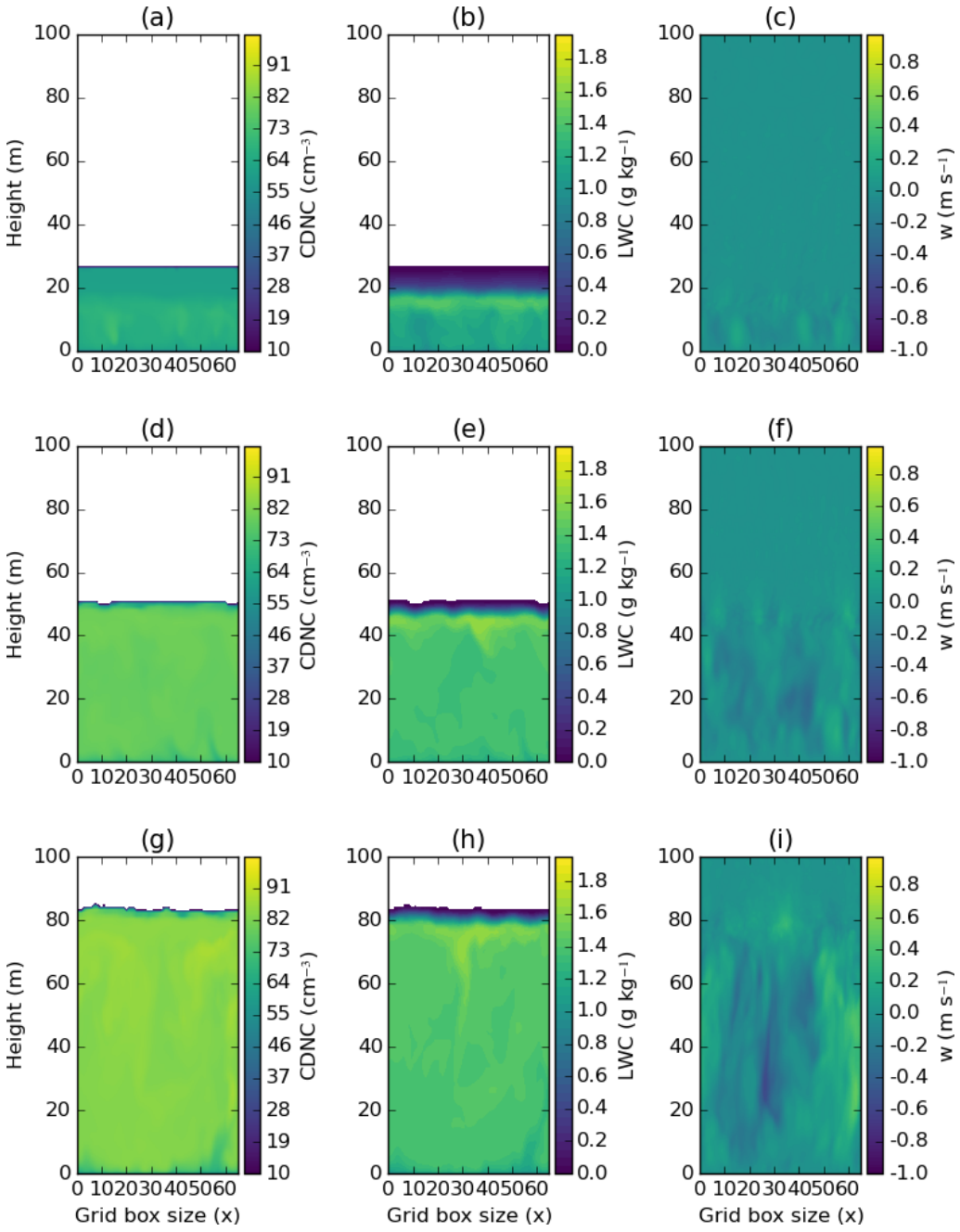

Figure 6.4: Contour slices at y = 66 m of (a) - CDNC (cm^{-3}), (b) - LWC ($g\ kg^{-1}$) and (c) - Vertical motion ($m\ s^{-1}$) at 1900 UTC during T_cloud. Sub-figures (d)-(f): 2100 UTC, (g)-(i): 2300 UTC.

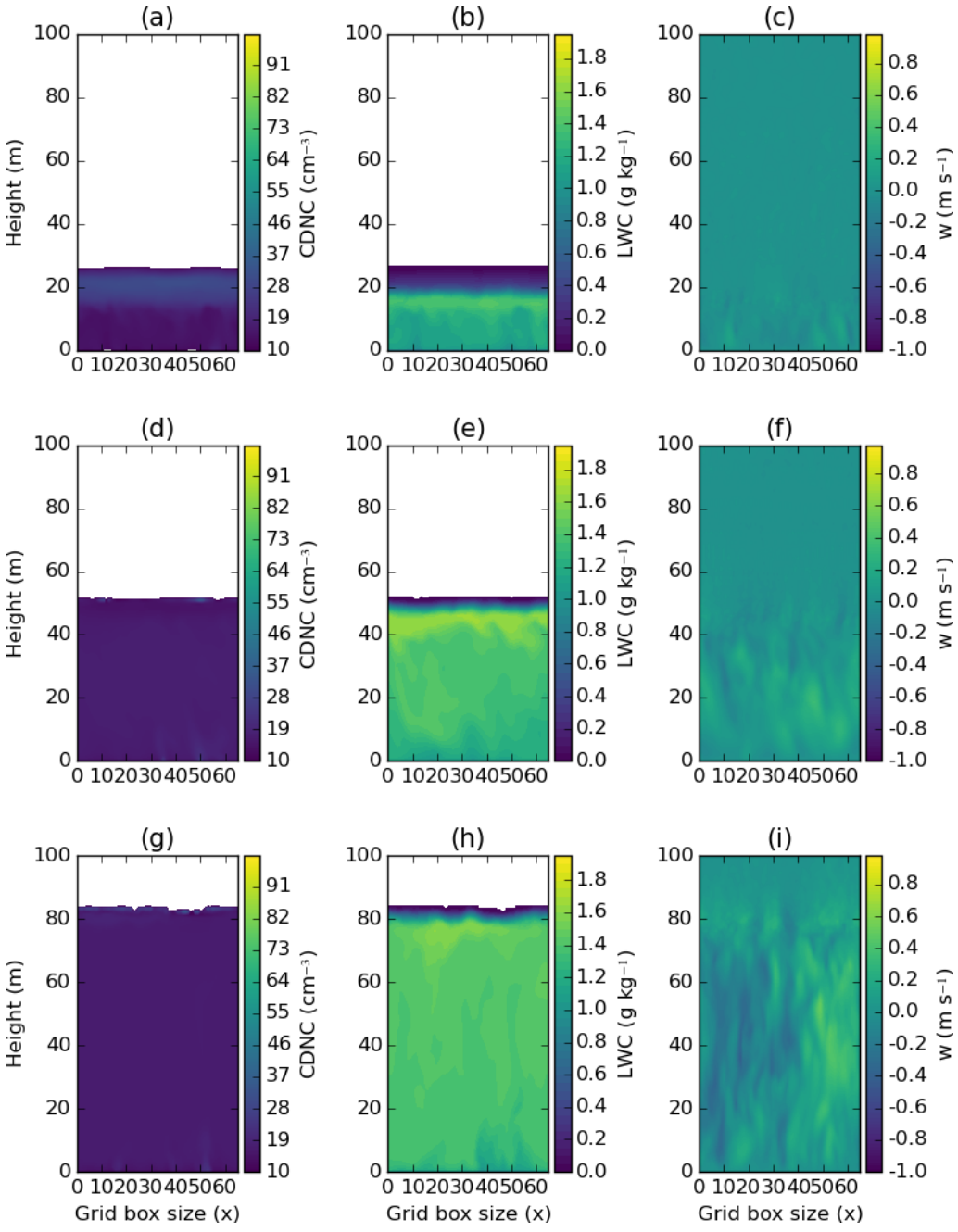

Figure 6.5: Same as Figure 6.4, but instead for T_cloud_processing.

a stratocumulus cloud (Wood, 2012), where the grid box size is important to resolve this motion. However, it is more likely that the differences in liquid water are due to rounding errors being slightly different between T_cloud and T_cloud_processing.

Figure 6.6 shows time series of CDNC and CDNC mean droplet size during tests T_off, T_cloud and T_cloud_processing. As the rate of liquid water production was relatively high for T_cloud and T_cloud_processing, when compared to T_off, this highlights the unsuitability in the choice of r_e for cases for nucleation scavenging. At all heights, T_off has an average droplet radius between 12 to 15 μm, with T_cloud and T_cloud_processing having an average radius of 17 and 27 μm respectively (Figures 6.6b, d and f). The average droplet size in all tests is greater than $r_e = 10$ μm, signalling that the rate of radiative cooling at the fog top is too strong. This may be important for nucleation scavenging representation when cloud-radiation interactions are accounted for.

6.3.3 Nucleation scavenging coupled with sedimentation only

Previous studies (e.g. Zhang et al., 2014) have shown the importance of sedimentation in modelling fog, and that it is required to produce sensible levels of liquid water shown in observations (such as Roach et al., 1976). The inclusion of sedimentation (T_sedimentation) results in the formation of a thinner fog compared to T_off, shown by the larger value of the near-surface visibility (Figure 6.7a). Between 1700 and 2100 UTC, the mean near-surface visibility during T_sedimentation agrees well with observations, and after 2100 UTC, the modelled near-surface visibility eventually decreases to around 375 m. In addition, the mean LWP decreases by a factor of 10 at its maximum between T_off and T_sedimentation, and is lower than the observed mean LWP by a factor of 5 (Figure 6.7b). Although it appears that T_sedimentation results in a better agreement with the observed near-surface visibility, this is due to a high CDNC being calculated (as discussed in Chapter 4 and 5) alongside a much lower LWC, therefore resulting in an inaccurate representation of the fog evolution.

The inclusion of both sedimentation and nucleation scavenging results in the fog layer being unable to develop (Figure 6.7a). Between 1700 and 1900 UTC, the near-surface

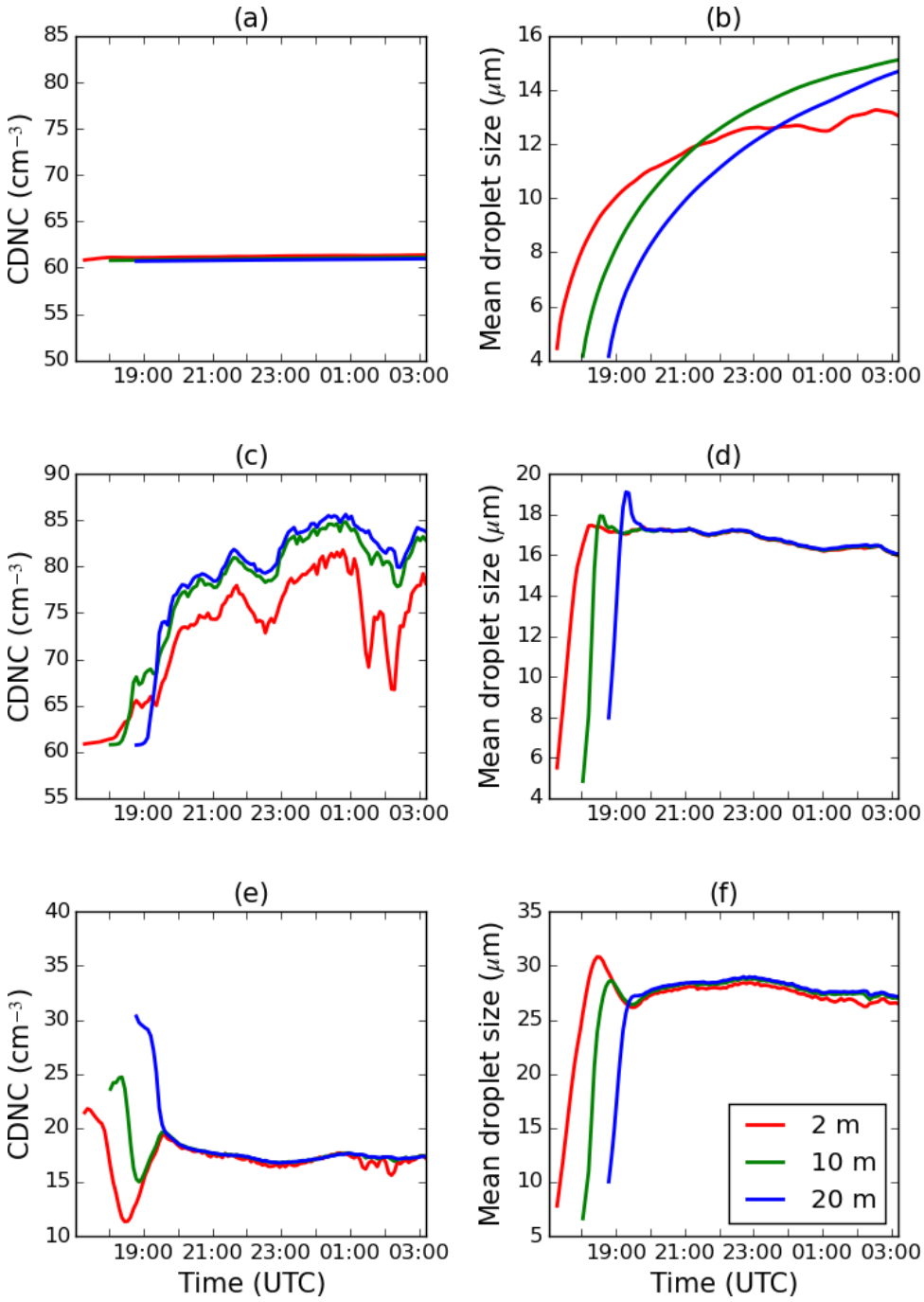

Figure 6.6: Time series of CDNC (a) and mean droplet size (b) at altitudes of 2, 10 and 20 m during T_off. (c) and (d): T_cloud; (e) and (f): T_cloud_processing.

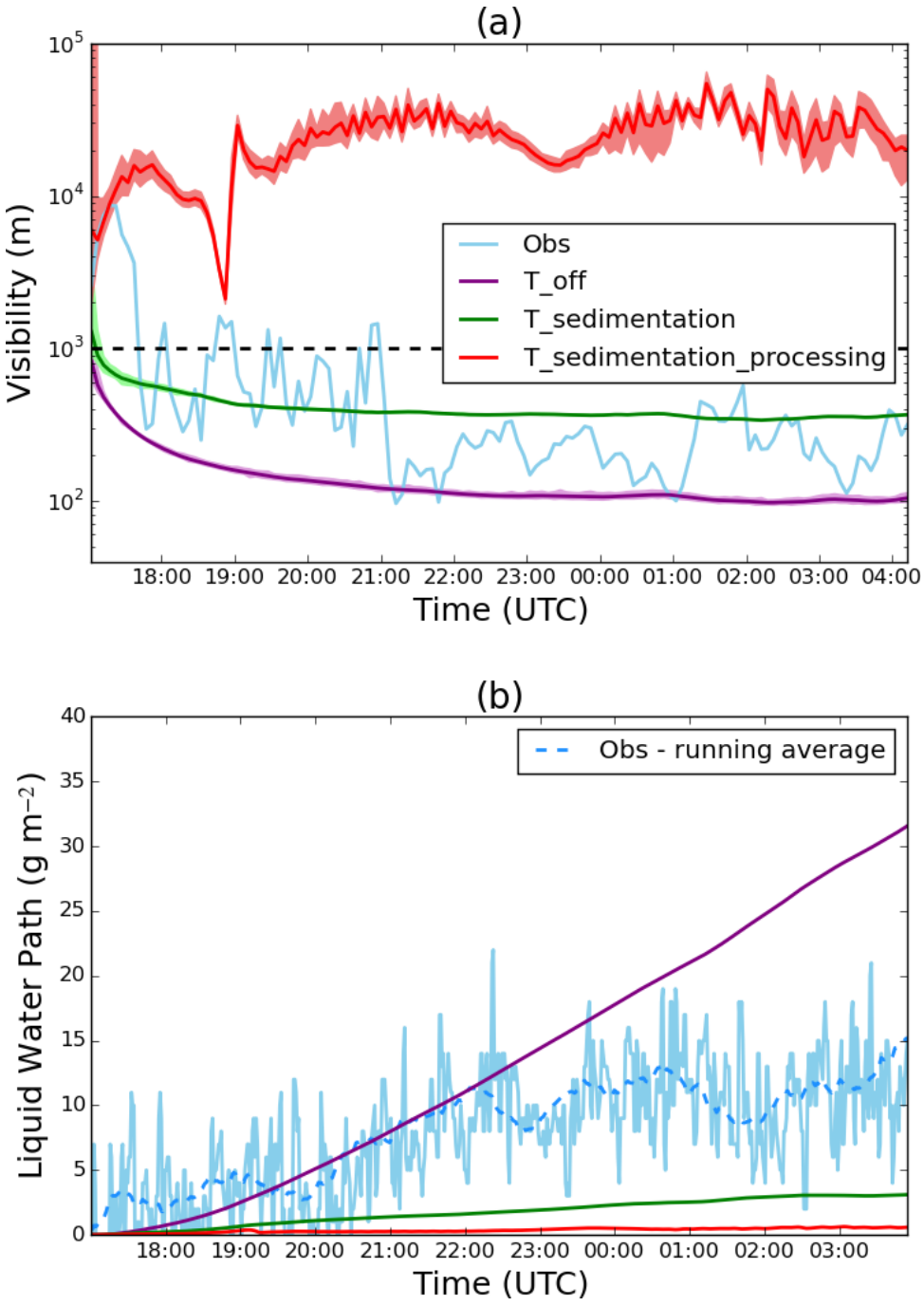

Figure 6.7: (a) - Time series of the mean visibility (m) at a 2 m altitude. Purple - T_off; green - T_sedimentation; red - T_sedimentation_processing; light blue - observations. Minimum and maximum visibility are marked on the figure by the shaded area. (b) - Time series of the liquid water path (g m^{-2}). Purple - T_off; green - T_sedimentation; red - T_sedimentation_processing; light blue - observations; blue dashed - running average over observations (40 points).

visibility in T_sedimentation_processing decreases from 5.5 to 2.1 km, where after this time, it suddenly increases and stays at around 30 km throughout the rest of the night. The visibility threshold for fog defined by WMO (1966), states that anything between 1 and 5 km is typically defined as mist. A consequence of the fog layer being unable to develop is that the LWP in T_sedimentation_processing is less than 1 g m^{-2} throughout the night (Figure 6.7b). The CDNC evolution is strongly influenced by a combination of sedimentation and nucleation scavenging, with the CDNC converging to 0 cm^{-3} at all heights from 1900 UTC onwards (Figure 6.8c). Nucleation scavenging results in the removal of available aerosol, and therefore the source for new droplets is reduced. Hence, by including sedimentation alongside aerosol removal, aerosol sources will eventually deplete to zero. In reality, both of these processes will occur in fog, however, sources of aerosol (either from the surface, mixing down from above, or advection) will balance the loss of aerosol through scavenging/sedimentation. This may improve the nucleation scavenging parameterisation used in CASIM and will be discussed in Section 6.5 of this chapter.

6.4 Sensitivity of scavenging to changes in microphysics

Section 6.3 showed that the fog evolution is sensitive to the interaction between nucleation scavenging, sedimentation and cloud top fluxes. As both sedimentation and cloud top fluxes are influenced by parameters such as CCN number and effective radius, this section aims to quantify the fog evolution's sensitivity to nucleation scavenging with a change in fog microphysics. Table 6.2 displays the list of tests that change the CCN concentration, shape parameter and effective radius which may change the fog evolution when nucleation scavenging is accounted for.

6.4.1 CCN concentration

Results from Chapter 4 showed the fog evolution being impacted by CCN properties, where for example, an increase in CCN concentration increases the vertical depth of the fog, due to an increase in the cloud's optical thickness. This section will analyse how

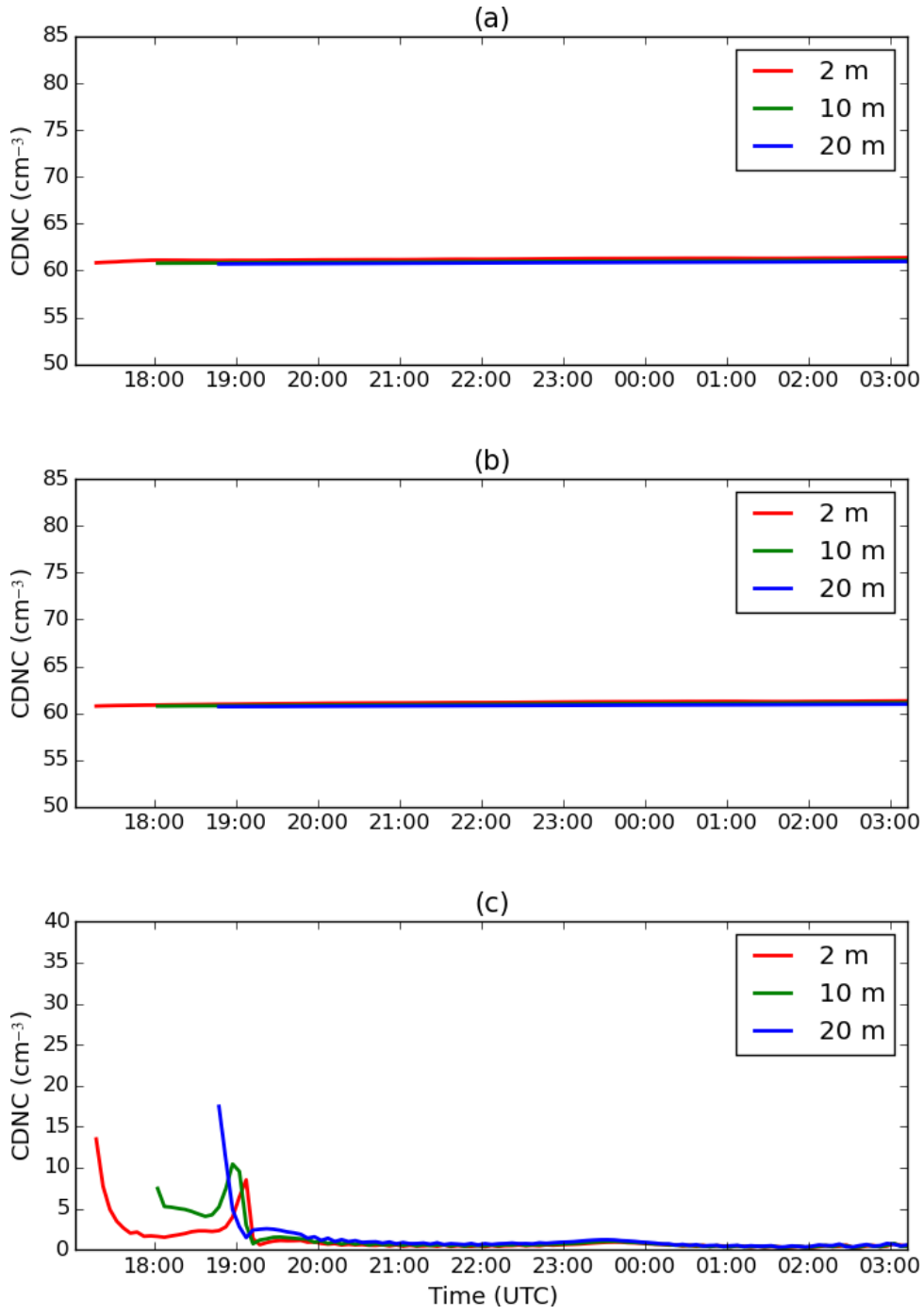

Figure 6.8: Time series of cloud droplet number concentration (CDNC) at altitudes of 2, 10 and 20 m. Red - 2 m; green - 10 m; blue - 20 m. (a) - T_off; (b) - T_sedimentation; (c) - T_sedimentation_processing.

Test	CCN concentration (cm^{-3})	Shape parameter	r_e (μm)
T_control	100	3.0	10.0
T_ccn_50	50	3.0	10.0
T_ccn_200	200	3.0	10.0
T_ccn_500	500	3.0	10.0
T_mu_5	100	5.0	10.0
T_mu_7	100	7.0	10.0
T_er_15.0	100	3.0	15.0
T_er_20.0	100	3.0	20.0

Table 6.2: A list of tests referred to in Section 6.4, which includes changes to different parameters that change the fog's microphysical properties.

nucleation scavenging is controlled by the initial CCN concentration.

Between 1700 and 1845 UTC, the mean near-surface visibility in T_control initially increases from 5.3 to 15.1 km, before decreasing to a minimum near-surface visibility of 2.4 km (Figure 6.9). After 1845 UTC, the near-surface visibility sharply increases to 21.6 km at 1855 UTC and near-surface visibility remains good throughout the rest of the simulation. In reality, fog formation accounts for in-cloud removal through nucleation scavenging, and the fog layer sustains itself as it grows enough in optical depth. However, turning on in-cloud removal in CASIM results in the fog layer dissipating relatively quickly (in this example, after 2 hours). Increasing (decreasing) the CCN concentration not only decreases (increases) the mean near-surface visibility but also increases (decreases) the time when the fog dissipates (visibility less than 1 km). As an example, between T_control and T_ccn_500, the near-surface visibility decreases by a maximum of 1.5 km, with the time for the near-surface visibility to become greater than the 1 km fog threshold again increasing by 20 minutes in T_ccn_500. These results demonstrate that aerosol properties such as CCN concentration indirectly control the scavenging effects within the fog. However, the

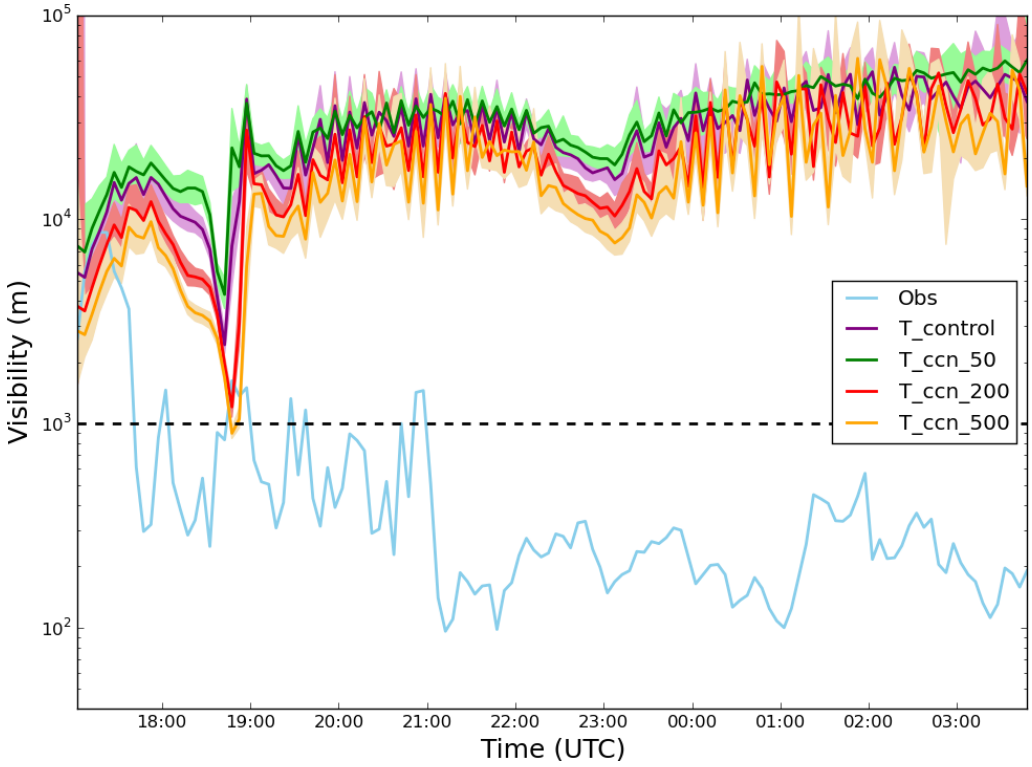

Figure 6.9: Time series of the mean visibility (m) at a 2 m altitude. Purple – T_control; green – T_ccn_50; red – T_ccn_200; orange – T_ccn_500; light blue – observations. Minimum and maximum visibility are marked on the figure by the shaded area.

number of droplets that form and subsequently sediment out of the fog layer, results in the layer failing to become optically thick and quickly dissipating. Therefore, this suggests the need to introduce an additional aerosol source, to better model what would occur in reality.

A consequence of the fog layer in T_control (and for all subsequent CCN sensitivity tests) being unable to develop in optical thickness, is that both the surface precipitation rate and LWP are both underestimated (Figures 6.10a and b). Between 1700 and 1905 UTC, the rate of surface precipitation increases to a maximum of 7 g m^{-2} hr^{-1}, before it sharply decreases to 2 g m^{-2} hr^{-1} and it slowly increasing again to a value of 5 g m^{-2} hr^{-1} towards the end of the night. As the initial decrease in the surface precipitation rate occurs at a later time than the increase in near-surface visibility at a 2 m height (see Figure 6.9), this indicates that the cause of this behaviour is due to the sedimentation of fog droplets out of the layer. Increasing the CCN concentration delays the time at which the maxima in the surface precipitation rate occurs. Although the sedimentation rate would decrease, there is more liquid water in the system that will fall to the surface (due to an increase in CDNC) resulting in an increase in the surface precipitation rate. Therefore, this provides further evidence that the sedimentation rate of droplets may be the cause of the behaviour being shown in the fog layer's evolution.

There are problems with the simulation output, resulting in noticeable oscillations in the simulated surface precipitation rate, near-surface visibility and LWP after 1900 UTC (Figures 6.9 and 6.10). To explain the reason for these oscillations, the time series of the CDNC were taken at a range of heights between 2 and 60 m (Figure 6.11a-d). During T_control (Figure 6.11a) the CDNC initially rises at all heights due to new droplets forming through activation, before eventually all decreasing to a value to zero. For CDNC levels up to 20 m, there is an initial rise of CDNC to 8 cm^{-3} and it drops to around zero just after 1900 UTC; remaining at this value throughout the rest of the night. At a height of 40 m, the CDNC increases to 10 cm^{-3}, before eventually decreases to zero in a couple of hours (with a similar pattern occurs at a height of 60 m). Through this, the source of these oscillations is due to the formation of droplets occurring at each grid level in these

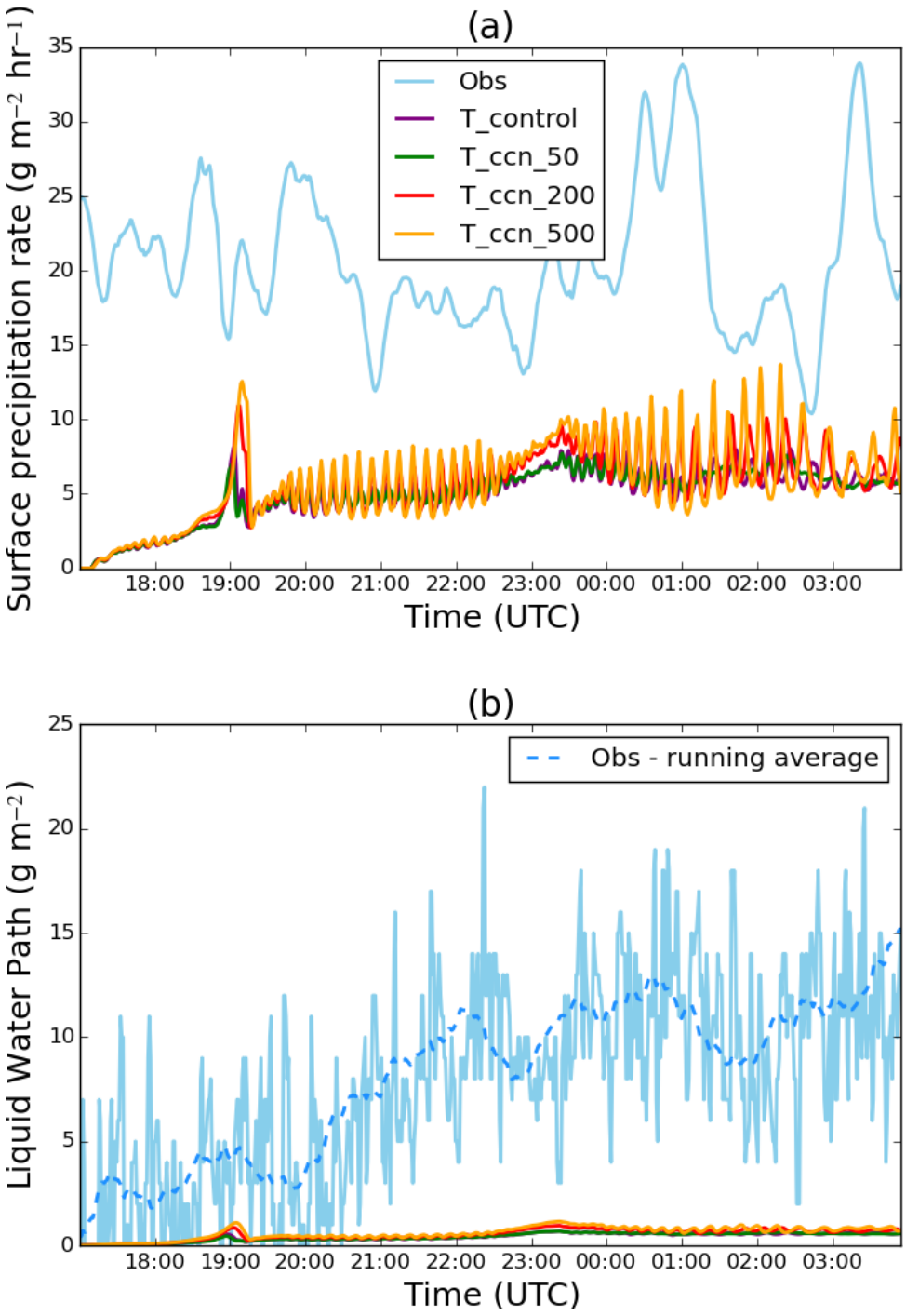

Figure 6.10: (a) - Time series of the surface precipitation rate (g m^{-2} hr^{-1}). Purple – T_control; green – T_ccn_50; red – T_ccn_200; orange – T_ccn_500; light blue – observations. (b) - Time series of the liquid water path (g m^{-2}). Purple – T_control; green – T_ccn_50; red – T_ccn_200; orange – T_ccn_500; light blue – observations; blue dashed - running average over observations (40 points).

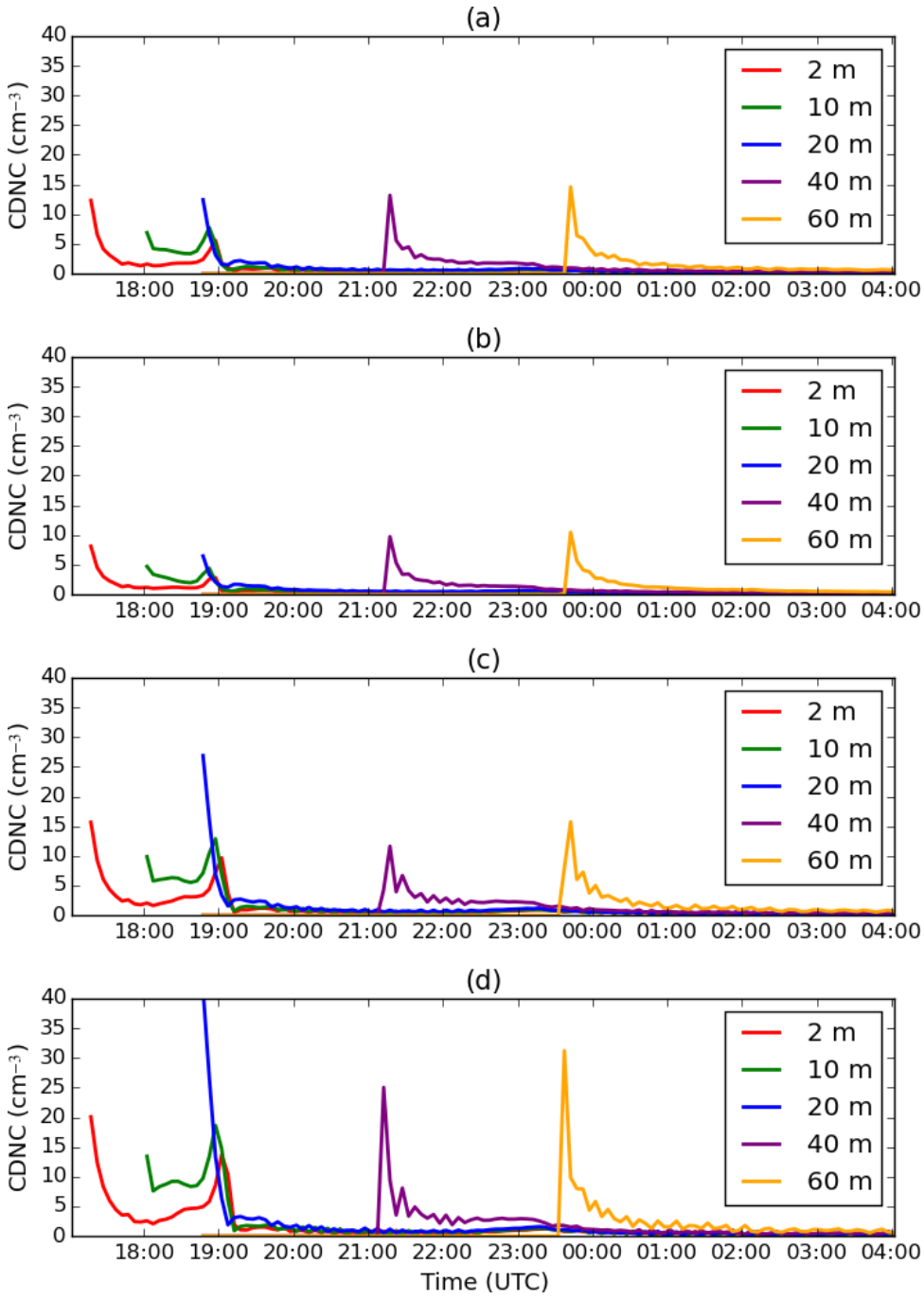

Figure 6.11: Time series of cloud droplet number concentation (CDNC; cm^{-3}) at altitudes of 2, 10 20 and 60 m. Red - 2 m; green - 10 m; blue - 20 m; purple - 40 m; orange - 60 m. (a) - T_control; (b) - T_ccn_50; (c) - T_ccn_200; (d) - T_ccn_500.

simulations, where the pattern of the CDNC approaching zero is resulting in a sudden increase and decrease in the sedimentation rate. The increase in CCN concentration results in the formation of more droplets of a smaller size (Figure 6.11d), therefore slowing down the droplet fall out speed, but increases the strength in oscillation due to the cloud being slightly deeper (Figure 6.9).

6.4.2 Sensitivity to the shape parameter

Results from Chapter 4 showed that increasing the shape parameter changed the skew of the drop-size distribution to emphasise the abundance of smaller droplets. This reduced the sedimentation rate and allowed for the fog layer to become optically thick. When the shape parameter was increased, in-cloud aerosol removal was turned off. However, the results so far have shown that the chosen shape parameter of $\mu_d = 3$ may not be high enough to allow for the fog to grow in optical thickness. To account for aerosol removal, two tests were setup based on the configuration of T_control, where the shape parameter was increased to $\mu_d = 5$ and $\mu_d = 7$.

Although an increase in the shape parameter results in a decrease in the minimum near-surface visibility, there is not enough growth in optical thickness to sustain the fog layer (not shown). In addition, the oscillations in the simulated precipitation rate are still present as shown in the CCN sensitivity tests (Figure 6.12). As the sedimentation flux in CASIM is the product of the weighted mean velocity and CDNC, poor representation in either quantity will result in the fog being unable to sustain and grow in optical depth. The justification for the chosen shape parameter initially was due to it best representing the observed cloud-drop size distribution (see Chapter 4). Therefore, even if increasing the shape parameter did result in an improved fog evolution, changing its value is not a suitable solution to negate the effects of nucleation scavenging impacts in these simulations.

6.4.3 Effective radius

Results from Section 6.3.2 show that the mean droplet size radius is bigger than the prescribed $r_e = 10$ μm, therefore suggesting that the longwave fluxes due to liquid water

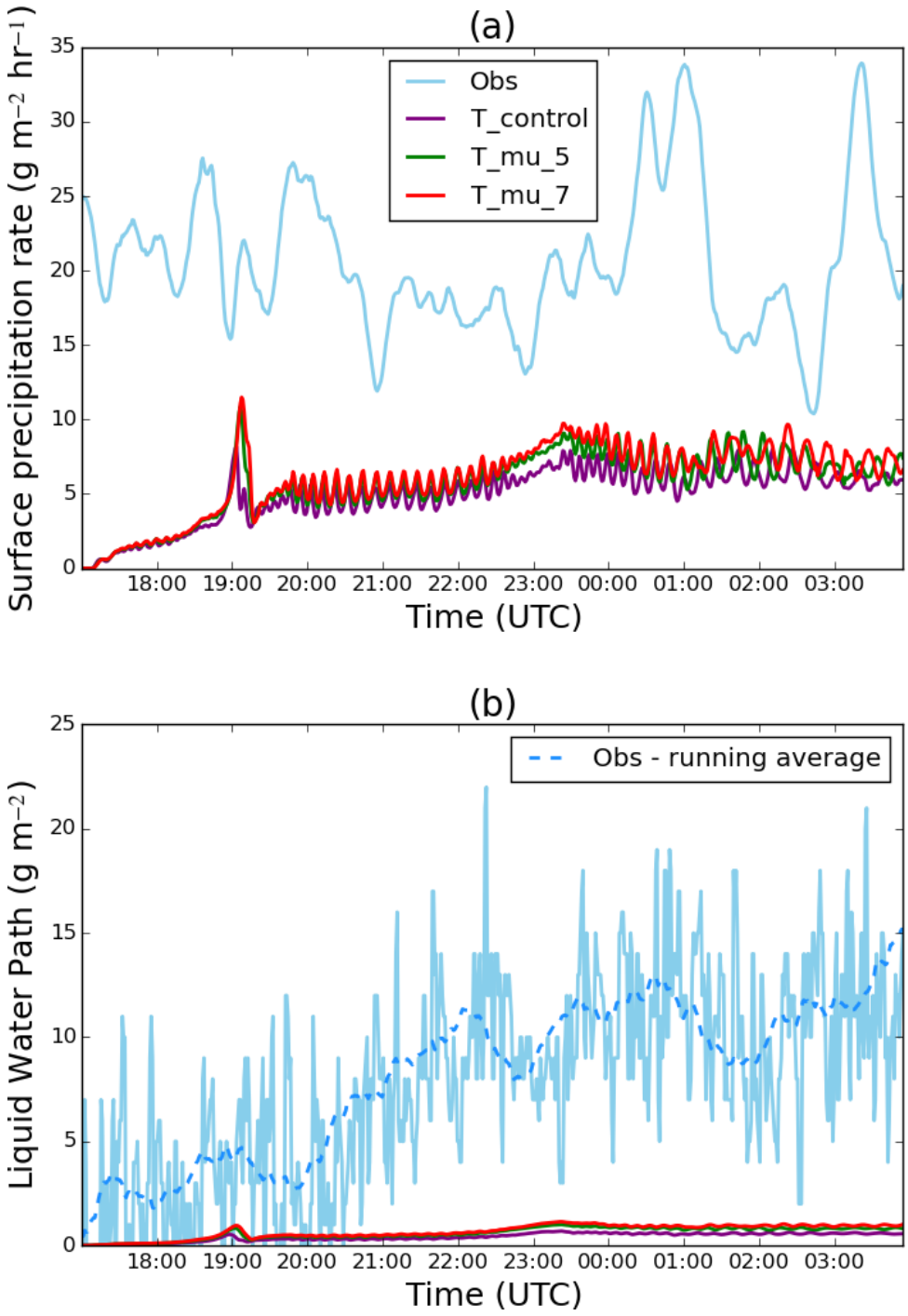

Figure 6.12: (a) - Time series of the surface precipitation rate (g m^{-2} hr^{-1}). Purple – T_control; green – T_mu_5; red – T_mu_7; light blue – observations. (b) - Time series of the liquid water path (g m^{-2}). Purple – T_control; green – T_mu_5; red – T_mu_7; light blue – observations; blue dashed - running average over observations (40 points).

are overemphasised. To understand how fog evolution with nucleation scavenging turned on is impacted by the choice in effective radius, two tests were setup where r_e was increased to 15 and 20 μm. Whilst an increase in the effective radius led to a decrease in liquid water, the changes made to the fog evolution were minimal (not shown). Changes in the effective radius account for a change in CDNC. However, because the values of CDNC were relatively low, to begin with, an increase in effective radius would not allow for the fog layer to further develop.

6.4.4 Choice in vertical resolution

With the current model assumptions, the results this section have shown the parameterisation for nucleation scavenging does not allow for the fog to become optically thick, leading to unrealistic behaviours within the fog evolution. As discussed in Section 4.2 of Chapter 4, these simulations are run with a vertical resolution of 1 m, as studies such as Bergot et al. (2007) have shown that a coarser resolution may result in the fog behaviours not being accurately captured. However, their study did not account for a nucleation scavenging parameterisation, and hence a finer resolution may be required to improve model performance. However, upon running a test where the vertical resolution was reduced to 0.5 m for the first 50 m of the domain, there were no visible improvements in fog evolution (not shown).

6.5 Advection of CCN - impact on fog evolution

6.5.1 Motivation behind model development

Section 6.4 has highlighted that the current parameterisation used for nucleation scavenging is unsuitable for fog. The simulated CDNC in all tests was appreciably lower than the observed CDNC (not shown), resulting in the fog being unable to develop and hence dissipating. In reality, local depletion of aerosol through scavenging/sedimentation can be partially balanced by advection or local sources of aerosol. The objective of this section is to understand whether simulations including an additional aerosol source and nucleation

scavenging can develop and sustain fog. The capability to apply a large scale forcing to vary both the aerosol mass and number has been implemented into MONC. In this chapter, applying a large scale forcing allows for new aerosol particles to be advected into the model domain, therefore adding a constant source of aerosol at every timestep.

Given that this development is relatively new, three tests were setup that advected aerosol at a rate of 50 (T_advect_50_non_proc), 100 (T_advect_100_non_proc) and 200 cm^{-3} hr^{-1} (T_advect_200_non_proc), with an average diameter of 0.15 μm. These tests were run without nucleation scavenging to check that the advection tendencies were all configured correctly in MONC. Next, three additional tests were setup based on the T_control configuration, and applied a large-scale tendency of aerosol at a rate of 50 (T_50_per_hour), 100 (T_100_per_hour) and 200 cm^{-3} hr^{-1} (T_200_per_hour), all with an average diameter of 0.15 μm. The aim of these tests was investigating how much nucleation scavenging changed with the addition of a new aerosol source, and whether this should be included in future work.

Although these tests are idealistic, these values represent aerosol measurements found in clean air masses in rural environments (e.g. Wiedensohler et al., 1997; Birmili et al., 1999). For reference, the advective tendency is configured for the first 300 m of the vertical domain, and it tends towards zero at the top of the domain.

6.5.2 Advective tendency results

Figure 6.13 shows the results of the tests without aerosol processing. The first two hours (time of simulation) show the same rate of increase in both the accumulation number and mass for each respective test, resulting in the average CCN radius being 0.075 $\pm 3 \times 10^{-5}$ μm. The deviation from the average set mean is due to the precision in which the rate of change could be set in MONC. Despite this deviation, it is to be expected that this change will not have a great impact on the fog evolution, given the results from Chapter 4.

Although an increase in the aerosol advection rate results in the fog beginning to develop and grow in optical depth (Figure 6.14), all tests show a sudden increase in near-surface visibility due to the sedimentation of formed droplets out of the developing fog

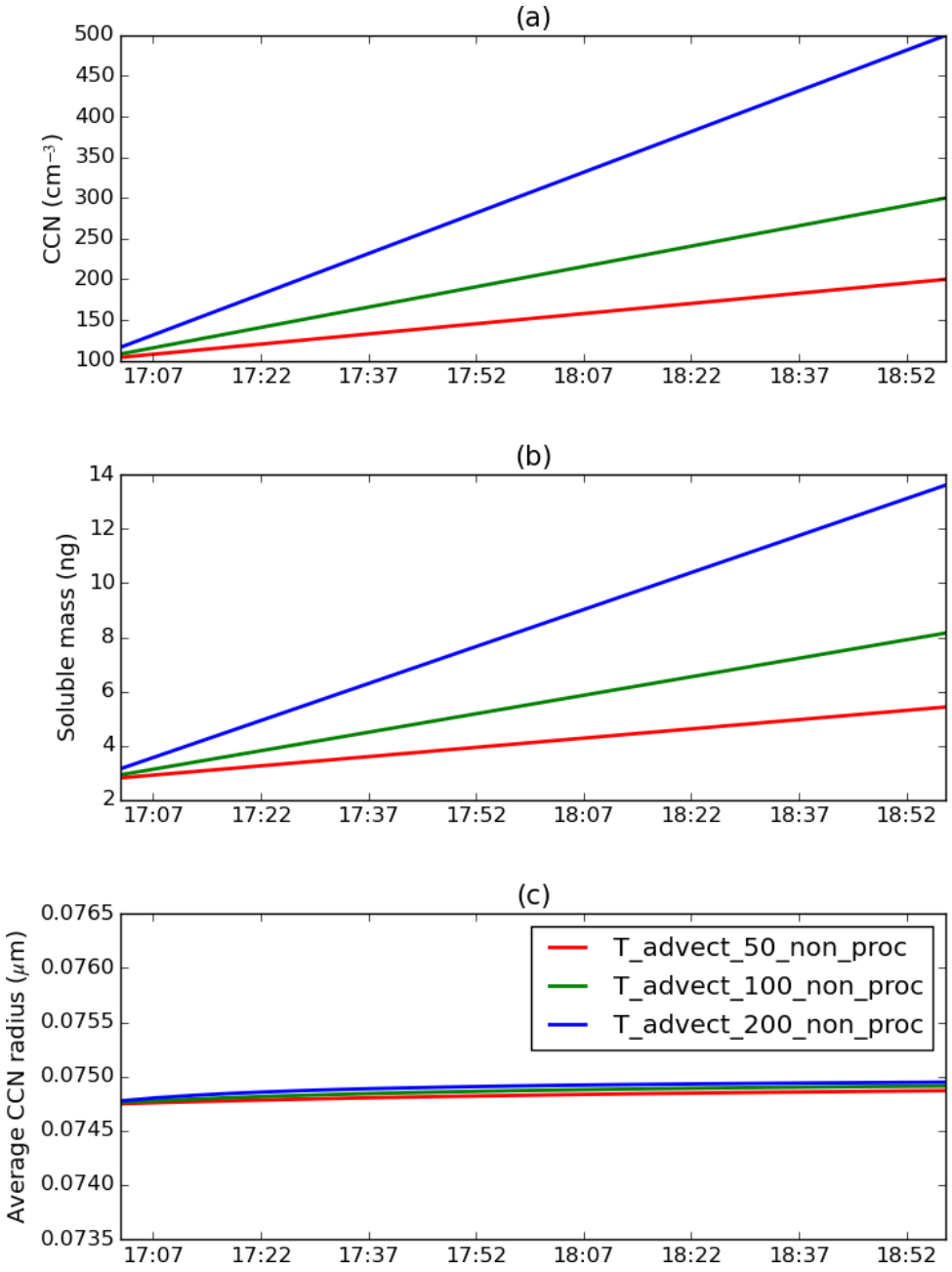

Figure 6.13: Time series of (a) the accumulation soluble number (cm^{-3}); (b) the accumulation soluble mass (ng); (c) the average CCN radius (μm). Red - T_advect_50_non_proc; green - T_advect_100_non_proc; blue - T_advect_200_non_proc.

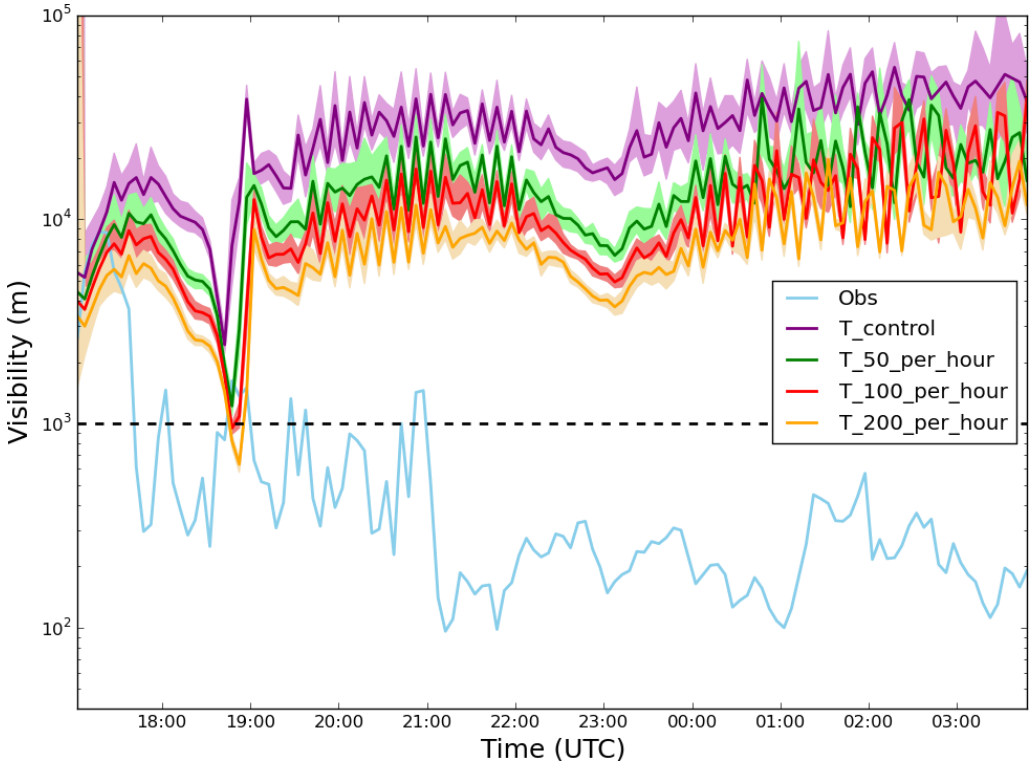

Figure 6.14: Time series of the mean visibility (m) at a 2 m altitude. Purple – T_control; green – T_50_per_hour; red – T_100_per_hour; orange – T_200_per_hour; light blue – observations. Minimum and maximum visibility are marked on the figure by the shaded area.

layer. Between T_control and T_200_per_hour, the minimum mean near-surface visibility decreases by 1.8 km. However, the oscillation in T_200_per_hour is still present, which is in line with previous results presented in this chapter. In addition, the increase in advection rate results in a higher production rate of liquid water (Figure 6.15). Between T_control and T_200_per_hour, the maximum LWC increases from 0.037 to 0.099 g kg^{-1}, and the fog's dissipating time increases by 20 minutes. However, the CDNC is still not great enough for the fog layer to develop (not shown) and hence the fog still dissipates relatively quickly, indicating that the liquid water is not great enough to allow for cooling at the top of the fog.

Relaxing aerosol fields

As part of the development to introduce an aerosol source, code was introduced to relax of aerosol fields to a mean profile, as described in Chapter 3 of this thesis. For reference, for the accumulation number and mass, $N_i, i = 1, 2$, the change in N_i due to a relaxation is defined as:

$$\left.\frac{\partial N_i}{\partial t}\right|_{relax} = G(N_i - N_{i0}), \tag{6.2}$$

where N_{i0} is the mean profile value of aerosol (number and mass), and G is the relaxation timescale used in Equation (6.2).

As advecting aerosol still did not allow for fog development, an experiment was conducted that used a relaxation method to introduce aerosol into the system. To do this, three experiments were setup, where the timescale for relaxation, G, was defined at 5, 15 and 30 minutes. However, there is no improvement in the fog evolution with large scale forcing in the form of a relaxation to the aerosol fields (results are not shown). Therefore, although a large-scale forcing may be required when investigating nucleation scavenging in fog, the results presented in this chapter cannot provide a concrete conclusion.

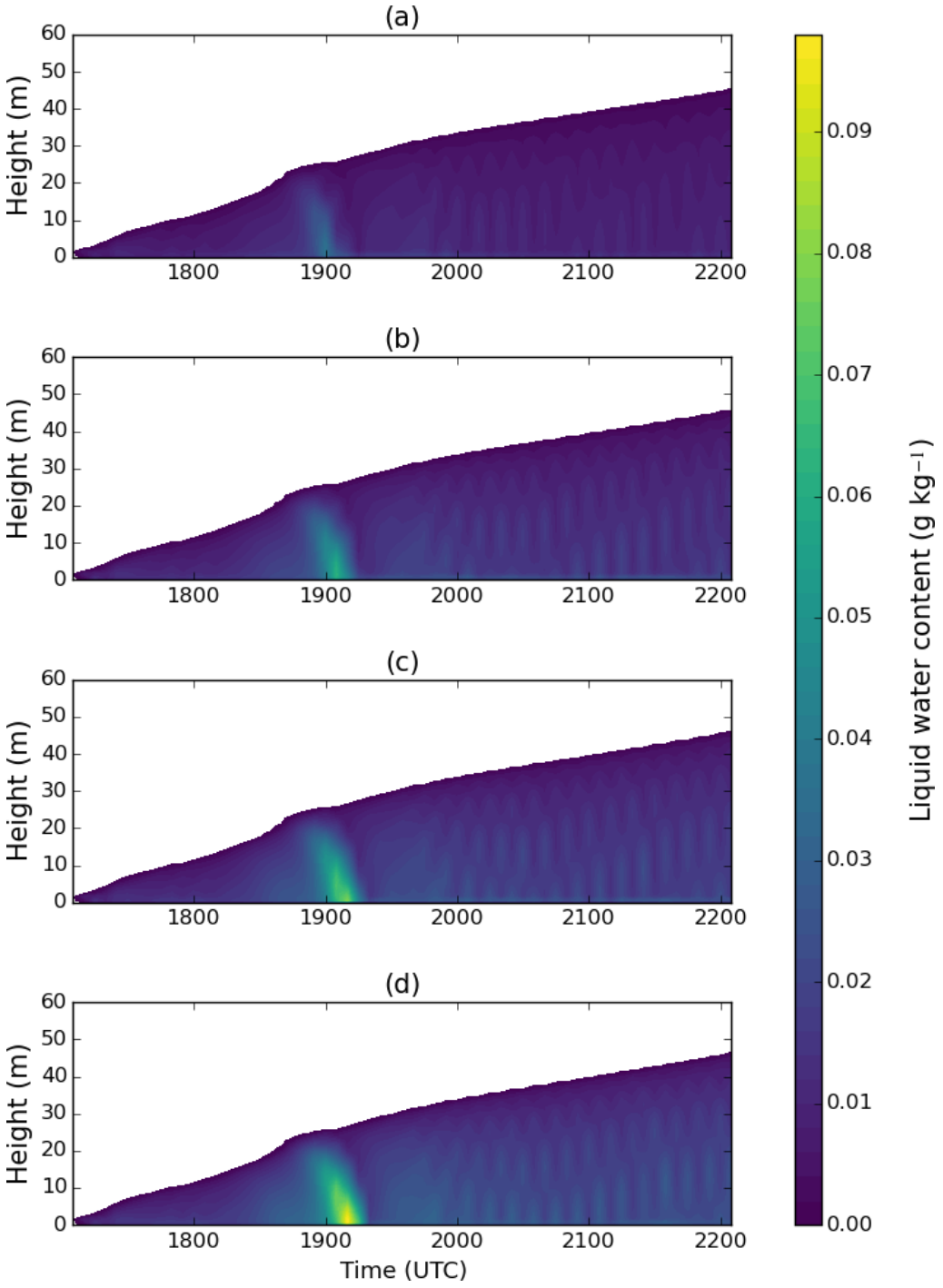

Figure 6.15: Time-height slice of the LWC (g kg^{-1}). (a) – T_control; (b) – T_50_per_hour; (c) – T_100_per_hour; (d) – T_200_per_hour.

6.6 Discussion

In this chapter, it has been shown that turning on nucleation scavenging results in the fog layer being unable to further develop and eventually it dissipating after a couple of hours; a lot quicker than was observed during IOP1. The focus of this section will discuss the limitations in the model setup, and what should be considered for future work when accounting for a nucleation scavenging parameterisation in fog.

6.6.1 Saturation adjustment

These results show that the current representation in CASIM seems to produce unrealistic levels of aerosol depletion. Boutle et al. (2018) conducted simulations of IOP1, which included the use of the UCLA Large-Eddy Simulation Code and the Sectional Aerosol module for Large-Scale Applications (UCLALES–SALSA) model (Tonttila et al., 2017). Their LES model utilised a prognostic calculation for supersaturation, combined with a bin microphysics scheme, therefore accounting for fog scavenging by moving aerosol into the cloud droplet spectrum as they activate. Currently, MONC calculates liquid using a saturation adjustment scheme and CDNC with an aerosol activation scheme (e.g. Abdul-Razzak and Ghan, 2000). Recent studies have shown that the fog is sensitive to the method of calculating condensation. Using a saturation adjustment scheme as opposed to a prognostic for supersaturation can result in the fog becoming too deep, due to too much liquid water production (Schwenkel and Maronga, 2019). This suggests that the use of a saturation adjustment scheme in these simulations may be too simplistic, depending on the level of complexity within the aerosol-fog interaction representation (i.e. the inclusion of nucleation scavenging).

Chapter 5 discussed the limitations in activation schemes for fog, and in particular, that several schemes do not account for droplets that form in sub-saturated environments. This may be of importance for IOP1, given that was predicted that the population of droplets consisted of a high fraction of hydrated aerosols (Boutle et al., 2018). Using either a saturation adjustment scheme or even a bulk microphysics scheme may not be

the most suitable method to model nucleation scavenging in fog, due to both assuming all aerosol activate, a process that does not always occur in fog formation.

6.6.2 Aerosol source

An objective addressed in this chapter was to investigate whether it was necessary to include an aerosol source, to balance the loss of aerosols through nucleation scavenging. Initially, aerosol mass and concentration were only specified in the configuration file for each simulation, with no other mechanism to replenish the aerosol particles that had been removed due to nucleation. For this work, a technique was developed to apply large-scale forcing to the aerosol fields in the form of an advection tendency, increasing both the accumulation number and mass at a rate specified by the user. Although in these tests, the dissipation time did increase, it did not negate the fog being unable to develop due to relatively low levels of liquid water.

6.7 Summary

The focus of this chapter investigated how the inclusion of nucleation scavenging impacted on simulations of IOP1. This was split into three objectives. The first objective investigated how turning on nucleation scavenging impacted the fog, and why this may change in conjunction with other parameters such as sedimentation and cloud-radiation interactions. It was shown that turning on nucleation scavenging has a big impact on the fog, causing it to dissipate quickly in comparison to observations, due to the aerosol source being depleted through sedimentation. Consequently, the lower CDNC population meant the fog could not sustain itself, due to it not being able to grow in optical depth.

The second objective investigated nucleation scavenging's sensitivity to to parameters that control fog microphysics. Increasing the CCN concentration led to more droplet formation, allowing for a decreased sedimentation rate. However, even when the CCN concentration increased from 100 to 500 cm^{-3}, the fog eventually dissipated due to sedimentation after a couple of hours. There were some unusual model behaviours, in partic-

ular, the surface precipitation rate, due to new droplets forming in the higher levels of the domain and quickly sedimenting out of the layer. In addition, the shape parameter and effective radius, as well as the vertical resolution had little to no effect on the fog evolution in comparison to the control run. The final objective investigated the introduction of an additional aerosol source to account for the removal of aerosol, and whether or not it would improve the fog evolution when compared to observations. However, despite both an advection tendency and aerosol relaxation being applied in two separate experiments, the fog did not grow enough in optical depth to allow for it to develop, and as a result dissipated relatively quickly.

This chapter has highlighted the importance of nucleation scavenging, and the work may be required for it to be used when modelling fog using a bulk microphysics scheme. Fundamentally, aerosol activation may not occur in fog (e.g. Gerber, 1981; Haeffelin et al., 2013; Boutle et al., 2018). Therefore, accounting for nucleation scavenging in a bulk microphysics scheme that assumes activation may be unsuitable for simulations of fog, however, further work is required to form a conclusion. Although not explored in this work, Gilardoni et al. (2014) showed that nucleation scavenging is impacted by the efficiency of certain CCN that condenses water vapour onto them. This result suggests more complex chemistry is required to account for the indirect effects due to scavenging, however, the lack of aerosol measurements during IOP1 make it difficult to quantify the importance of nucleation scavenging in this example.

In reality, nucleation scavenging occurs in fog, and so it seems necessary to include it in models. However, current deficiencies in either scavenging representation or other aspects of aerosol processing mean that this added realism in terms of modelled processes does not translate into improved predictions. This demonstrates the need for further work to understand the fog's sensitivity to nucleation scavenging in future modelling studies.

Chapter 7

Conclusions and future work

The end doesn't mean that it's over.

Stephen Sondheim's *Assassins*

7.1 Overview of thesis aims

The research presented in this thesis aimed to understand how aerosols impact the formation and development of nocturnal radiation fog. Aerosols are important, as they provide a substrate for fog droplets to form, which will determine both the optical depth and life span of the fog layer. Bott (1991) first highlighted their importance to the fog life cycle, showing that an increase in aerosol concentration led to a deeper fog layer, delaying the dissipation time as a result. Although additional modelling studies expanded on the work by Bott (e.g. Rangognio et al., 2009; Stolaki et al., 2015; Maalick et al., 2016), they all model fog cases located in "polluted" aerosol regimes. More recently, Boutle et al. (2018) discussed that the representation of aerosol-fog interactions is crucial to model a slow transitioning fog that forms in a relatively "clean" environment. Therefore, this thesis focused on understanding aerosol-fog interactions during a stable fog case based in the UK, where a suite of sensitivity tests changing aerosol characteristics and its representation were conducted. This thesis had three key three research questions:

1. Chapter 4: Given default modelling assumptions, how important are aerosol-fog interactions in capturing the behaviour of a slow transitioning fog?

2. Chapter 5: Could a more suitable representation for aerosol activation capture the behaviours during fog formation and if so, why?

3. Chapter 6: Given that aerosol scavenging has previously been shown to strongly impact the aerosol-size distribution, how would the fog evolution be impacted should scavenging be included in simulations?

These questions were answered using MONC, a LES model that can resolve turbulent flow. For this work, MONC was coupled with CASIM, a multi-moment bulk microphysics scheme designed to simulate aerosol-cloud interactions. The case chosen to be simulated was IOP1 from the recent LANFEX field campaign (Price et al., 2018). IOP1 was chosen as it was one of the cleanest examples of local fog development, with minimal influence by advection.

7.1.1 MONC and CASIM parameter validation

Both MONC and CASIM are still in development and hence have not been used to study nocturnal radiation fog prior this work. Therefore, an objective of Chapter 4 was to validate the appropriate microphysics and technical parameters that should be used throughout the thesis.

Based on previous literature, Aitken and coarse mode aerosol may not be important for simulations of fog. To verify if this would impact the fog evolution, a test running with a multi-mode aerosol size distribution was setup, and then compared to a simulation that only ran with just accumulation mode aerosol. The multi-mode aerosol was limited to only an hour of simulation output. However, when compared to a run with just accumulation mode aerosol, there were no appreciable differences in the fog's initial formation. Therefore, Aitken and coarse mode aerosol were not accounted for in all simulations presented in this thesis.

The suitability of the cloud drop-size distribution and its shape parameters were investigated. It was shown that based on observations of cloud-droplet spectra, the shape parameter of the drop-size distribution should be changed from $\mu_d = 0$ to $\mu_d = 3$. Increasing the shape parameter resulted in the simulated cloud-drop size distribution being more in line with observations. This led to a more reasonable sedimentation rate of liquid water in the simulated fog. Finally, the suitability of the chosen fixed effective radius was explored and it was shown that an increase in r_e decreased the LWP, whilst increasing the mean near-surface visibility. As changes in the CDNC influenced the fog evolution, it was important to consider adapting r_e when exploring the suitability of aerosol activation schemes in Chapter 5.

Chapter 4 was used to validate the choice in domain size for all simulations presented in this thesis. The results from these tests showed that a horizontal domain size of 132 $\times$ 132 m^2 made a relatively small difference to the structures of the fog layer, when compared to a simulation that had a domain size of 800 $\times$ 800 m^2. An advantage of this result was that more simulations could be conducted at a reduced computational expense. Therefore, this allowed for a greater range of sensitivity studies that would improve the overall understanding of aerosol-fog interactions during a stable fog.

7.2 Summary of key results

The following section will now present the key findings from each results chapter.

7.2.1 Chapter 4: How important are aerosol-fog interactions for the successful modelling of nocturnal radiation fog?

For this chapter, all simulations were run using the Abdul-Razzak and Ghan (2000) activation scheme. The control simulation had the aerosol parameters initialised with a concentration of 100 cm^{-3} and total soluble mass of 2.7 ng throughout the vertical depth of the boundary layer, based on the model setup by Boutle et al. (2018). This chapter analysed two sets of tests that altered both of the aerosol parameters.

Doubling (halving) the CCN concentration resulted in an increase (decrease) in LWP by up to 21% (36%). However, by decreasing the CCN concentration to 50 cm^{-3}, the reduced CDNC was more in line with the observed CDNC and resulted in a slower transition to an optically thicker fog. As the CDNC is determined by the aerosol activation scheme, this result highlighted why the assumptions used in several schemes are unsuitable for fog. For example, Abdul-Razzak and Ghan (2000) was designed for clouds driven by an adiabatic ascent, and imposes a minimum vertical velocity threshold of 0.1 m s^{-1}, to account for poorly resolved cloud top turbulence in GCMs/NWPs. However, both of these assumptions do not occur in fog formation, therefore overestimating aerosol activation and consequently can impact the time at which the fog becomes well-mixed. Finally, these results showed that doubling (halving) the CCN soluble mass led to an increase (decrease) in the LWP by both 14%. Changing the soluble mass impacts the likelihood that an aerosol can activate, which may be important when accounting for processes that remove aerosol, i.e. nucleation scavenging.

To conclude, this chapter demonstrated that the CDNC is important for the fog evolution, where its overestimation may result in the fog developing to a well-mixed layer too quickly. Unlike previous studies (Stolaki et al., 2015; Maalick et al., 2016), this work investigated aerosol impacts on simulating a stable fog case formed in a relatively "clean" environment, highlighting aerosol treatment when modelling optically thin fog.

7.2.2 Chapter 5: Can a more accurate representation of aerosol activation improve simulations of fog?

This chapter was motivated by the results of Chapter 4, which demonstrated that using a scheme designed for a convective cloud is unsuitable for fog. Although activation may not occur in radiation fog (Gerber, 1981), an aerosol activation scheme is a computationally cheap method that can account for aerosol treatment. The work in this chapter was split into two key themes. Motivated by Boutle et al. (2018), the first investigated the suitability of w_{min} used in aerosol activation schemes, and how it may directly impact simulations of fog. The second investigated why a more physically based activation scheme is more

appropriate for fog, therefore improving the timing of when the fog becomes well-mixed. Both of these themes were addressed using the Shipway (2015) activation scheme, as Abdul-Razzak and Ghan (2000) overestimates condensation for low aerosol concentrations. For the second theme, a new scheme was developed, known as Shipway_v2, which accounts for an increase in supersaturation due to both adiabatic and non-adiabatic cooling sources.

Using an offline box model, it was shown that aerosol activation is overestimated by up to 70%, if the default $w_{min} = 0.1$ m s^{-1} is used rather than a cooling rate typical of those found in fog. Of the three aerosol modes tested, accumulation mode aerosol was most influenced by the w_{min} assumption. Aitken mode aerosol made a negligible impact on the activated aerosol population, providing evidence that they can be disregarded for simulations of fog. Next, the suitability of a w_{min} was applied to the Shipway scheme in MONC. It was shown that reducing w_{min} to 0.01 m s^{-1} led to an extension in the fog's transition time to a well-mixed layer by two and a half hours, due to less turbulent mixing driven by induced Kelvin-Helmholtz instabilities.

For the Shipway_v2 scheme, a new derivation for the change in supersaturation was formulated, and it showed that the difference between the adiabatic and non-adiabatic contribution to cooling is caused by the removal of a pressure term. The Shipway_v2 scheme was tested in an offline model and compared to the Shipway scheme; only accounting for a non-adiabatic cooling source. It was shown that should a scheme which only accounts for adiabatic cooling could underestimate aerosol activation by 20% in an environment that forms cloud without an updraft (i.e. fog). Part of this work involved implementing the Shipway_v2 scheme into CASIM, to then be run in MONC. The results showed that in comparison to the Shipway (2015) scheme, using Shipway_v2 had a slower transition to a well-mixed fog, and was in better agreement with observations of the downwelling longwave radiation and LWP.

To conclude, this chapter demonstrated the importance of an improved physical representation for aerosol activation, and has provided a framework for future work that can investigate aerosol impacts in fog.

7.2.3 Chapter 6: Aerosol removal in radiation fog: does it matter?

Fog forming will result in aerosols being removed from the atmosphere through nucleation scavenging. Studies modelling fog do not typically account for nucleation scavenging, and those that do, use methods (e.g. bin microphysics) that are too computationally expensive for operational NWP models. CASIM has an option to parameterise nucleation scavenging, which works by removing both aerosol mass and number as droplets activate. Therefore, this study focused on understanding the impact of accounting for nucleation scavenging on simulations of fog; the first of study of this kind, to date.

Turning on nucleation scavenging in CASIM leads to fog dissipating much quicker than in the observations. This effect was due to the aerosol source being depleted through sedimentation, decreasing the likelihood of new droplet formation. An additional consequence of turning on nucleation scavenging was clear oscillations being displayed in the modelled liquid water. This was due to fog forming higher in the vertical domain and quickly dissipating due to sedimentation. To try and negate this effect, the parameters that control the fog microphysics (e.g. shape parameter) were changed. However, all sensitivity tests conducted did not make any appreciable difference to the fog's evolution. Finally, MONC was developed to be capable of applying a large scale forcing to vary both the aerosol mass and number through advection. However, turning this on with a realistic advection rate alongside nucleation scavenging still did not allow for the fog to develop.

Therefore, it was concluded that for this chapter, nucleation scavenging results in fog dissipation through sedimentation, as the fog layer can not become optically thick enough to sustain itself.

7.2.4 Limitation to results

IOP1 did not have direct observations of aerosol mass or number concentrations. The aerosol profiles chosen throughout this thesis were an ideal representation of an environment such as Cardington, however, this limited some of the questions that could be answered. Some of these questions include:

- What was the proportion of aerosols that activated into droplets, and how does this compare to simulation output?

- What were the properties of the interstitial aerosol population as the fog formed and developed, and could they provide an insight in improving a nucleation scavenging parameterisation suitable for fog?

There were limitations in other measurements of IOP1. Ice formation occurred on the radiometer from 2300 UTC, the instrument measuring surface longwave downwelling and upwelling radiation. Consequently, the timing when the fog layer may have become optically thick was not observed in these measurements. Although the transition to a deeper fog can be observed in measurements such as near-surface visibility, this can be limited option if the fog is patchy throughout the night. Finally, investigating the fog's sensitivity to w_{min} in Chapter 5 highlighted that the initial fog formation was impacted by the model's spin-up period. For this work, spin-up time is required for the model to approach nearly steady values (Mirocha et al., 2018). Unfortunately, initialising the model to prevent fog formation coinciding with the model's spin-up period was unavoidable. The earliest radiosonde for IOP1 occurred during the time of initial fog formation in simulations using in MONC. This should be something to be a factor when choosing a case for future work studying fog formation and development.

Although not explored, MONC assuming condensation through a saturation adjustment scheme potentially led to results displayed in Chapter 6. Work by Schwenkel and Maronga (2019) demonstrated that using a saturation adjustment scheme for fog overestimates the LWC, resulting in an optically thicker fog. A saturation adjustment scheme assumes condensation at a relative humidity of 100%, therefore not accounting for droplets in sub-saturated environments. This may be key for studying nucleation scavenging in fog and should be a subject for future work.

7.3 Recommendations for improved NWP fog forecasts

The work in this thesis highlights the impact of aerosols during fog formation and development. Although this work was done in the context of LES modelling, it can provide a good insight of how to provide an improved accuracy to operational fog forecasts. Here are some recommendations based on these results.

- **Constraining of aerosol measurements**: IOP1 was limited in not having any measurements of the aerosol population. However, Chapter 4 showed the fog's sensitivity to both aerosol number and mass. To date, the MetUM currently relies on the aerosol-size distribution to diagnose surface visibility (Clark et al., 2008; Haywood et al., 2008). Work in this thesis has provided motivation for field campaigns collecting aerosol measurements, and can help constrain the role of aerosol, both for fog and for future NWP development.

- **Coupling the effective radius**: Initial tests of the Shipway_v2 scheme in Chapter 5 suggested that the scheme did not perform well. However, modifying the effective radius for a change in CDNC led to overall improvements. Future developments should include a coupled effective radius between the radiation scheme and CASIM. If, however, a coupling is unavailable, an increased effective radius of $r_e = 20$ μm should be used to account for a CDNC found in fog.

- **Implementing the Shipway_v2 scheme**: Chapter 5 showed that the Shipway_v2 scheme more accurately represents aerosol activation, and its interaction between the fog and radiative cooling. When investigating the implementation of Shipway_v2 into an operational NWP model, it is recommended to account for non-adiabatic processes by using the model's change in temperature than a radiative tendency. There are two benefits to this approach. Firstly, using a change in temperature due to non-adiabatic cooling processes results in a more complete solution to the Shipway_v2 scheme. Secondly, it removes the dependency of the Shipway_v2 scheme depending on additional code source terms, making it a computationally viable op-

tion in a NWP. The Shipway_v2 scheme does not make use of a w_{min}. Therefore, a characteristic subgrid updraft velocity will need to be applied, similar to the work by Malavelle et al. (2014); another area for future work.

- **Lowering of** w_{min}: The default w_{min} of 0.1 m s^{-1} has been shown to overestimate aerosol activation. However, removing w_{min} or making it too low may result in the formation being impacted by the model's potential spin-up period. Therefore, whilst work on implementing the Shipway_v2 scheme is ongoing, it is recommended to reduce w_{min} to 0.04 m s^{-1}. This will equate to a cooling rate of 1.5 K hr^{-1}; a cooling rate typically found in initial fog formation.

7.4 Suggestions for future research

The following section now presents suggestions for further research investigating aerosol impacts on fog.

7.4.1 Coupled land-surface scheme

The motivation for studying IOP1 was that it was observed to be a stable fog that slowly transitions to a well-mixed layer. Surface fluxes were observed to be close to zero or negative, therefore implying that there were minimal interactions between the fog layer and its surface. This meant that it was possible to simulate IOP1 with MONC, without the need for a land-surface scheme. To date, MONC does not have a coupled land-surface and consequently is limited in the number of fog cases it can simulate and hence be analysed. However, adding the option to simulate land-surface interactions to MONC will remove this limitation. An example land-surface scheme that could be coupled to MONC is the Joint UK Land Environment Simulator (JULES; Best et al., 2011). JULES is the land-surface scheme used in the MetUM, and has been used to simulate radiation fog events (Smith et al., 2018). There are current plans to coupled JULES to MONC, so this line of work will be possible in the future.

Studies have shown that surface properties such as soil moisture (e.g. Duynkerke, 1991),

soil temperature (e.g. Maronga and Bosveld, 2017) and vegetation (e.g. Von Glasow and Bott, 1999) are important in timings for fog's evolution. Therefore, coupling a land-surface scheme to MONC can allow a study on how these features may impact IOP1. In addition, a land-surface scheme is required to accurately study the fog during the diurnal cycle. Sunrise will result in a positive surface heat flux and Maalick et al. (2016) showed that these fluxes could be sensitive to changes in aerosol processes (e.g. inclusion of black carbon). Therefore, the inclusion of a coupled land-surface scheme can study the role of aerosol-fog interactions during phases such as the dissipation stage.

7.4.2 Direct and semi-direct effect: fog formation and dissipation

The focus of this thesis has been to investigate how aerosol indirectly controls fog evolution. However, fog can be impacted by the state of the atmosphere, which is directly influenced by the Earth's radiative forcing. The term "radiative forcing", is defined as an imposed perturbation in the radiative energy budget of the Earth's climate system (IPCC, 2001). Aerosol can change the Earth's radiative forcing, either by scattering or absorbing solar radiation, resulting in a negative and positive forcing respectively. This is defined as a direct effect. More specifically, a positive forcing may warm the atmosphere and decrease its relative humidity, resulting in breaking up low cloud cover; i.e. the semi-direct effect (Hansen et al., 1997). Although studies have investigated the impact of the semi-direct effect on clouds such as marine stratocumulus (e.g. Johnson et al., 2004; Hill and Dobbie, 2008), the number of studies that investigate this effect on radiation fog are limited.

A conclusion by Bott (1991) was that the presence of absorbing aerosols (e.g. black carbon) may impact the onset of fog. They showed that absorbing aerosol resulted in the boundary layer warming, however, the surface was prevented to being warmed. This resulted in the lower levels of the boundary layer approaching saturation quicker, resulting in an earlier fog. However, this result differed for Maalick et al. (2016), in which the presence of absorbing aerosols did not have an impact on fog onset. The difference in results may be due to the methodology. Bott (1991) initialised the model a few hours before sunset using a SCM, whereas Maalick et al. (2016) used a LES and the model was

initialised much closer to sunset, therefore not allowing for as much development to the boundary layer before formation.

The semi-direct effect may result in a faster fog dissipation period caused by solar radiation. Maalick et al. (2016) investigated the impact of the semi-direct effect on the dissipation phase, and showed that the inclusion of black carbon within the aerosol concentration population will impact on the dissipation time. An increase in black carbon led to an increase in the amount of solar radiation above the fog layer being absorbed increased. This resulted in the air above the fog warming, therefore promoting dissipation. However, Maalick et al. (2016) showed that the inclusion of black carbon did not impact surface conditions, implying that the dissipation was being promoted due to the entrainment of drier air into the fog layer. Future work should quantify the impact of the semi-direct effect on fog, and verify the physics that may be promoting its dissipation.

For a wider context, both the direct and semi-direct effect may be important for a fog that forms in areas of high pollution. As an example, fog is a common occurrence during the winter months in India, with fog episodes steadily increasing over the last 40 years (Srivastava et al., 2016). The increase in fog episodes is due to India's pollution levels, which has been shown to have major impacts on human health quality (WHO, 2006). Understanding the role of the semi-direct effect may not only provide insight into aerosol treatment in fog but can provide evidence to government bodies investigating cleaner air initiatives.

Bibliography

Abdul-Razzak, H. and Ghan, S. J. (2000). A parameterization of aerosol activation: 2. Multiple aerosol types. *Journal of Geophysical Research: Atmospheres*, 105(D5):6837–6844.

Abdul-Razzak, H., Ghan, S. J., and Rivera-Carpio, C. (1998). A parameterization of aerosol activation: 1. Single aerosol type. *Journal of Geophysical Research: Atmospheres*, 103(27):6123–6131.

Abramowitz, M. and Stegun, I. (1965). *Handbook of mathematical functions*. Courier Corporation.

Ackerman, A. S., Kirkpatrick, M. P., Stevens, D. E., and Toon, O. B. (2004). The impact of humidity above stratiform clouds on indirect aerosol climate forcing. *Nature*, 432(7020):1014–1017.

Albrecht, B. A. (1989). Aerosols, cloud microphysics, and fractional cloudiness. *Science*, 245(4923):1227–30.

Barahona, D. and Nenes, A. (2007). Parameterization of cloud droplet formation in large-scale models: Including effects of entrainment. *Journal of Geophysical Research*, 112(D16).

BBC (2013). Sheppey crossing crash: Dozens hurt as 130 vehicles crash - BBC News.

Bergot, T. (2013). Small-scale structure of radiation fog: A large-eddy simulation study. *Quarterly Journal of the Royal Meteorological Society*, 139(673):1099–1112.

Bergot, T., Escobar, J., and Masson, V. (2015). Effect of small-scale surface heterogeneities and buildings on radiation fog: Large-eddy simulation study at Paris-Charles de Gaulle airport. *Quarterly Journal of the Royal Meteorological Society*, 141(686):285–298.

Bergot, T., Terradellas, E., Cuxart, J., Mira, A., Liechti, O., Mueller, M., and Nielsen, N. W. (2007). Intercomparison of Single-Column Numerical Models for the Prediction of Radiation Fog. *Journal of Applied Meteorology and Climatology*, 46(4):504–521.

Best, M. J., Pryor, M., Clark, D. B., Rooney, G. G., Essery, R. L. H., Ménard, C. B., Edwards, J. M., Hendry, M. A., Porson, A., Gedney, N., Mercado, L. M., Sitch, S., Blyth, E., Boucher, O., Cox, P. M., Grimmond, C. S. B., and Harding, R. J. (2011). The Joint UK Land Environment Simulator (JULES), model description – Part 1: Energy and water fluxes. *Geoscientific Model Development*, 4(3):677–699.

Birmili, W., Yuskiewicz, B., Wiedensohler, A., Stratmann, F., Choularton, T., and Bower, K. (1999). Climate-relevant modification of the aerosol size distribution by processes associated with orographic clouds. *Atmospheric Research*, 50(3-4):241–263.

Blyth, A. M. and Latham, J. (1991). A Climatological Parameterization for Cumulus Clouds. *Journal of the Atmospheric Sciences*, 48(21):2367–2371.

Böing, S. J., Dritschel, D. G., Parker, D. J., and Blyth, A. M. (2019). Comparison of the Moist Parcel-in-Cell (MPIC) model with large-eddy simulation for an idealized cloud. *Quarterly Journal of the Royal Meteorological Society*, 145(722):1868–1881.

Bott, A. (1991). On the influence of the physico-chemical properties of aerosols on the life cycle of radiation fogs. *Boundary-Layer Meteorology*, 56(1-2):1–31.

Bott, A., Sievers, U., Zdunkowski, W., Bott, A., Sievers, U., and Zdunkowski, W. (1990). A Radiation Fog Model with a Detailed Treatment of the Interaction between Radiative Transfer and Fog Microphysics. *Journal of the Atmospheric Sciences*, 47(18):2153–2166.

Boutle, I., Price, J., Kokkola, H., Romakkaniemi, S., Kudzotsa, I., Kokkola, H., and

Romakkaniemi, S. (2018). Aerosol-fog interaction and the transition to well-mixed radiation fog. *Atmos. Chem. Phys*, 18:7827–7840.

Bretherton, C. S., Blossey, P. N., and Uchida, J. (2007). Cloud droplet sedimentation, entrainment efficiency, and subtropical stratocumulus albedo. *Geophysical Research Letters*, 34(3).

Brown, A. R., Derbyshire, S. H., and Mason, P. J. (1994). Large-eddy simulation of stable atmospheric boundary layers with a revised stochastic subgrid model. *Quarterly Journal of the Royal Meteorological Society*, 120(520):1485–1512.

Brown, N., Weiland, M., Hill, A., and Shipway, B. (2018). In situ data analytics for highly scalable cloud modelling on Cray machines. *Concurrency and Computation: Practice and Experience*, 30(1):e4331.

Brown, N., Weiland, M., Hill, A., Shipway, B., Maynard, C., Allen, T., and Rezny, M. (2015). A Highly Scalable Met Office NERC Cloud Model. In *Proceedings of the 3rd International Conference on Exascale Applications and Software*, page 137. University of Edinburgh.

Brown, R. and Roach, W. T. (1976). The physics of radiation fog: II - a numerical study. *Quarterly Journal of the Royal Meteorological Society*, 102(432):335–354.

Businger, J. A., Wyngaard, J. C., Izumi, Y., and Bradley, E. F. (1971). Flux-Profile Relationships in the Atmospheric Surface Layer. *Journal of the Atmospheric Sciences*, 28(2):181–189.

Clark, P. A., Harcourt, S. A., Macpherson, B., Mathison, C. T., Cusack, S., and Naylor, M. (2008). Prediction of visibility and aerosol within the operational Met Office Unified Model. I: Model formulation and variational assimilation. *Quarterly Journal of the Royal Meteorological Society*, 134(636):1801–1816.

Cohard, J.-M., Pinty, J.-P., and Bedos, C. (1998). Extending Twomey's Analytical Es-

timate of Nucleated Cloud Droplet Concentrations from CCN Spectra. *Journal of the Atmospheric Sciences*, 55(22):3348–3357.

Collett, J. L., Herckes, P., Youngster, S., and Lee, T. (2008). Processing of atmospheric organic matter by California radiation fogs. *Atmospheric Research*, 87(3-4):232–241.

Collett, Jr., J. L., Sherman, D. E., Moore, K. F., Hannigan, M. P., and Lee, T. (2001). Aerosol Particle Processing and Removal by Fogs: Observations in Chemically Heterogeneous Central California Radiation Fogs. *Water, Air and Soil Pollution: Focus*, 1(5-6):303–312.

Corradini, C. and Tonna, G. (1979). On the reliability of the parameterization of microphysics in fog models. *Journal of Applied Meteorology*, 18:487 – 494.

Curry, J. A. and Khvorostyanov, V. I. (2012). Assessment of some parameterizations of heterogeneous ice nucleation in cloud and climate models. *Atmospheric Chemistry and Physics*, 12(2):1151–1172.

Dearden, C., Hill, A., Coe, H., and Choularton, T. (2018). The role of droplet sedimentation in the evolution of low-level clouds over southern West Africa. *Atmos. Chem. Phys*, 18:14253–14269.

Duynkerke, P. (1999). Turbulence, Radiation and fog in Dutch Stable Boundary Layers. *Boundary-Layer Meteorology*, 90(3):447–477.

Duynkerke, P. G. (1991). Radiation Fog: A Comparison of Model Simulation with Detailed Observations. *Monthly Weather Review*, 119(2):324–341.

Duynkerke, P. G. and Driedonks, A. G. M. (1988). Turbulent Structure of a Shear-Driven Stratus-Topped Atmospheric Boundary Layer: A Comparison of Model Results with Observations. *Journal of the Atmospheric Sciences*, 45(16):2343–2351.

Edwards, J. M. and Slingo, A. (1996). Studies with a flexible new radiation code. I: Choosing a configuration for a large-scale model. *Quarterly Journal of the Royal Meteorological Society*, 122(531):689–719.

Elias, T., Dupont, J.-C., Hammer, E., Hoyle, C. R., Haeffelin, M., Burnet, F., and Jolivet, D. (2015). Enhanced extinction of visible radiation due to hydrated aerosols in mist and fog. *Atmospheric Chemistry and Physics*, 15(12):6605–6623.

Ferrier, B. S. (1994). A Double-Moment Multiple-Phase Four-Class Bulk Ice Scheme. Part I: Description. *Journal of the Atmospheric Sciences*, 51(2):249–280.

Field, P., Shipway, B., Hill, A., Wilkinson, J., Furtado, K., Grosvenor, D., Miltenberger, A., and Stevens, R. (2016). MOSAC and SRG Meetings 2016 Cloud microphysics and aerosols. Technical report, Met Office, UK.

Flossmann, A. I., Hall, W. D., and Pruppacher, H. R. (1985). A Theoretical Study of the Wet Removal of Atmospheric Pollutants. Part I: The Redistribution of Aerosol Particles Captured through Nucleation and Impaction Scavenging by Growing Cloud Drops. *Journal of the Atmospheric Sciences*, 42(6):583–606.

Fuzzi, S. (1992). The Po Valley fog experiment 1989. An overview. *Tellus*, 44B:448–468.

Garrett, T. J., Radke, L. F., and Hobbs, P. V. (2002). Aerosol Effects on Cloud Emissivity and Surface Longwave Heating in the Arctic. *Journal of the Atmospheric Sciences*, 59(3):769–778.

Gerber, H. (1991). Supersaturation and Droplet Spectral Evolution in Fog. *Journal of the Atmospheric Sciences*, 48(24):2569–2588.

Gerber, H. E. (1981). Microstructure of a Radiation Fog. *Journal of the Atmospheric Sciences*, 38(2):454–458.

Ghan, S., Chuang, C., Easter, R., and Penner, J. (1995). A parameterization of cloud droplet nucleation. Part II: Multiple aerosol types. *Atmospheric Research*, 36(1-2):39–54.

Ghan, S. J., Abdul-Razzak, H., Nenes, A., Ming, Y., Liu, X., Ovchinnikov, M., Shipway, B., Meskhidze, N., Xu, J., and Shi, X. (2011). Droplet nucleation: Physically-based

parameterizations and comparative evaluation. *Journal of Advances in Modeling Earth Systems*, 3(4).

Ghan, S. J., Chung, C. C., and Penner, J. E. (1993). A parameterization of cloud droplet nucleation part I: single aerosol type. *Atmospheric Research*, 30(4):198–221.

Ghan, S. J., Leung, L. R., Easter, R. C., and Abdul-Razzak, H. (1997). Prediction of cloud droplet number in a general circulation model. *Journal of Geophysical Research: Atmospheres*, 102(D18):21777–21794.

Gilardoni, S., Massoli, P., Giulianelli, L., Rinaldi, M., Paglione, M., Pollini, F., Lanconelli, C., Poluzzi, V., Carbone, S., Hillamo, R., Russell, L. M., Facchini, M. C., and Fuzzi, S. (2014). Fog scavenging of organic and inorganic aerosol in the Po Valley. *Atmospheric Chemistry and Physics*, 14(13):6967–6981.

Gray, M. E. B., Petch, J., Derbyshire, S. H., Brown, A. R., Lock, A. P., Swann, H. A., and Brown, P. R. A. (2001). Version 2.3 of the Met. Office large eddy model. *Met Office (APR) Turbulence and Diffusion Rep*, 276.

Grosvenor, D. P., Field, P. R., Hill, A. A., and Shipway, B. J. (2017). The relative importance of macrophysical and cloud albedo changes for aerosol-induced radiative effects in closed-cell stratocumulus: insight from the modelling of a case study. *Atmospheric Chemistry and Physics*, 17(8):5155–5183.

Gultepe, I., Müller, M. D., Boybeyi, Z., Gultepe, I., Müller, M. D., and Boybeyi, Z. (2006). A New Visibility Parameterization for Warm-Fog Applications in Numerical Weather Prediction Models. *Journal of Applied Meteorology and Climatology*, 45(11):1469–1480.

Gultepe, I., Tardif, R., Michaelides, S. C., Cermak, J., Bott, A., Bendix, J., Müller, M. D., Pagowski, M., Hansen, B., Ellrod, G., and Others (2007). Fog research: A review of past achievements and future perspectives. *Pure and Applied Geophysics*, 164(6-7):1121–1159.

Haeffelin, M., Bergot, T., Elias, T., Tardif, R., Carrer, D., Chazette, P., Colomb, M., Drobinski, P., Dupont, E., Dupont, J. C., Gomes, L., Musson-Genon, L., Pietras, C., Plana-Fattori, A., Protat, A., Rangognio, J., Raut, J. C., Rémy, S., Richard, D., Sciare, J., and Zhang, X. (2010). PARISFOG: Shedding new light on fog physical processes. *Bulletin of the American Meteorological Society*, 91(6):767–783.

Haeffelin, M., Dupont, J. C., Boyouk, N., Baumgardner, D., Gomes, L., Roberts, G., and Elias, T. (2013). A Comparative Study of Radiation Fog and Quasi-Fog Formation Processes During the ParisFog Field Experiment 2007. *Pure and Applied Geophysics*, 170(12):2283–2303.

Hammer, E., Gysel, M., Roberts, G. C., Elias, T., Hofer, J., Hoyle, C. R., Bukowiecki, N., Dupont, J.-C., Burnet, F., Baltensperger, U., and Weingartner, E. (2014). Size-dependent particle activation properties in fog during the ParisFog 2012/13 field campaign. *Atmos. Chem. Phys*, 14:10517–10533.

Hansen, J., Sato, M., and Ruedy, R. (1997). Radiative forcing and climate response. *Journal Of Geophysical Research*, 102(D6):6831–6864.

Haywood, J., Bush, M., Abel, S., Claxton, B., Coe, H., Crosier, J., Harrison, M., Macpherson, B., Naylor, M., and Osborne, S. (2008). Prediction of visibility and aerosol within the operational Met Office Unified Model. II: Validation of model performance using observational data. *Quarterly Journal of the Royal Meteorological Society*, 134(636):1817–1832.

Hill, A. A., Brown, N., and Shipway, B. (2018). Met Office/NERC Cloud Model (MONC): User documentation. Technical report, Met Office, UK.

Hill, A. A. and Dobbie, S. (2008). The impact of aerosols on non-precipitating marine stratocumulus. II: The semi-direct effect. *Quarterly Journal of the Royal Meteorological Society*, 134(634):1155–1165.

Hill, A. A., Feingold, G., and Jiang, H. (2009). The Influence of Entrainment and Mixing

Assumption on Aerosol-Cloud Interactions in Marine Stratocumulus. *Journal of the Atmospheric Sciences*, 66:1450–1464.

Hoose, C., Lohmann, U., Bennartz, R., Croft, B., and Lesins, G. (2008). Global simulations of aerosol processing in clouds. *Atmospheric Chemistry and Physics*, 8(23):6939–6963.

IPCC (2001). Climate Change 2001: The Scientific Basis. *Cambridge University Press*.

Jaenicke, R. (1988). Aerosol physics and chemistry.

Johnson, B. T., Shine, K. P., and Forster, P. M. (2004). The semi-direct aerosol effect: Impact of absorbing aerosols on marine stratocumulus. *Meteorol. Soc*, 130:1407–1422.

Kiehl, J. T. and Trenberth, K. E. (1997). Earth's Annual Global Mean Energy Budget. *Bulletin of the American Meteorological Society*, 78(2):197–208.

Köhler, H. (1936). The nucleus in and the growth of hygroscopic droplets. *Transactions of the Faraday Society*, 32:1152–1161.

Lebo, Z. J. and Morrison, H. (2013). A Novel Scheme for Parameterizing Aerosol Processing in Warm Clouds. *Journal of the Atmospheric Sciences*, 70(11):3576–3598.

Lilly, D. (1996). A comparison of incompressible, anelastic and Boussinesq dynamics. *Atmospheric Research*, 40(2-4):143–151.

Lilly, D. K. (1992). A proposed modification of the Germano subgrid-scale closure method. *Physics of Fluids A: Fluid Dynamics*, 4(3):633–635.

Maalick, Z., Kühn, T., Korhonen, H., Kokkola, H., Laaksonen, A., and Romakkaniemi, S. (2016). Effect of aerosol concentration and absorbing aerosol on the radiation fog life cycle. *Atmospheric Environment*, 133:26–33.

Malavelle, F. F., Haywood, J. M., Field, P. R., Hill, A. A., Abel, S. J., Lock, A. P., Shipway, B. J., and McBeath, K. (2014). A method to represent subgrid-scale updraft velocity in kilometer-scale models: Implication for aerosol activation. *Journal of Geophysical Research: Atmospheres*, 119(7):4149–4173.

Maronga, B. and Bosveld, F. C. (2017). Key parameters for the life cycle of nocturnal radiation fog: a comprehensive large-eddy simulation study. *Quarterly Journal of the Royal Meteorological Society*, pages 2463–2480.

Mauritsen, T., Sedlar, J., Tjernström, M., Leck, C., Martin, M., Shupe, M., Sjogren, S., Sierau, B., Persson, P. O. G., Brooks, I. M., and Swietlicki, E. (2011). An Arctic CCN-limited cloud-aerosol regime. *Atmospheric Chemistry and Physics*, 11(1):165–173.

Mazoyer, M., Burnet, F., Roberts, G. C., Haeffelin, M., Dupont, J.-C., and Elias, T. (2016). Experimental study of the aerosol impact on fog microphysics. *Atmospheric Chemistry and Physics Discussions*, pages 1–35.

Mazoyer, M., Lac, C., Thouron, O., Bergot, T., Masson, V., and Musson-Genon, L. (2017). Large eddy simulation of radiation fog: impact of dynamics on the fog life cycle. *Atmospheric Chemistry and Physics*, 17(21):13017–13035.

McDonald, J. E. (1953). Erroneous cloud-physics applications of Raoult's law. *Journal of Meteorology*, 10(1):68–70.

Meskhidze, N., Nenes, A., Conant, W. C., and Seinfeld, J. H. (2005). Evaluation of a new cloud droplet activation parameterization with in situ data from CRYSTAL-FACE and CSTRIPE. *Journal of Geophysical Research: Atmospheres*, 110(D16).

Miltenberger, A. K., Field, P. R., Hill, A. A., Rosenberg, P., Shipway, B. J., Wilkinson, J. M., Scovell, R., and Blyth, A. M. (2018). Aerosol–cloud interactions in mixed-phase convective clouds – Part 1: Aerosol perturbations. *Atmospheric Chemistry and Physics*, 18(5):3119–3145.

Ming, Y., Ramaswamy, V., Donner, L. J., Phillips, V. T. J., Klein, S. A., Ginoux, P. A., and Horowitz, L. W. (2007). Modeling the interactions between aerosols and liquid water clouds with a self-consistent cloud scheme in a general circulation model. *Journal of the Atmospheric Sciences*, 64(4):1189–1209.

Mirocha, J. D., Churchfield, M. J., Muñoz-Esparza, D., Rai, R. K., Feng, Y., Kosović, B., Haupt, S. E., Brown, B., Ennis, B. L., Draxl, C., Sanz Rodrigo, J., Shaw, W. J., Berg, L. K., Moriarty, P. J., Linn, R. R., Kotamarthi, V. R., Balakrishnan, R., Cline, J. W., Robinson, M. C., and Ananthan, S. (2018). Large-eddy simulation sensitivities to variations of configuration and forcing parameters in canonical boundary-layer flows for wind energy applications. *Wind Energy Science*, 3(2):589–613.

Monin, A. S. and Obukhov, A. M. (1954). Basic laws of turbulent mixing in the surface layer of the atmosphere. *Tr. Akad. Nauk SSSR Geophiz. Inst*, 24(151):163–187.

Morrison, H. and Gettelman, A. (2008). A New Two-Moment Bulk Stratiform Cloud Microphysics Scheme in the Community Atmosphere Model, Version 3 (CAM3). Part I: Description and Numerical Tests. *Journal of Climate*, 21(15):3642–3659.

Musson-Genon, L. (1987). Numerical Simulation of a Fog Event with a One-Dimensional Boundary Layer Model. *Monthly Weather Review*, 115(2):592–607.

Nakanishi, M. (2000). Large-eddy simulation of radiation fog. *Boundary-Layer Meteorology*, 94(3):461–493.

Nakanishi, M. and Niino, H. (2004). An Improved Mellor–Yamada Level-3 Model with Condensation Physics: Its Design and Verification. *Boundary-Layer Meteorology*, 112(1):1–31.

Nenes, A. and Seinfeld, J. H. (2003). Parameterization of cloud droplet formation in global climate models. *Journal of Geophysical Research*, 108(D14).

Noone, K. J., Ogren, J. A., Hallberg, A., Heintzenberg, J., StrÖm, J., Hansson, H.-C., Svenningsson, B., Wiedensohler, A., Fuzzi, S., Facchini, M. C., Arends, B. G., and Berner, A. (1992). Changes in aerosol size- and phase distributions due to physical and chemical processes in fog. *Tellus B: Chemical and Physical Meteorology*, 44(5):489–504.

Ogura, Y. and Phillips, N. A. (1962). Scale Analysis of Deep and Shallow Convection in the Atmosphere. *Journal of the Atmospheric Sciences*, 19(2):173–179.

Penner, J. E., Dong, X., and Chen, Y. (2004). Observational evidence of a change in radiative forcing due to the indirect aerosol effect. *Nature*, 427(6971):231–234.

Pielke, R. A. and Cram, J. M. (1987). An Alternate Procedure for Analyzing Surface Geostraphic Winds and Pressure over Elevated Terrain. *Weather and Forecasting*, 2(3):229–236.

Poku, C., Ross, A. N., Blyth, A. M., Hill, A. A., and Price, J. D. (2019). How important are aerosol–fog interactions for the successful modelling of nocturnal radiation fog? *Weather*, pages 237–243.

Porson, A., Price, J., Lock, A., and Clark, P. (2011). Radiation Fog. Part II: Large-Eddy Simulations in Very Stable Conditions. *Boundary-Layer Meteorology*, 139(2):193–224.

Price, J. (2011). Radiation Fog. Part I: Observations of Stability and Drop Size Distributions. *Boundary-Layer Meteorology*, 139(2):167–191.

Price, J. D. (2019). On the Formation and Development of Radiation Fog: An Observational Study. *Boundary-Layer Meteorology*, pages 1–31.

Price, J. D. and Clark, R. (2014). On the Measurement of Dewfall and Fog-Droplet Deposition. *Boundary-Layer Meteorology*, 152(3):367–393.

Price, J. D., Lane, S., Boutle, I. A., Smith, D. K. E., Bergot, T., Lac, C., Duconge, L., McGregor, J., Kerr-Munslow, A., Pickering, M., and Clark, R. (2018). LANFEX: a field and modeling study to improve our understanding and forecasting of radiation fog. *Bulletin of the American Meteorological Society*, pages 2061–2077.

Pruppacher, H. and Klett, J. (2010). *Microphysics of Clouds and Precipitation*, volume 18 of *Atmospheric and Oceanographic Sciences Library*. Springer.

Rangognio, J., Tulet, P., Bergot, T., Gomes, L., Thouron, O., and Leriche, M. (2009). Influence of aerosols on the formation and development of radiation fog. *Atmospheric Chemistry and Physics Discussions*, 9(5):17963–18019.

Roach, W. T. (1976). On the effect of radiative exchange on the growth by condensation of a cloud or fog droplet. *Quarterly Journal of the Royal Meteorological Society*, 102(432):361–372.

Roach, W. T., Brown, R., Caughey, S. J., Garland, J. A., and Readings, C. J. (1976). The physics of radiation fog: I - A field study. *Quarterly Journal of the Royal Meteorological Society*, 102(432):313–333.

Rogers, R. and Yau, M. K. (1989). *A short course in cloud physics*. Butterworth-Heinemann.

Schwenkel, J. and Maronga, B. (2019). Large-eddy simulation of radiation fog with comprehensive two-moment bulk microphysics: impact of different aerosol activation and condensation parameterizations. *Atmospheric Chemistry and Physics*, 19(10):7165–7181.

Shine, K. P. and Forster, P. M. F. (1999). The effect of human activity on radiative forcing of climate change: a review of recent developments. *Global and Planetary Change*, 20(4):205–225.

Shipway, B. and Abel, S. (2010). Analytical estimation of cloud droplet nucleation based on an underlying aerosol population. *Atmospheric Research*, 96(2-3):344–355.

Shipway, B. J. (2015). Revisiting Twomey's approximation for peak supersaturation. *Atmospheric Chemistry and Physics*, 15(7):3803–3814.

Shipway, B. J. and Hill, A. A. (2012). Diagnosis of systematic differences between multiple parametrizations of warm rain microphysics using a kinematic framework. *Quarterly Journal of the Royal Meteorological Society*, 138(669):2196–2211.

Sky News (2018). Fog sparks cancellations and delays at airports as Storm Diana looms.

Slingo, A. (1989). A GCM parameterization for the shortwave radiative properties of water clouds. *Journal of the Atmospheric Sciences*, 46(10):1419–1427.

Smagorinsky, J. (1963). General Circulation Experiments with the Primitive Equations: 1. The Basic Experiment. *Monthly Weather Review*, 91(3):99–164.

Smith, D. K. E., Renfrew, I. A., Price, J. D., and Dorling, S. R. (2018). Numerical modelling of the evolution of the boundary layer during a radiation fog event. *Weather*, 73(10):310–316.

Squires, P. (1952). The Growth of Cloud Drops by Condensation. I. General Characteristics. *Australian Journal of Chemistry*, 5(1):59.

Squires, P. (1958). The Microstructure and Colloidal Stability of Warm Clouds: Part II-The Causes of the Variations in Microstructure. *Tellus*, 10(2):262–271.

Srivastava, S. K., Sharma, A. R., and Sachdeva, K. (2016). Spatial and Temporal Variability of Fog Over the Indo-Gangetic Plains, India. *International Journal of Environmental and Ecological Engineering*, 10(11):1042–1057.

Stevens, R. G., Loewe, K., Dearden, C., Dimitrelos, A., Possner, A., Eirund, G. K., Raatikainen, T., Hill, A. A., Shipway, B. J., Wilkinson, J., Romakkaniemi, S., Tonttila, J., Laaksonen, A., Korhonen, H., Connolly, P., Lohmann, U., Hoose, C., Ekman, A. M. L., Carslaw, K. S., and Field, P. R. (2018). A model intercomparison of CCN-limited tenuous clouds in the high Arctic. *Atmospheric Chemistry and Physics*, 18(15):11041–11071.

Stolaki, S., Haeffelin, M., Lac, C., Dupont, J.-C., Elias, T., and Masson, V. (2015). Influence of aerosols on the life cycle of a radiation fog event. A numerical and observational study. *Atmospheric Research*, 151:146–161.

Stull, R. (2017). *Practical Meteorology: An Algebra-based Survey of Atmospheric Science*. Univ. of British Columbia, 1.02b edition.

Stull, R. B. (1988). *An introduction to boundary layer meteorology*. Kluwer Academic Publishers.

Tardif, R. and Rasmussen, R. M. (2007). Event-Based Climatology and Typology of Fog in the New York City Region. *Journal of Applied Meteorology and Climatology*, 46(8):1141–1168.

Taylor, G. I. (1917). The formation of fog and mist. *Quarterly Journal of the Royal Meteorological Society*, 43(183):241–268.

Tonttila, J., Maalick, Z., Raatikainen, T., Kokkola, H., Kühn, T., and Romakkaniemi, S. (2017). UCLALES–SALSA v1.0: a large-eddy model with interactive sectional microphysics for aerosol, clouds and precipitation. *Geoscientific Model Development*, 10(1):169–188.

Turton, J. D. and Brown, R. (1987). A comparison of a numerical model of radiation fog with detailed observations. *Quarterly Journal of the Royal Meteorological Society*, 113(475):37–54.

Twomey, S. (1959). The nuclei of natural cloud formation part II: The supersaturation in natural clouds and the variation of cloud droplet concentration. *Pure and Applied Geophysics*, 43(1):243–249.

Twomey, S. (1974). Pollution and the planetary albedo. *Atmospheric Environment (1967)*, 8(12):1251–1256.

Twomey, S. (1977). The Influence of Pollution on the Shortwave Albedo of Clouds. *Journal of the Atmospheric Sciences*, 34(7):1149–1152.

van der Velde, I. R., Steeneveld, G. J., Wichers Schreur, B. G. J., and Holtslag, A. A. M. (2010). Modeling and Forecasting the Onset and Duration of Severe Radiation Fog under Frost Conditions. *Monthly Weather Review*, 138(11):4237–4253.

Vie, B., Pinty, J. P., Berthet, S., and Leriche, M. (2016). LIMA (v1.0): A quasi two-moment microphysical scheme driven by a multimodal population of cloud condensation and ice freezing nuclei. *Geoscientific Model Development*, 9(2):567–586.

Von Glasow, R. and Bott, A. (1999). Interaction of radiation fog with tall vegetation. *Atmospheric Environment*, 33(9):1333–1346.

Warner, J. (1968). The supersaturation in natural clouds. *Journal de recherches atmospheriques*, 3(3):233–237.

West, R. E. L., Stier, P., Jones, A., Johnson, C. E., Mann, G. W., Bellouin, N., Partridge, D. G., and Kipling, Z. (2014). The importance of vertical velocity variability for estimates of the indirect aerosol effects. *Atmos. Chem. Phys*, 14:6369–6393.

Whitby, K. T. (1978). The physical characteristics of sulfur aerosols. *Atmospheric Environment (1967)*, 12(1-3):135–159.

WHO (2006). Air quality guidelines for particulate matter, ozone, nitrogen dioxide and sulfur dioxide. Technical report, Geneva: World Health Organization.

Wiedensohler, A., Hansson, H.-C., Orsini, D., Wendisch, M., Wagner, F., Bower, K., Chourlarton, T., Wells, M., Parkin, M., Acker, K., Wieprecht, W., Facchini, M., Lind, J., Fuzzi, S., Arends, B., and Kulmalao, M. (1997). Night-time formation and occurrence of new particles associated with orographic clouds. *Atmospheric Environment*, 31(16):2545–2559.

WMO (1966). International Meteorological Vocabulary.

Wood, R. (2012). Stratocumulus Clouds. *Monthly Weather Review*, 140(8):2373–2423.

Yuan, T., Li, Z., Zhang, R., and Fan, J. (2008). Increase of cloud droplet size with aerosol optical depth: An observation and modeling study. *Journal of Geophysical Research*, 113(D4).

Zdunkowski, W. G. and Nielsen, B. C. (1969). A preliminary prediction analysis of radiation fog. *Pure and Applied Geophysics PAGEOPH*, 75(1):278–299.

Zhang, X., Musson-Genon, L., Dupont, E., Milliez, M., and Carissimo, B. (2014). On the influence of a simple microphysics parametrization on radiation fog modelling: A case study during ParisFog. *Boundary-layer Meteorology*, 151(2):293–315.